Revisiting U-Pb and ^{26}Al-^{26}Mg systematics of calcium aluminum-rich inclusions: Applications on early Solar System chronology and evolution history

Thesis by
Haoyu Li

In Partial Fulfillment of the Requirements for the
Degree of
Doctor of Philosophy

CALIFORNIA INSTITUTE OF TECHNOLOGY
Pasadena, California

2024
Defended May 16, 2024

ACKNOWLEDGEMENTS

The past six years at Caltech have been incredible and memorable times in my life, for the small and sweet campus dominated by Spanish-themed architecture, for the sunshine in Southern California that can get rid of any depressed emotions, and especially for the many individuals that I would like to express my appreciation for their support along the way towards the completion of my PhD journey.

First and foremost, I would like to express my deepest appreciation to my advisor, Prof. François Tissot, for the scientific training I received in the Isotoparium. Francois is always responsive and patient while answering my questions. He spent a lot of time discussing with me every aspect of research and was excited about every piece of my progress during scientific exploration. I benefit from being exposed to various aspects as an independent investigator, including not only the development of lab skills, independence in problem-solving, and paper writing but also the opportunity to write proposals and mentor students. His positive attitude and detail-oriented standards shaped my comprehension of how to perform high-quality research. This thesis would not have been possible without input and support from Francois.

I would like to thank my committee members, Prof. John Eiler, Prof. Woodward Fischer, Prof. Yuri Amelin, and Dr. Alexander Krot, for their constructive feedback and discussions, which have given me new insights to refine my research. Thanks also go to my academic advisor, Prof. Jess Adkins, for his guidance on my first-year project and especially the time he spent on weekly reading, which sparked my interest in oceanography.

I would like to thank the current and previous group members of the Isotoparium. Special thanks to Prof. Michael Kipp for teaching me various lab skills in the clean lab and mass spectrometry, which helped me to become a qualified isotope geochemist; Prof. Gerrit Budde for being a role model in the clean lab for setting up a high-standard and careful in performing experiments; Prof. Nicole (Xike) Nie for chatting about the difficulties and concerns that I encountered as an early career researcher. As the first two graduate students in the lab, I would also thank Dr. Ren Marquez for being my office mate for six years and for all the discussions on research and life. Thanks to other members with an incomplete list of Dr. Eugenia Hyung, Dr. Rosa Grigoryan, Teng Ee (Tony) Yap, Hayward Melton, Shane Houchin, Weiyi Liu, and Emily Miaou. I would also thank my collaborators: Prof. Haolan Tang for helping me develop magnesium isotope techniques and advice on career development; and Dr. Yankun Di for the great discussion on chronology. My thanks also extend to Dr. Chi Ma and Dr. Yunbin Guan for the helpful discussion when I conducted analyses with GPS facilities.

Finally, a heartfelt thank you to my family for their unconditional love and encouragement. To my parents, Qinting Zhao and Shuanming Li, for their endless support and belief in me. To my partner, Dr. Lue (Leo) Wu for your unconditional support and the joyful time we spent together, which makes overcoming the difficulties during the PhD life much easier.

Thank you all for your support and for making this journey a truly memorable and enriching experience.

ABSTRACT

Stable isotope systematics are powerful tools for understanding the evolution history of the Earth and Solar system. In this thesis, I present applications of uranium (U) and magnesium (Mg) isotopes in both geochemistry and cosmochemistry.

Uranium is sensitive to the dissolved oxygen level in aqueous environment, and these redox reactions are associated with resolvable isotopic fractionation. Thus, U isotopes (^{238}U/^{235}U, expressed as δ^{238}U) are widely used in paleo-environment reconstruction as a proxy of marine anoxia. *Chapter 4* includes two pieces of work for this application. Firstly, I explored the potential of bioapatite as a novel paleoredox proxy. The results demonstrate that U was incorporated into shark teeth postmortem during burial. Fluctuations of Cenozoic shark teeth δ^{238}U values are comparable to the variability observed in marine carbonate sediments, indicating U isotope composition of fossil shark teeth is influenced by local redox conditions and depositional environments, which complicate their application as a paleo-redox archive. The second part re-calibrated the U isotope composition of seawater. Subtle isotopic heterogeneity is observed in the ocean, which results from local and/or global impacts of processes that fractionate U isotopes.

Long-lived and short-lived systematics provide constraints on the time sequence and composition of the early Solar System. Of all absolute chronometers, dual decay Pb-Pb system (^{238}U→^{206}Pb, ^{235}U→^{207}Pb) provided the highest resolution on the events in the early Solar System (∼4.57 Gyr). On the other hand, the short-lived ^{26}Al-^{26}Mg decay system is the most widely used relative chronometer of calcium-aluminum rich inclusions (CAIs): internal isochrons date the crystallization age while bulk isochrons provide unique information about their precursors. *Chapter 5* investigated ^{26}Al-^{26}Mg systematics of bulk CAIs. I found CAIs cover a wide range of initial (pre-^{26}Al decay) Mg isotope composition, indicating the infalling materials that formed the early protoplanetary disk were heterogeneous and experienced continuous evolution during the CAI-forming epoch. *Chapter 4* includes combined Pb-Pb and ^{26}Al-^{26}Mg systematics on CAIs to resolve the discrepancies between these two chronometers and I found these two mostly widely chronometers can be decoupled reset.

This thesis also presents the analytical techniques developed for the studies above (*Chapter 2*), which includes U and Mg isotope analyses, in-situ ^{26}Al-^{26}Mg SIMS analyses, and distribution coefficients determination. Furthermore, I introduce a comprehensive uranium isotope database in *Chapter 3*, which significantly improved the data retrieval efficiency for the U isotope community.

PUBLISHED CONTENT AND CONTRIBUTIONS

Li, H., Kipp, M. A., Kim, S. L., Kast, E. R., Eberle, J. J., and Tissot, F. L. H. (2024). Exploring uranium isotopes in shark teeth as a paleo-redox proxy. *Geochimica et Cosmochimica Acta* 365, 158–173. DOI: 10.1016/j.gca.2023.11.034.

H.L. participated in methodology, formal analysis, investigation, data curation, visualization and writing the original draft.

Li, H. and Tissot, F. L. H. (2023). UID: The uranium isotope database. *Chemical Geology* 618, 121221. DOI: 10.1016/j.chemgeo.2022.121221.

H.L. participated in conceptualization, methodology, formal analysis, investigation, data curation, visualization and writing the original draft.

Kipp, M. A., Li, H., Ellwood, M. J., John, S. G., Middag, R., Adkins, J. F., and Tissot, F. L. H. (2022). ^{238}U, ^{235}U and ^{234}U in seawater and deep-sea corals: A high-precision reappraisal. *Geochimica et Cosmochimica Acta* 336, 231–248. DOI: 10.1016/j.gca.2022.09.018.

H.L. participated for investigation, validation, and reviewing & editing the draft.

Li, H., Tissot, F. L. H., Lee, S.-G., Hyung, E., and Dauphas, N. (2020). Distribution coefficients of the REEs, Sr, Y, Ba, Th, and U between α-HIBA and AG50W-X8 resin. *ACS Earth and Space Chemistry* 5.1, 55–65. DOI: 10.1021/acsearthspacechem.0c00273.

H.L. participated in formal analysis, data curation, visualization and writing the original draft.

TABLE OF CONTENTS

Acknowledgements . . . iii
Abstract . . . v
Published Content and Contributions . . . vi
Table of Contents . . . vi
List of Illustrations . . . x
List of Tables . . . xiv
Chapter I: Introduction . . . 1
  1.1 Redox-sensitive trace metals as paleo-environmental indicators . . . 1
  1.2 Long-lived and short-lived radionuclides . . . 4
    1.2.1 Radioactive decay . . . 4
    1.2.2 U-Pb systematics . . . 5
    1.2.3 Al-Mg systematics . . . 6
  1.3 Scientific questions . . . 8
  1.4 Outline of the thesis . . . 9
Chapter II: Analytical techniques . . . 12
  2.1 Determination of distribution coefficients . . . 12
    2.1.1 Motivation . . . 13
    2.1.2 Experimental setup . . . 15
    2.1.3 Results . . . 23
    2.1.4 Discussion . . . 26
  2.2 Mg isotope analyses for CAIs . . . 32
    2.2.1 Magnesium chromatography . . . 32
    2.2.2 Mass spectrometry for Mg isotope analyses . . . 33
    2.2.3 Determination of ^{27}Al/^{24}Mg ratio . . . 34
  2.3 In-situ ^{26}Al-^{26}Mg analyses . . . 37
  2.4 U isotope analyses . . . 39
    2.4.1 Chromatography . . . 39
    2.4.2 Mass spectrometry . . . 42
Chapter III: Introduction the UID: Uranium isotope database . . . 45
  3.1 Motivation . . . 45
  3.2 A brief history of U isotope measurements . . . 47
  3.3 Guide to the UID database . . . 49
    3.3.1 Data source and general considerations . . . 49
    3.3.2 Structure of the database . . . 51
    3.3.3 Data retrieval . . . 56
  3.4 Data representation . . . 56
    3.4.1 Notations for uranium isotopes . . . 56
    3.4.2 Normalization of ^{238}U/^{235}U data . . . 58
    3.4.3 Normalization of ^{234}U/^{238}U data . . . 61
  3.5 Discussion . . . 64
    3.5.1 δ^{238}U in uranium standards and geostandards . . . 64

3.5.2 Scope of uranium isotopic studies and future direction 69
3.6 Conclusions 93
Chapter IV: Uranium isotopes as a paleo-redox proxy: Explore new archive and calibrate seawater composition 95
4.1 Exploring uranium isotopes in shark teeth as a paleo-redox proxy . . 96
4.1.1 Motivation 96
4.1.2 Methods 98
4.1.3 Results 105
4.1.4 Discussion 109
4.1.5 Conclusion 123
4.2 High-precision reappraisal of U isotope composition in modern seawater and deep-sea corals 124
4.2.1 Motivation 124
4.2.2 Sample 124
4.2.3 Results 125
Chapter A: 128
Chapter V: Continuously heterogeneous infall of the early Solar System from magnesium isotopes in refractory inclusions 132
5.1 Motivation 132
5.2 Materials and method 133
5.2.1 Sample selection 133
5.2.2 Sample preparation 133
5.2.3 Petrological characterization 134
5.2.4 Mg isotope analyses 134
5.2.5 In-situ Al-Mg analyses 135
5.3 Results 135
5.3.1 Description of CAIs 135
5.3.2 Mg isotopes of bulk CAIs 145
5.3.3 Internal Al-Mg isochrons 149
5.4 Discussion 159
5.4.1 Initial Mg isotope composition of CAIs 159
5.4.2 Heterogeneous infalling materials during the CAI formation epoch 165
Chapter B: 168
Chapter VI: Decoupled resetting of Pb-Pb and Al-Mg chronometers in CAIs challenges the starting point of the Solar System 172
6.1 Motivation 172
6.2 Sample and method 175
6.2.1 Sample preparation 175
6.2.2 Mineralogy and petrology characterization 176
6.2.3 U isotope analyses 176
6.2.4 U-Pb isotope analyses 178
6.2.5 In-situ Al-Mg analyses 178
6.3 Results 179
6.3.1 Brief description of CAIs 179
6.3.2 U isotopes 180
6.3.3 Pb isotopes and Pb-Pb ages 181
6.3.4 Al-Mg ages 184

6.4 Discussion 184
6.4.1 Comparison of the Pb-Pb ages between CAIs from different host chondrites 184
6.4.2 Decoupled resetting of Pb-Pb and Al-Mg chronometers 185
Bibliography 187

LIST OF ILLUSTRATIONS

Number *Page*
1.1 Box model of modern U isotope budget 2
1.2 U isotope composition of modern carbonate sediments from Bahamas 3
1.3 The impact of U isotope variations in CAIs on Pb-Pb age determination 6
1.4 Internal and bulk ^{26}Al-^{26}Mg isochrons 7
2.1 Illustration of REEs separation using α-HIBA and AG50W-X8 14
2.2 Sensitivity tests for the elution simulations depending on column dimensions. 20
2.3 Sensitivity tests for the elution simulations depending on resin properties. 21
2.4 Distribution coefficients of REEs and Ba, Sr, Y, Th, and U on AG50W-X8 resin as a function of α-HIBA molarity. 23
2.5 Distribution coefficients of REEs on AG50W-X8 resin in logarithmic scale as a function of α-HIBA molarity. 24
2.6 The 95% confidence intervals of best-fit linear regression lines for determination of REE K_d as a function of α-HIBA molarity. 25
2.7 Slope and intercept of the linear regressions as a function of the reciprocal of ionic radii. 28
2.8 Experimental and simulated elution profiles of Elution 1 31
2.9 Experimental and simulated elution profiles of Elution 2 31
2.10 Elution profile of DTS-2 for Mg separation. 33
2.11 The ^{27}Al/^{24}Mg ratios of geostandards and CAIs 36
2.12 Schematic illustration of standard addition method for concentration determination. 36
2.13 IMF characterization in one session 38
2.14 Photo of preFAST System 41
2.15 SEM-Faraday cup yield calibration through 16 consecutive analytical sequences 43
2.16 Limits on internal precision of U isotope analyses. 44
3.1 The number of publications per year reporting ^{238}U/^{235}U and ^{238}U/^{235}U analyses published per year. 46
3.2 Structure of the UID 52
3.3 Flowchart of the protocol for the normalization of ^{238}U/^{235}U data in the UID. 58
3.4 Flowchart of the protocol for the normalization of ^{234}U/^{238}U data in the UID. 62

3.5 Summary of U isotope compositions of certified U isotope and concentration standards . . . 65
3.6 Summary of δ^{238}U values of rock geostandards . . . 67
3.7 Summary of δ^{238}U values of ore and mineral geostandards . . . 68
3.8 Summary of δ^{238}U values of widely used geostandards . . . 69
3.9 Compilation of δ^{238}U uncertainties obtained using different analytical techniques . . . 70
3.10 Relationship between δ^{238}U uncertainties and mass of U analyzed in nanograms . . . 73
3.11 Compilation of δ^{238}U values in carbonates and shales . . . 76
3.12 Compilation of δ^{238}U values in water samples and world map illustrating the water sample locations . . . 77
3.13 Compilation of δ^{238}U values in ore deposits. . . . 80
3.14 Compilation of δ^{238}U values iof extraterrestrial samples. . . . 82
3.15 Relationship between the isotope fractionation factor (α) and half-life of aqueous U(VI) for various U removal reactions. . . . 90
4.1 Histology of shark tooth. . . . 96
4.2 Localities of the fossil shark teeth and sediments used in this study. . . 99
4.3 Histogram of U concentrations in enameloid of modern and fossil shark teeth. . . . 105
4.4 U concentration trends across tissues . . . 106
4.5 δ^{238}U vs. δ^{234}U$_{\text{sec}}$ in the shark teeth enameloid from different localities, and different tissues . . . 107
4.6 δ^{238}U vs. δ^{18}O$_{\text{PO4}}$ and δ^{234}U$_{\text{sec}}$ vs. δ^{18}O$_{\text{PO4}}$ in the enameloid of fossil shark teeth . . . 109
4.7 Schematic impact of various processes on U isotope composition . . . 112
4.8 δ^{238}U vs. U/Th and δ^{234}U$_{\text{sec}}$ vs. U/Th in enameloid tissues of fossil shark teeth . . . 114
4.9 U isotope trends vs. U/Th concentration ratios in enameloid tissues of fossil shark teeth . . . 115
4.10 U isotope vs. U concentration in sediments and the enameloid of fossil shark teeth . . . 116
4.11 Predicted δ^{234}U$_{\text{sec}}$ vs. grain radius in porewater-sediments system . . 119
4.12 U isotopes variations in Cenozoic (up to 66 Ma) shark teeth and various archives used for paleoredox reconstructions . . . 123
4.13 Locations of seawater and coral samples . . . 125
A.1 Photos of shark teeth investigated in this study. . . . 128
A.2 U concentration trends across fossil shark tooth LMS001-05 . . . 130

A.3 Replicate measurements of δ^{238}U and δ^{234}U$_{\text{sec}}$ in enameloid of a *Otodus megalodon* tooth . . . 130
5.1 Petrography of CG*ft*-4 . . . 136
5.2 Petrography of CG*ft*-5 . . . 137
5.3 Petrography of CG*ft*-6 . . . 138
5.4 Petrography of CG*ft*-7 . . . 139
5.5 Petrography of CG*ft*-8 . . . 140
5.6 Petrography of CG*ft*-10 . . . 141
5.7 Petrography of CG*ft*-11 . . . 142
5.8 Petrography of CG*ft*-12 . . . 143
5.9 Petrography of CG*ft*-12 . . . 144
5.10 ^{26}Al-^{26}Mg isochron diagram and probability density plot of Δ_0^{26} for bulk CAIs . . . 147
5.11 Summary of Δ_0^{26} for CAIs. . . . 148
5.12 ^{26}Al-^{26}Mg isochron diagrams for CAIs (a) W(285)429 and (b) L2628-12-AM. . . . 152
5.13 ^{26}Al-^{26}Mg isochron diagrams for L2628-13-AM (a) without anorthite and (b) with anorthite. . . . 152
5.14 ^{26}Al-^{26}Mg isochron diagrams for CG*ft*-4 measured at (a) CRPG and (b) UCLA. . . . 153
5.15 ^{26}Al-^{26}Mg isochron diagrams for CG*ft*-5 measured at (a) CRPG and (b) UCLA. . . . 153
5.16 ^{26}Al-^{26}Mg isochron diagrams for CG*ft*-6 measured at (a) CRPG and (b) UCLA. . . . 154
5.17 ^{26}Al-^{26}Mg isochron diagrams for CG*ft*-7 measured at (a) CRPG and (b) UCLA. . . . 154
5.18 ^{26}Al-^{26}Mg isochron diagrams for CG*ft*-8 measured at (a) CRPG and (b) UCLA; melilite + spinel nodules (c)–(g). . . . 155
5.19 ^{26}Al-^{26}Mg isochron diagrams for CG*ft*-10 measured at (a, b) CRPG and (c) UCLA. . . . 156
5.20 ^{26}Al-^{26}Mg isochron diagrams for CG*ft*-11 Epoxy mount X measured at (a, b) CRPG and (c) UCLA. . . . 157
5.21 ^{26}Al-^{26}Mg isochron diagrams for CG*ft*-11 Epoxy mount 3 measured at (a) CRPG and (b) UCLA. . . . 158
5.22 ^{26}Al-^{26}Mg isochron diagrams for CG*ft*-13 measured at (a) CRPG and (b) UCLA. . . . 158
5.23 $\delta^{26}\text{Mg}_0^*$ vs. $^{26}\text{Al}/^{27}\text{Al}$ obtained from internal isochrons, representing the Mg isotope evolution in CAIs. . . . 161
5.24 Comparison of initial Mg isotope composition of CAIs: Δ_0^{26} vs. $\delta^{26}\text{Mg}_{0,i}^*$ 162

5.25 Schematic diagram of CAI formation process and Δ_0^{26} vs. $\ln(^{26}\mathrm{Al}/^{27}\mathrm{Al})$ 166

B.1 Schematic bulk isochron, internal isochron, and Mg evolution diagrams showing the impact of closed system processing 168

B.2 Schematic bulk isochron, internal isochron, and Mg evolution diagrams showing the impact of open system processing that CAI re-equilibrated with the nebula gas 169

B.3 Schematic bulk isochron, internal isochron, and Mg evolution diagrams showing the impact of open system processing that CAI exchanged with the nebula gas 170

B.4 Schematic bulk isochron, internal isochron, and Mg evolution diagrams showing the impact of partial evaporation 171

6.1 Discrepancies between Pb-Pb ages and ^{26}Al-^{26}Mg ages in the ESS chronology. 173

6.2 Minerals separated from CAI. (a) transparent, (b) white, (c) grey, and (d) black fractions. The diameter of the bottle is ~ 2 cm. 176

6.3 U isotope composition of bulk CAIs and mineral separates 180

6.4 Pb-Pb age of CAI CG*ft*-6 183

6.5 Pb-Pb age of 6 CAIs investigated in this study 184

6.6 U corrected Pb-Pb ages of CAIs from Allende and Efremovka 185

6.7 Comparison of ^{26}Al-^{26}Mg and Pb-Pb ages. 186

LIST OF TABLES

Number *Page*

2.1 Faraday Cup Configuration Used for REE Concentration Measurements on the MC–ICPMS 17
2.2 Architecture of the chromatography simulation code 19
2.3 Distribution Coefficients (K_d) of REEs, Sr, Y, Ba, Th, and U, at pH = 4.50^a 22
2.4 Linear regression statistics for determination of REE K_d as a function of α-HIBA molarity at pH=4.50^a. 24
2.5 Magnesium ion exchange chromatography 32
2.6 Cup configurations for Mg isotope measurements on MC-ICPMS 33
2.7 Uranium ion exchange chromatography 40
2.8 Cup configurations for U isotope measurements on MC-ICPMS 42
3.1 Acronyms for terminologies in technique column 50
3.2 Sorting criteria in the UID and subdatabases 57
3.3 Summary of recommended δ^{238}U and ^{238}U/^{235}U of standards, relative to CRM-145. 59
3.4 How published U isotope data are consistently renormalized into the UID 61
4.1 Summary of locality, formation, age, U isotope compositions, U and Th concentrations, U/Th ratios, and O isotope composition of shark teeth and sediments measured in this study. 100
4.2 Parameters in alpha recoil model in porewater system 118
4.3 Summary of U isotopes in paleoredox archives in Cenozoic (up to 66 Ma).122
4.4 Uranium isotope data of modern seawater and deep-sea corals 126
4.4 Uranium isotope data of modern seawater and deep-sea corals 127
A.1 Major and trace element concentrations (in ppm) of shark teeth and sediments measured in this study. 131
5.1 Mg isotope and ^{27}Al/^{24}Mg data for bulk CAIs 145
5.2 Internal ^{26}Al-^{26}Mg isochron of CAIs. Inferred ^{26}Al/^{27}Al ratios, $\delta^{26}\mathrm{Mg}^*_0$, goodness of fit, and number of point analyses used for regression. 151
6.1 Sample information of CAIs investigated in this study, and analyses conducted on each sample. 175
6.2 U isotope composition of bulk CAIs, CAI mineral separates, and bulk chondrite. 181

Chapter 1

INTRODUCTION

The appearance of the Multi-Collector Inductively Coupled Plasma Mass Spectrometer (MC-ICPMS) in the early 1990s (Walder and Freedman 1992) has significantly improved the analytical precision of metal isotope analyses. The technical advances of MC-ICP-MS instruments to resolve isotopic variations at the sub-permil level marks the start of the field of non-traditional isotopes. After two decades of efforts, numerous applications have been developed for non-traditional isotope systematics, letting them already become traditional (remaining powerful) approaches in geochemistry and cosmochemistry. This chapter aimed to introduce the principle and applications of the two isotope systematics (*i.e.,* uranium and magnesium), as well as the scientific questions addressed in this thesis. **Section 1.1** introduces the application of U isotopes in geochemistry, which covers Chapter III and IV. Then, **Section 1.2** moves the gear to the cosmochemistry, which covers Chapter V and VI.

1.1 Redox-sensitive trace metals as paleo-environmental indicators

The redox history (especially molecular oxygen, O_2) of the atmosphere and ocean is of interest in paleoenvironmental studies because of its cause-effect relationships with the evolution of life on Earth. During the Phanerozoic, many mass extinction events are related to the expanded marine anoxia. However, the timing and magnitude of oceanic oxygenation are less well-constrained than the atmosphere. Many trace metals (*e.g.,* Mn, Cr, V, Re, Fe, U, Mo, and Se) are redox-sensitive elements whose authigenic enrichment in marine sediments is controlled by redox conditions (*e.g.,* Anbar et al. 2007; Arnold et al. 2004; Frei et al. 2009; Pogge von Strandmann et al. 2015; Rouxel et al. 2005; Scott et al. 2008). Redox-sensitive trace metals remain soluble in oxic settings but can be immobilized through reduction reactions in anoxic conditions, so the enrichments of these metals in marine sediments can indicate low-O_2 bottom waters (Tribovillard et al. 2006). As a redox-sensitive metal, U has long residence time (τ ~400 kyr in the well-oxygenated modern ocean, Dunk et al. 2002; Ku et al. 1977), much longer than global ocean mixing time (~1 kyr, Broecker and Peng 1982). The conservative behavior of U makes it considered a global proxy for marine anoxia, which is a major advantage over many other redox-sensitive metals that act as local redox indicators. Uranium has two oxidation states in the terrestrial surface environment: insoluble U(IV) and soluble U(VI) (Langmuir 1978). Decreases in dissolved oxygen in the aqueous environment can reduce U(VI) to U(IV) and lead to U removal from the water column and enrichment in the sediments. However, organic carbon flux can influence the enrichment of authigenic U (*e.g.,* Chase et al. 2001; McManus et al. 2005), making it complicated to disentangle redox controls from productivity controls on U accumulation in sediments. Given the limitations, U enrichment (indicated by elemental abundances) is limited as a qualitative proxy of local paleo-redox conditions.

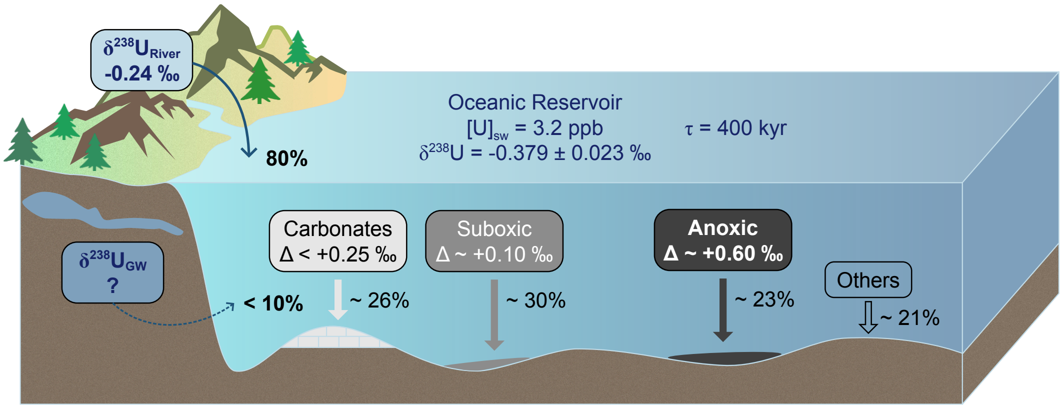

Figure 1.1: Box model of modern U isotope budget. The U source to the ocean is dominated by riverine inputs. The U sinks are primarily composed of carbonates, suboxic, and anoxic sediments, while other minor outputs includes ferromanganese crusts/nodules, hydrothermal circulation, and oceanic crust alteration.

The discovery of U isotope variations in natural terrestrial materials (Stirling et al. 2007; Weyer et al. 2008) provides an opportunity to use uranium to reconstruct the paleo-redox conditions in a quantitative approach. **Fig. 1.1** shows the U cycling in the modern ocean. Uranium inputs to the ocean are dominated riverine flux from continental weathering, with a $^{238}U/^{235}U$ composition identical to that of the continental crust (Andersen et al. 2016; Tissot and Dauphas 2015), suggesting a lack of significant fractionation during oxic weathering and transport of U to the ocean. In the modern ocean, U output is composed of three main sinks: carbonates, suboxic/hypoxic sediments, and anoxic/euxinic sediments (Dunk et al. 2002). The process of U reduction is associated with an average isotopic fractionation (Δ_{anoxic}) of ~+0.6 ‰ (Andersen et al. 2014), meaning that ^{238}U is preferentially scavenged into anoxic/euxinic sediments. This depletes the ocean of ^{238}U; as a result, modern seawater has an average $\delta^{238}U$ value of -0.379 ± 0.023 ‰ (Kipp et al. 2022), which is isotopically lighter than the bulk crust. Measurements of other U sinks and mass-balance calculations suggest that U isotopic fractionation during incorporation into oxic-suboxic sediments is typically small (<0.25 ‰), with a net effect <0.05 ‰ on a global scale (Lau et al. 2016; Tissot and Dauphas 2015). With this being the case, the U isotopic composition of seawater is dominantly controlled by the size of the anoxic sink. When anoxic sediments are more widespread, more ^{238}U is scavenged from the ocean, causing $\delta^{238}U_{SW}$ to become more negative. The usefulness of uranium as a global redox proxy requires the assumption that seawater has a homogeneous U isotope composition, which has not been well characterized by high-precision analyses. This fundamental assumption is further justified in Chapter IV by revisiting the U isotope composition of modern seawater from several locations of the Pacific and Atlantic Oceans.

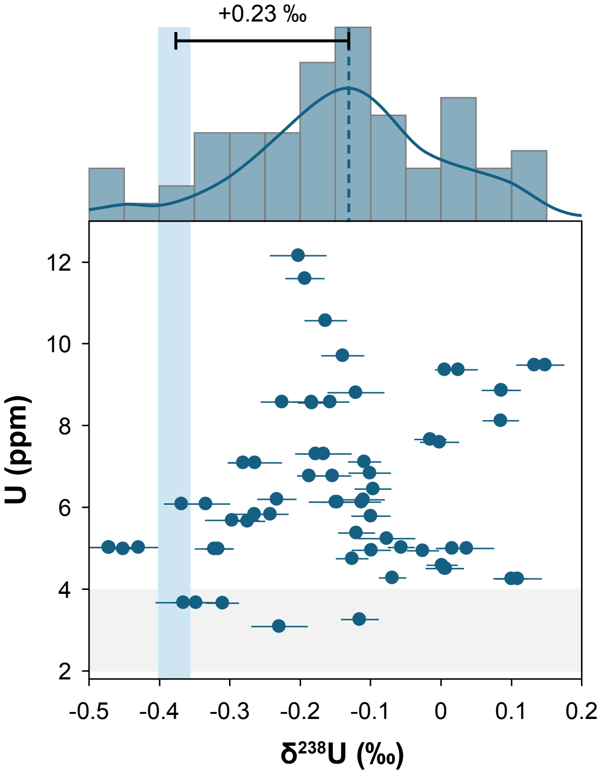

Figure 1.2: U isotope composition of modern carbonate sediments from Bahamas. Vertical blue band denotes $\delta^{238}U_{SW}$ = -0.379 ± 0.023 ‰ (Kipp et al. 2022); horizontal grey band represents [U] of carbonates precipitated from seawater (2–4 ppm). Modern carbonates have variable U concentration and isotope composition and typically enriched in ^{238}U relative to seawater by +0.23 ‰ offset, which is most likely as a result of U addition during early diagensis.

One key aspect when reconstructing past oceanic redox states with U isotopes is to work on a reliable seawater δ^{238}U archive. Carbonate sediments are the most popular and straightforward archive to date since they tend to directly record the primary seawater δ^{238}U signal. U(VI) mainly exists as uranyl carbonate complexes $UO_2(CO_3)_3^{4-}$ in seawater, which is incorporated into marine carbonates with no significant isotopic fractionation (Chen et al. 2018a). Equipped with this potential, many studies have measured δ^{238}U in carbonates deposited during known intervals of marine redox fluctuations, and have used those data to quantify the extent of seafloor anoxia. Even if carbonate precipitates perfectly record $\delta^{238}U_{SW}$, post-depositional modification of carbonate δ^{238}U values can confound paleo-redox interpretations. Bahamian carbonate sediments have δ^{238}U values that are higher than seawater (Chen et al. 2018b; Romaniello et al. 2013; Tissot et al. 2018). Notably, these sediments also have higher U concentrations than primary carbonate precipitates, suggesting addition of isotopically-heavy U is either occurring during diagenesis or via detrital contamination.

This diagenetic overprinting on primary seawater signature complicates using U isotopes to quantitatively reconstruct the paleo-redox conditions (Kipp and Tissot 2022), thus undermining the utility of carbonates as a U isotope archive. The shortcoming of carbonates raises the need to seek alternative archives that are more resistant to secondary alterations, and such efforts have been extended to biogenic carbonates, such as deep-sea corals and stromatolites (Martin et al. 2023). To address this issue, Chapter IV explores the potential to use bio-apatite as a U isotope archive, since the enameloid tissues are considered more robust than carbonates during the secondary processing.

1.2 Long-lived and short-lived radionuclides

Nuclides heavier than lithium were produced during the nucleosynthesis processes in previous generations of stars. A small proportion of nuclides are unstable and can decay to daughter nuclei, with the overall decay rate expressed as decay constant or half-life ($t_{1/2}$), which is defined as the time required for a quantity radionuclide to reduce to half of its initial value. Half-lives can be used to categorize long-lived and short-lived radionuclides (a.k.a. radioactive isotopes): long-lived radioactive isotopes have half-lives over a few million years and still exist today; short-lived radioactive isotopes have much shorter half-lives thus they only existed in the earth Solar System (ESS) but extinct now. The radioactivity of these radionuclides provides the foundation of geochronology and comsochronology.

1.2.1 Radioactive decay

The decay of both long-lived and short-lived radioactive (parent) isotopes to the final stable (daughter) isotope can be described by the decay law:

$$P_t = P_0 \times e^{-\lambda t} \tag{1.1}$$

where P_t and P_0 are current and initial abundance of parent isotopes; t is the time since the decay system closed; λ is the decay constant defined as $\ln(2)/t_{1/2}$. The decay law suggests the number of parent radioactive nuclei at present is proportional to the initial number of atoms. The number of radiogenic daughter isotopes equals the amount of parent isotopes that decayed during this period:

$$D_t^* = P_0 - P_t = P \times (e^{\lambda t} - 1) \tag{1.2}$$

where D^* is the abundance of radiogenic daughter isotopes. Since the daughter isotopes could have a non-radiogenic origin, the total amount of daughter isotopes is the sum of initial and radiogenic fractions:

$$D_t = D_0 + P \times (e^{\lambda t} - 1) \tag{1.3}$$

where D and D_0 are the current and initial abundance of daughter isotopes. Given that the isotopes are measured more precisely as ratios than absolute abundance, Eq. 1.3 needs to normalize to a stable isotope of the daughter element (D_s):

$$\frac{D_t}{D_s} = \frac{D_0}{D_s} + \frac{P_t}{D_s} \times (e^{\lambda t} - 1) \tag{1.4}$$

An isochron plots D/D_s versus P/D_s, and the slope ($e^{\lambda t}$–1) can be used to calculate the age.

1.2.2 U-Pb systematics

Of all long-lived chronometers, the Pb-Pb chronometer based on dual U-Pb decay (^{238}U→^{206}Pb, $t_{1/2}$ = 4.469 Gyr, ^{235}U→^{207}Pb, $t_{1/2}$ = 0.703 Gyr, Jaffey et al. 1971) provide the highest precision absolute ages of CAIs and ESS materials. For Pb-Pb system, Eq. 1.4 can be written as:

$$\frac{^{207}\mathrm{Pb}^*}{^{206}\mathrm{Pb}^*} = \frac{^{235}\mathrm{U}}{^{238}\mathrm{U}} \times \frac{e^{\lambda_{235} t} - 1}{e^{\lambda_{238} t} - 1} \tag{1.5}$$

where * denotes radiogenic lead, λ_{235} and λ_{238} are decay constants for ^{235}U and ^{238}U, and t is the age of the sample. The dual U-Pb decay chronometer uses the same parent and daughter elements and can determine the age simply by measuring lead isotope composition, eliminating the necessity for the parent-to-daughter ratio. Due to the limited analytical accuracy of mass spectrometry, U isotope variations in natural samples were not observed for a long time, therefore a ^{238}U/^{235}U consensus value of 137.88 was adopted in the late 1970s for Pb–Pb dating (Steiger and Jäger 1977). This important assumption was, however, overthrown by the discovery of resolvable U isotopic variations in natural samples (*e.g.,* Amelin et al. 2010; Bopp et al. 2009; Brennecka et al. 2010a; Hiess et al. 2012; Stirling et al. 2007; Tissot and Dauphas 2015; Weyer et al. 2008). The impact of these variations on the accuracy of U-Pb and Pb–Pb ages has been extensively discussed (Hiess et al. 2012; Tissot and Dauphas 2015; Tissot et al. 2017, 2019a), and it is now accepted that both U and Pb isotopes need to be measured to obtain both precise and accurate dates. The age corrections caused by U variability is given by the following equation (Tissot and Dauphas 2015; Tissot et al. 2017):

$$\Delta t = \frac{\Delta \mathrm{U} \left(e^{\lambda_{238} t} - 1\right)\left(e^{\lambda_{235} t} - 1\right)}{1000 \left[\lambda_{238} e^{\lambda_{238} t} - \lambda_{235} e^{\lambda_{235} t} + (\lambda_{235} - \lambda_{238}) e^{(\lambda_{238} + \lambda_{235}) t}\right]} \tag{1.6}$$

where ΔU is the difference between the actual and assumed U isotope composition of the sample. Among all extraterrestrial materials, calcium-aluminum-rich inclusions

(CAIs) are featured by the most notable U isotope variations. CAIs are the oldest dated solids in the solar nebular (Amelin et al. 2010; Connelly et al. 2012; Gray et al. 1973) and are therefore used to define the starting point of the ESS (t_0). Hence, precise determination of U isotope is particularly important for high-precision chronology of CAIs, since the U isotope variability in CAIs can lead to age correction up to ~10 Myr (**Fig. 1.3**).

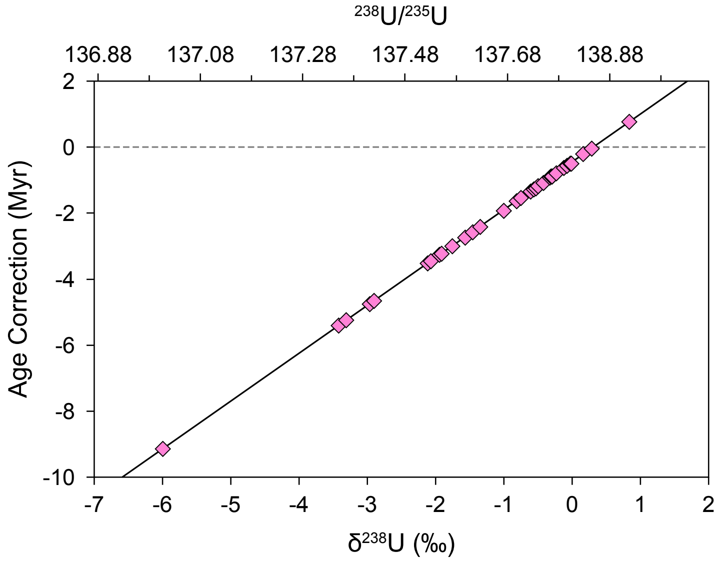

Figure 1.3: The impact of U isotope variations in CAIs on Pb-Pb age determination. For CAIs, the age corrections due to U isotope variations are linearly correlated with the U isotope offsets.

Over the last decade, high-precision chronological data has revealed discrepancies in the construction of a fine-scale chronology of CAIs. Of particular interest is the fact that the two most precise ages of the oldest CAIs do not agree with-in uncertainty: 4567.30 ± 0.16 Myr (Amelin et al. 2010) vs 4567.94 ± 0.31 Myr (Bouvier et al. 2011a), which is conflict with the short formation window of CAIs. The cause of this discrepancy is unknown, but poses the question of the reliability, within stated uncertainties, of CAI Pb-Pb ages. Chapter VI aims to resolve this discrepancy and evaluate if the true starting point of the Solar System can be defined.

1.2.3 Al-Mg systematics

The short half-lives of short-lived radionuclides allow them to resolve extra high temporal resolution than long-lived chronometers. Short-lived radioactive isotope were found in 1960s, because of the observation of ^{129}Xe excesses correlated with the abundance of ^{129}I (Jeffery and Reynolds 1961). In mid 1970s, ^{26}Al was discovered by ^{26}Mg excesses correlated with ^{27}Al/^{24}Mg ratios in Allende CAIs (Lee et al. 1976). Driven by technique advancement in secondary ion mass spectrometry, ^{26}Al-^{26}Mg system ($t_{1/2}$=0.70 Myr) turns out to be the most widely used relative chronometer, and Eq. 1.4 can be written as:

$$\left(\frac{^{26}\mathrm{Mg}}{^{24}\mathrm{Mg}}\right)_t = \left(\frac{^{26}\mathrm{Mg}}{^{24}\mathrm{Mg}}\right)_0 + \left(\frac{^{26}\mathrm{Al}}{^{24}\mathrm{Mg}}\right)_0 \times e^{-\lambda t} \tag{1.7}$$

Since ^{26}Al is already extinct and not detectable at present, the stable ^{27}Al isotope is added to Eq. 1.7 as a surrogate for ^{26}Al with the same geochemical behavior:

$$\left(\frac{^{26}\mathrm{Mg}}{^{24}\mathrm{Mg}}\right)_t = \left(\frac{^{26}\mathrm{Mg}}{^{24}\mathrm{Mg}}\right)_0 + \left(\frac{^{26}\mathrm{Al}}{^{27}\mathrm{Al}}\right)_0 \left(\frac{^{27}\mathrm{Al}}{^{24}\mathrm{Mg}}\right)_t \times e^{-\lambda t} \tag{1.8}$$

where $(^{26}\mathrm{Al}/^{27}\mathrm{Al})_0$ represents the initial ^{26}Al abundance before decay, $(^{27}\mathrm{Al}/^{24}\mathrm{Mg})_t$ is the present ratio, which should remains as a constant in closed system. The correlation between ^{26}Mg excesses and $^{27}\mathrm{Al}/^{24}\mathrm{Mg}$ ratio can represent an isochron. There are two different types of ^{26}Al-^{26}Mg isochron, which record distinct events and information: the internal isochron is obtained by measuring Mg isotope composition and Al/Mg ratios of various mineral phases from a single CAI, and records the last melting/crystallization events; the bulk isochron is based on multiple CAIs, and records the condensation of CAI precursor materials from the solar nebula.

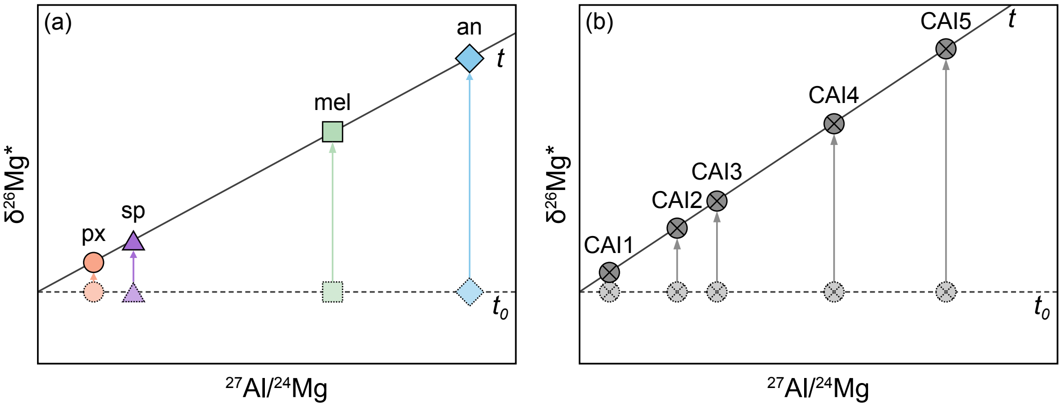

Figure 1.4: Internal and bulk ^{26}Al-^{26}Mg isochrons: (a) internal isochron determined by different mineral phases of a single CAI; (b) bulk isochron determined by multiple CAIs. For these two types of isochron, the internal isochron is more sensitive to subsequent secondary processes (*e.g.,* thermal processing and secondary alterations).

The slope of the ^{26}Al-^{26}Mg isochron carries the age information by characterizing the initial abundance of the short-lived radioactive parent isotope relative to its stable counterpart. Quantitative interpretations on relative ages requires an essential assumption that ^{26}Al is homogeneously distributed in the ESS, and thus difference in initial $^{26}\mathrm{Al}/^{27}\mathrm{Al}$ abundance only reflects the time difference. There is a long-time debate on this fundamental assumption for ^{26}Al-^{26}Mg chronometer that a homogeneous distribution of ^{26}Al in protoplanetary disk is challenged by significantly lower initial ^{26}Al abundance in some special types of refractory inclusions, such as FUN CAIs (Fractionated with Unknown Nuclear effects), spinel-hibonite spherules

(SHIBs), and platy-hibonite crystals (PLACs). The ^{26}Al abundance observed in these objects is interpreted as they formed before ^{26}Al was injected/homogenized in the ESS. Heterogeneous distribution of ^{26}Al in the solar nebula is also commonly considered to account for the discrepant estimates on the ages of CAIs, chondrule and achondrites between absolute Pb-Pb and Al-Mg chronometers. Chapter VI aims to resolve the CAI age discrepancy by evaluating the two chronometers in the same set of CAIs to test if the discordance is due to ^{26}Al/^{27}Al heterogeneity or robustness of these chronometers.

The initial ^{26}Al/^{27}Al abundance in large CAIs from CV3 chondrites are well-characterized by bulk ^{26}Al-^{26}Mg isochron (Jacobsen et al. 2008), which suggests ^{26}Al was homogeneously distributed in the CAI-forming region with a ^{26}Al/^{27}Al ratio of $(5.23 \pm 0.13) \times 10^{-5}$. Besides the slope, the intercept of the bulk ^{26}Al-^{26}Mg isochrons can be used to characterized the pre-^{26}Al decay Mg isotope composition. Magnesium isotope heterogeneity has been resolved by high-precision Mg isotope analyses on bulk CAIs. Chapter V revisited this question by investigating a larger set of CAIs that covered all known CAI types from various hosting chondrites.

1.3 Scientific questions

This thesis covers diverse topics in isotope geochemistry and cosmochemistry. For geochemistry, we aim to answer the following scientific questions:

1. How to overcome the limitation of carbonate sediments archive for using U isotopes to reconstruct paleoredox conditions?
    a) Searching for new approach: Are there any alternative archives that can more faithfully preserve the primary $\delta^{238}\mathrm{U}_{\mathrm{SW}}$? The first part of Chapter IV explores the potential of bioapatite as a novel archive, given that it is considered more resistant to diagenetic alterations.
    b) Refining the current approach: How to correct non-primary U isotope signature in carbonates? The second part of Chapter IV includes a preliminary test for this question in that we tested the key assumption of using U isotopes as a global proxy that U isotopes are homogeneously distributed in seawater.
2. Motivated by dealing with big data in U isotope studies (especially in paleoredox reconstruction), Chapter III addressed this issue by developing the Uranium Isotope Database.

For cosmochemistry, we aim to answer the following scientific questions:

1. Whether CAIs carry a single snapshot or a series of evolving records of the ESS? Chapter V addressed this issue from the prespective of Mg isotopes.

2. How to reconcile the discrepancies in ESS chronology between Pb-Pb and Al-Mg chronometers? Chapter VI focuses on the discrepancies in CAI ages, and tested the relative robustness of Pb-Pb and Al-Mg systems.

1.4 Outline of the thesis

Chapter I focuses on introducing the principle of long-lived and short-lived chronometers in the early solar system chronology, as well as U isotopes ($^{238}U/^{235}U$) to reconstruct the paleo-redox conditions in the ocean. This chapter also presents an outline for the thesis.

Chapter II focuses on the analytical techniques used and/or developed for the work in the thesis. These methods are summarized in this chapter, given that several techniques are used across different chapters. Analytical techniques presented in this chapter included (1) U isotope analyses for terrestrial and extraterrestrial samples (2) high-precision Mg isotope analyses and $^{27}Al/^{24}Mg$ ratio measurements for Ca-rich samples (3) in-situ ^{26}Al-^{26}Mg analyses by secondary ion mass spectrometry and (4) determination of distribution coefficients of the REEs, Sr, Y, Ba, Th, and U between α-HIBA and AG50W-X8 resin.

Chapter III introduces the uranium isotope database (UID) As the parent element in the U-Pb and Pb-Pb radiochronometers, U was one of the first heavy elements whose isotopic composition was carefully determined. Thought to be constant until the end of the 20^{th} century, the ratio of the long-lived isotopes of U ($^{238}U/^{235}U$) has since been shown to be variable at the permil to sub-permil levels in natural materials. Today, the study of U isotopes has found applications in a variety of fields including geo/cosmochronology, oceanic paleoredox reconstruction, magmatic differentiation, environmental remediation, and forensic studies. With thousands of newly reported U isotopic data each year, a real need exists for a comprehensive U isotope database. This chapter introduces a global, updatable, U isotope database (UID), which not only contains the most expansive, internally consistent U isotopic dataset to date (15,188 entries from 345 papers), but also includes all other sample data from the original publications, as well as the relevant metadata and sample information to facilitate further analysis. The UID is freely accessible and will be updated regularly. All data are normalized to the widely-used CRM-145 standard, and all assumptions used to convert the published data are explicitly detailed in the paper and the database itself. New data can be easily formatted and submitted for incorporation into the database. Using the UID we provide new recommended $\delta^{238}U$ values for certified U standards and geostandards and discuss important applications and future directions for U isotope studies.

Chapter IV focuses on the application of U isotopes as a paleo-redox proxy. The uranium isotope composition (δ^{238}U) of seawater is a powerful proxy for the extent of marine anoxia. For paleo-redox reconstructions, carbonates are the most popular U isotope archive, but they have recently come under increased scrutiny as their δ^{238}U values are subject to diagenetic alteration after deposition. Therefore, there is a need to investigate other archives that may record and preserve the original seawater δ^{238}U signal. In this study, we explore whether shark teeth provide such an archive. Shark teeth enameloid consisting of crystalline fluorapatite is more resistant to post-depositional alteration and less sensitive to isotopic exchange than marine carbonates due to the lower solubility of the crystalline fluorapatite. Since U is readily incorporated into phosphate, shark teeth could incorporate and preserve the original δ^{238}U signature of seawater. To assess whether U isotopes in shark teeth can record seawater signatures, we measured the U isotopes (both δ^{238}U and $\delta^{234}U_{\mathrm{sec}}$) in fossil shark teeth from various locations, including Banks Island, the Gulf of Mexico, and Pisco Basin, and ranging in age from modern to Cretaceous. Our results show that (1) U is incorporated into shark teeth postmortem during burial; (2) diagenetic overprinting of seawater U isotope ratios is common among shark teeth, and (3) δ^{238}U data are influenced by local depositional environments. Nonetheless, the U isotope variations observed in shark teeth are comparable to those seen in marine carbonates, indicating that the samples with less diagenetic alterations might offer useful insight into the past extent of ocean anoxia. The second part of this chapter revisits the foundational assumption of homogeneity of the marine U reservoir, and the capacity of deep-sea corals to record the U isotope composition of ambient seawater.

Chapter V focuses on ^{26}Al-^{26}Mg systematics of bulk CAIs to understand the composition of their precursors. CAIs are the oldest solids that formed in the solar nebula and thus can capture the snapshots of the infalling materials onto the nascent Sun, whose properties remain poorly understood. Short-lived ^{26}Al–^{26}Mg systematics provides unique age and composition information about CAI precursors. This work reported high-precision magnesium isotope data for 19 CAIs that cover a broad representation of the known CAI population and show that CAIs cover a wide range of initial (pre-^{26}Al decay) magnesium isotope composition. The results suggest the infalling materials that formed the early protoplanetary disk were heterogeneous and experienced continuous evolution during the CAI-forming epoch.

Chapter VI focuses on the chronology of the early solar system. Long-lived (Pb-Pb) and short-lived (^{26}Al-^{26}Mg) dating methods can constrain the time sequence of the evolution processes in the early Solar System (ESS). However, the increasing number of high-precision data has revealed the inconsistencies between Pb-Pb and ^{26}Al-^{26}Mg chronometers: (1) existence of a 0.71 Myr difference for the Pb-Pb ages proposed for the oldest CAIs, which do not match their ^{26}Al-^{26}Mg records and conflict with the short formation interval of primary CAIs; (2) age differences between CAIs and chondrules/achondrites obtained from Pb-Pb chronometer are typically shorter than those resolved from ^{26}Al-^{26}Mg chronometer. These discrepancies between the two chronometers are all related to CAIs, which play a pivotal role in defining the starting point of the ESS and anchoring absolute and relative chronometers. The cause of these discrepancies remains an open question, whose investigation is impeded by the limited number of CAIs that have been comprehensively analyzed by both Pb-Pb and ^{26}Al-^{26}Mg chronometers. This work determined the U-corrected Pb-Pb ages and ^{26}Al-^{26}Mg ages for a new set of CAIs and compared them with literature data to reevaluate the chronology of CAIs. The results demonstrate the Pb-Pb system can be reset for ~1 Myr without significantly disturbing the Al-Mg system, indicating the resetting of these two systems can be decoupled. I also performed U isotope analyses of both mineral separates and bulk material to test the impact of intermineral U isotope fractionation on Pb-Pb ages of CAIs. Uranium isotope variations are observed between the melilite fraction and the bulk CAI, while the $\delta^{238}U$ difference for pyroxene is not resolved at the current level of analytical precision. The magnitude of this age offset is unlikely to reconcile the discrepancy of the age difference between the two oldest known CAIs.

Chapter 2

ANALYTICAL TECHNIQUES

Part of this chapter has been published in:

Li, H., Tissot, F.L.H., Lee, S.-G., Hyung, E., and Dauphas, N. (2020). Distribution coefficients of the REEs, Sr, Y, Ba, Th, and U between α-HIBA and AG50W-X8 resin. *ACS Earth and Space Chemistry* **5.1**, 55–65.

Kipp, M.A., **Li, H.**, Ellwood, M.J., John, S.G., Middag, R., Adkins, J.F., and Tissot, F.L.H. (2022). ^{238}U, ^{235}U and ^{234}U in seawater and deep-sea corals: A high-precision reappraisal. *Geochimica et Cosmochimica Acta* **336**, 231–248

Li, H., Kipp, M.A., Kim, S.L., Kast, E.R., Eberle, J.J., and Tissot, F.L.H. (2024). Exploring uranium isotopes in shark teeth as a paleo-redox proxy. *Geochimica et Cosmochimica Acta* **365**, 158–173

2.1 Determination of distribution coefficients

Rare-earth elements (REEs) are known for their similar behaviors, which make their purification through chromatographic techniques particularly challenging. The use of α-hydroxyisobutyric acid (α-HIBA) in combination with a cation-exchange resin is perhaps the most widely used chromatographic technique to separate individual REEs from each other. However, only limited REE partition data between α-HIBA and cation resins exist, which makes it challenging to develop and optimize purification techniques using this platform. Here, we report distribution coefficients (K_d) of REEs, as well as Sr, Y, Ba, Th, and U, between α-HIBA at pH = 4.50 and AG50W-X8 cation-exchange resin, obtained by batch equilibration experiments. For all 19 elements, the distribution coefficients decrease with increasing acid concentration. For the REEs, a linear relationship is observed in log-log space between K_d values and α-HIBA molarity. While the K_d values have been calibrated at pH = 4.50, formulas are provided allowing recasting of the K_d values at any pH. To test the accuracy of the data, we compare elution curves simulated using the newly determined distribution coefficients to actual elution curves. The close agreement between simulated and experimental elution curves demonstrates that the distribution coefficients obtained in this study are effective to devise multielement extraction and purification scheme for high-precision elemental and isotopic analyses of REEs for various applications.

2.1.1 Motivation

The characterization of isotopic variations for the rare-earth elements (REEs) has found diverse applications in the fields of geo- and cosmochemistry (Albalat et al. 2012; Andreasen and Sharma 2006, 2007; Bennett et al. 2007; Bouvier and Boyet 2016; Boyet and Carlson 2005; Burkhardt et al. 2016; Carlson et al. 2007; Caro et al. 2003; Gannoun et al. 2011; O'Neil et al. 2008; Saji et al. 2020; Shollenberger and Brennecka 2020; Thrane et al. 2010). For instance, the Sm-Nd decay system, which is arguably the best-known and most-studied of the REE systematics, contains two radiogenic isotopes (^{147}Sm → ^{143}Nd, $t_{1/2} = 106$ Byr (Faure and Mensing 2005); ^{146}Sm → ^{142}Nd, $t_{1/2} = 103$ Myr (Friedman et al. 1966), which are widely used in (i) geochronology (Li et al. 2000; Marks et al. 2014); (ii) the tracing of mantle sources, (Blichert-Toft and Puchtel 2010; White and Hofmann 1982) and (iii) the study of the differentiation history of planetary silicate reservoirs. (Blichert-Toft et al. 2002; Bouvier et al. 2008; Boyet and Carlson 2005; Caro et al. 2006) In cosmochemistry, Nd nucleosynthetic anomalies have recently proven to be critical to our understanding of planetary formation and early solar-system dynamics, (Bouvier and Boyet 2016; Burkhardt et al. 2016; Render et al. 2017). In recent years, high-precision isotopic investigations of other REE systematics have also been pioneered (*e.g.,* Ce, Eu, Dy, Er, and Yb isotopes, Lee and Tanaka 2019; Pourkhorsandi et al. 2021; Segal et al. 2003; Shollenberger and Brennecka 2020; Willig and Stracke 2018) as new possible tools to solve geo- and cosmochemical questions (Hu et al. 2021; Shollenberger and Brennecka 2020; Willig and Stracke 2019), revealing a growing need for robust purification protocols for all REEs.

Geochemically, REEs are well known for their near identical behavior, which stems from (i) their very similar ionic radii, and (ii) the fact that most of these metal ions exist primarily in the trivalent oxidation state in geological samples (Eu and Ce can also exist as Eu^{2+} and Ce^{4+}, respectively). These characteristics make the separation of REEs especially difficult (Nash and Jensen 2001). As the most well-studied REE isotope system, methods for separating Sm and Nd (Boyet and Carlson 2005; Caro et al. 2006, 2008; Debaille et al. 2007; DePaolo and Wasserburg 1976; Jacobsen and Wasserburg 1980, 1984; Lugmair et al. 1975; Rehkämper et al. 1996; Wasserburg et al. 1981) are well established. To a lesser extent, routine protocols also exist for Lu (part of the Lu–Hf system, Blichert-Toft et al. 1997; Münker et al. 2001; Patchett and Tatsumoto 1981; Pin and Gannoun 2017; Yang et al. 2010), Ce (part of the La–Ce system, Hayashi et al. 2004; Makishima and Nakamura 1991; Pourkhorsandi et al. 2021; Shimizu et al. 1990; Tanaka and Masuda 1982; Tanaka et al. 1987), and Sm/Gd (for characterization of cosmogenic effects, Hidaka et al. 1995, 1999, 2009; Leya et al. 2003; Sands et al. 2001). For high-precision isotopic investigations of other REE systems, optimized methods are not yet readily available.

To streamline the development and optimization of REE purification protocols, knowledge of the partition behavior of the elements of interest between the eluent and the resin is necessary (**Fig. 2.1**). The affinity of a resin for a particular element is given by a distribution coefficient, K_d, which quantifies the partitioning of the element between the eluent (mobile phase) and the extractant (stationary phase) and is defined as

$$K_d = \frac{C_s}{C_l} \tag{2.1}$$

where C_s is the concentration of the element exchanged with the resin, in μg per gram of dry resin, and C_l is the concentration of the element remaining in the solution after the equilibrium has been achieved between the mobile and the stationary phases, in μg per mL of solution. For REEs, one of the most widely used separation techniques is the α-hydroxyisobutyric acid (α-HIBA) ion-exchange chemistry (Amakawa et al. 1991; Borg et al. 1997; Campbell 1973, 1976; Carlson et al. 2007; Choppin and Chopoorian 1961; Choppin 1956; Deelstra and Verbeek 1965; Eugster et al. 1970; Garçon et al. 2018; Harvey and Baxter 2009; Hyung and Jacobsen 2020; Jacobsen and Wasserburg 1980; Lugmair et al. 1975; Marks et al. 2014; Massart and Bossaert 1968; Meisel et al. 2002; Qaim et al. 1979; Rizo et al. 2011; Sisson et al. 1972; Smith and Hoffman 1956; Story and Fritz 1974), in which the eluent is the α-HIBA, $(CH_3)_2$-COH-COOH, and the stationary phase is the AG50W-X8 strong cation-exchange resin. α-HIBA is a weak acid with a pK_a (pK_a = -log$_{10}(K_a)$, where K_a is the acid dissociation constant)of 3.79. Despite its popularity, a dearth of distribution coefficient data exists for this particular eluent/resin combination, making calibrations of REE separation an unnecessarily lengthy process of trial and errors.

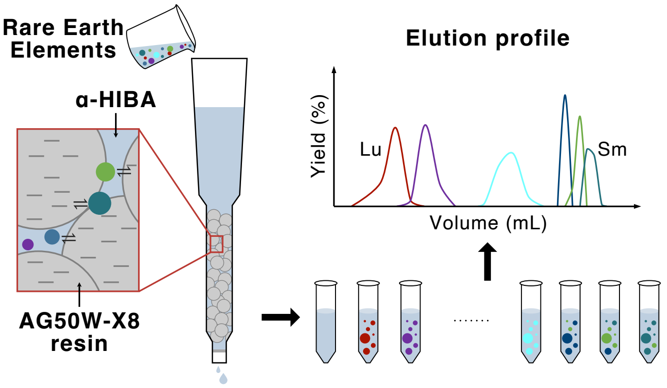

Figure 2.1: Illustration of REEs separation using α-HIBA and AG50W-X8

Here, we report the determination of distribution coefficients of the REEs, as well as Sr, Y, Ba, Th, and U between α-HIBA at pH = 4.50 (±0.01) and the AG50W-X8 resin over a range of molarities from 0.010 to 2.123 M α-HIBA. Although the REEs are the focus of this paper, Sr, Ba, Y, Th, and U were also investigated to better assess how similar their partition behavior is compared to REEs during the α-HIBA chemistry (Fuping et al. 1993; Strelow 1980) and should separation of these elements be necessary to avoid matrix effects. While these K_d values have been calibrated at pH = 4.50, formulas are provided allowing recasting of the REEs K_d values at any pH. To test the accuracy of the REE distribution coefficients, we compare simulated elution profiles to both coarse (used for concentration determinations) and fine (used for high-precision isotopic analyses) experimentally determined elution curves.

2.1.2 Experimental setup

2.1.2.1 Reagents and Analytical Materials

AG50W-X8 resin (200-400 mesh, hydrogen form) was purchased from Bio-Rad, and α-HIBA from Alfa Aesar, as 2-hydroxyisobutyric acid (99 % dry wt, molar mass 104.11 g/mol). Other acids used in this work (HCl, HNO_3) were procured at the analytical grade and double distilled in quartz and/or PTFE Teflon distillation units (PicoTrace at University of Chicago; Savillex at Caltech). Milli-Q water (Millipore, resistivity ~18.2 MΩ/cm) was used for cleaning, acid dilutions, and chromatography. All Teflon labware were precleaned with successive leaching in boiling nitric acid and aqua regia. All chemical treatments in this study were performed inside a clean laboratory environment, at room temperature.

2.1.2.2 Preparation of α-HIBA Solutions

For K_d batch experiments, the α-HIBA stock solution was prepared in glassware precleaned by rinsing in 10 % vol HCl, followed by overnight immersion in 6 M HCl on a hot plate. α-HIBA powder weighing 208.30 g was dissolved in 650 mL of Milli-Q (hereafter, MQ) water and left to react for 2 h, after which the solution was filtered to remove any nondissolved acid particles. For reference, the solubility of α-HIBA in water is 484 g/L. Filtration took 6 h and was done with a PTFE-faced funnel, base glass filter holder, and 0.45 μm Fluoropore hydrophobic PTFE membranes (Millipore), prewetted with alcohol. The pH of the filtered solution was adjusted to 4.50 by the addition of 95 mL NH_4OH (ammonium hydroxide; $pK_b = 4.77$, $pK_b = -\log_{10}(K_b)$, where K_b is the base dissociation constant) solution. The pH-adjusted solution (718.48 g) was transferred into a triple-cleaned Teflon bottle and diluted with MQ-water to a final weight of 1000.04 g, corresponding to an α-HIBA concentration in the final solution of ~2.123 M.

For the elution conducted at Caltech, a 0.2 M α-HIBA stock solution was prepared by adding MQ-water to 41.64 g of α-HIBA powder in a graduated cylinder until the solution volume added up to 2.00 L. The pH of the 0.2 M α-HIBA solution was subsequently adjusted to 4.62 by adding ~36 mL of Optima-grade NH_4OH.

2.1.2.3 Batch Equilibration Experiment

Distribution coefficients were determined through batch equilibration of the elements of interest in various molarities of the α-HIBA solution. From the α-HIBA stock solution (2.123 M), twenty-four dilutions were prepared covering the molarities between 0.010 and 1.064 M. A multielement mixture containing the 14 REEs, as well as Sr, Y, Ba, Th, and U, was prepared by adding ~3.6 g of single-element inductively coupled plasma mass spectrometry (ICP-MS) standard solutions (each 1000 ± 5 ppm, SPEX CertiPrep). These solutions are available in a combination of dilute HF, H_2O_2, HCl, and/or HNO_3. If present in solution during the batch equilibration, even trace amounts of these reagents could potentially modify the partitioning of elements between the resin and solution. To avoid such complications, aliquots of standard solutions were transferred to a precleaned Teflon beaker and evaporated to dryness. Right before complete evaporation, the residual droplet was taken back into 5 mL of 3 M HNO_3, transferred to a clean centrifuge tube, and diluted with MQ-water to 50 mL (0.3 M HNO_3). Remaining insoluble particles were removed by centrifugation, after which an aliquot of the multielement standard solution was sampled, diluted, and analyzed by MC-ICPMS. All elements added to the standard were detected at levels of at least three orders of magnitude above blank 0.3 M HNO_3 solutions, and the concentrations of each element in the multielement solution were ~72 ppm. The AG50W-X8 resin was precleaned and converted to ammonium form in a 1 L Teflon column with MQ-water (3 column volume; cv), followed by a 6 M HCl rinse (3 cv) and another MQ water rinse (3 cv). The resin was then transferred to a triple cleaned Teflon bottle, soaked in 1 M NH4OH for 1 h, rinsed with MQ-water (2 cv), and finally soaked in MQ-water (*i.e.,* neutral pH, ammonium form).

The protocols for the equilibration experiments were modified from those described in ref (75). Batch experiments were conducted in α-HIBA solution ranging from 0.010 to 2.123 M. For each molarity, 4.7 mL of cleaned resin (equivalent to 2 g of dry mass) was pipetted into a precleaned Teflon beaker and dried on a hot plate at ~60 °C to remove the water remaining in the resin. Then, 10 mL of α-HIBA solution at the adequate molarity for the equilibration was added to the beakers and left to equilibrate overnight to convert the resin to the α-HIBA form. The solution was then pipetted out, and the beakers were placed in a blowing hood to dry the resin. In another clean Teflon beaker, the molarity specific standard solution was prepared by adding 0.2 mL of the ~72 ppm multielement standard solution (0.3 M HNO_3) into 7 mL α-HIBA solution at the chosen molarity (0.010-2.123 M α-HIBA). A 1 mL aliquot of the solution was saved and used as a standard for concentration normalization. The remainder of the molarity-specific standard solution (6 mL, containing ~12.4 μg of each element of interest) was added to the resin, resulting in an element to resin ratio of ~6.2 μg/g. The resin and the acid-standard solutions were stirred by placing the beakers on a Thermolyne Vortex shaker (1000 rpm) for 5-10 min every 2 h. After 8 h of equilibration, the mixture was filtered using precleaned Bio-Rad Poly-Prep chromatography columns, to separate the resin from the mobile phase. The acid solutions were collected in centrifuge tubes and transferred back into cleaned Teflon beakers. The equilibrated solutions (hereafter "sample") and the nonequilibrated aliquots (hereafter "standard") were dried on a hot plate and taken back into 5 mL of 0.3 M HNO_3. For each sample and standard, an aliquot was taken and diluted 20-fold to achieve concentrations of at most $\sim$100 ppb for an element that would have remained entirely in the liquid phase during the equilibration experiment.

2.1.2.4 Mass Spectrometry

Concentration measurements on the diluted "sample" and "standard" solutions were performed on a Thermo Finnigan Neptune MC-ICPMS at the Origins Lab, following a protocol modified from Pourmand et al. (2012). In brief, the 14 REEs were measured using 3 cup subconfigurations with ^{159}Tb, ^{141}Pr, and ^{169}Tm on the axial Faraday cup, respectively. Then, ^{88}Sr, ^{89}Y, ^{138}Ba, ^{232}Th, and ^{238}U were measured in the center cup, in five successive subconfigurations (*i.e.,* peak jumping) (**Table 2.1**). Measured isotopes were selected with preference given to higher relative abundances and absence of isobaric/polyatomic interferences. The 0.3 M HNO_3 solutions were introduced into the MC-ICPMS using a 100 μL/min PFA Teflon self-aspirating nebulizer. Measurements were performed in wet plasma mode, using a combined quartz cyclonic and Scott-type spray chamber (Stable Introduction System from ESI). Instrumental drift was corrected for by bracketing every batch of three unknowns with a multielement standard solution (std-smp-smp-smp-std). The procedural blank and acid contributions (generally < 1 %) were subtracted from each analysis.

Table 2.1: Faraday Cup Configuration Used for REE Concentration Measurements on the MC–ICPMS[a]

configuration	**L4**	**L3**	**L2**	**L1**	**axial**	**H1**	**H2**	**H3**	**H4**
main	^{149}Sm	^{151}Eu	^{157}Gd		^{159}Tb	^{163}Dy		^{165}Ho	^{167}Er
sub sequence 1			^{139}La	^{140}Ce	^{141}Pr		^{146}Nd		
sub sequence 2			^{167}Er		^{169}Tm	^{173}Yb		^{175}Lu	
sub sequence 3					^{88}Sr				
sub sequence 4					^{89}Y				
sub sequence 5					^{138}Ba				
sub sequence 6					^{232}Th				
sub sequence 7					^{238}U				

[a] ^{167}Er was measured twice: in the main sequence and in subsequence 2. The results from these two measurements agreed with each other within error, so distribution coefficients of Er were calculated as the mean of the two measurements.

For the elution conducted at Caltech (Elution 2), concentration in each elution cut was measured using an iCAP RQ (Thermo Fisher) ICP-MS and an SC-2 DX autosampler (Elemental Scientific). Instrumental tuning parameters (*e.g.,* nebulizer gas flow, torch alignment, sample uptake rate, and quadrupole ion deflector) were optimized to pass the standard performance check using an iCAP Q/RQ solution (Thermo Fisher Scientific) containing 1.0 ppb Ba, Bi, Ce, Co, In, Li, and U in 2 % HNO_3 and 0.5 % HCl. After tuning, REE standard solutions covering a range of concentrations were measured to generate calibration curves that establish the signal to concentration correspondence (*i.e.,* counts per second per ppm) for the analytical session. Analyses were conducted in the STD mode. The typical signal variability from instrumental drift in these conditions is around ±1 % within any given session.

2.1.2.5 Elution Tests

We conducted two elution tests to assess the accuracy of the distribution coefficients obtained from the batch equilibration experiments. Matrix elements were omitted in the artificial solution used in these tests as REE separation are typically performed on a preconcentrated REE fraction after removal of matrix elements in the sample.

Elution 1 was conducted at the Origins Lab (University of Chicago) at room temperature by using a gravity driven custom-made quartz column (1.9 mm ID × 21 cm length) to achieve a bulk separation for concentration measurements. A multielement standard solution containing 10 ppm of each REE was loaded on the column filled with AG50W-X8 resin (200-400 mesh) in 1 mL 0.06 M α-HIBA. Lu, Yb, and Tm were eluted with 36 mL of 0.06 M α-HIBA, followed by Er, Eu, Sm, and Nd in 16 mL of 0.2 M α-HIBA and finally Pr and Ce in 10 mL of 0.3 M α-HIBA. The concentration measurements were performed with the same experimental setup as the distribution coefficient measurements, and the yield for each REE was above 90 %.

Elution 2 was conducted at the Isotoparium (Caltech) with a borosilicate column (2.0 mm ID × 30 cm length) at ambient temperature and pressurized to 1.0 psi (frit porosity: 35 μm) using compressed air, which produces a fine separation of Ce-Nd-Sm for high-precision isotopic analysis of Nd. The flow rate was 1 drop/min, and each elution fraction consisted of four drops (~47 μL/drop). A standard mixture with 60 ppm of each REE was loaded on the column filled with AG50W-X4 resin (200-400 mesh) in 150 μL of 0.75 M HCl, and an isocratic elution was done with 8.3 mL of 0.2 M α-HIBA at a pH of 4.62. Elution fractions were collected in four drop increments in 5 mL Teflon vials, dried down at 90 °C, and redissolved into 0.48 M HNO_3. Concentrations were measured on the iCAP RQ ICP-MS, and yields for all REEs were above 90 %.

2.1.2.6 Elution Simulations

To simulate the elutions, we used an optimized (∼18× faster) version of the Mathematica code from Ireland et al. (2013), which is based on the plate theory of chromatography developed by Martin and Synge (1941). The plate theory states that a chromatographic column can be divided into a finite number of theoretical plates of defined height (noted HETP, for height equivalent to a theoretical plate). Within each plate, and at any point in time, equilibrium is achieved between the liquid (mobile) phase and the solid (stationary) phase. Using this framework, it is possible to model the behavior of elements onto a resin and test various elution schemes to optimize the separation of the elements of interest. The architecture of the simulation code is summarized in **Table 2.2**. This simulation code allows users to model the behavior of elements onto a specific resin and rapidly test complex elution schemes to optimize the separation of the elements of interest prior to implementation in the laboratory. Sensitivity tests were performed to evaluate the influence of uncertainties on parameters such as column dimensions (*i.e.,* length and radius, **Fig. 2.2**) and resin properties (*i.e.,* porosity and density, **Fig. 2.3**). Within the accuracy of typical determination of these parameters, they do not influence the results of the simulations presented here.

Table 2.2: Architecture of the chromatography simulation code

```
1. Set collection volume of the elution scheme
2. Import resin characteristics:   HETP (cm),
                                   Column height (cm),
                                   Column radius (cm),
                                   Resin porosity,
                                   Density of extractant-loaded beads (g/mL).
3. Import elution details:         Number of elution steps,
                                   Volume of each elution step (mL),
                                   Element concentration in each elution step (mol/mL),
                                   $K_d$ of elements in each elution step.
4. Elution simulation loop
   For each elution step:
       ○ The characteristics of the liquid volume to inject are updated,
       ○ The liquid in the last plate is eluted,
       ○ The liquid in each plate above the last one is moved down one plate,
       ○ The liquid to inject is added to the first plate,
       ○ Liquid-solid equilibrium is calculated in each plate.
End of the loop
       Plot the simulated elution curve (% recovery vs. volume).
       Two graphs are plotted,
           ○ in the first one, the volume step is the plate column,
           ○ in the second one it is the collection volume specified by the user.
Export the results as xls or xlsx file.
```

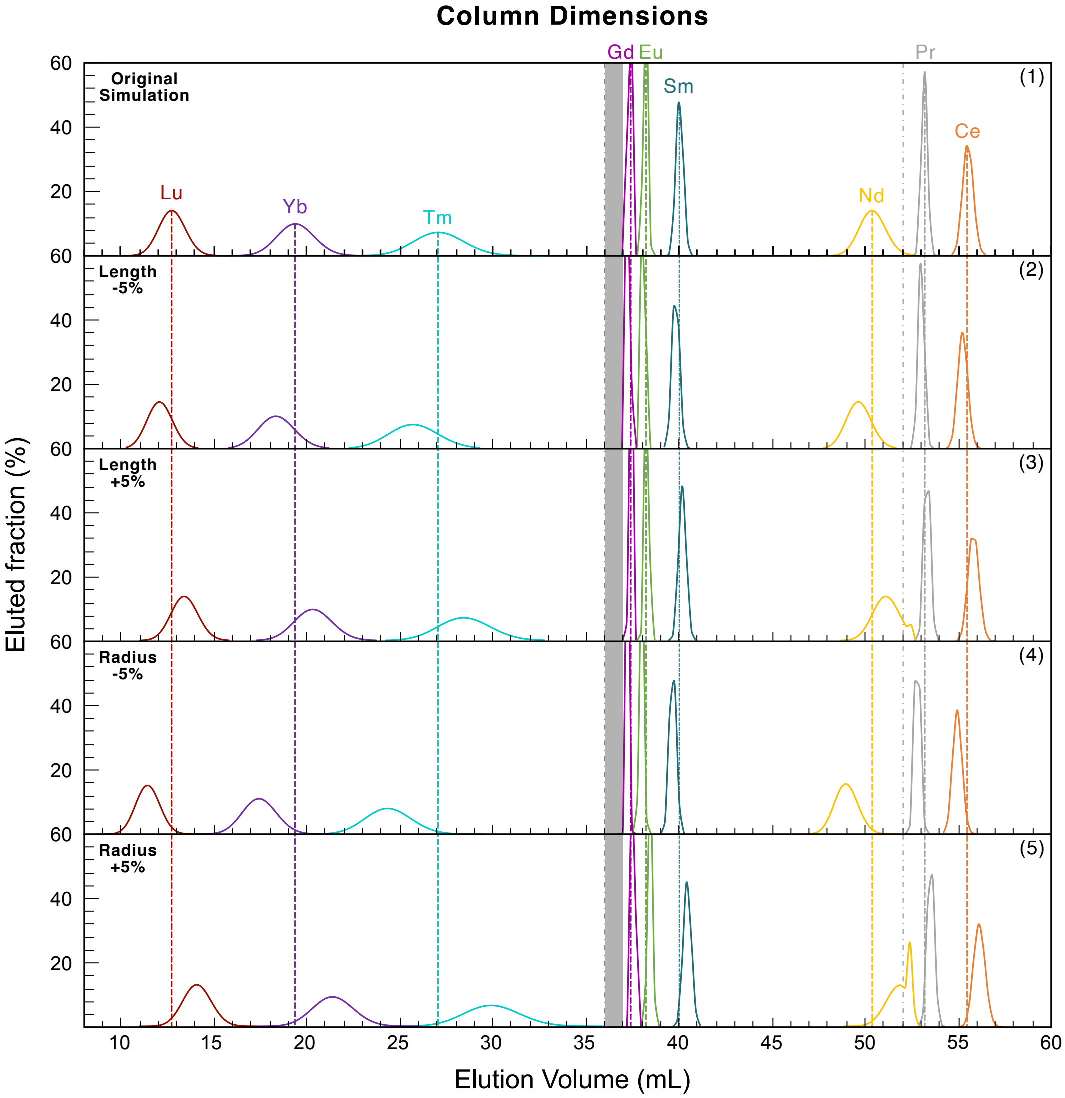

Figure 2.2: Panel (1) shows the original simulation (collected volume = 0.25 mL); while panels (2)-(5) shows the labeled parameters changed by ±5 %, while keeping other parameters constant. The grey dot dash lines represent the transitions of α-HIBA molarity, and the dash lines represent the positions of peaks in the original simulated elution profile. The grey band denotes the position of elution of Er, Ho, Dy and Tb, whose simulations do not change with input parameters.

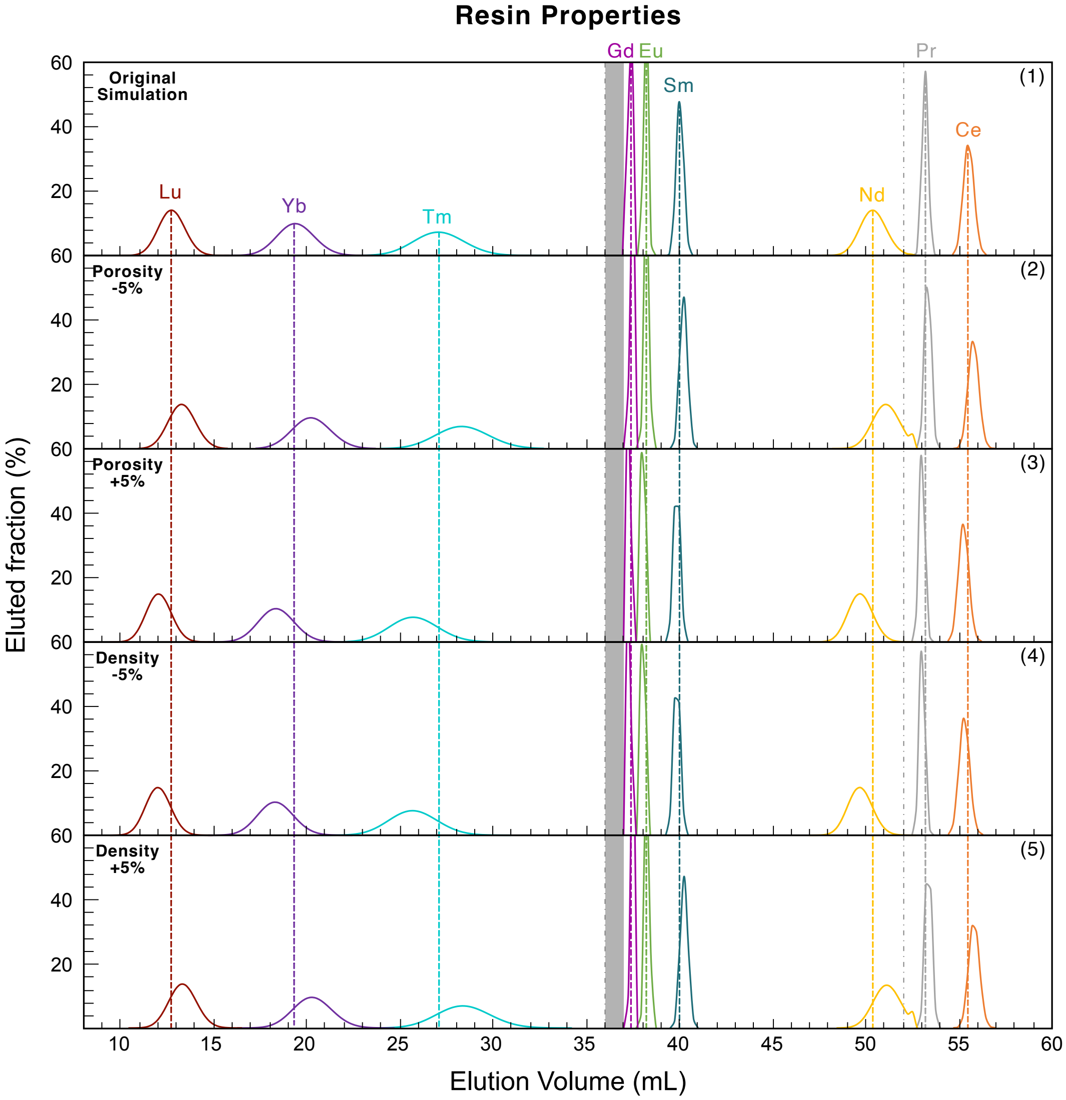

Figure 2.3: Sensitivity tests for the elution simulations depending on resin properties. Panel (1) shows the original simulation (collected volume = 0.25 mL); while panels (2)-(5) shows the labeled parame-ters changed by ±5 %, while keeping other parameters constant. The grey dot dash lines represent the transitions of α-HIBA molarity, and the dash lines represent the positions of peaks in the original simulated elution profile. The grey band denotes the position of elution of Er, Ho, Dy and Tb, whose simulations do not change with input parameters.

Table 2.3: Distribution Coefficients (K_d) of REEs, Sr, Y, Ba, Th, and U, at pH = 4.50[a]

α-HIBA (M)	Sr	Y	Ba	La	Ce	Pr	Nd	Sm	Eu	Gd	Gd*[b]	Tb	Dy	Ho	Er	Tm	Yb	Lu	Th	U
0.010	10142	**	8028	**	**	**	**	**	**	**	**	**	**	**	**	**	**	**	**	8976
0.016	8773	**	18913	**	**	**	**	**	**	**	**	**	**	**	**	**	**	**	20747	3209
0.026	7905	19518	15363	**	**	**	**	**	**	**	**	**	**	**	21606	13422	7938	5754	2736	497
0.041	6630	4708	13846	**	**	**	**	**	**	31265	21224	12155	6290	3760	2109	1248	745	517	206	116
0.063	4616	420	9876	**	**	28858	19439	7007	3701	3770	2235	995	488	285	159	91.6	53.7	36.0	18.5	27.1
0.083	2990	62.5	7519	22221	9983	5741	3774	1144	601	612	521	148	71.0	40.7	22.3	12.8	*	*	*	*
0.107	2706	22.6	7424	10098	4117	2347	1519	433	222	226	131	53.3	25.9	15.1	*	*	*	*	*	*
0.135	2384	*	6717	3995	1556	895	577	159	80.6	84.9	39.0	19.9	10.3	*	*	*	*	*	*	*
0.160	1733	*	4791	1407	540	313	202	54.6	27.8	30.9	15.9	*	*	*	*	*	*	*	*	*
0.187	1220	*	3448	570	217	126	81.0	21.7	10.9	13.2	*	*	*	*	*	*	*	*	*	*
0.214	1034	*	2756	214	82.5	46.7	29.9	*	*	*	*	*	*	*	*	*	*	*	*	*
0.241	1153	*	2975	256	98.6	56.3	36.1	10.6	*	*	*	*	*	*	*	*	*	*	*	*
0.267	780	*	650	114	44.0	25.0	15.9	*	*	*	*	*	*	*	*	*	*	*	*	*
0.293	668	*	1658	79.3	30.8	17.6	11.2	*	*	*	*	*	*	*	*	*	*	*	*	*
0.321	502	*	1154	37.6	14.8	*	*	*	*	*	*	*	*	*	*	*	*	*	*	*
0.348	576	*	1331	37.5	15.8	*	*	*	*	*	*	*	*	*	*	*	*	*	*	*
0.375	312	*	729	15.5	*	*	*	*	*	*	*	*	*	*	*	*	*	*	*	*
0.403	345	*	768	14.3	*	*	*	*	*	*	*	*	*	*	*	*	*	*	*	*
0.426	259	*	584	*	*	*	*	*	*	*	*	*	*	*	*	*	*	*	*	*
0.533	164	*	393	*	*	*	*	*	*	*	*	*	*	*	*	*	*	*	*	*
0.691	102	*	275	*	*	*	*	*	*	*	*	*	*	*	*	*	*	*	*	*
0.849	52.2	*	156	*	*	*	*	*	*	*	*	*	*	*	*	*	*	*	*	*
1.064	32.0	*	106	*	*	*	*	*	*	*	*	*	*	*	*	*	*	*	*	*
2.123	*	*	21.8	*	*	*	*	*	*	*	*	*	*	*	*	*	*	*	*	*

[a] For distribution coefficients, * denotes values smaller than 10 and ** values larger than $10^{4.5}$.

[b] Gd* represents the corrected distribution coefficients of Gd (recommended value, see text for details.

2.1.3 Results

2.1.3.1 Distribution Coefficients

To calculate the distribution coefficients for each element (*i.e.,* μg of element per g of resin divided by μg of element per mL of solution), an extended form of Eq 2.1 was used as follows:

$$K_d = \frac{(C_b/C_a - 1) \times V}{w} \tag{2.2}$$

where C_b and C_a are the elemental concentrations in ppm in the solution before and after equilibration, respectively, w is the weight of dry AG50W-X8 resin in grams, and V is the volume of acid solution in mL. The distribution coefficients are given in **Table 2.3** and **Fig. 2.4** (base-10 logarithmic scale). For a given concentration, a high K_d value means that the element is preferentially retained on the resin, while a low K_d indicates the release of the element to the mobile phase. Only values within the range $10 < K_d < 10^{4.5}$ are considered reliable in this study, because below 10, insufficient change in the solution concentrations occur, while above $10^{4.5}$, solution concentrations approach the detection limits of the MC-ICPMS.

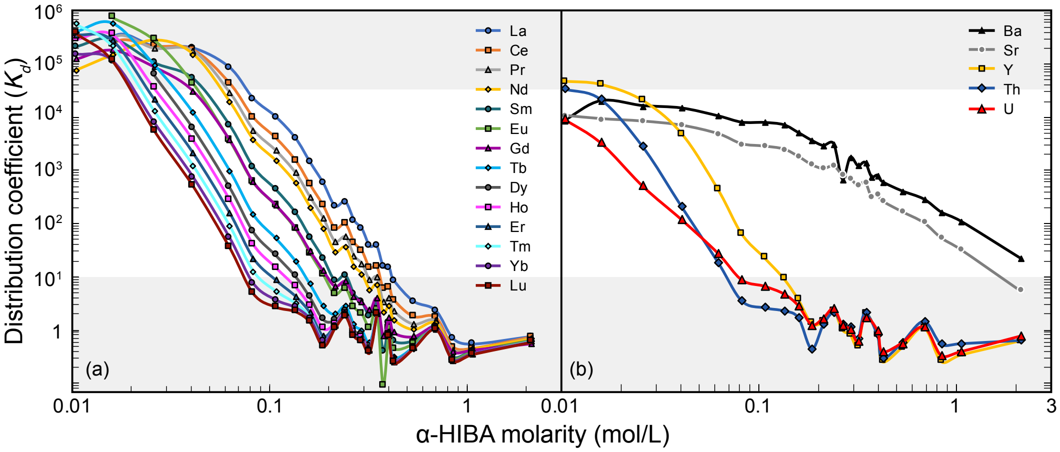

Figure 2.4: Distribution coefficients of (a) REEs and (b) Ba, Sr, Y, Th, and U on AG50W-X8 resin as a function of α-HIBA molarity. Only values within the $10 < K_d < 10^{4.5}$ range are considered reliable and reported in **Table 2.3**. For $K_d < 10$ (lower grey band), insufficient change in the solution concentrations occurred, while above $10^{4.5}$ (upper grey band), the analyte concentrations approached the limits of detection of the instrument.

For all 19 elements investigated, the distribution coefficients decrease with increasing α-HIBA molarity (**Fig. 2.4**). For the REEs, a negative linear relationship is observed between distribution coefficients and α-HIBA molarity in a log-log space. As α-HIBA forms stronger complexes with heavier REEs (Sivaraman et al. 2002), at a given molarity, lighter REEs have higher K_d than heavier REEs, and elution occurs in decreasing order of atomic numbers (Barkley et al. 1986; Fuping et al. 1993). **Table 2.4** gives the linear regression statistics for each element, and the best-fit lines are shown in **Fig. 2.5 and 2.6**. Slopes, intercepts, and the goodness of fits are determined using the LINEST function in Microsoft Excel. R^2 values on these regressions range from 0.987 to 0.998. The equations include a pH term, to account for K_d variations as a function of the α-HIBA solution pH (see below).

Table 2.4: Linear regression statistics for determination of REE K_d as a function of α-HIBA molarity at pH=4.50[a].

Element	**Equation**	**r^2**
La	$\log_{10}(K_d) = -(4.83 \pm 0.30)\ [\log_{10}([\text{HIBA}]) + \text{pH}-4.50] - (0.73 \pm 0.21)$	0.989
Ce	$\log_{10}(K_d) = -(4.77 \pm 0.35)\ [\log_{10}([\text{HIBA}]) + \text{pH}-4.50] - (1.08 \pm 0.25)$	0.988
Pr	$\log_{10}(K_d) = -(4.81 \pm 0.32)\ [\log_{10}([\text{HIBA}]) + \text{pH}-4.50] - (1.35 \pm 0.26)$	0.991
Nd	$\log_{10}(K_d) = -(4.84 \pm 0.32)\ [\log_{10}([\text{HIBA}]) + \text{pH}-4.50] - (1.56 \pm 0.27)$	0.991
Sm	$\log_{10}(K_d) = -(5.07 \pm 0.45)\ [\log_{10}([\text{HIBA}]) + \text{pH}-4.50] - (2.30 \pm 0.43)$	0.992
Eu	$\log_{10}(K_d) = -(5.11 \pm 0.44)\ [\log_{10}([\text{HIBA}]) + \text{pH}-4.50] - (2.63 \pm 0.42)$	0.993
Gd	$\log_{10}(K_d) = -(5.05 \pm 0.27)\ [\log_{10}([\text{HIBA}]) + \text{pH}-4.50] - (2.54 \pm 0.27)$	0.997
Gd*[b]	$\log_{10}(K_d) = -5.28\ [\log_{10}([\text{HIBA}]) + \text{pH}-4.50] - 3.00$	
Tb	$\log_{10}(K_d) = -(5.44 \pm 0.64)\ [\log_{10}([\text{HIBA}]) + \text{pH}-4.50] - (3.54 \pm 0.71)$	0.990
Dy	$\log_{10}(K_d) = -(5.45 \pm 0.72)\ [\log_{10}([\text{HIBA}]) + \text{pH}-4.50] - (3.85 \pm 0.80)$	0.987
Ho	$\log_{10}(K_d) = -(5.88 \pm 0.79)\ [\log_{10}([\text{HIBA}]) + \text{pH}-4.50] - (4.61 \pm 0.93)$	0.991
Er	$\log_{10}(K_d) = -(5.92 \pm 0.56)\ [\log_{10}([\text{HIBA}]) + \text{pH}-4.50] - (4.98 \pm 0.75)$	0.996
Tm	$\log_{10}(K_d) = -(5.99 \pm 0.54)\ [\log_{10}([\text{HIBA}]) + \text{pH}-4.50] - (5.30 \pm 0.72)$	0.996
Yb	$\log_{10}(K_d) = -(5.67 \pm 0.55)\ [\log_{10}([\text{HIBA}]) + \text{pH}-4.50] - (5.05 \pm 0.77)$	0.998
Lu	$\log_{10}(K_d) = -(5.76 \pm 0.54)\ [\log_{10}([\text{HIBA}]) + \text{pH}-4.50] - (5.33 \pm 0.76)$	0.998

[a] Uncertainties of slope and y-intercept are reported as two standard errors.

[b] Gd* represents the corrected regression statistics of Gd (recommended value, see text for details).

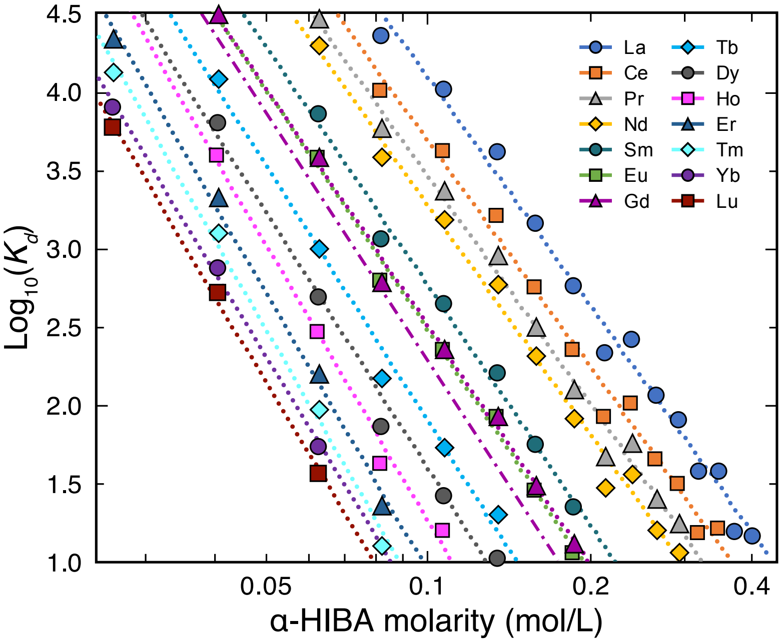

Figure 2.5: Distribution coefficients of REEs on AG50W-X8 resin in logarithmic scale as a function of α-HIBA molarity. Dotted lines show linear regressions using partition coefficients between 10 and $10^{4.5}$ (see equations in **Table 2.4**). The dotted-dashed line represents the corrected distribution coefficients of Gd (see text for details).

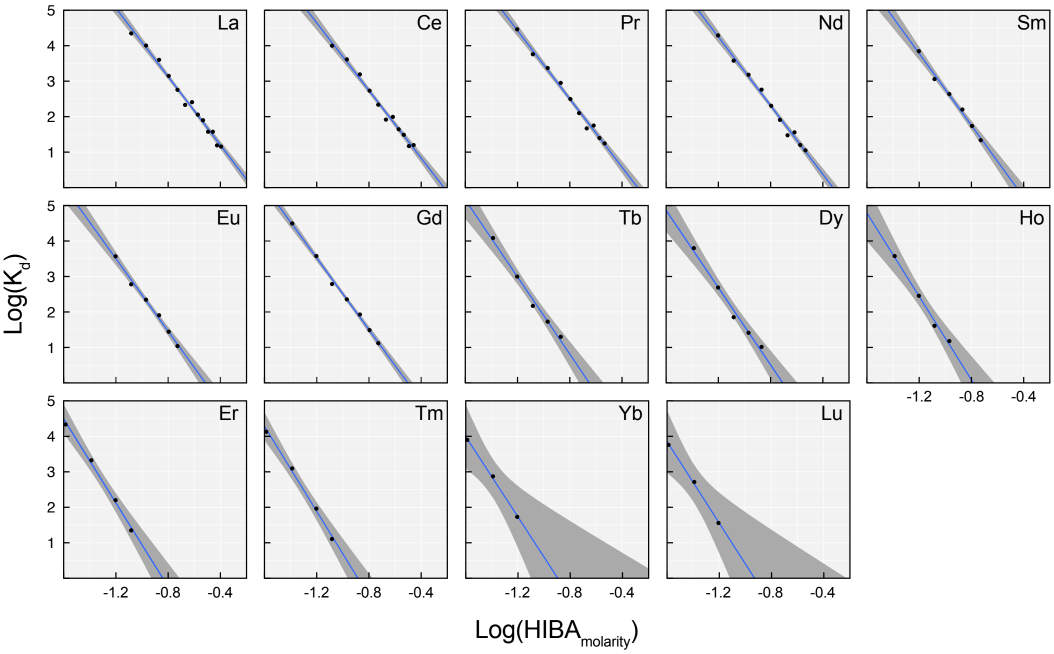

Figure 2.6: The 95% confidence intervals of best-fit linear regression lines for determination of REE K_d as a function of α-HIBA molarity. Black points = measured K_d values at given α-HIBA molarities; blue lines = best-fit linear regression lines; dark grey band = 95% confidence intervals.

2.1.3.2 Accounting for pH Variations

The mobile phase pH can significantly influence the K_d values of REEs for the α-HIBA chemistry (Deelstra and Verbeek 1965; Pourjavid et al. 2009). Indeed, as a weak monobasic acid, the dissociation of α-HIBA is described by the chemical reaction:

$$[\text{HIBA}] \leftrightarrow [\text{H}^+] + [\text{L}^-] \tag{2.3}$$

where L represents the ligand of α-HIBA. Through the dissociation constant of this reaction, the ligand concentration can thus be expressed as:

$$[\text{L}^-] = \frac{K_a[\text{HIBA}]}{[\text{H}^+]} \tag{2.4}$$

or in log form, as:

$$p\text{L} = -log_{10}([\text{L}^-]) = pK_a - pH - log_{10}([\text{HIBA}]). \tag{2.5}$$

This relationship is well known, and for instance, Deelstra and Verbeek (1965) showed that the $\log_{10}(K_d)$ of the REEs was linearly related to pL. At constant pH, the ligand concentration (which determines the value of the partition distribution, K_ds) is only a function of the α-HIBA molarity (see **Fig. 2.5**).

As shown by Eq. 2.5, changes in ligand concentration can be similarly produced by variations in α-HIBA molarity or pH. Although the K_d values reported here were obtained at constant pH (=4.50), these values can be adjusted to account for changes in pH by equating them to the change in molarity that would be needed to maintain a constant ligand concentration. For instance, if the pH of α-HIBA solution is changed by ΔpH, the following relationship can be written as follows:

$$p\mathrm{L} = pK_a - (pH + \Delta pH) - log_{10}([\mathrm{HIBA}]) - \Delta pH. \tag{2.6}$$

A pH change of magnitude +ΔpH is therefore equivalent to a change in log α-HIBA molarity of magnitude -ΔpH. For any α-HIBA molarity, the appropriate K_d values at different pH values can simply read on **Fig. 2.5** by moving horizontally by -ΔpH (relative to the pH = 4.50). Mathematically, this means modifying the intercepts of the linear regression equations in Table 3 by a value m × ΔpH (where m is the slope of regression lines). In **Table 2.4**, we present general formulas accounting for pH difference relative to the calibration pH of 4.50.

2.1.4 Discussion

2.1.4.1 Correction of the Gd Distribution Coefficients

Unlike other REEs, the distribution coefficients of Gd and Eu obtained from the batch experiments overlap. If correct, this would indicate that both elements should elute together during the α-HIBA chemistry, which conflicts with observations in previous studies (Campbell 1973, 1976; Deelstra and Verbeek 1965; Garcia-Valls et al. 2001; Massart and Bossaert 1968; Matsui et al. 1981; Qaim et al. 1979; Raut et al. 2004; Sisson et al. 1972; Story and Fritz 1974). The apparently higher distribution coefficients measured for Gd are very likely due to $^{141}\mathrm{Pr}^{16}\mathrm{O}$ interferences. At a given α-HIBA molarity, the distribution coefficient of Pr is always larger than that of Gd. Hence, the impact of the PrO interference on Gd in the nonequilibrated solution is larger than in the equilibrated solution, leading to systematically higher K_d values for Gd. Using a quartz spray chamber for sample introduction into the MC-ICPMS (as was done here) typically produces several to several tens of percent of Pr oxide, which significantly affects the determination of Gd K_d values. This effect was, unfortunately, not precisely quantified during mass spectrometric analysis. However, a correction of the Gd K_d values is possible when considering the K_d values across all REEs. Below, we present derivations of the estimated influence of $^{141}\mathrm{Pr}^{16}\mathrm{O}$ interference on the K_d determination of $^{157}\mathrm{Gd}$. By definition, the distribution coefficient is the ratio of the concentration of an element of interest in the immobile phases (here the resin) over the concentration in the mobile phase (here the α-HIBA solution. Therefore, the K_ds for Pr and Gd can be expressed as (after simplifying for volume and weight of resin):

$$K_d^{Pr} = \frac{[\mathrm{Pr}]_b - [\mathrm{Pr}]_a}{[\mathrm{Pr}]_a} \tag{2.7}$$

$$K_d^{Gd} = \frac{[\mathrm{Gd}]_b - [\mathrm{Gd}]_a}{[\mathrm{Gd}]_a} \tag{2.8}$$

where the subscript a and b refer to before and after resin-liquid equilibration. In the presence of a PrO interference, the measured (subscript m) K_d of Gd can be expressed as:

$$\begin{aligned} K_d^{Gd_m} &= \frac{([\mathrm{Gd}]_b + [\mathrm{PrO}]_b) - ([\mathrm{Gd}]_a + [\mathrm{PrO}]_a)}{([\mathrm{Gd}]_a + [\mathrm{PrO}]_a)} \\ &= \frac{([\mathrm{Gd}]_b + [\mathrm{Pr}]_b f) - ([\mathrm{Gd}]_a + \mathrm{Pr}]_a f)}{([\mathrm{Gd}]_a + [\mathrm{Pr}]_a f)} \end{aligned} \tag{2.9}$$

where f is the fraction of oxidized Pr detected at mass 157. From the Eq. 2.8, the Gd concentration before equilibration is:

$$[\mathrm{Gd}]_b = (K_d^{Gd} + 1)[\mathrm{Gd}]_a \tag{2.10}$$

Substituting Eq. 2.10 into Eq. 2.9, one obtains that:

$$K_d^{Gd_m} = \frac{[(K_d^{Gd} + 1)[\mathrm{Gd}]_a + \mathrm{Pr}]_b f] - ([\mathrm{Gd}]_a + \mathrm{Pr}]_a f)}{([\mathrm{Gd}]_a + \mathrm{Pr}]_a f)} \tag{2.11}$$

To estimate f (the oxide production rate for Pr) in these equations, and based on the measured K_d values (Table 2.3), we can assume that $10K_d^{Gd_m} \approx K_d^{Pr}$, and therefore:

$$[\mathrm{Pr}]_b = (K_d^{Pr} + 1)[\mathrm{Pr}]_a \approx (10K_d^{Gd_m} + 1)[\mathrm{Pr}]_a \tag{2.12}$$

Given that the concentration of Pr and Gd before the equilibration were the same in the batch experiments solution, after equilibration, the concentration of Gd in the liquid will be about 10 times higher than that of Pr (*i.e.,* [Gd]=10[Pr], since $0K_d^{Gd_m} \approx K_d^{Pr}$). The measured and actual concentration of Gd in the liquid before and after equilibration can thus be written as:

$$[\mathrm{Gd}] = [\mathrm{Gd}]_m - [\mathrm{Pr}]f \approx (10 - f)[\mathrm{Pr}] \tag{2.13}$$

Substituting Eq. 2.13 into Eq. 2.11 yield the K_d^{Gd} corrected for PrO interferences as:

$$K_d^{Gd} \approx K_d^{Gd_m} - \frac{9K_d^{Gd_m} \times f}{(10 - f)} \tag{2.14}$$

The fraction of Pr oxidized is thus equal to:

$$f = \frac{10(K_d^{Gd_m} - K_d^{Gd})}{(10K_d^{Gd_m} - K_d^{Gd})} \tag{2.15}$$

Considering ^{141}Pr and ^{157}Gd were the measured isotopes during the mass spectrometry, the abundance of ^{157}Gd ($A_{157} = 15.65$ %) and 141Pr ($A_{141} = 100$ %) should be taken into account during the derivation, which yields:

$$f = \frac{10(K_d^{Gd_m} - K_d^{Gd})}{(10K_d^{Gd_m} - K_d^{Gd})} \times \frac{A_{157}}{A_{141}} \tag{2.16}$$

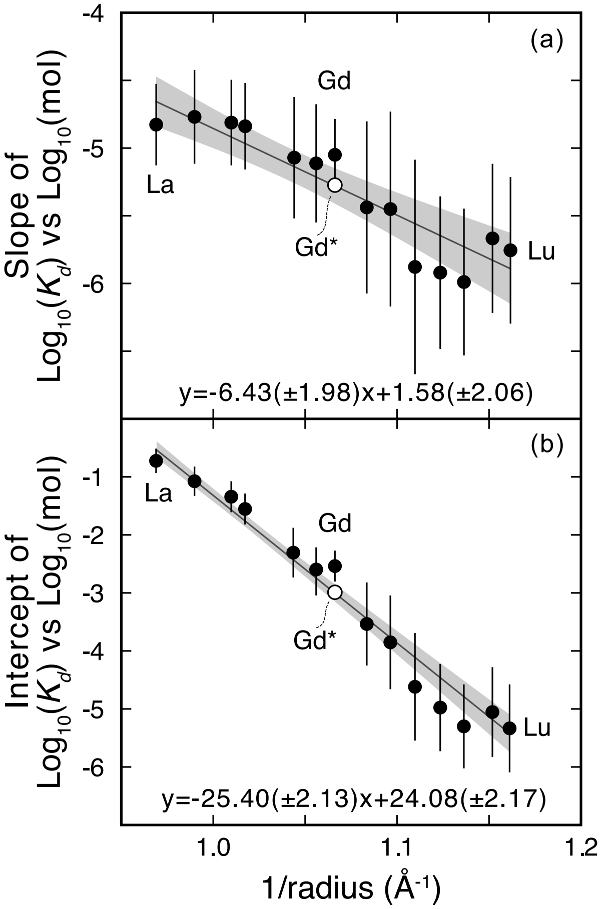

Figure 2.7: Slope (a) and intercept (b) of the linear regressions, as shown in **Fig 2.5**, as a function of the reciprocal of ionic radii (Shannon 1976). The open symbol denotes Gd* (see text for details).

If using the corrected slope and intercept of Gd (**Fig 2.5** and **Table 2.4**)) to calculate the actual K_d of Gd, the f in Eq. 2.16 is approximately 10 %, which is a typical oxide production rate for MC-ICPMS with the spray chamber, supporting the need for the correction of the K_d values for Gd.

To first-order, electrostatics controls REE partitioning on the cation-exchange resin. Elements with smaller ionic radii and higher charge densities are expected to be surrounded by larger hydration spheres, which in turn decreases the surface charge density and the affinity for the resin (*i.e.,* hydrated radius decreases with increasing ionic radius and vice versa, Korkisch 2017). Accordingly, $\log_{10}(K_d)$ should thus depend linearly on the reciprocal of the ionic radius (Nash and Jensen 2001). **Fig 2.7** shows the slope (a) and intercept (b) of the $\log_{10}(K_d)$ versus $\log_{10}$([HIBA]) best-fit lines for all REEs, plotted against the reciprocal of the ionic radius (radii from Shannon (1976)). Both the slope and the intercept of the best-fit lines are linearly correlated to the reciprocal of the ionic radius. Interestingly, Gd falls off the 95% CI of the intercept versus 1/r correlation defined by the other REEs (**Fig 2.6b**). It is also slightly offset from (although within uncertainty of) the correlation defined by other REEs in the slope versus 1/r space (**Fig 2.7a**). By bringing Gd on the regression lines defined by other REEs in **Fig 2.7**, we obtain a new value of the slope and intercept of the $\log_{10}(K_d)$ versus $\log_{10}([\mathrm{HIBA}])$ best-fit line, referred to in **Table 2.3, 2.4** as Gd*. We will show below that the corrected values for Gd* accurately predict the position of the Gd peak in our elution tests, and therefore, we recommend use of the corrected Gd* values.

2.1.4.2 Comparison of Actual and Simulated Elution Curves

To avoid potentially unsuccessful and time-consuming elution tests when trying to optimize a separation protocol, an efficient approach consists in using a computational chromatography code to simulate the elution results. Knowledge of the distribution coefficients of the elements of interest in each elution step is, however, a prerequisite to perform such simulations. To test the reliability of the distribution coefficients obtained in this study, we carried out simulations to try and reproduce two elutions using different column sizes and experimental setups. The accuracy and applicability of the K_d reported here are assessed by inspecting the consistency of the simulated and actual elution curves.

Elution 1:

A gravity-driven separation of most REEs was conducted using a custom-made quartz column (see **Fig 2.8**), and the simulated results are shown in **Fig 2.8b**. While the K_d values calculated using the regression, as shown in **Table 2.4**, mainly impact peak position, the HETP mainly controls peak width and was determined to be 0.50 ± 0.20 mm (by adjusting the value of the HETP to fit the actual elution profile). Overall, the simulation successfully reproduces the actual elution. To perfectly match the heavy REE peak position, the α-HIBA molarity of the first elution step had to be very slightly adjusted, from the 0.060 M value used in the actual elution to 0.058 M. This slight (3.3 %) discrepancy likely stems for the imprecision associated with the preparation of such a dilute α-HIBA solution (during the batch experiment and/or the elution).

Elution 2:

As the α-HIBA chemistry is widely used for Nd purification for high-precision isotope analysis (Amakawa et al. 1991; Borg et al. 1997; Carlson et al. 2007; Garçon et al. 2018; Hyung and Jacobsen 2020; Jacobsen and Wasserburg 1980; Lugmair et al. 1975; Marks et al. 2014; Rizo et al. 2011), our second comparison aimed at testing the usefulness of the reported K_d values when predicting fine-scale separations (*i.e.,* drop-by-drop), even under slightly different experimental conditions than those used for the K_d determinations. We conducted an isocratic elution with 0.2 M α-HIBA on AG50W-X4 (200–400 mesh) at pH = 4.62 (**Fig 2.9a**). The resin cross-linkage and eluent pH were different from those used for K_d determination, providing an adequate challenge to test the reliability of our data and methods for correcting pH effects, since slight pH variations are ubiquitous for column chemistry set up at different labs. Given that both pH and resin cross-linkage can influence the distribution coefficients (Pourjavid et al. 2009; Sisson et al. 1972; Van der Walt et al. 1985), a perfect match between the actual elution (X4 resin, pH = 4.62) and simulated elution (X8 resin, pH = 4.50) was not expected and was not obtained, even when accounting for the pH difference. Indeed, the light REEs eluted too late in the simulation, consistent with the general tendency of K_d values to increase with higher cross-linkage (Barkley et al. 1986). Adjusting the eluent molarity to 0.213 M (6.5% higher than the actual α-HIBA molarity used) in **Fig 2.9b** produces an exact match for the position of the Pr peak. The HETP was found to be 1.5 ± 0.2 mm. At this molarity, the peak positions of Nd and Ce are also satisfactorily matched. While Sm and the heavier REEs are predicted to elute too early, we note that the K_d values of these elements at this molarity were below the detection limit of the batch equilibration experiments, and we are thus working beyond the validity domain of the best-fit lines used to predict the K_d values (**Table 2.4**). The small (6.5%) adjustment in molarity accounts for the combined impact of all systematic biases (resin cross-linkage, eluent molarity offsets, and other experimental conditions such as T), which are only resolvable owing to the drop-by-drop (*i.e.,* fine-scale) nature of the elution.

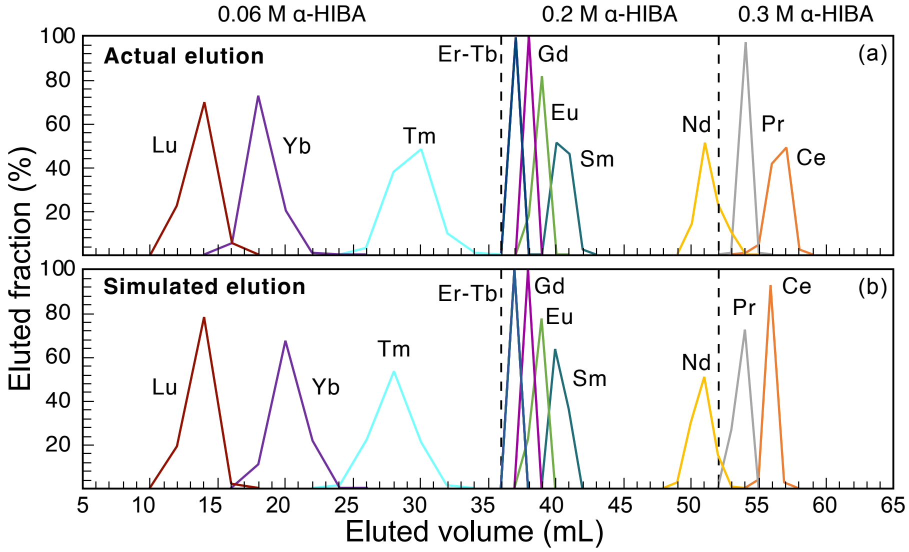

Figure 2.8: Experimental and simulated elution profiles of Elution 1. (a) Experimental elution profile of REEs using a gravity-driven quartz column: 1.9 mm ID × 21 cm length. Condition: AG50W-X8 resin (200–400 mesh) with α-HIBA (pH = 4.50), at room temperature (∼22 °C). (b) Simulated elution profile, assuming: resin porosity, 49%; (88) density of the extractant-loaded beads, 0.70 g/mL; (HETP = 0.50 ± 0.20 mm).

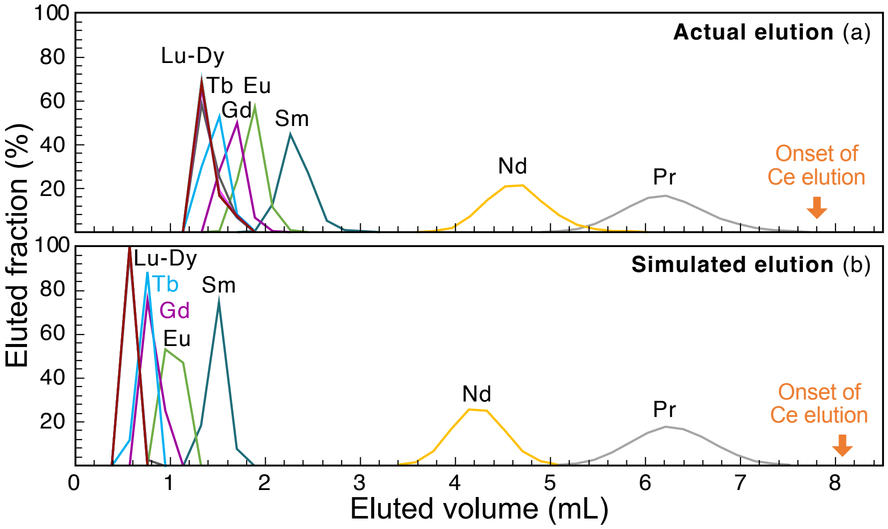

Figure 2.9: Experimental and simulated elution profiles of Elution 2. (a) Experimental elution profile of REEs using a pressurized (1.0 psi) borosilicate column (2.0 mm ID × 30 cm length), with AG50W-X4 resin (200–400 mesh) and α-HIBA (pH = 4.62), at room temperature (∼22 °C). The resulting flow rate was 47 μL/min. (b) Simulated elution profile, assuming: resin porosity, 57%; (88) density of the extractant-loaded beads, 0.70 g/mL; (HETP = 1.5 ± 0.2 mm).

2.2 Mg isotope analyses for CAIs

2.2.1 Magnesium chromatography

In this section, we optimized the Mg column chemistry for CAIs. The Mg chromatography was modified from the established method (Tang et al. 2021; Wombacher et al. 2009; Young et al. 2009) to be more suitable for Ca-rich samples to obtain a better separation of Mg and Ca, which is described in **Table 2.5**.

Table 2.5: Magnesium ion exchange chromatography

Step	Volume	Acid
Cleaning	10 mL	MQ H_2O
	10 mL	0.5 M HCl
	15 mL	6 M HCl
	10 mL	MQ H_2O
	15 mL	6 M HCl
Pre-condition	10 mL	0.5 M HCl
Load sample	0.5 mL	0.5 M HCl
Rinse Matrix	34.5 mL	0.5 M HCl
Elute Al and Ti	7 mL	0.15 M HF
	2 mL	MQ H_2O
Elute Fe	9 mL	95% Acetone + 0.5 M HCl
	3 mL	MQ H_2O
Elute Mg	26 mL	1 M HCl

Magnesium separation was conducted using 10 mL Bio-Rad Poly-Prep columns filled with 2 mL AG50W-X8 resin (200-400 mesh, hydrogen form). Approximately 0.5–1 mL sample solution was loaded on the columns, which had been cleaned and pre-conditioned with a sequence of Milli-Q (MQ) water and acids. Matrix elements (alkali elements and Cr) were firstly removed from the column in 34.5 mL 0.5 M HCl and then Al and Ti were eluted in 7 mL 0.15 M HF. The resin was rinsed with 2 mL MQ to condition the column. Nine mL freshly made 95% acetone–0.5 M HCl was added to remove Fe, followed by the addition of 3 mL MQ water to wash the remaining acetone. The freshly-made acetone-HCl mixture and MQ rinse after the Fe removal are critical for the chemistry because the acetone-HCl mixture can self-catalyze to increase the viscosity of the solution and thus create matrix effects for the following isotopic analyses. Magnesium was finally eluted in 26 mL 1 M HCl.

The Mg elution is the major optimization for CAIs, which used a more diluted HCl than established scheme in Tang et al. (2021). The modification takes advantage of a significant distribution coefficient difference between Mg and Ca in 1 M HCl than 2 M HCl. Elution test of this modified chemistry was conducted with DTS-2, whose elution profile is shown in **Fig. 2.10**. For CAIs and quality control geostandards, this purification procedure was repeated twice, and then an aliquot of each sample was used for concentration determination to ensure the sufficient removal of interference elements, including Cr, Ti, and Ca. With this modified procedure, the Ca/Mg ratios in the Mg sample solutions were less than 10 % after two rounds of column chemistry.

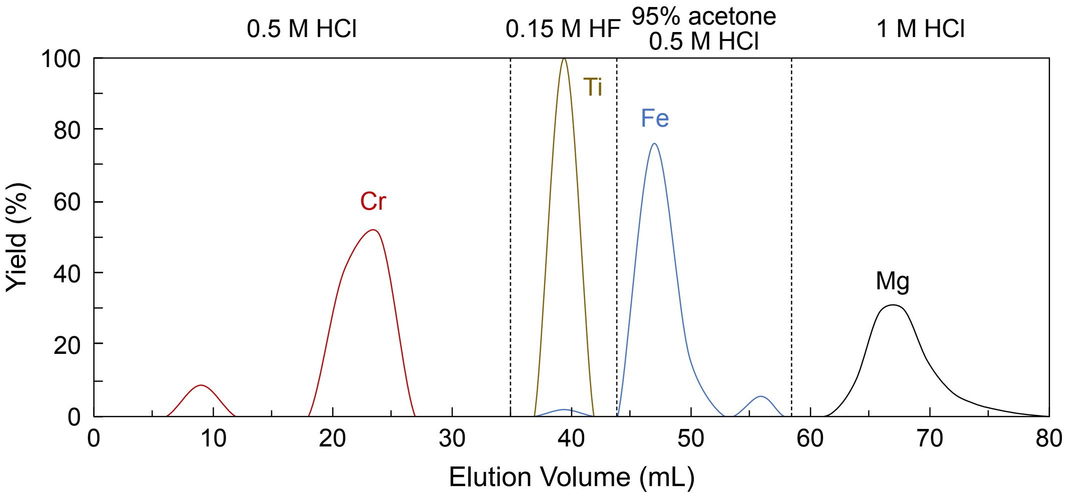

Figure 2.10: Elution profile of DTS-2 for Mg separation. The collect volume is 2–3 mL, and the elution curves of interference elements Cr, Ti, and Fe are also shown. DTS-2 is a standard with high Mg and low Ca contents, and the purpose of this elution test is to calibrate the collecting volume for Mg cut. Calcium is partially eluted with Mg at the end using 1 M HCl, but the remaining Ca in the Mg cut is less than 10 % and would not influence the Mg isotope measurements. Using a more diluted HCl could achieve complete separation between Mg and Ca, and the reason for choosing 1 M HCl is to balance a manageable collecting volume and separation.

The yields of Mg after the entire purification procedure are >99 %, with procedural blank ~40 ng, negligible relative to the amount of Mg processed through column chemistry (<0.4 % of Mg in sample). After purification, the Mg cut was evaporated to dryness and 0.25 mL H_2O_2 and 0.20 mL concentrated HNO_3 were added to oxidize any residual acetone or organic matter released from the resin. After refluxing overnight at 120 °C, the mixture was completely dried and then reconstituted into 3 vol% HNO_3 for Mg isotope analyses.

2.2.2 Mass spectrometry for Mg isotope analyses

Magnesium isotope analyses were performed on a Neptune*Plus* (ThermoFisher) MC-ICPMS, using Jet sample and X-skimmer cone combination, coupled with a dual cyclonic quartz spray chamber. The measurements were conducted in middle-resolution mode using a static cup configuration in **Table** 2.6.

Table 2.6: Cup configurations for Mg isotope measurements on MC-ICPMS

Faraday cup	L2	C	H2	H4
Amplifier (Ω)	10^{11}	10^{11}	10^{11}	10^{11}
Isotope	^{24}Mg	^{25}Mg	^{26}Mg	^{27}Al

Samples were diluted to 0.5 ppm in 3 vol% HNO_3 and introduced to the mass spectrometer at a ~100 μL/min uptake flow rate for 40 s. Each analysis consisted of 50 cycles of 4.194 s integration time. The blank was measured before and after each session, with ^{24}Mg signal in rinse of ~25 mV without obvious elevation through the session. The sample measurements were bracketed by an in-house standard, with δ^{25}Mg = -0.805 ‰, and δ^{26}Mg = -1.556 ‰ relative to the primary DSM-3 standard (Galy et al. 2003) obtained from long-term measurements.

Stable Mg isotope compositions are reported in δ notation (permil unit, ‰) relative to DSM-3 standard, which is defined as:

$$\delta^{i}\mathrm{Mg} = \left[\frac{(^{i}\mathrm{Mg}/^{24}\mathrm{Mg})_{\mathrm{smp}}}{(^{i}\mathrm{Mg}/^{24}\mathrm{Mg})_{\mathrm{DSM\text{-}3}}} - 1\right] \times 1000 \tag{2.17}$$

where i denotes 25 or 26. The ^{26}Mg excesses deviating from the mass dependent fractionation is represented as $\delta^{26}\mathrm{Mg}^{*}$, calculating using the formula in Davis et al. (2015) and Wasserburg et al. (2012):

$$\delta^{26}\mathrm{Mg}^{*} = \delta^{26}\mathrm{Mg} - \left[\left(1 + \frac{\delta^{25}\mathrm{Mg}}{1000}\right)^{\frac{1}{\beta}} - 1\right] \times 1000 \tag{2.18}$$

where β is the mass dependent fractionation factor. The choice of exponent β remains a long-lasting debate to correct the mass dependent fractionation of CAIs (*e.g.,* Davis et al. 2015). Here, we applied the widely-used kinetic fractionation factor (Jacobsen et al. 2008), which is defined as:

$$\beta = \frac{ln(m_{24}/m_{25})}{ln(m_{24}/m_{26})} = 0.51101 \tag{2.19}$$

where m_{24}, m_{25}, and m_{26} are the masses of three Mg isotopes: ^{24}Mg, ^{25}Mg, and ^{26}Mg, with values of 23.985042, 24.985837, and 25.982593, respectively (Wang et al. 2012). Uncertainties are reported as 2 standard error (2SE, 95 % Confidence Interval, CI) and calculated using 2 standard deviation (2SD) divided by the square root of the number of replicate measurements for a given sample (*i.e.,* 2SE = 2SD/$\sqrt{n}$). For stable Mg isotope compositions, standard deviation used the daily external reproducibility of the standard, while the $\delta^{26}\mathrm{Mg}^{*}$ used the standard deviation of the replicates measurements of the sample.

2.2.3 Determination of ^{27}Al/^{24}Mg ratio

To measure ^{27}Al/^{24}Mg ratios, aliquots of samples before Mg chemistry were dried and redissolved into 3 vol% HNO_3. A concentration standard (50 ppb Mg, 150 ppb Al) was prepared by diluting SPEX CertiPrep ICP-MS single-element standards. The Al/Mg ratio of the prepared concentration standard was calibrated as 3.042 by the gravimetric method. The ^{27}Al/^{24}Mg ratios were measured on MC-ICPMS using the same setting up as Mg isotopes, given that ^{27}Al and ^{24}Mg can be measured simultaneously with the current cup configuration. Sample standard bracketing method was applied, and all data were collected in 10 cycles of 4.194 s integration time. The $^{27}\text{Al}/^{24}\text{Mg}$ ratios of samples were derivated by normalizing to the gravimetrically calibrated standard using the equation:

$$\left(\frac{^{27}\text{Al}}{^{24}\text{Mg}}\right)^{\text{corr}}_{\text{smp}} = \left(\frac{^{27}\text{Al}}{^{24}\text{Mg}}\right)^{\text{meas}}_{\text{smp}} \times \frac{\left(\frac{\text{Al}}{\text{Mg}}\right)^{\text{grav}}_{\text{std}} \Big/ \frac{M(\text{Al})}{M(\text{Mg})} \times \frac{Ab(^{27}\text{Al})}{Ab(^{24}\text{Mg})}}{\left(\frac{^{27}\text{Al}}{^{24}\text{Mg}}\right)^{\text{meas}}_{\text{std}}} \tag{2.20}$$

where $\left(\frac{^{27}\text{Al}}{^{24}\text{Mg}}\right)^{\text{meas}}_{\text{smp}}$ and $\left(\frac{^{27}\text{Al}}{^{24}\text{Mg}}\right)^{\text{meas}}_{\text{std}}$ are the measured intensity ratio of sample and standard, respectively; $\left(\frac{\text{Al}}{\text{Mg}}\right)^{grav}_{std}$ is the Al/Mg ratio of the gravimetrically calibrated standard; M(Al) and M(Mg) are the atomic mass of Al and Mg, which used 26.98154 and 24.3053; Ab(^{27}Al) and Ab(^{24}Mg) are the abundance of ^{27}Al and ^{24}Mg. The abundance of ^{24}Mg is calculated using the Mg isotope composition of the SPEX Mg standard. The uncertainties on $^{27}\text{Al}/^{24}\text{Mg}$ ratios were calculated as:

$$\sigma_{\frac{^{27}\text{Al}}{^{24}\text{Mg}}} = \left(\frac{^{27}\text{Al}}{^{24}\text{Mg}}\right)^{\text{meas}}_{\text{smp}} \times \sqrt{\left(\frac{\sigma_{^{27}\text{Al}}}{^{27}\text{Al}}\right)^2 + \left(\frac{\sigma_{^{24}\text{Mg}}}{^{24}\text{Mg}}\right)^2} \tag{2.21}$$

where ^{27}Al and ^{24}Mg are intensities of signals, and $\sigma_{^{27}\text{Al}}$ and $\sigma_{^{24}\text{Mg}}$ are the corresponding uncertainties. To monitor the accuracy of analyses, geostandards BCR-2 and BHVO-2 were processed along with CAIs, with differences between measured and certified $^{27}\text{Al}/^{24}\text{Mg}$ ratios ~ ±1 % (**Fig. 2.11a**).

The potential bias from the matrix effects was evaluated by the standard addition – a method that minimizes the matrix effects by adding the gravimetric Al/Mg standard to unknown CAIs (illustrated in **Fig. 2.12**). By increasing volumes of standard solution in the mixture, the Al and Mg concentrations can be determined by extrapolating the signals from a series of standard additions. The concentration of the isotope of interest A is calculated as:

$$[A]_{\text{smp}} = -\frac{b_A}{m_A} \times [A]_{\text{std}} \tag{2.22}$$

where A denotes ^{27}Al or ^{24}Mg; [A] is the molar concentration; b and m are the intercept and slope of the linear regression of intensity of A vs. proportion of standard **Fig. 2.11**. The $^{27}\text{Al}/^{24}\text{Mg}$ ratio of sample is:

$$\left(\frac{^{27}\text{Al}}{^{24}\text{Mg}}\right)_{\text{smp}} = \frac{b_{^{27}\text{Al}}/m_{^{27}\text{Al}}}{b_{^{24}\text{Mg}}/m_{^{24}\text{Mg}}} \times \left(\frac{^{27}\text{Al}}{^{24}\text{Mg}}\right)_{\text{std}} \tag{2.23}$$

Fig. 2.11b demonstrates that the direct measurements of sample solution reproduced $^{27}\text{Al}/^{24}\text{Mg}$ ratios as standard addition method within ±2 % (**Fig. 2.11b**). The results suggest the matrix effects are negligible for the direct measurement methods and thus can be used to preciously determine $^{27}\text{Al}/^{24}\text{Mg}$ ratios in CAIs.

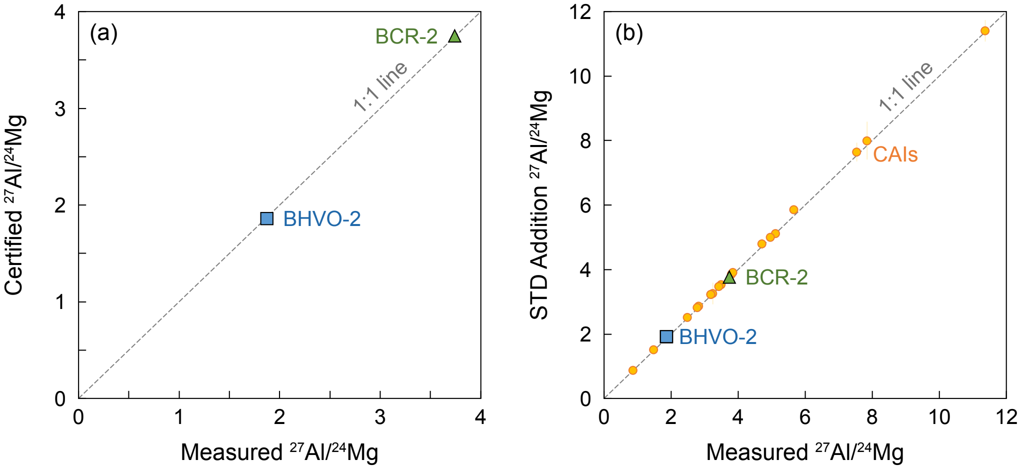

Figure 2.11: The ^{27}Al/^{24}Mg ratios of geostandards and CAIs. (a) Certified vs. measured ^{27}Al/^{24}Mg ratios of BCR-2 and BHVO-2. (b) The ^{27}Al/^{24}Mg ratios of geostandards and CAIs obtained from direct measurements vs. standard addition method.

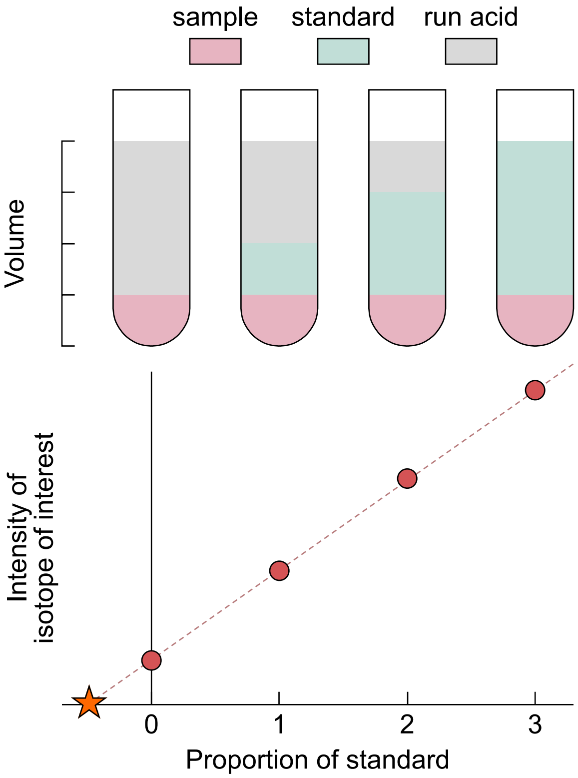

Figure 2.12: Schematic illustration of standard addition method for concentration determination. The upper panel shows the experimental scheme of the standard addition used in this work. To determine the Al and Mg concentration, four solutions were prepared for each sample. Each solution had 1/4 of sample solution, with proportion of standard solution 0, 1/4, 1/2, and 3/4, respectively. The remaining proportion was filled up with run acid (*i.e.,* 3 vol% HNO_3). The bottom panel illustrates the intensity of ^{27}Al or ^{24}Mg for the series of 4 solutions. The x intercept is proportional to the concentration of isotope of interest in the standard.

2.3 In-situ ^{26}Al-^{26}Mg analyses

An initial search for targeted areas on the epoxy mounts of CAIs for in-situ ^{26}Al-^{26}Mg measurements was performed with a ZEISS 1550VP Field Emission SEM at Caltech. Approximately 10 spots for each major mineral phase of interest were selected, based on the following criteria: (1) the grain size exceeds 10 μm; (2) the mineral is free of alteration and surface defects such as cracks and inclusions. Minor phases such as hibonite, and perovskite were also selected when available. For each area of interest, both BSE and secondary electron (SE) images were made for secondary ion mass spectrometer (SIMS) navigation.

In-situ ^{26}Al-^{26}Mg isotope analyses were performed on CAMECA IMS 1270-E7 and IMS 1280-HR2 at CRPG following the method described in previous studies (Luu et al. 2013; Piralla et al. 2023; Villeneuve et al. 2009). Measurements were conducted in multicollection mode on 4 Faraday cups (FC): ^{24}Mg on L1 equipped with a 10^{11} Ω resistor, ^{25}Mg and ^{26}Mg on C and H1 equipped with 10^{12} Ω resistors and ^{27}Al on H'2 equipped with a 10^{11} Ω resistor. Mass resolution was set to 2500 (*i.e.,* exit slit 1 on multicollection trolleys) to separate the doubly charged interference ^{48}Ca^{2+} and ^{48}Ti^{2+}. Selected spots were bombarded with a <10 μm, 5 nA O_2^- primary ion beam generated by a Hyperion-II oxygen plasma source accelerated at 13 keV. Magnesium isotope compositions are reported in δ' notation (in permil unit):

$$\delta^i\mathrm{Mg}' = ln\left[\frac{\left({}^i\mathrm{Mg}/{}^{24}\mathrm{Mg}\right)_{\mathrm{meas}}}{({}^i\mathrm{Mg}/{}^{24}\mathrm{Mg})_{\mathrm{ref}}}\right] \times 1000 \tag{2.24}$$

where i denotes 25 or 26; $({}^i\mathrm{Mg}/{}^{24}\mathrm{Mg})_{\mathrm{ref}}$ assumed terrestrial Mg isotope compositions, with values of $^{25}\mathrm{Mg}/^{24}\mathrm{Mg} = 0.12663$, and $^{26}\mathrm{Mg}/^{24}\mathrm{Mg} = 0.13932$ (Catanzaro et al. 1966). To derive ^{26}Mg excesses, instrumental mass fractionation (IMF) of Mg isotopes need to be introduced:

$$\alpha_i = \frac{\left({}^i\mathrm{Mg}/{}^{24}\mathrm{Mg}\right)_{\mathrm{meas}}}{({}^i\mathrm{Mg}/{}^{24}\mathrm{Mg})_{\mathrm{true}}} \tag{2.25}$$

The relationship between α_{25} and α_{26} is described by an exponential mass fractionation law:

$$\alpha_{25} = (\alpha_{26})^{\beta} \tag{2.26}$$

where β is the IMF exponential factor. The Eq. 2.26 can also be written as:

$$ln(\alpha_{25}) = ln(\alpha_{26}) \times \beta \tag{2.27}$$

The IMF was calibrated by a series of international and in-house standards, including San Carlos olivine, Burma spineal, CLDR01 MORB glass, gold enstatite, and Allende melilite (Mel-1) glass. Using the IMF to express the δ'^iMg can obtain:

$$\delta^i\mathrm{Mg}' = ln(\alpha_i) \times 1000 \tag{2.28}$$

substituting Eq. 2.28 into Eq. 2.27 leads to:

$$\delta^{25}\mathrm{Mg}' = \delta^{26}\mathrm{Mg}' \times \beta \tag{2.29}$$

For terrestrial standards, mass-independent fractionation of Mg isotopes are assumed to be negiligible, and thus the β can be derived by the linear regression through the standard data in δ^{25}Mg' vs. δ^{26}Mg', which can be expressed as:

$$\delta^{25}\mathrm{Mg}'_{\mathrm{std}} = \delta^{26}\mathrm{Mg}'_{\mathrm{std}} \times a + b \tag{2.30}$$

where b represents the analytical parameters of SIMS analyses, such as FC inter-calibration. The β values varied from 0.510 to 0.516 during different sessions (**Fig. 2.13**).

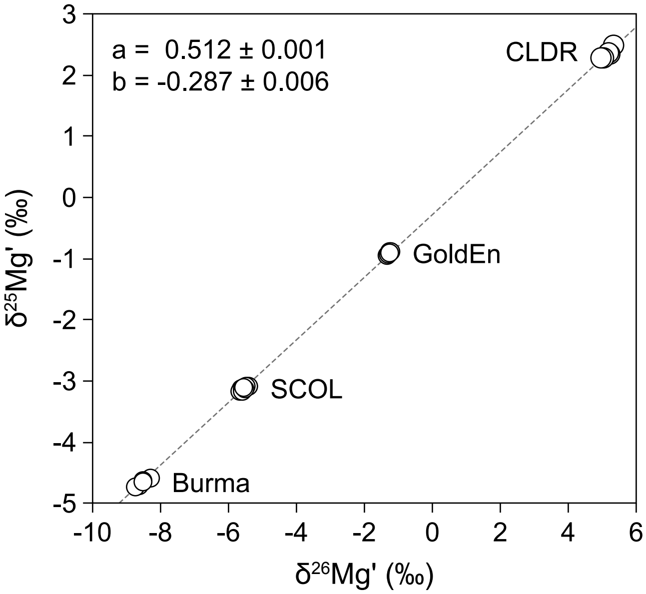

Figure 2.13: IMF characterization using the linear regression of terrestrial standards in δ^{25}Mg' vs. δ^{26}Mg' space: Burma – Burma spinel, SCOL – San Carlos Olivine, GoldEn – gold enstatite, and CLDR – CLDR MORB glass. The a and b represent the slope and intercept in Eq. 2.30.

The ^{26}Mg excess was calculated with the formula:

$$\delta^{26}\mathrm{Mg}^{*} = \delta^{26}\mathrm{Mg}' - (\delta^{25}\mathrm{Mg}' - b)/a \tag{2.31}$$

The uncertainty of δ^{26}Mg* is calculated as:

$$\sigma_{26^*} = \sqrt{\sigma_{26'}^2 + (\sigma_{25'}/a)^2 \times (\sigma_{25'} \times \sigma_{26'} \times r_{25,26}/\beta)} \tag{2.32}$$

where σ_{26^*}, $\sigma_{26'}$, and $\sigma_{25'}$ are uncertainties of δ^{26}Mg*, δ^{26}Mg', and δ^{25}Mg', respectively; $r_{25,26}$ is the cross-correlation of $^{25}\mathrm{Mg}/^{24}\mathrm{Mg}$ and $^{26}\mathrm{Mg}/^{24}\mathrm{Mg}$.

To precisely determine the $^{27}\mathrm{Al}/^{24}\mathrm{Mg}$ ratios for isochron, the measured values must be corrected using the relative sensitivity factor (RSF) for different mineral phases, since Al and Mg have slightly different ion yields during SIMS analyses. The RSF is defined as:

$$\mathrm{RSF} = \frac{(^{27}\mathrm{Al}/^{24}\mathrm{Mg})_{\mathrm{meas}}}{(^{27}\mathrm{Al}/^{24}\mathrm{Mg})_{\mathrm{true}}} \tag{2.33}$$

which were characterized by the corresponding standards with well-characterized $^{27}\mathrm{Al}/^{24}\mathrm{Mg}$ ratios. The true $^{27}\mathrm{Al}/^{24}\mathrm{Mg}$ ratios of CAI minerals, including melilite, spinel, anorthite, and hibonite were calibrated by RSFs determined by Mel-1, 2 glass, Burma spinel, An-2 glass, Al-rich pyroxene glass, and Hib-A-00, respectively. The uncertainty on $^{27}\mathrm{Al}/^{24}\mathrm{Mg}$ was calculated as:

$$\sigma_{\mathrm{true}}^{27/24} = \sqrt{(\sigma_{\mathrm{meas}}^{27/24})^2 + [(^{27}\mathrm{Al}/^{24}\mathrm{Mg})_{\mathrm{meas}} \times \sigma_{\mathrm{RSF}}^{r}]^2} \tag{2.34}$$

where $\sigma_{\mathrm{true}}^{27/24}$ and $\sigma_{\mathrm{meas}}^{27/24}$ are the uncertainty of the true and measured $^{27}\mathrm{Al}/^{24}\mathrm{Mg}$ ratios; $\sigma_{\mathrm{RSF}}^{r}$ is the relative uncertainty (%) of RSFs.

The in-situ $^{26}\mathrm{Al}$-$^{26}\mathrm{Mg}$ analyses of CAIs CG-*ft*-4–8, 10, 11, and 13 were also performed on a CAMECA ims-1290 ion microprobe at UCLA following the method described in Liu et al. (2018). The data reduction is similar to the method described before. In breif, Selected mineral phases were bombarded with a ∼5 μm, 1-3 nA O_2^- primary ion beam generated by a Hyperion-II oxygen plasma source. With this experimental setting, secondary ion signals of Mg and Al were intense enough to be simultaneously measured with multiple Faraday cups without switching the magnetic field setting. Each spot analysis had a 45 s sputtering and 30 cycles (10s/cycle) of data acquisition, resulting in craters ∼5 μm wide and ∼1–2 μm depth. A suite of terrestrial standards, including Burma spinel, San Carlos olivine, San Carlos pyroxene, and synthetic glass of fassaite composition, were used to characterize instrumental mass fractionation. Isoplot regressions for all measurements were calculated using Model 1 (the maximum likelihood) in IsoplotR (Vermeesch 2018).

2.4 U isotope analyses

2.4.1 Chromatography

Uranium separation and purification are performed with U-TEVA resin (diamyl, amylphosphonate, DAAP, 50–100 μm), using the property that U has strong retention with UTEVA with concentrated acid, while can be stripped out with a small volume of dilute acid (Horwitz et al. 1992). In this section, manual and automatic column chemistry are described in **Table 2.7**.

2.4.1.1 Bench top chromatography by vacuum box

Uranium purification was performed on pre-packed 2 mL Eichrom UTEVA cartridges (⌀ = 1.14 cm, l = 2.56 cm) and a vacuum box for bench top column chemistry in

Table 2.7: Uranium ion exchange chromatography

Step	Acid	Volume		
		Normal	Low U	prepFAST
Cleaning	0.05 M HCl	30 mL	40 mL	mL
Pre-condition	3 M HNO_3	10 mL	10 mL	mL
Load sample	3 M HNO_3	5-10 mL	5-10 mL	5-10 mL
Rinse Matrix	3 M HNO_3	12 mL	30 mL	mL
Conversion to HCl	10 M HCl	5 mL	5 mL	mL
Elute Th	5 M HCl	8 mL	12 mL	mL
Elute U	0.05 M HCl	20 mL	32 mL	4 mL

the hood. Barrels of 10 mL BD Luer-Lok syringe were used as the acid reservoir on the top of the cartridge, and 1 mL pipette tips were connected to the bottom of the cartridge to elute the liquid.

For typical terrestrial samples (with abundant U), the resin was cleaned with 30 mL 0.05 M HCl and then conditioned with 10 mL 3 M HNO_3. Samples were loaded onto the resin in 5 mL 3 M HNO_3, and matrix elements were eluted in 12 mL 3 M HNO_3. The resin was then converted with 5 mL 10 M HCl, followed by Th removal in 8 mL 5 M HCl. U was finally eluted in 20 mL 0.05 M HCl and collected in cleaned 30 mL beakers. The U cut was evaporated to dryness, and 0.25 mL H_2O_2 and 0.20 mL concentrated HNO_3 were added to oxidize any organic matter released from the resin. After refluxing overnight at 120 °C, the mixture was completely dried and taken back into 3 M HNO_3. The column chemistry was repeated a second time to ensure precise and accurate measurements of $^{234}U/^{238}U$ (Tissot et al. 2018). The final U cuts were evaporated to dryness before being redissolved in concentrated HNO_3. Samples were then evaporated to near dryness and ultimately diluted to 3 vol% HNO_3 for isotopic measurements.

The protocol is modified for low U samples, including meteorites (and their component), igneous rocks, and mass-limited samples (*e.g.,* single zircon). The resin is cleaned with a larger volume of (40 mL) 0.05 HCl to completely remove any U retained on U-TEVA resin. After loading, 30 mL of 3 M HNO_3, 5 mL of 10 M HCl, and 12 mL of 5 M HCl were used in sequence to elute matrix elements and Th. The U was finally eluted in 32 mL 0.05 M HCl at the end. An increased volume of acids is used to achieve a more thorough removal of matrix elements and full recovery of U in samples.

2.4.1.2 Automated chromatography by PrepFAST

Uranium isotope application on paleo-redox construction raises the need to process large number of samples to obtain high-resolution profiles of the periods of interest. However, the labor-intensive sample purification process is time-consuming and remains a bottleneck for high throughput analyses. The appearance of the ESI prepFAST System can significantly improve the efficiency of the sample processing process. The prepFAST is a syringe-driven system (dual FAST valves with 4 syringe pumps) equipped with several reagent stock bottles. The U chemistry uses a 0.6 mL packed U-TEVA cartridge (CF-MC-U-0600), which can be reused at least 60 times. Reagent stock bottles are filled with 3 M HNO_3, 0.05 M, 5 M, and 10 M HCl, and column chemistry is similar to manual feed chromatography. Uranium is eluted in 4 mL 0.05 M HCl, and 1 mL concentrated HNO_3 is added to the U cut for the second round of chemistry.

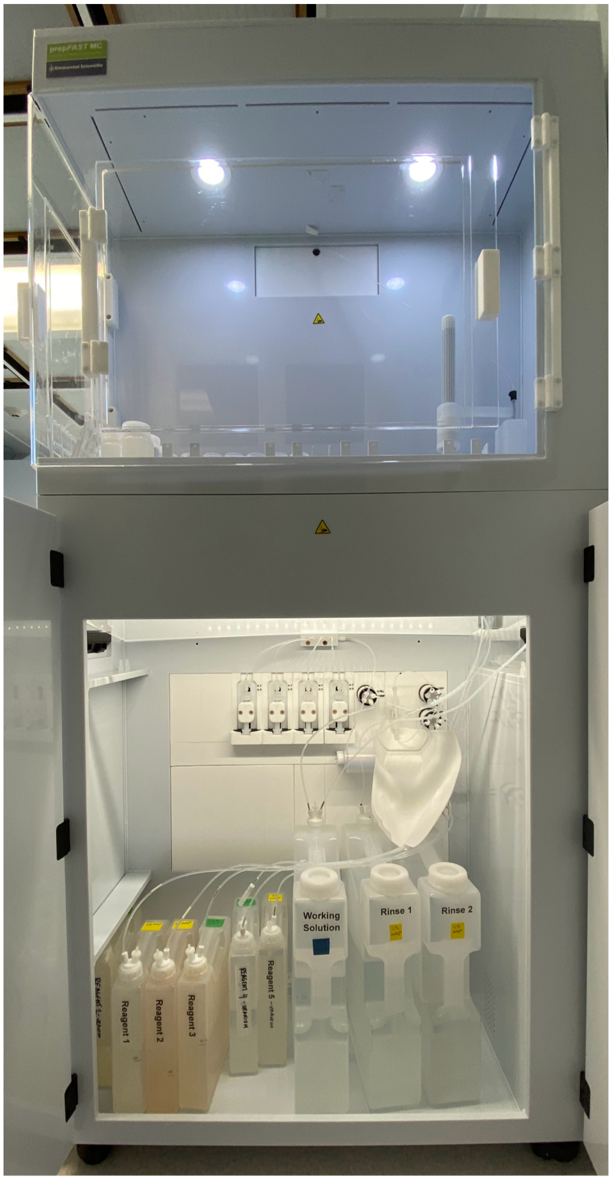

Figure 2.14: Photo of preFAST System. The top part mainly consists of an auto-sampler to place samples and collection tubes/beakers; the bottom part includes the resin cartridge, syringe system, and acid storage bottles.

2.4.2 Mass spectrometry

Uranium isotope analyses were performed on a NeptunePlus (ThermoFisher) multiple collector inductively coupled plasma mass spectrometer (MC-ICPMS). The Jet sample and X-skimmer cones were used in combination with an Aridus3 or Apex Omega HF desolvating nebulizer. The measurements were conducted in low-resolution mode using a static cup configuration (**Table 2.8**).

Table 2.8: Cup configurations for U isotope measurements on MC-ICPMS

Faraday cup	L2	L1	C	H1	H2	H3
Amplifier	10^{11}	10^{11}	SEM	10^{11}	10^{11}	10^{11}
Isotope	^{232}Th	^{233}U	^{234}U	^{235}U	^{236}U	^{238}U

For most terrestrial samples, each analysis consisted of 50 cycles of 4.194 s integration time. For extraterrestial materials, the take-up time was reduced to 36 s (minimal time to achieve stable signal) to avoid wasting samples. Each analysis consisted of 40–60 cycles of 4.194 s integration time depending on the available sample masses. The sample measurements were bracketed by the CRM-112a standard spiked with IRMM-3636 at a similar U_{spike}/U_{sample} ratio as the samples. Instrumental mass fractionation was corrected by standard-sample-bracketing and double spike deconvolution. Amplifier gain calibrations were performed daily. The ^{234}U signal was measured with a secondary electron multiplier (SEM) on the axial mass. The SEM-Faraday cup gain was calibrated manually with replicate analyses of the CRM-112a standard solution in both SEM and Faraday mode at the beginning and end of each analytical sequence (Kipp et al. 2022).

A calibration was conducted at the beginning and end of each analytical session to ensure that we accurately determined the yield between SEM and FC modes. The calibration used the same bracketing CRM-112a standard solution that were measured with two sub-sequences: the center cup (^{234}U) signal was measured by the SEM and a Faraday cup with a 10^{12} Ω amplifier in the two sub-sequence respectively. In a typical run, 3 replicates of this “cps/V calibration” method were conducted to to determine the yield by the average value of these replicates. When using this method, the yield of the SEM diminished throughout a multi-week analytical session (**Fig. 2.15**), as is expected due to degradation of the SEM as a linear function of counts. Since individual yield calibrations are not very precise, owing to the small ^{234}U ion beam (1–2 mV), a linear trend was fitted through the cps/V values as a function of cumulative counts registered by the SEM and used the corresponding values to correct our data through a multi-sequence analytical session (typically 5–15 days long).

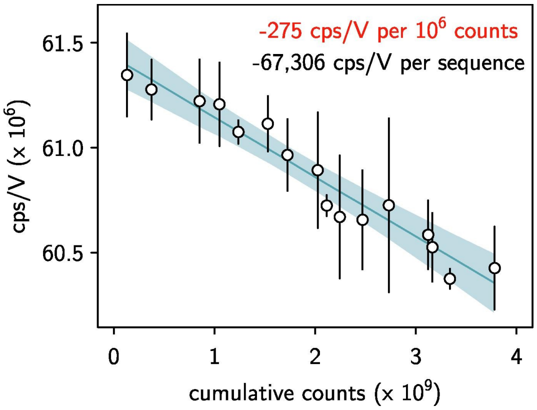

Figure 2.15: SEM-Faraday cup yield calibration through 16 consecutive analytical sequences. One sequence was run per day and the yield was measured at the beginning and end of each sequence; the points and error bars represent the mean and 95 % CI of these yield determinations. The total number of counts registered in the SEM per session were then tallied and the yield determinations were fit against cumulative counts. Solid line denotes linear trend through data with 95 % CI in shaded region as determined by Monte Carlo simulation. We find that the yield diminishes by about 275 cps/V per million counts.

The maximum theoretically achievable precision for a single measurement (*i.e.,* the internal precision). There are two contributions to analytical error that we must consider in this calculation: 1) electronic noise, called Johnson noise or shot noise (σ_{Johnson}) and 2) counting statistics (σ_{counting}). Johnson noise is a function of detector temperature (T), amplifier resistance (R), and measurement time (t), such that:

$$\sigma_{\text{Johnson}} = \sqrt{\frac{4kTt}{e^2R}} \tag{2.35}$$

where k is the Boltzmann constant and e is the elementary charge. The error from counting statistics is in contrast related only to the number of counts registered by a detector. In this case, the counts are ions hitting a Faraday cup or being counted in the SEM. John and Adkins (2010) define an operational variable, n_{eff}, calculated as:

$$n_{\text{eff}} = \frac{n_a n_b}{n_a + n_b} \tag{2.36}$$

which can be used to describe the number of counts made by two detectors for a given isotope ratio measurement. Here, n_a and n_b refer to the number of atoms of the two isotopes of interest that are counted. For the SEM, this is equal to the measurement reported in units of counts-per-second (cps) multiplied by the integration time for a single measurement. For Faraday cups, the voltage registered can be related to counts assuming a cps/V value of 6.25×10^7 (small fluctuations in this value have a negligible effect in this calculation, but will be considered in detail below). Using the n_{eff} notation, the error from counting statistics can be calculated as

$$\sigma_{\text{counting}} = \frac{1}{\sqrt{n_{\text{eff}}}} \tag{2.37}$$

We also note that despite achieving sub-optimal precision, the use of a 10^{12} Ω amplifier on the minor isotope still outperforms matched 10^{11} Ω amplifiers in the region of neff space where Johnson noise is the dominant source of error ($n_{\mathrm{eff}} < 10^8$). As this is the region of n_{eff} space for all $\delta^{234}U_{\mathrm{sec}}$ measurements undertaken here, we utilized a 10^{12} Ω amplifier in all tests where ^{234}U was measured in a Faraday cup.

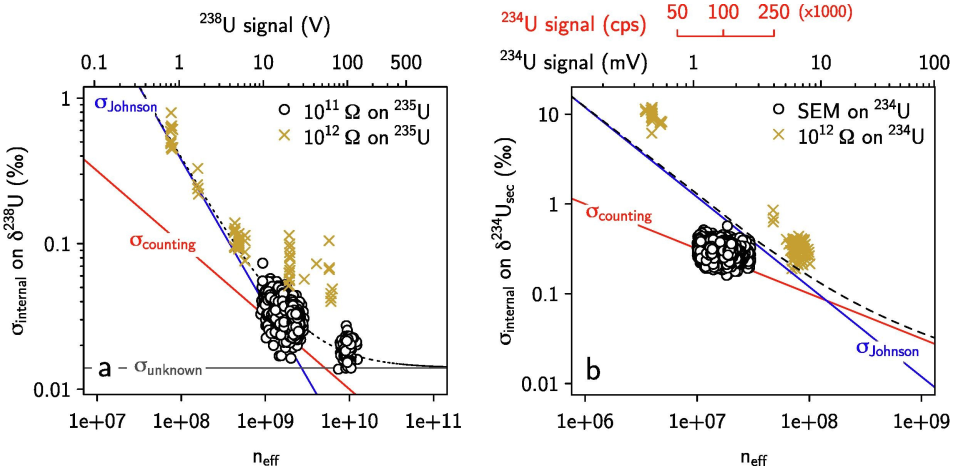

Figure 2.16: Limits on internal precision of U isotope analyses. Internal precision on (a) $\delta^{238}U$ and (b) $\delta^{234}U_{\mathrm{sec}}$ measurements is limited by Johnson noise ($\sigma_{\mathrm{Johnson}}$; blue lines) and counting statistics ($\sigma_{\mathrm{counting}}$; red lines). All sample data (white circles) plot at the theoretical maximum internal precision (represented by the dashed black curve, which is the sum of the red and blue lines). Standards analyzed with a 10^{12} Ω amplifier on ^{235}U show poorer internal precision (gold crosses, panel a). The subset of samples for which ^{234}U was measured in a Faraday cup (gold crosses, panel b; 10^{12} Ω amplifier) are limited by both Johnson noise and counting statistics; all other samples for which ^{234}U was measured in the SEM (white circles) were only limited by counting statistics. Theoretical error from Johnson noise was calculated for a 10^{11} Ω amplifier on ^{235}U in panel (a) and 10^{12} Ω amplifier on ^{234}U in panel (b); 10^{11} Ω amplifier was used for ^{238}U in all calculations. Top x-axes denote signal intensity on ^{238}U and ^{234}U in panels (a) and (b), respectively. In panel (b), the secondary (red) top x-axis denotes the signal in cps registered on the SEM for SEM-FAR measurements; the primary (black) top x-axis denotes the signal in mV registered on the Faraday cup for FAR-FAR measurements.

Chapter 3

INTRODUCTION THE UID: URANIUM ISOTOPE DATABASE

Work presented in this chapter has been published in:

Li, H., Tissot, F.L.H., (2023). UID: The uranium isotope database. *Chemical Geology* **618**, 121221.

3.1 Motivation

In 1939, Alfred O. Nier reported the first analysis of the isotopic composition of uranium (U), the heaviest primordial element, establishing the $^{238}U/^{235}U$ ratio as 139 (± 1 %) (Nier 1939). Since this pioneering work, the study of U isotopes has found applications in a wide range of scientific fields, including geochemistry, cosmochemistry, nuclear chemistry, and environmental engineering. Today, more than 320 papers reporting $^{238}U/^{235}U$ measurements have been published – most of them in the last two decades – and the U isotope field keeps on rapidly expanding, with on average over 20 new studies and 1270 new data generated each year since 2015 (**Fig. 3.1**).

With such numerous data, a real need for a global U isotope database has arisen. In fact, some efforts have been made to collect different subsets of U isotopic data, particularly in the context of paleoredox reconstruction (Andersen et al. 2020; Cao et al. 2020; Chen et al. 2021a; Lu et al. 2020; Tissot and Dauphas 2015; Wei et al. 2021; Zhang et al. 2018a, 2020b). While these compilations are useful, they usually only focus on specific rock types (organic-rich mudrocks: Lu et al. 2020; carbonates, shales, and iron-rich rocks: Chen et al. 2021a), geological time periods (Permian-Triassic: Zhang et al. 2018a, 2020b; late Neoproterozoic-early Paleozoic: Wei et al. 2021) or event (Shuram excursion: Cao et al. 2020). Even when more global compilations are undertaken (*e.g.,* Tissot and Dauphas 2015), they rapidly become obsolete as new data gets published, but the compilations are not updated. Beyond the U isotope data, these datasets generally include only a limited amount of relevant information/data for each sample. As a result, when attempting to use these existing compilations, users often lack sufficient related information to contextualize the data.

To address the need for a global U database and the shortcomings of available compilations, we introduce the UID: a comprehensive, updatable, uranium isotope database, in which all $^{238}U/^{235}U$ data published over an 80-year period

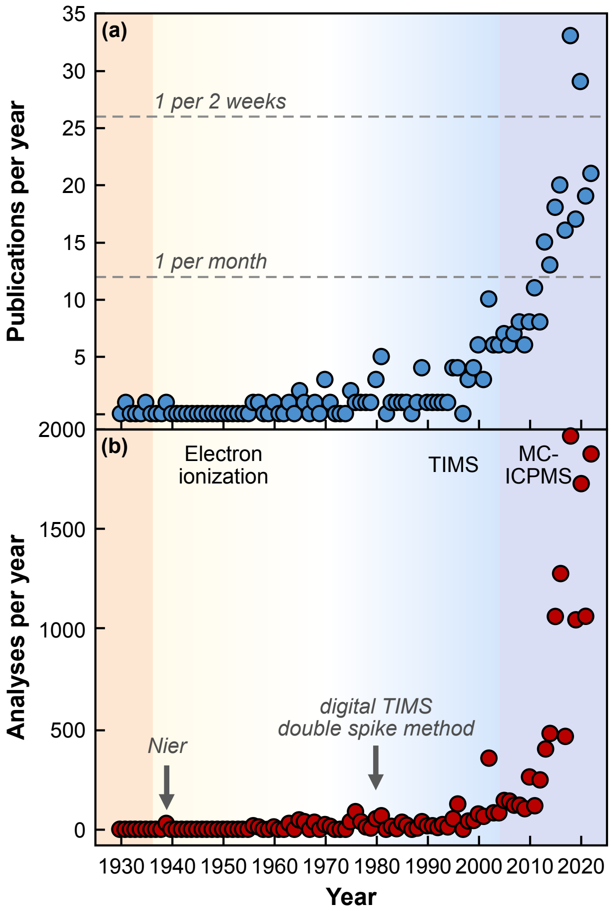

Figure 3.1: The number of publications per year reporting ^{238}U/^{235}U and ^{238}U/^{235}U analyses published per year. (a) The number of publications per year reporting ^{238}U/^{235}U data through time. The dashed lines represent the number of papers that would be published if one paper on U isotopes was published every month (12 papers) and every two weeks (26 papers). (b) The number of ^{238}U/^{235}U analyses published per year. The advent of MC-ICP-MS in the early 2000s made possible to resolve small ^{238}U/^{235}U variations and led to the exponential growth of U isotopic studies. (Updated Dec. 2022)

have been compiled and consistently (and transparently) renormalized relative to the CRM-145 standard. At this writing, the UID, which is freely accessible at: https://isotoparium.org/uid, contains already over 15000 data point. To preserve the potential for data analysis, all other available metadata from the original publications were also included in the database, such as sample type, concentrations (*e.g.,* major and trace elements), other isotopic data (*e.g.,* $\delta^{98/95}$Mo), or measurement technique.

Below, we first briefly review the evolution of U isotope measurements over time before describing the structure and content of the database, as well as the normalization procedures for U isotopic compositions. We then use the UID to provide a compilation of recommended δ^{238}U values for certified U standards and geostandards (*i.e.,* reference materials). Finally, we conduct a brief review of U isotopic studies according to their various applications and discuss important future directions of research for the field.

3.2 A brief history of U isotope measurements

Initially motivated by the discovery of the naturally occurring radioactive decay chains of ^{238}U and ^{235}U (at the time known as U_I and A_{cU}, respectively), uranium was amongst the first elements to see its isotopic composition carefully characterized. Using spark-source mass-spectrography, Aston (1931) determined that ^{235}U accounted for at most 2-3 % of U atoms, and Dempster (1935) moved this limit down to only 1 %. The first quantitative determination of the isotopic composition of U, however, was made by Nier (1939) who, using a unique mass spectrometer he had just developed (Nier 1938), reported in U ore samples a ^{238}U/^{235}U ratio of 139 (1 % relative error), and a ^{238}U/^{234}U of 17,000 (10 % relative error). Following this seminal work, early studies of U isotopes mainly focused on ore deposits (Cowan and Adler 1976; Hamer and Robbins 1960; Lancelot et al. 1975; Lounsbury 1956; Rosholt et al. 1965; Rosholt et al. 1963; Senftle et al. 1957; Smith 1961), whose unusually high U concentrations enabled high-precision analyses despite the large quantity of U required, which led to the discovery of the first, and so far only, known natural reactor of Oklo (Gabon) (Baudin et al. 1972; Bodu et al. 1972; Lancelot et al. 1975; Neuilly et al. 1972). Although some attempts were made to investigate the U isotopic composition of lunar samples and meteorites, the precision was generally insufficient to resolve any variation (Rosholt and Tatsumoto 1970; Rosholt and Tatsumoto 1971; Shimamura and Lugmair 1981; Tatsumoto and Rosholt 1970).

As for other heavy elements, the introduction of digital Thermal Ionization Mass Spectrometer (TIMS) instruments was a transformative technological advance in U isotopic analysis (*e.g.,* Wasserburg et al. 1969). The improved precision and sensitivity of digital instruments and ionization techniques enabled permil level precision to be achieved for nanogram quantities of sample U. This development allowed U isotope analysis to grow beyond the study of U-rich materials and to be applied in a wider range of fields. This was particularly important in cosmochemistry, where earlier claims of extremely high ^{235}U excess in meteorites and their inclusions (*e.g.,* Arden 1977; Tatsumoto and Shimamura 1980) were then systematically reassessed and found to be the results of analytical artefacts rather than evidence of a high abundance of live ^{247}Cm in the early solar system (Chen 1988; Chen and Wasserburg 1980, 1981a,b,c). Using the same instrument, Chen et al. (1986) later determined in a seminal study the U isotope composition of seawater.

The revolution, however, that precipitated U isotope analysis into the age of high-precision (better than $\sim$0.1 ‰, see Tissot and Ibañez-Mejia 2021), was the appearance in the early 2000s of Multi-Collector Inductively Coupled Plasma Mass Spectrometer

(MC-ICP-MS). The ability of MC-ICP-MS instruments to resolve isotopic variations at the sub-permil level marks the start of the field of so-called “stable” U isotopes (^{238}U/^{235}U, expressed as δ^{238}U in δ notation), which is investigating non-radiogenic and non-fissiogenic U isotopic fractionation that occurred during geo(bio)chemical cycles/processes. Initial studies reported resolvable natural U isotopic variations in a range of terrestrial environments (Stirling et al. 2007; Weyer et al. 2008). This discovery challenged the conventional assumption in the field of geochronology of a homogenous and constant ^{238}U/^{235}U ratio (assumed to be equal to 137.88, Steiger and Jäger 1977), and thus highlighted the importance of measuring ^{238}U/^{235}U ratios when attempting to obtain high-precision ages via Pb–Pb dating (Amelin et al. 2010, 2011; Bollard et al. 2017; Bouvier et al. 2011a,b; Brennecka et al. 2010a; Brennecka and Wadhwa 2012; Brennecka et al. 2015, 2018; Connelly et al. 2012; Goldmann et al. 2015; Iizuka et al. 2014; Larsen et al. 2011; Merle et al. 2020; Spivak-Birndorf et al. 2015; Tissot et al. 2017). The prevalence of U isotopic variations in low-temperature surface environments, and in particular the ~1 ‰ heavier U isotope composition of reduced sediments relative to seawater, suggested that U isotopes could be used as a paleoredox proxy to reconstruct the extent of oceanic anoxia. Indeed, the magnitude and direction of these fractionations matched those expected for Nuclear Field Shift effects during exchange reactions between oxidized and reduced U (Abe et al. 2008; Bigeleisen 1996; Schauble 2007) and an extensive body of work in both natural and lab-controlled environments soon confirmed that redox reactions could lead to significant U isotopic fractionation in natural materials (Basu et al. 2014, 2015, 2020; Brown et al. 2016, 2018; Jemison et al. 2018; Murphy et al. 2014; Stirling et al. 2007, 2015; Stylo et al. 2015b; Wang et al. 2015a). Today, U is arguably the most widely used paleoredox proxy (see review in Zhang et al. 2020c), and methods are being developed to ensure the most consistent and robust quantitative assessment of marine anoxia using U isotopes (Kipp and Tissot 2022; Pimentel-Galvan et al. 2022). Because the magnitude of mass-dependent fractionation decreases with increasing temperature, U isotope effects have traditionally been assumed to be negligible at magmatic temperatures. Yet, modern instrumentation enables the resolution of minor δ^{238}U variations in igneous rocks, and studies have started to investigate the potential of U isotopes as tracers of magmatic processes in bulk rocks (Andersen et al. 2015; Avanzinelli et al. 2018; Casalini 2018; Freymuth et al. 2019; Gaschnig et al. 2021; Telus et al. 2012; Tissot et al. 2017), and even single-crystals of accessory minerals (Tissot et al. 2019a; Yamamoto et al. 2021). Besides geochemical applications, U isotopes are also used as tracer of U contamination/remediation in environmental engineering (Basu et al. 2014, 2015; Bopp et al. 2010; Brown et al. 2016; Dang et al. 2016; Jemison et al. 2018; Lefebvre et al. 2019, 2021, 2022; Murphy et al. 2014; Placzek et al. 2016; Rademacher et al. 2006; Shiel et al. 2013, 2016; Stylo et al. 2015a;

Wang et al. 2015a,b) and have long-standing importance in nuclear chemistry and forensic studies (Al.-Zamel et al. 2005; Awudu and Darko 2011; Barescut et al. 2009; Boulyga et al. 2000; Bros et al. 1996; Christensen et al. 2004; Curtis et al. 1989; Danesi et al. 2003a,b; De Laeter et al. 1980; Ejnik et al. 2000; Fernández-Dıaz et al. 2000; Fujikawa et al. 2003; Hamilton and Stevens 1985; Hidaka and Holliger 1998; Hidaka et al. 1999; Hidaka and Gauthier-Lafaye 2000; Holliger and Devillers 1981; Horan et al. 2002; Horie et al. 2004; Howe et al. 2002; Joshi et al. 1983; Kikawada et al. 2015; Kikuchi and Hidaka 2009; Krachler et al. 2018; Lancelot et al. 1975; Lloyd et al. 2009; Loss et al. 1989; Marin et al. 2013a; Meyers et al. 2014; Minteer et al. 2007; Mishra et al. 2019; Parrish et al. 2006; Pazukhin and Rudya 2002; Pöml et al. 2013; Schramel 2002; Sobotovich and Bondarenko 2001; Stebelkov et al. 2018; Sus et al. 1979; Tamborini 2004; Tripathi et al. 2013; Veerasamy et al. 2020; Warneke et al. 2002; Yamamoto et al. 2002).

3.3 Guide to the UID database

3.3.1 Data source and general considerations

The UID aims to gather all published $^{238}U/^{235}U$ data, as well as any supporting sample metadata to facilitate data contextualization and interpretation. The UID focuses on $^{238}U/^{235}U$ ratios, so publications only containing ^{234}U data are not included. To the best of our knowledge, all available data was incorporated in the UID. For the sake of completeness, no attempt to screen the resolution or quality of the data was done. If the data were transcribed from tables in the main text or supplements, the table number is given in the UID. For U isotopic data, the UID includes both the original data from publications and the normalized data following the method described in Section 3.4.2. The supporting metadata combines both sample information and geochemical data, which can be quite extensive for some samples.

3.3.1.1 UID ID

To avoid confusion caused by inconsistent nomenclatures, each sample in the UID is assigned a unique ID along with its original sample name in the publication. The UID ID is composed of three sections separated by hyphens (*e.g.,* 2021-CRM-T001). The first section is the publication year. The second part combines the first initial of the first three authors' surnames (*e.g.,* CRM represents Chen, Romaniello, and McCormick). For papers with fewer than three authors, this section contains the first initial of all authors. In some rare cases where three letters were insufficient to distinguish between articles published in the same year by the same research group, the first initial of the fourth author's surname was added to the second section to ensure the uniqueness of the UID ID. The last section is separated into

Table 3.1: Acronyms for terminologies in technique column

Acronyms	Terminology
MC	Multi-Collector
SC	Single Collector
HR	High Resolution
DF	Double Focusing
Q	Quadrupole
SF	Sector Field
LA	Laser Ablation
FT	Fission Track
SN	Solution Nebulization
DRC	Dynamic Reaction Cell
HEX	Hexapole Collision Cell
ICP	Inductively Coupled Plasma
MS	Mass Spectrometer
SIMS	Secondary-Ion Mass Spectrometer
TIMS	Thermal Ionization Mass Spectrometer
OES	Optical Emission Spectrometer
GRS	Gamma Ray Spectrometer
NAA	Neutron Activation Analysis
SHRIMP	Sensitive High Mass-Resolution Ion Microprobe

two components to represent each data point. The letter specifies the subdatabase category (S = Standard, T = Terrestrial, M = Meteorite, E = Experimental, F = Forensic, and P = Precision), and the three-digit number denotes the sample number within that category. Using the nomenclature given above, each sample in the UID has a unique identification, with no duplicates.

3.3.1.2 Methodology

This section gathers information on the standard, spike (if applicable), and mass spectrometric technique used, since the methodology employed influences the achieved precision and data reduction. Detailed information about standards and spikes are described in Sections 3.3.2.2 Standard, 3.3.2.9 Spikes. For mass spectrometry, we included the instrument's type (*e.g.,* TIMS, MC-ICP-MS) and model (*e.g.,* NuPlasma, ThermoFisher Neptune), and for ICPMS analyses, details on the desolvating nebulizer (if applicable), and cones combination. The most extensively used instruments for high-precision U isotope measurements in geochemistry are the Neptune and Neptune Plus (ThermoFisher) and the Nu Plasma MC-ICP-MS. The range of applications of other types of mass spectrometers are discussed in Section 3.5.2.1, and the abbreviations used in these techniques are listed in **Table 3.1**. The sensitivity of measurements can be greatly influenced by sample introduction systems. The highest precision U isotope determinations use liquid sample introduction. Membrane desolvating nebulizer systems can both enhance the sensitivity up to tenfold and significantly reduce solvent-based interferences. Meanwhile, sensitivity is also affected by the cones combination, with the highest sensitivities achieved with a combination of a Jet sample cone and an X-skimmer cone.

3.3.1.3 Reference

The source publication details are provided for each sample, using a short citation style composed of the author(s) name(s), the year of publication, and the abbreviated journal name. A full version of the bibliography is included in the Reference tab of the UID (Section 3.3.2.1).

3.3.1.4 Assumptions

Because not all studies report U isotope data against the same standard, or in the same way (δ^{238}U values vs absolute ratios), a clear and transparent normalization algorithm stating what assumptions have been made is critical. In the Assumptions columns, we included any original assumptions made by the authors in the original publication, as well as those we made during data normalization. These pertain to the absolute or relative compositions of U reference materials, in house standards or important solar system reservoirs. These assumptions are numbered and summarized in the Assumptions tab of the UID (see Section 3.3.2.8). The normalization algorithms are described in Section 3.4.2. Users can easily renormalize the UID data by simply adjusting the input numbers in the Assumptions tab of the UID.

3.3.2 Structure of the database

The UID consists of 10 spreadsheets. The first six, named Standard, Terrestrial, Meteorites, Experimental, Forensic, and Precision, are subdatabases containing the U isotopic data. These categories were chosen to be as independent and unambiguous as possible, and they are non-overlapping, meaning that no data is duplicated between sub-databases (**Fig. 3.2**). The remaining four tabs, named *References*, *Assumptions*, *Spike*, and *Constants*, provide supplementary information for the database.

All samples were distributed into the various subdatabases, using a set of standardized criteria based on the sample type and the scope of the study (**Fig. 3.2**). This not only minimizes ambiguity, but also allows users to rapidly isolate all publications/data within a major theme (*e.g.,* chronology, paleoredox, forensic etc.), and build custom-compilations for future studies. For each subdatabase, definitions and descriptions of selected data components are included in the supplementary tables in Li and Tissot (2023).

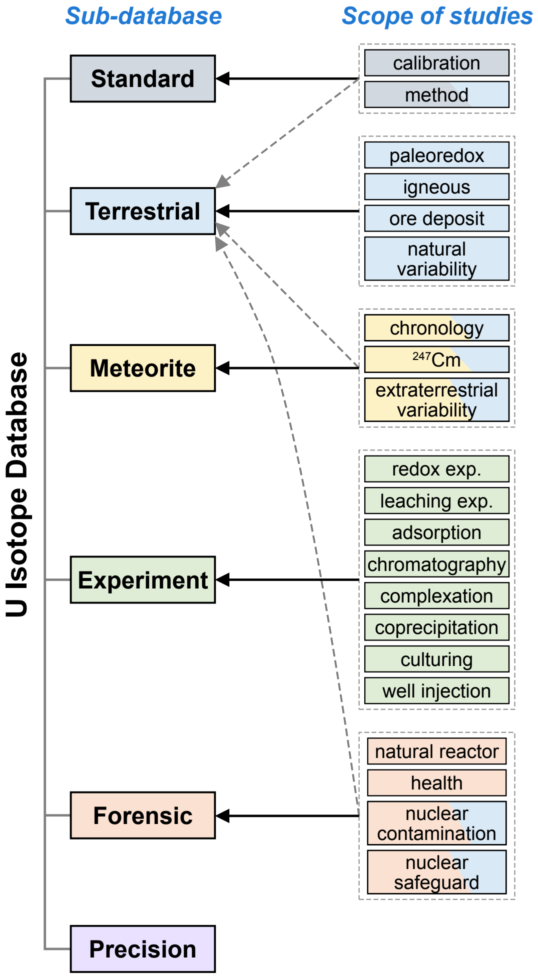

Figure 3.2: The UID structure, illustrating the relationships between subdatabases and the scope of U isotopic studies. The solid arrows indicate that the majority of data from papers in a given field of study are distributed to the linked subdatabase, whereas the dash arrows indicate only a minor contribution.

3.3.2.1 References

The *References* table contains the full bibliographic information for publications in the database, including the publication's UID ID, short reference, full reference, DOI link, area of study, the number of U data it reported, the name and email of the corresponding author, and whether the authors of the original publication have reviewed the UID entry. The UID ID is composed of the first two parts of the UID ID of each data point (*e.g.*, 2021-CRM-). The short reference is given as Author-Year-Journal, whereas the full reference includes author(s) name(s), the publication year, the publication's title, the journal/book title, volume number/book chapter, and the article number or pagination where applicable. The DOI links for articles are placed in a separate column for rapid redirection to the publisher's page.

The main area of study relevant for the publication is then listed, allowing users to filter the papers based on specific applications. Finally, a summary of the total number of data points in each article is given, and their distribution throughout subdatabases, which will assist users in locating data in subdatabases.

Some studies only display their U isotopic data graphically. These publications are listed at the end of the publication table since they do not have a data table to transcribe and incorporate into the database. In this scenario, only a brief reference, a complete reference, a DOI link, and the area of study are provided. We encourage all researchers to submit such data to the UID to make it more complete and useful to the community.

3.3.2.2 Standard

The Standard table contains three types of samples: (i) isotopically certified U standards, (ii) concentration standards, and (iii) other U materials such as metal, compound, reagent, and U-bearing glass. Standard measurements mainly have three purposes: quality control, standard calibration, and method development. In the first scenario, secondary standards are measured alongside unknown samples during an analytical session, and the data is reported to demonstrate the accuracy of the measurements. For standard calibration, on the other hand, the most accurate and precise isotopic compositions of standards are obtained by performing repeated measurements with well-established techniques. We provide recommended δ^{238}U on these widely used standards by integrating data from these two purposes (Section 3.5.1). Another use of standard analysis is to evaluate the performance of newly developed methods. These data are typically less precise because the tested method is designed for specific applications that may not demand high precision. For method development studies, we incorporated the investigated methodologies and technical innovations in the *Standard* table as well.

3.3.2.3 Terrestrial

The *Terrestrial* table contains U isotope data for virtually all natural solid and liquid terrestrial samples, including common geostandard materials. The only exception is data from the Oklo reactors, which have been included in the Forensic table, along with other data on depleted uranium samples. Solid samples include igneous, sedimentary, metamorphic rocks, and minerals, while liquid samples mainly contain seawaters, lake waters, river waters, and pore waters. This subdatabase includes metadata about the location, age, lithology, concentration, concentration ratio, the isotopic composition of other systems, and other relevant information.

3.3.2.4 Meteorite

The *Meteorite* table contains U isotope data for all extraterrestrial materials including meteorites, their components, and lunar samples. This subdatabase is named meteorite rather than extraterrestrial to avoid confusion during UID assignment for sample in this subdatabase and the *Experimental* subdatabase (as both start with the same letter).

3.3.2.5 Experimental

The *Experimental* table contains all data from lab and field-controlled experiments. For lab-controlled experiments, the table provides the experimental setup information. The field-controlled metadata also includes the locations of the sites.

3.3.2.6 Forensic

The *Forensic* table contains the U isotope data of samples affected by anthropogenic activities, as well as the data from the natural fission reactor of Oklo (Gabon). This table thus gathers all data relevant to nuclear contamination, nuclear safeguard, and health physics studies.

3.3.2.7 Precision

In MC-ICP-MS studies, it is common practice to report the average value and standard deviation of self-bracketed standard measurements. By definition, such an exercise should return a δ^{238}U value of 0 (the standard is identical to itself, and no deviation should be found), and the uncertainty can be used to quantify the external reproducibility of the measurements. Indeed, the standard being measured tens of times per analytical sessions, the dispersion in its data is more representative compared to that of the samples, which are only measured a handful of times. We have gathered these data in the *Precision* table, which can be used to assess some aspects of the data quality.

3.3.2.8 Assumptions

The Assumptions spreadsheet contains the assumptions used in the original publications reporting the data, as well as those used for normalization in the database. We divided the assumptions into two categories: assumptions for ^{238}U and assumptions for ^{234}U. For ^{238}U, assumptions pertain to historical name changes (*e.g.,* NBS SRM960 was recertified and renamed NBL CRM-112a in 1987), ^{238}U/^{235}U absolute ratios, δ^{238} values of standards relative to one another, and alpha activity ratio (^{233}U/^{238}U). For ^{234}U, assumptions pertain to the half-lives of ^{234}U and ^{238}U as they determine the ^{234}U/^{238}U ratio at secular equilibrium, ^{234}U/^{238}U of standards (certified values and ^{234}U/^{238}U compositions applied in the publication). How these assumptions play into the data normalization is discussed in Section 3.4.

3.3.2.9 Spikes

For elements with 4 isotopes or more, the double spike technique (Dodson 1963) is the gold-standard to achieve high-precision isotopic measurements, as it allows to correct for mass fractionation arising from sample purification and mass spectrometry. While U only has 3 naturally occurring isotopes, the introduction of a man-made ^{233}U-^{236}U double spike in the early 1980s highly improved the precision of U isotopic analysis (Chen and Wasserburg 1980, 1981b,c). Nowadays, the most widely used double spike is the commercially available IRMM-3636 (^{233}U/^{236}U = 1.01906(16), Verbruggen et al. 2008). Nevertheless, a range of in-house double spikes, with variable U isotopic compositions, have been and/or still are being used (Amelin et al. 2010; Bopp et al. 2009, 2010; Bouvier et al. 2011b; Brennecka et al. 2010a, 2011a,b; Bros et al. 1993; Chen and Wasserburg 1980, 1981b,c; Cheng et al. 2000, 2013; Chernyshev et al. 2014; Holmden et al. 2015; Noordmann et al. 2016; Parrish et al. 2006; Rademacher et al. 2006; Richter et al. 2010; Shiel et al. 2013; Shimamura and Lugmair 1981; Stirling et al. 2005, 2007; Tatsumoto and Shimamura 1980; Wang et al. 2015a, 2016; Wei et al. 2018, 2020, 2021; Weyer et al. 2008). Because the composition of a double-spike is an essential factor controlling the achievable precision of the measurement (Marquez and Tissot 2022; Rudge et al. 2009), the isotopic composition of the IRMM-3636 and all in-house spikes can be found in the Spikes table. A specific abbreviation was given to each spike (*e.g.,* 36CW80): the first two digits represent the enriched isotopes in this spike (*i.e.,* ^{233}U and ^{236}U in this case); the letters in the middle stand for the initials of the authors' last name using the same logic as the UID ID; the last part denotes the year of publication. The U isotopic compositions were converted to ^{i}U/^{236}U, where i is isotope 233, 234, 235, or 238.

3.3.2.10 Constants

The Constants tab provides a summary of all constants used to homogenize concentration data. In the UID, we report elemental concentrations. This required converting originally published oxide concentrations, which was done by calculating an oxide to element conversion factor (Table C1 in the Constants spreadsheet) using the atomic masses from the 2013 IUPAC technical report (Meija et al. 2016). For concentration ratios, Table C2 provides the atomic masses to convert molar ratios to weight ratios. Table C3 shows the abundance of specific isotopes to transform the concentration ratios of the isotopes of two different elements to the elemental ratio. Table C4 shows the atomic masses of uranium isotopes to convert mass fractions of two U isotopes to atomic U isotopic compositions (Section 3.4.3).

3.3.3 Data retrieval

One of the primary applications of the UID is as a quick-reference library for U isotope research. To help users extract data, a quick search panel is provided right after the sample name (Column F-M in each subdatabase) in which the samples δ^{238}U, ^{238}U/^{235}U, δ^{234}U, and (^{234}U/^{238}U) values are gathered, along with their associated uncertainties. Users can search for specific data in the database using either the scope of studies or sample types. Drop-down menus are available in the subdatabases and reference spreadsheets to implement this functionality. This filtering system uses criteria to subdivide the subdatabases, which are defined based on the properties of each subdatabase (**Table** 3.2).

3.4 Data representation

3.4.1 Notations for uranium isotopes

The ^{238}U/^{235}U data are reported both as absolute ratio and in δ-notation (permil unit, ‰), which is defined as:

$$\delta^{238}\mathrm{U} = \left(\frac{^{238}\mathrm{U}/^{235}\mathrm{U}_{\mathrm{smp}}}{^{238}\mathrm{U}/^{235}\mathrm{U}_{\mathrm{std}}} - 1 \right) \times 1000 \tag{3.1}$$

To ensure the internal consistency of the UID, all δ^{238}U data have been renormalized relative to the CRM-145 standard (a solution made from an aliquot of the CRM-112a metal), and ^{238}U/^{235}U ratios are calculated assuming that CRM-145 has the same isotopic compositions as CRM-112a with a ^{238}U/^{235}U ratio of 137.837 as reported by the inter-laboratory calibration of Richter et al. (2010).

The ^{234}U/^{238}U data are reported as absolute ratios, (^{234}U/^{238}U) (the brackets denote activity ratios) and δ^{234}U, the latter two being defined as:

$$\left(^{234}\mathrm{U}/^{238}\mathrm{U}\right) = \frac{^{234}\mathrm{U}/^{238}\mathrm{U}_{\mathrm{smp}}}{^{234}\mathrm{U}/^{238}\mathrm{U}_{\mathrm{sec.\ eq}}} \tag{3.2}$$

$$\delta^{234}\mathrm{U}_{\mathrm{sec}} = \left[\left(^{234}\mathrm{U}/^{238}\mathrm{U}\right) - 1\right] \times 1000 \tag{3.3}$$

In Eq. 3.2, $^{234}\mathrm{U}/^{238}\mathrm{U}_{\mathrm{sec.\ eq}}$ denotes the secular equilibrium ^{234}U/^{238}U ratio, which is the ratio of the decay constants of ^{238}U and ^{234}U, and was calculated here using the recently determined decay constants from Cheng et al. (2013): $\lambda_{238}/\lambda_{234} = (1.55125 \times 10^{-10})/(2.8220 \times 10^{-6}) = 5.4970 \times 10^{-5}$. For both ^{238}U/^{235}U and ^{234}U/^{238}U data, errors were adjusted to 2SD, or 2SE when applicable.

Table 3.2: Sorting criteria in the UID and subdatabases

Criteria			Lists
Criterion 1	**Criterion 2**	**Criterion 3**	
All Subdatabases			
Scope of study			magmatic, ore deposit, paleoredox, natural variability ^{247}Cm, chronology, extraterrestrial variability adsorption, chromatography, complexation, coprecipitation, culturing, leaching experiment, redox experiment, well injection health, natural reactor, nuclear contamination, nuclear safeguard method, calibration
Standard Subdatabase			
Purpose			quality control, method development, calibration
Sample type	standard		name of the standard (*e.g.,* CRM-145)
	conc std		Ricca, single elemental standard
	other		compound, metal, reagent, U-bearing glass
Terrestrial Subdatabase			
Sample type	solid	igneous	basalt, basaltic andesite, core sample, glass, granite, granitoids, lamproites, lava, lherzolite, oceanic crust, scoria, shoshonite, tonalite
		sedimentary	carbonate, carbonate-bio, chimney, clay, evaporite, Fe oxide, Fe-Mn curst, Fe-Mn deposit, hydrothermal vein, iron formation, marl, Mn crust, mudrock, mudstone, organic-rich sediments, paleosol, quartzite, reduction spheroid, sandstone, seafloor, sediments, shale, siliciclastic sediments, siltstone, soil
		metamorphic	gneiss, milonite
		mineral	apatite, baddeleyite, monazite, pyrite, titanite, uraninite, xenotime, zircon
		ore	
		reference	name of the geostandard (*e.g.,* BCR-2)
	liquid		groundwater, hydrothermal water, lake water, pore water, river water, seawater
		reference	seawater
Extraterrestrial Subdatabase			
Meteorite classification	chondrite	carbonaceous	CB, CI1, CM2, CR2, CV3
		ordinary	H3, H3-6, H4, H5, H6, L/LL4, L/LL5, L/LL6, L3, L3.10, L4, L5, L6, LL3.6, LL6
		enstatite	EH3, EH4
	achondrite		Acapulcoite, Angrite, Aubrite, Eucrite, Howardite, iron meteorite, primitive, ungrouped
	lunar sample		
Precision Subdatabase			
Sample type			name of the standard (*e.g.,* CRM-145)

3.4.2 Normalization of ^{238}U/^{235}U data

The path to data normalization depends on whether the original publication reported δ^{238}U values or absolute ^{238}U/^{235}U ratios. These two scenarios are presented in detail below and summarized in a flowchart in **Fig. 3.3**.

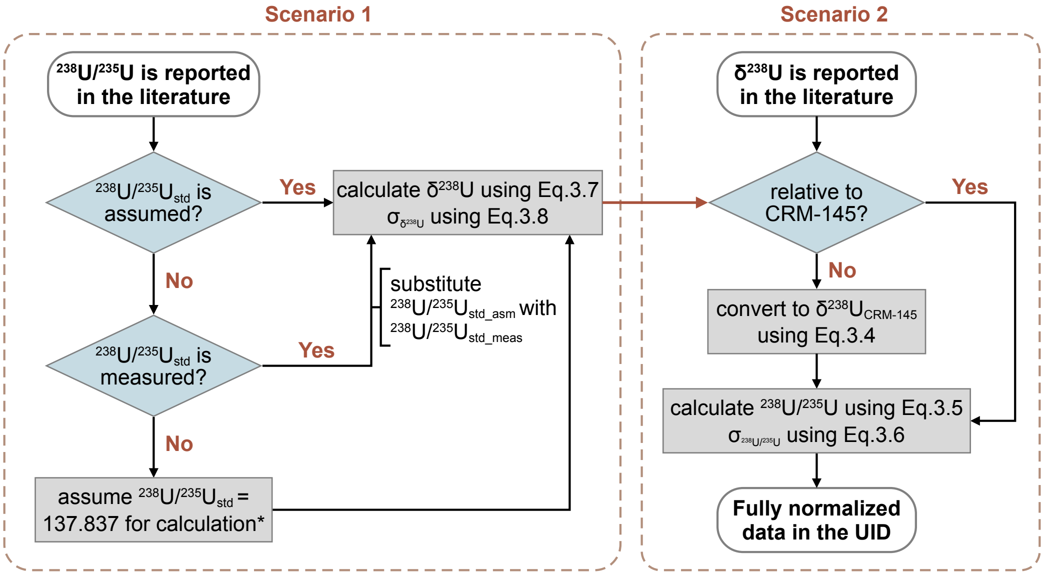

Figure 3.3: Flowchart of the protocol for the normalization of ^{238}U/^{235}U data in the UID. *The ^{238}U/^{235}U$_{\text{std}}$ comes from Richter et al. (2010). For publications before 2010, the data quality is generally insufficient to resolve the difference between the assumed value and the normalization using the 'consensus' value of 137.88.

3.4.2.1 When δ^{238}U is reported in the literature

For studies reporting δ^{238}U values against standards other than CRM-145, a correction was applied to the originally published data to account for the offset between the U isotopic composition of the standard used in the study and that of the CRM-145. This correction is simply implemented as:

$$\delta^{238}\text{U}_{\text{UID}} = \delta^{238}\text{U}_{\text{CRM145}} = \delta^{238}\text{U}_{\text{published}} + \Delta^{238}\text{U}_{\text{STD-CRM145}} \tag{3.4}$$

where $\delta^{238}\text{U}_{\text{UID}}$ is the δ^{238}U value of the sample relative to CRM-145, $\delta^{238}\text{U}_{\text{published}}$ is the originally reported δ^{238}U relative to the standard used in the paper, and $\Delta^{238}\text{U}_{\text{STD-CRM145}}$ is the δ^{238}U offset between the standard and CRM-145. To ensure the self-consistency of the UID data, we compiled all published high-precision U isotopic measurements of widely (and less-widely) used standards and provide recommended $\Delta^{238}\text{U}_{\text{STD-CRM145}}$ values for these materials (**Table 3.3** and Section 3.5.1.1).

In some studies, the authors already corrected the offsets between the standard(s) they used and CRM-145, but sometimes using different $\Delta^{238}\text{U}_{\text{STD-CRM145}}$ values

Table 3.3: Summary of recommended δ^{238}U and ^{238}U/^{235}U of standards, relative to CRM-145.

Standard	δ^{238}U (‰)	^{238}U/^{235}U	n	MSWD	Comments
NU standards					
CRM-129	-1.709 ± 0.009	137.601 ± 0.001	39	0.60	Batch 1
	-1.48 ± 0.16	137.634 ± 0.021	2	n.a.	Batch 2
IRMM-3184	-1.14 ± 0.15	137.680 ± 0.021	2	n.a.	
IRMM-184	-1.160 ± 0.013	137.677 ± 0.002	15	0.85	
Ricca	-0.220 ± 0.014	137.807 ± 0.002	17	0.79	
Reimep-18a	-0.130 ± 0.005	137.819 ± 0.001	23	9.49[a]	Batch 1
	-0.26 ± 0.01	137.802 ± 0.002	2	n.a.	Batch 2
	0.12 ± 0.07	137.854 ± 0.010	1	n.a.	Batch 3
CRM-112a	-0.001 ± 0.006	137.837 ± 0.001	12	3.04	
CRM-145	0.01 ± 0.04	137.838 ± 0.005	4	n.a.	
SRM-950a	0.046 ± 0.008	137.843 ± 0.001	6	1.77	
EU standards					
U970	-999.9608 ± 0.0003	0.00540 ± 0.00004	1		
CRM-149	-999.5856 ± 0.0001	0.05712 ± 0.00001	1		
U900	-999.30086 ± 0.00004	0.09637 ± 0.00001	8		
U750	-999.7094 ± 0.0003	0.31573 ± 0.00004	4		
U630	-995.985 ± 0.001	0.5534 ± 0.0002	4		
IRMM-074-1	-992.747 ± 0.001	0.9998 ± 0.0003	1		
IRMM-199	-992.746 ± 0.001	0.9999 ± 0.0002	3		
U500	-992.74 ± 0.01	1.001 ± 0.002	46		
U200	-971.28 ± 0.25	3.96 ± 0.03	9		
U100	-934.7 ± 2.8	9.00 ± 0.38	9		
IRMM-2024	-863.77 ± 0.04	18.778 ± 0.005	1		
U050	-862.01 ± 0.94	19.02 ± 0.13	2		
IRMM-187	-846.70 ± 0.05[b]	21.130 ± 0.006	3		
U045	-846.70 ± 0.02	21.130 ± 0.003	9		
IRMM-2029	-835.31 ± 0.05	22.700 ± 0.007	1		
CRM-125	-828.49 ± 0.02	23.640 ± 0.002	9		
IRMM-2027	-826.09 ± 0.05	23.971 ± 0.007	1		
IRMM-2028	-806.93 ± 0.06	26.613 ± 0.008	1		
Reimep-18b	-794.48 ± 0.58	28.329 ± 0.080	1		
IRMM-2023	-785.87 ± 0.03	29.515 ± 0.005	1		
U030	-768.74 ± 0.26	31.876 ± 0.036	19		
IRMM-186	-764.23 ± 0.07	32.498 ± 0.010	1		
IRMM-2026	-717.48 ± 0.08	38.942 ± 0.011	1		
Reimep-18d	-699.1 ± 1.0	41.48 ± 0.14	1		
U020	-651.20 ± 0.62	48.078 ± 0.085	8		
IRMM-2025	-644.99 ± 0.10	48.934 ± 0.013	1		
IRMM-185	-638.251 ± 0.002	49.8624 ± 0.0002	4		
U015	-532.4 ± 8.0	64.5 ± 1.1	3		
U010	-284.81 ± 0.55	98.579 ± 0.076	21		
DU standards					
SPEX U Lot #14-163U	85.09 ± 0.30	149.566 ± 0.041	1		
SPEX CLU2-2Y	93.25 ± 0.56	150.691 ± 0.071	1		
U005	424.96 ± 0.93	196.41 ± 0.13	7		
IRMM-2021	646.90 ± 0.27	227.004 ± 0.037	1		
Reimep-18c	654.5 ± 2.3	228.05 ± 0.31	1		
Inorganic Ventures MSU-100 ppm	927.86 ± 0.92	265.73 ± 0.13	1		
Alfa ICP/DCP	1084.2 ± 3.6	287.28 ± 0.50	1		
Alfa ICP	1084.2 ± 5.3	287.27 ± 0.73	1		
Alfa AA	1085.6 ± 2.9	287.47 ± 0.40	1		
IRMM-183	1256.8 ± 1.2	311.06 ± 0.17	5		
Merck 170360	1643.2 ± 1.9	364.33 ± 0.27	1		
Aldrich AA	1673.1 ± 7.4	368.5 ± 1.0	1		
Assurance U (5% HNO_3)	1861.7 ± 6.3	394.45 ± 0.87	1		
Assurance U (2% HNO_3)	1957.0 ± 4.9	407.58 ± 0.68	1		
SRM-610	2039.8 ± 1.3	419.00 ± 0.19	40		
IRMM-2020	2461.8 ± 1.0	477.17 ± 0.14	1		
Inorganic Ventures CGU1-125mL	2449.8 ± 2.5	475.51 ± 0.34	1		
Perkin-Elmer N9303844	2633.1 ± 2.7	500.78 ± 0.29	1		
SPEX XSTC-3213	2694.9 ± 5.6	509.29 ± 0.78	1		
IRMM-2019	3324.9 ± 1.2	596.13 ± 0.17	1		
U0002	39390 ± 952	5567 ± 131	1		

[a] The MSDW of Reimep-18a represents the potential heterogeneity.

[b] The uncertainty on IRMM-187 represents the analytical error because the three measurements have the same δ^{238}U value.

(*e.g.,* Bopp et al. 2009, 2010; Dang et al. 2018). Since the δ^{238}U of a specific standard relative to CRM-145 is invariant (provided the standard is homogenous), and to ensure the self-consistency of the UID data, the offset applied in the original publications were undone, and the recommended $\Delta^{238}\mathrm{U}_{\text{STD-CRM145}}$ (Section 3.5.1.1) were applied instead. Because all data is corrected using a unique set of recommended $\Delta^{238}\mathrm{U}_{\text{STD-CRM145}}$ values, we did not propagate the uncertainties of these offsets onto the final data. The error on δ^{238}U in the UID is thus the same as that reported in the literature because any conversion discussed above would not influence the measurement uncertainties.

From the δ^{238}U values and their associated errors, the absolute $^{238}\mathrm{U}/^{235}\mathrm{U}$ ratios in the UID are calculated as:

$$^{238}\mathrm{U}/^{235}\mathrm{U}_{\mathrm{UID}} = \left(\delta^{238}\mathrm{U}/1000 + 1\right) \times^{238} \mathrm{U}/^{235}\mathrm{U}_{\mathrm{CRM145}} \tag{3.5}$$

$$\sigma_{^{238}\mathrm{U}/^{235}\mathrm{U}} = (\sigma_{\delta^{238}\mathrm{U}}/1000) \times^{234} \mathrm{U}/^{238}\mathrm{U}_{\mathrm{CRM145}} \tag{3.6}$$

where $^{238}\mathrm{U}/^{235}\mathrm{U}_{\mathrm{CRM145}}$ is the absolute $^{238}\mathrm{U}/^{235}\mathrm{U}$ ratio of CRM-145. In the UID, this value is taken as 137.837 (Richter et al. 2010).

3.4.2.2 When $^{238}\mathrm{U}/^{235}\mathrm{U}$ is reported in the literature

For studies reporting absolute $^{238}\mathrm{U}/^{235}$ ratios, the data is first converted to δ^{238}U values. If an assumption on the standard $^{238}\mathrm{U}/^{235}\mathrm{U}$ is provided in the original publication, δ^{238}U and the uncertainty on the sample data are calculated as:

$$\delta^{238}\mathrm{U} = \left(\frac{^{238}\mathrm{U}/^{235}\mathrm{U}_{\mathrm{smp}}}{^{238}\mathrm{U}/^{235}\mathrm{U}_{\mathrm{std.asm}}} - 1\right) \times 1000 \tag{3.7}$$

$$\sigma_{\delta^{238}\mathrm{U}} = \left(\frac{^{238}\mathrm{U}/^{235}\mathrm{U}_{\mathrm{smp}}}{^{238}\mathrm{U}/^{235}\mathrm{U}_{\mathrm{std.asm}}}\right) \times 1000 \tag{3.8}$$

where $^{238}\mathrm{U}/^{235}\mathrm{U}_{\mathrm{smp}}$ and $\sigma_{\delta^{238}U}$ are, respectively, the absolute ratio and associated error of the sample presented in the original publication; and $^{238}\mathrm{U}/^{235}\mathrm{U}_{\mathrm{std.asm}}$ is the absolute ratio of the standard assumed in the original publication. In some cases, the paper reported the $^{238}\mathrm{U}/^{235}\mathrm{U}$ without any assumption for the absolute ratio of the standard. If a standard with known isotopic composition was measured along with the samples, we used this measurement (*i.e.,* $^{238}\mathrm{U}/^{235}\mathrm{U}_{\mathrm{std.meas}}$) to substitute $^{238}\mathrm{U}/^{235}\mathrm{U}_{\mathrm{std.asm}}$ in Eq. (3.7), (3.8). In the absence of a stated $^{238}\mathrm{U}/^{235}\mathrm{U}$ ratio for the standard, we assumed $^{238}\mathrm{U}/^{235}\mathrm{U}_{\mathrm{std.asm}} = 137.837$ (Richter et al. 2010). This assumption naturally holds for papers published after 2010. For papers before 2010, the quality of data is generally not good enough to resolve the difference between our calculation and the normalization using 137.88, the consensus ratio from Steiger and Jäger (1977). This additional assumption is clearly stated in the "Assumption for calculation" column for clarification. For each sample, the δ^{238}U value obtained was then renormalized to CRM-145, and used to recalculate the sample ^{238}U/^{235}U ratio and their uncertainty against the ^{238}U/^{235}U absolute ratio of CRM-145 using Eq. (3.5), (3.6).

3.4.2.3 When both δ^{238}U and ^{238}U/^{235}U are reported in the literature

In this case, we used the same normalization strategy as presented in Section 3.4.2.1 the rationale is that the δ^{238}U value of a sample relative to a specific standard is invariant regardless of the assumed ^{238}U/^{235}U ratio of the standard.

3.4.2.4 Other circumstances

In addition to δ^{238}U and ^{238}U/^{235}U, other notations have been used in the literature to report U isotopic compositions: namely, activity ratios, and epsilon notations. **Table 3.4** lists the frequently used notations and their relationship to δ^{238}U values. For these notations, we converted them into δ^{238}U or ^{238}U/^{235}U at first, and then used the same approaches mentioned in Section 3.4.2.1 and 3.4.2.2 to conduct the normalization.

Table 3.4: How published U isotope data are consistently renormalized into the UID

Reported	Expression	Conversion	Approach
$^{235}\mathrm{U}/^{238}\mathrm{U}$	Absolute atomic ratio	$^{238}\mathrm{U}/^{235}\mathrm{U} = \frac{1}{^{235}\mathrm{U}/^{238}\mathrm{U}}$	3.4.2.2
$(^{238}\mathrm{U}/^{235}\mathrm{U})$	Alpha activity ratio	$^{238}\mathrm{U}/^{235}\mathrm{U} = (^{238}\mathrm{U}/^{235}\mathrm{U})/(\lambda_{238}/\lambda_{235})$	3.4.2.2
$\varepsilon^{238}\mathrm{U}$	$\varepsilon^{238}\mathrm{U} = \left(\frac{^{238}\mathrm{U}/^{235}\mathrm{U}_{\mathrm{smp}}}{^{238}\mathrm{U}/^{235}\mathrm{U}_{\mathrm{std}}} - 1\right) \times 10000$	$\delta^{238}\mathrm{U} = \varepsilon^{238}\mathrm{U}/10$	3.4.2.1
$\delta^{235}\mathrm{U}$	$\delta^{235}\mathrm{U} = \left(\frac{^{235}\mathrm{U}/^{238}\mathrm{U}_{\mathrm{smp}}}{^{235}\mathrm{U}/^{238}\mathrm{U}_{\mathrm{std}}} - 1\right) \times 1000$	$\delta^{238}\mathrm{U} = [1000/(\delta^{235}\mathrm{U} + 1000)] \times 1000$	3.4.2.1
$\varepsilon^{235}\mathrm{U}$	$\varepsilon^{235}\mathrm{U} = \left(\frac{^{235}\mathrm{U}/^{238}\mathrm{U}_{\mathrm{smp}}}{^{235}\mathrm{U}/^{238}\mathrm{U}_{\mathrm{std}}} - 1\right) \times 10000$	$\delta^{238}\mathrm{U} = [1000/(\varepsilon^{235}\mathrm{U}/10 + 1000)] \times 1000$	3.4.2.1

3.4.3 Normalization of ^{234}U/^{238}U data

While δ^{234}U and (^{234}U/^{238}U) are defined relative to secular equilibrium (*i.e.*, a theoretical value), in practice the majority of high-precision ^{234}U/^{238}U measurements are done using the sample-standard bracketing (SSB) method and calculated relative to a U isotopic standard. If the ^{234}U/^{238}U composition of the standard used in the paper is clearly stated, we can correct the offset between this value and the certified ^{234}U/^{238}U absolute ratio of the standard to ensure the consistency of the UID data. The formulas for this correction are slightly different depending on the information provided in the literature. The flowchart for the normalization protocol is illustrated in **Fig. 3.4**.

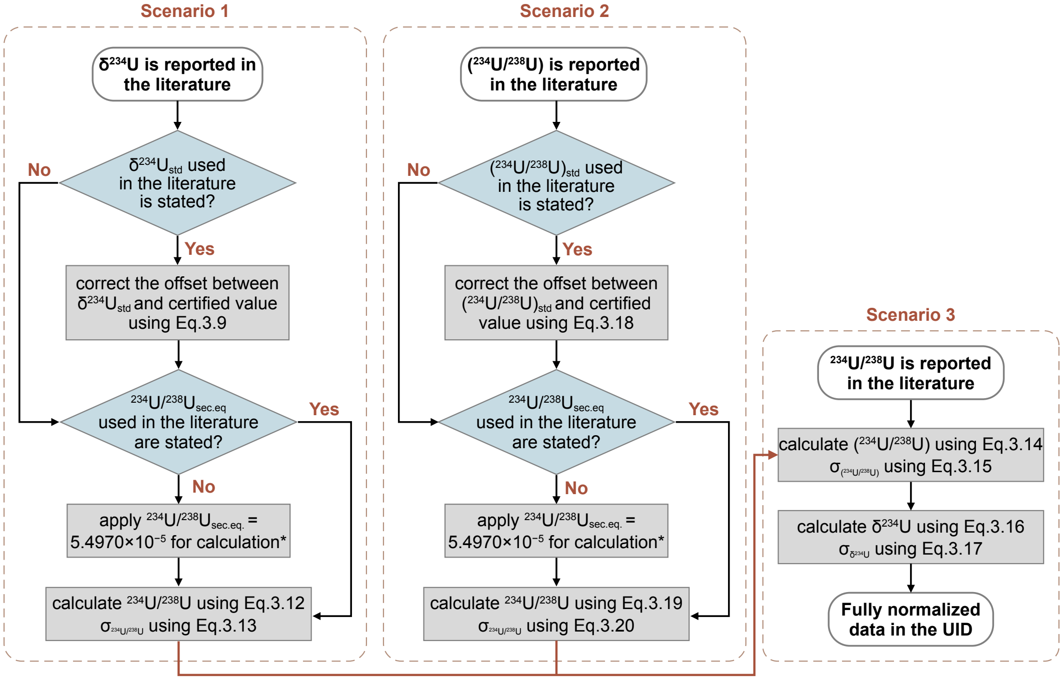

Figure 3.4: Flowchart of the protocol for the normalization of $^{234}\mathrm{U}/^{238}\mathrm{U}$ data in the UID. *We apply 5.4970×10^{-5} (Cheng et al. 2013) for publications after 2013, 5.4891×10^{-5} (Cheng et al. 2000) for publications between 2000 and 2013, and 5.472×10^{-5} (Chen et al. 1986) for publications before 2000.

3.4.3.1 When δ^{234}U is reported in the literature

If the $^{234}\mathrm{U}/^{238}\mathrm{U}$ composition of the standard is stated in the literature, the corrected δ^{234}U of the samples in the database are calculated using the following formulas:

$$\delta^{234}\mathrm{U}_{\mathrm{UID}} = \delta^{234}\mathrm{U}_{\mathrm{published}} + \delta^{234}\mathrm{U}_{\mathrm{std.cert}} - \delta^{234}\mathrm{U}_{\mathrm{std.lit}} \tag{3.9}$$

where $\delta^{234}\mathrm{U}_{\mathrm{published}}$ is the originally reported δ^{234}U value; $\delta^{234}\mathrm{U}_{\mathrm{std.lit}}$ is δ value of the standard used in the literature; $\delta^{234}\mathrm{U}_{\mathrm{std.cert}}$ is δ value of the standard derived from the standard's certificate. For CRM-145 ($^{234}\mathrm{U}/^{238}\mathrm{U} = 0.000052841$, Laboratory 2010), $(^{234}\mathrm{U}/^{238}\mathrm{U})_{\mathrm{std.cert}}$ and $\delta^{234}\mathrm{U}_{\mathrm{std.cert}}$ are defined as:

$$\left(^{234}\mathrm{U}/^{238}\mathrm{U}\right)_{\mathrm{std.cert}} = \frac{^{234}\mathrm{U}/^{238}\mathrm{U}_{\mathrm{std.cert}}}{^{234}\mathrm{U}/^{238}\mathrm{U}_{\mathrm{sec.\ eq}}} = 0.9613 \tag{3.10}$$

$$\delta^{234}\mathrm{U}_{\mathrm{std.cert}} = \left[\left(^{234}\mathrm{U}/^{238}\mathrm{U}\right)_{\mathrm{std.cert}} - 1\right] \times 1000 = -38.7\text{‰} \tag{3.11}$$

From the corrected sample δ^{234}U value, the $^{234}\mathrm{U}/^{238}\mathrm{U}$ absolute ratio and its associated uncertainty are calculated as:

$$^{234}\mathrm{U}/^{238}\mathrm{U} = \left(\delta^{234}\mathrm{U}/1000 + 1\right) \times ^{234}\mathrm{U}/^{238}\mathrm{U}_{\mathrm{sec.eq.lit}} \tag{3.12}$$

$$\sigma_{^{234}\mathrm{U}/^{238}\mathrm{U}} = \left(\sigma_{\delta^{234}\mathrm{U}}/1000\right) \times ^{234}\mathrm{U}/^{238}\mathrm{U}_{\mathrm{sec.eq.lit}} \tag{3.13}$$

where ${}^{234}\mathrm{U}/{}^{238}\mathrm{U}_{\mathrm{sec.eq.lit}}$ is the absolute ${}^{234}\mathrm{U}/{}^{238}\mathrm{U}$ ratio at secular equilibrium used in the original publication to calculate the $\delta^{234}\mathrm{U}$ value. If the original paper did not state the ${}^{234}\mathrm{U}/{}^{238}\mathrm{U}$ at secular equilibrium value used for calculation of $\delta^{234}\mathrm{U}$ values, we assumed a value of 5.4970×10^{-5} (Cheng et al. 2013) for publications after 2013, 5.4891×10^{-5} (Cheng et al. 2000) for papers published between 2000 and 2013, and 5.472×10^{-5} (Chen et al. 1986) for papers published before 2000. Once again, we encourage all researchers to submit such missing data to the UID so we can address any erroneous assumptions and make the UID more complete and useful to the community.

To calculate $\delta^{234}\mathrm{U}_{\mathrm{UID}}$ and $({}^{234}\mathrm{U}/{}^{238}\mathrm{U})_{\mathrm{UID}}$ in the database, we use the absolute ${}^{234}\mathrm{U}/{}^{238}\mathrm{U}$ ratio and its associated error obtained above Eqs. (3.9)–(3.13):

$$\left({}^{234}\mathrm{U}/{}^{238}\mathrm{U}\right)_{\mathrm{UID}} = \frac{{}^{234}\mathrm{U}/{}^{238}\mathrm{U}}{{}^{234}\mathrm{U}/{}^{238}\mathrm{U}_{\mathrm{sec.eq}}} \tag{3.14}$$

$$\sigma_{({}^{234}\mathrm{U}/{}^{238}\mathrm{U})} = \frac{\sigma_{{}^{234}\mathrm{U}/{}^{238}\mathrm{U}}}{{}^{234}\mathrm{U}/{}^{238}\mathrm{U}_{\mathrm{sec.eq}}} \tag{3.15}$$

$$\delta^{234}\mathrm{U}_{\mathrm{UID}} = \left[\left({}^{234}\mathrm{U}/{}^{238}\mathrm{U}\right) - 1\right] \times 1000 \tag{3.16}$$

$$\sigma_{\delta^{234}\mathrm{U}_{\mathrm{UID}}} = \sigma_{({}^{234}\mathrm{U}/{}^{238}\mathrm{U})} \times 1000 \tag{3.17}$$

where ${}^{234}\mathrm{U}/{}^{238}\mathrm{U}_{\mathrm{sec.eq}}$ is the absolute ${}^{234}\mathrm{U}/{}^{238}\mathrm{U}$ ratio at secular equilibrium. In the UID, this value is taken as 5.4970×10^{-5} (Cheng et al. 2013).

3.4.3.2 When $({}^{234}\mathrm{U}/{}^{238}\mathrm{U})$ is reported in the literature

The first task is to correct the reported $({}^{234}\mathrm{U}/{}^{238}\mathrm{U})$ activity ratio for any difference between the standard composition used in the literature compared to its certified value:

$$\left({}^{234}\mathrm{U}/{}^{238}\mathrm{U}\right) = \left({}^{234}\mathrm{U}/{}^{238}\mathrm{U}\right)_{\mathrm{published}} + \left({}^{234}\mathrm{U}/{}^{238}\mathrm{U}\right)_{\mathrm{std.cert}} - \left({}^{234}\mathrm{U}/{}^{238}\mathrm{U}\right)_{\mathrm{std.lit}} \tag{3.18}$$

Then, we can calculate the absolute ratio as:

$${}^{234}\mathrm{U}/{}^{238}\mathrm{U} = \left({}^{234}\mathrm{U}/{}^{238}\mathrm{U}\right) \times^{234} U/^{238}\mathrm{U}_{\mathrm{sec.eq.lit}} \tag{3.19}$$

$$\sigma_{{}^{234}\mathrm{U}/{}^{238}\mathrm{U}} = \sigma_{({}^{234}\mathrm{U}/{}^{238}\mathrm{U})} \times^{234} \mathrm{U}/^{238}\mathrm{U}_{\mathrm{sec.eq.lit}} \tag{3.20}$$

The definition and the usage of ${}^{234}\mathrm{U}/{}^{238}\mathrm{U}_{\mathrm{sec.eq.lit}}$ is the same as Section 3.4.3.1. The subsequent calculations of $\delta^{234}\mathrm{U}_{\mathrm{UID}}$ and $({}^{234}\mathrm{U}/{}^{238}\mathrm{U})_{\mathrm{UID}}$, as well as their uncertainties in the database follow Eqs. (3.14)–(3.17).

3.4.3.3 When ^{234}U/^{238}U is reported in the literature

Although geochemical studies routinely report ^{234}U/^{238}U data as (^{234}U/^{238}U) and δ^{234}U, the ^{234}U/^{238}U absolute ratio is a more commonly used notation in nuclear chemistry, method development, and forensic studies. In the latter situation, Eqs. (3.14)–(3.17) are directly applied to calculate δ^{234}U and (^{234}U/^{238}U) and their uncertainties.

3.4.3.4 When mass fraction is reported in the literature

In some forensic studies, the U isotopic composition is reported as the mass fraction of each U isotope. In this case, we calculate the atomic ratio from the U mass fractions and molar masses, following:

$$\frac{^{i}\mathrm{U}}{^{238}\mathrm{U}} = \frac{f_{m_i}/M_i}{f_{m_{238}}/M_{238}} \tag{3.21}$$

$$\sigma_{^{i}\mathrm{U}/^{238}\mathrm{U}} = \frac{^{i}\mathrm{U}}{^{238}\mathrm{U}} \times \sqrt{\left(\frac{\sigma_{f_{m_i}}}{f_{m_i}}\right)^2 + \left(\frac{\sigma_{f_{m_{238}}}}{f_{m_{238}}}\right)^2} \tag{3.22}$$

where i denotes 234 or 235; f_{m_i} is the mass fraction of isotope i; M is the atomic mass and σ_{f_m} is the uncertainty on mass fraction. When mass ratios are reported, similarly:

$$\frac{^{i}\mathrm{U}}{^{238}\mathrm{U}} = \frac{m_{i/238}}{M_i/M_{238}} \tag{3.23}$$

$$\sigma_{^{i}\mathrm{U}/^{238}\mathrm{U}} = \frac{\sigma_{m_{i/238}}}{M_i/M_{238}} \tag{3.24}$$

where $m_{i/238}$ denotes the mass ratio of ^{i}U over ^{238}U ($m_{i/238}$= m_i/m_{238}).

3.5 Discussion

3.5.1 δ^{238}U in uranium standards and geostandards

Measurements of standards and reference materials are key to ensuring data accuracy and comparisons of results from different laboratories. Herein, we use the term 'standard' (or 'isotope standard') only to denote reference materials with certified U isotopic compositions (*e.g.,* CRM-145 and CRM-112a), whereas we use the term 'reference materials' for those other materials that are frequently measured alongside unknown samples but do not have certified U isotopic compositions. 'Reference materials' thus include artificial concentration standards (*e.g.,* ICP single elemental solutions) and natural geostandards. A large number of standards and reference materials are regularly used in U isotope studies, and we used the UID to provide the most up-to-date and reliable recommended δ^{238}U values for these materials (**Fig. 3.5–3.8**). In these figures, only high-precision measurements are shown (*e.g.,* with uncertainties below 0.10 ‰ for natural uranium (NU) standards

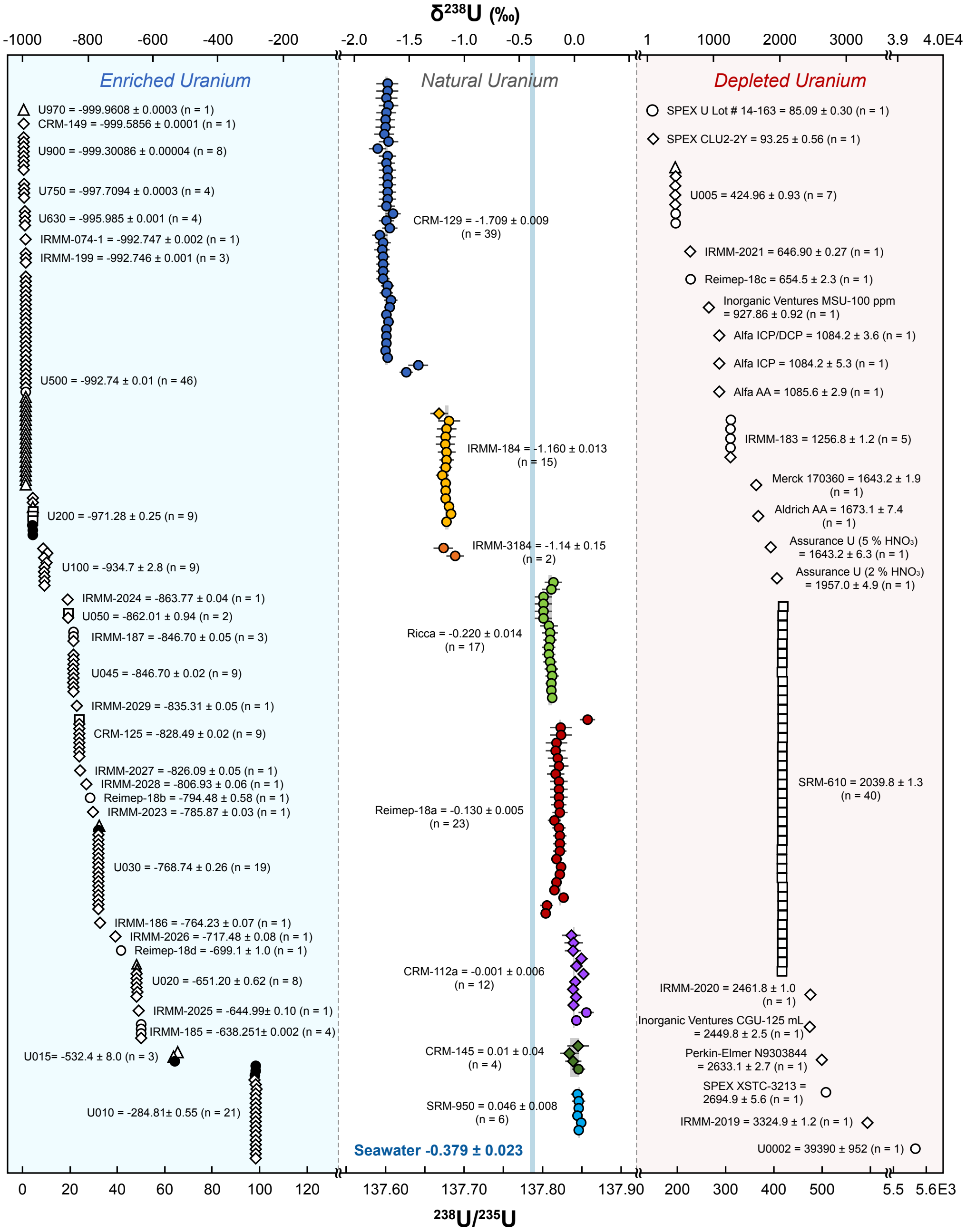

Figure 3.5: Summary of U isotope compositions of certified U isotope and concentration standards. δ^{238}U values are renormalized against CRM-145, and absolute ratios (^{238}U/^{235}U, lower x-axis) assume a $^{238}\text{U}/^{235}\text{U} = 137.837$ for CRM-145 (Richter et al. 2010). The symbols denote the data collection technique: circle (MC-ICP-MS), diamond (TIMS), triangle (ICP-MS), square (in-situ techniques), and black circle (other techniques). The blue band shows the U isotopic composition of modern seawater ($\delta^{238}\text{U}_{\text{SW}}$= -0.379 ± 0.023 ‰, Kipp et al. 2022; Tissot and Dauphas 2015)

and geostandards), and the data is rank ordered, from lower to higher precision. For standards or reference materials with only a single analysis in the literature, the recommended δ^{238}U and its error represent the result of said analysis. For well characterized NU standards and geostandards as well as enriched uranium (EU) and depleted uranium (DU) standards (at least 5 analyses), the recommended δ^{238}U and uncertainties are calculated as weighted average of independent measurements using the following equations:

$$\delta^{238}\mathrm{U}_{\mathrm{rec}} = \frac{\sum_i (\delta^{238}\mathrm{U}_i/\sigma_i^2)}{\sum_i (1/\sigma_i^2)} \tag{3.25}$$

$$2\sigma_{\delta^{238}\mathrm{U}}(95\% c.i.) = 2 \times \sqrt{\frac{1}{\sum_i (1/\sigma_i^2)}} \tag{3.26}$$

where $\delta^{238}\mathrm{U}_{\mathrm{rec}}$ is the recommended δ^{238}U in the UID; $\delta^{238}\mathrm{U}_i$ and σ_i are the δ^{238}U value and 1 sigma uncertainty of an independent analysis i, and $2\sigma_{\delta^{238}U}$ is the 2 standard error (*i.e.,* 95 % confidence interval) of the recommended δ^{238}U. To assess the adequacy of using an error-weighted average U isotopic composition, reduced-χ^2 statistics (*a.k.a.,* MSWD) were calculated as:

$$\chi^2_{\mathrm{red}} = \frac{1}{n-1} \sum_i \frac{(\delta^{238}\mathrm{U}_i - \delta^{238}\mathrm{U}_{\mathrm{rec}})^2}{\sigma_i^2} \tag{3.27}$$

3.5.1.1 Pure U standards

Fig. 3.5 summarizes the δ^{238}U of pure U isotope and concentration standards in the order of increasing δ^{238}U values. These materials fall in three broad categories: NU, DU, and EU standards. Today, the most widely used U isotope standard is the CRM-145, against which all UID data is normalized. Produced by the New Brunswick Laboratory (NBL), CRM-145 is the solution made from a piece of the CRM-112a U metal. The CRM-112a was initially produced and distributed by the National Bureau of Standard (NBS) as SRM-960 but was recertified and renamed NBL CRM-112a when the Special Nuclear Standard Reference Material (SRM) program was transferred to the NBL CRM (Certified Reference Material) program in 1987. Early papers also frequently used the SRM-950(a), a uranium oxide with indistinguishable ^{238}U/^{235}U from SRM-960, but with a distinct ^{234}U/^{238}U ratio (Condon et al. 2010; Richter et al. 2010). As a result, the δ^{238}U values of CRM-112a, CRM-145, SRM-950a, and SRM-960 are considered identical in the UID (an assumption that will be easily relaxed should differences be resolved by future measurements).

In addition to NBL CRM and NBS SRM programs, the Institute for Reference Materials and Measurements (IRMM) has produced two series of U isotopic standards that are currently used for geochemical measurements: IRMM183–187, and REIMEP 18A-D (the latter as part of the Regular European Interlaboratory Measurement

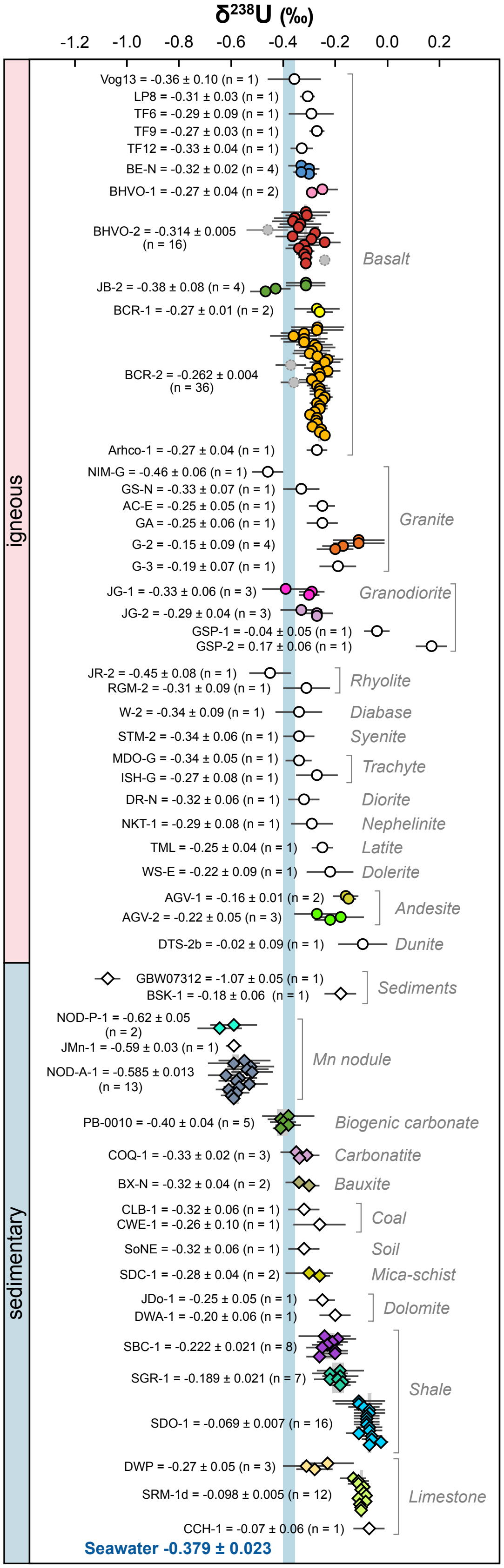

Figure 3.6: Summary of δ^{238}U values of rock geostandards. The symbol shapes denote the sample type: circle (igneous), diamond (sedimentary). The blue band shows the U isotopic composition of modern seawater ($\delta^{238}U_{SW}$= -0.379 ± 0.023 ‰, Kipp et al. 2022; Tissot and Dauphas 2015). Geostandards with at least 2 measurements are colored, and the error bands are shown only for those with more than 5 analyses. When n > 1, the uncertainties of the recommended δ^{238}U values are 2 standard deviations. When n=1, the uncertainty represents the analytical error of the single measurement. Grey symbols for BHVO-2 and BCR-2 denote analyses not use in the calculation of the recommended δ^{238}U values.

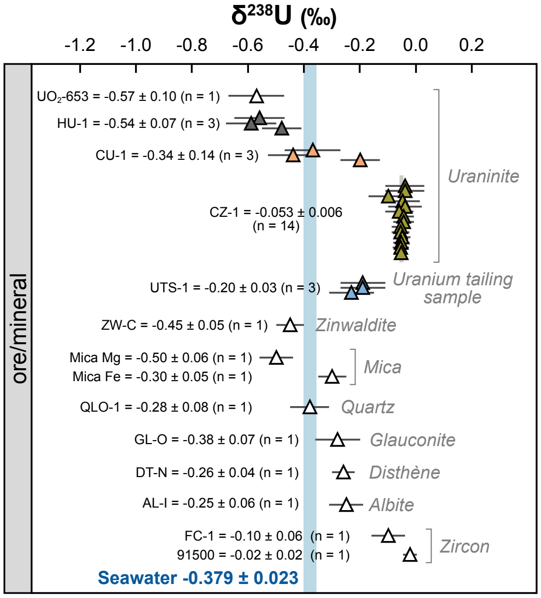

Figure 3.7: Summary of δ^{238}U values of ore and mineral geostandards. The blue band shows the U isotopic composition of modern seawater (δ^{238}U$_{SW}$= -0.379 ± 0.023 ‰, Kipp et al. 2022; Tissot and Dauphas 2015). Geostandards with at least 2 measurements are colored, and the error bands are shown only for those with more than 5 analyses. When n>1, the uncertainties of the recommended δ^{238}U values are 2 standard deviations. When n=1, the uncertainty represents the analytical error of the single measurement.

Evaluation Programme). Both series contain isotope standards ranging from depleted to low enriched uranium (Richter et al. 2005, 2006).

The homogeneity of these materials is key to their usefulness as standards or reference materials. Among NU standards, IRMM-184, CRM-112a, CRM-145, SRM-950a, SRM-960, and Ricca (concentration standard) exhibit good agreement during interlaboratory comparisons. As already pointed out by Andersen et al. (2017), CRM-129a appears to be heterogeneous, with published δ^{238}U values clustering around two values: one at ∼-1.5 ‰ (n = 91) (Jost et al. 2017; Lau et al. 2016, 2017; Lu et al. 2023) and the other one at ∼-1.7 ‰ (n = 1068). Furthermore, while Reimep-18a was until recently considered homogeneous (Andersen et al. 2017), heterogeneity is likely to exist in this standard as well, as δ^{238}U values in different batches range from -0.26 ‰ (Brüske et al. 2020b) to +0.12 ‰ (Basu et al. 2014). As a result, these isotopically heterogeneous standards are not ideal for interlaboratory comparison. If utilized as secondary standards in future U isotopic investigations, special care must be taken to cross-calibrate the U isotopic composition of the specific batch used.

3.5.1.2 Geostandards

At this writing, the U isotopic composition of 73 geostandards has been characterized, covering igneous rocks, sedimentary rocks, and U-bearing minerals (**Fig. 3.6**–

3.8). Except for two granodiorites data points, δ^{238}U variations in igneous rocks are generally smaller than in sedimentary rocks, reflecting the importance of low-temperature isotope fractionations in the latter. Although numerous geostandards have been analyzed, only a few of them are well characterized, by multiple laboratories, namely: basalts BCR-2 and BHVO-2, Fe-Mn nodule NOD-A-1, biogenic carbonates PB-0010, shales SBC-1, SGR-1, and SDO-1, limestone SRM-1-d, and uraninites CZ-1. For these, robust recommended δ^{238}U values, based on these inter-laboratory data, are provided (**Fig. 3.8**). Most geostandards have been less studied (measured 5 times, or less), and their δ^{238}U, even when highly precise, will benefit from seeing their accuracy confirmed by future works, which the UID will allow to easily assess as new data becomes available.

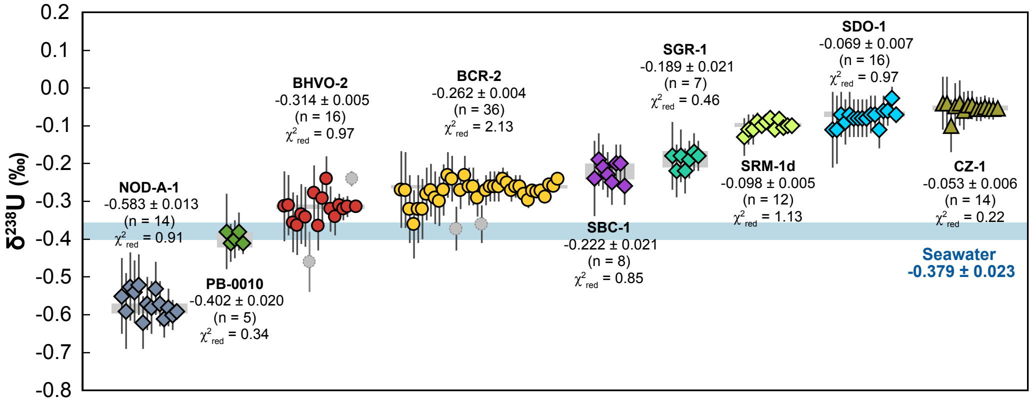

Figure 3.8: The error bands represent the 95 % confidence intervals of the data points. As in Fig. 3.6 and 3.7, symbol shapes denote sample types: circle (igneous), diamond (sedimentary), and triangle (ore/mineral). The grey symbol indicates that the data point meets the selection criterion but is not included in the calculation of recommended δ^{238}U, because of the significant offset relative to other measurements. Within each geostandard, the data are ordered by measurement uncertainty, reflecting the improvement in analytical precision (mostly as a function of time). The blue band shows the U isotopic composition of modern seawater ($\delta^{238}U_{SW}$= -0.379 ± 0.023 ‰, Kipp et al. 2022; Tissot and Dauphas 2015).

3.5.2 Scope of uranium isotopic studies and future direction

To facilitate searching and finding of data, the data within the UID is distributed between 6 sub-databases (**Fig. 3.2**). These categories were chosen to be as independent and unambiguous as possible, and they are non-overlapping, meaning that no data is duplicated between sub-databases. Within each sub-database, publications (and the data they report) are categorized according to their dominant scope/theme of study. This allows one to rapidly isolate all publications/data within a major theme (*e.g.,* chronology, paleoredox, etc.), and build custom-compilations for future studies. Below, we provide a brief review of the state-of-the-art for most of the themes used in the UID, in the order shown on **Fig. 3.2**.

3.5.2.1 Calibrations and method developments

Many methodologies for U isotopic determination have been established, with remarkable differences in their sensitivity, precision, analysis time, required material mass, and sample preparation processes, among others. The analytical toolbox contains various types of modern spectrometry to fulfill the requirements of a variety of applications, such as inductively-coupled-plasma mass-spectrometry (ICP-MS), TIMS, secondary ion mass spectrometry (SIMS), alpha spectrometry, gamma spectrometry, optical emission spectrometry (OES), optogalvanic spectroscopy (OGS), and neutron activation. As a first-order benchmark to evaluate the precision obtained from specific methods, we used the UID to plot in **Fig. 3.9** the full range (to-date) of analytical precision on δ^{238}U values achieved by each technique.

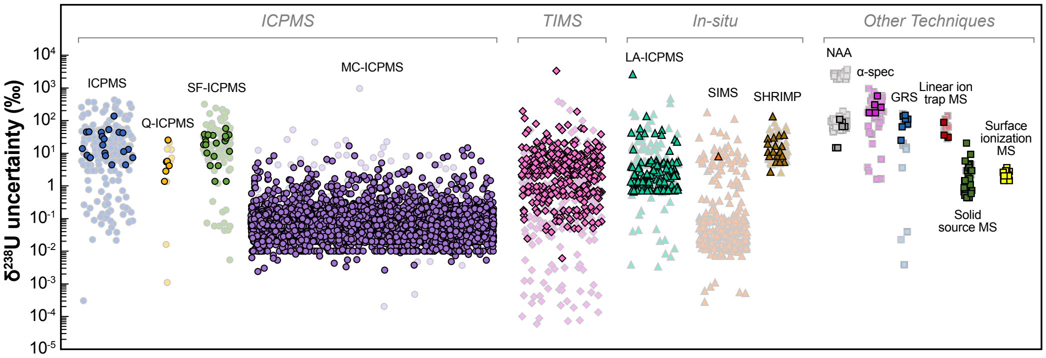

Figure 3.9: Compilation of δ^{238}U uncertainties obtained using different analytical techniques. Uncertainties are those reported in the original studies (2SD, 2SE or 95% CI depending on the study). Dark symbols represent NU samples and light symbols represent EU and DU samples. Symbol shapes denote the types of techniques: circle (ICPMS), diamond (TIMS), and triangle (in-situ techniques), square (other techniques).

ICPMS is the most widely used technique for analyzing U isotopic compositions of small amounts of material in geological, environmental, and forensic studies, taking advantage of the extraordinarily efficient ionization of argon plasma. The instruments used for U isotopic determination are further classified in the ICPMS scheme as MC-ICP-MS, quadrupole ICPMS, and sector-field (SF) ICPMS.

MC-ICP-MS is a well-established technology for high-precision ^{238}U/^{235}U determination, as the simultaneous detection of all ion beams alleviates most of the uncertainty stemming from plasma instabilities (relative to single collector instruments). In the geochemistry community, solution-based MC-ICP-MS is currently the most routine approach for analyzing U isotopes (see Tissot and Ibañez-Mejia 2021, **Fig. 2**). The performance of this technique can be further improved by employing a double spike (Richter et al. 2008; Stirling et al. 2007; Weyer et al. 2008), introducing samples with membrane desolvating nebulizer systems (*e.g.,* Aridus, DSN-100, and Apex), as well as coupling with multiple ion counting devices for ultra-trace level works (Snow and Friedrich 2005). Apart from its extensive usage in the field of geochemistry, MC-ICP-MS is also employed in the bulk analysis of environmental samples (*e.g.,* samples collected by safeguards inspectors in the surrounding environment of nuclear facilities) (Boulyga et al. 2016; Buchholz et al. 2007).

Since extensive sample preparation and purification are required beforehand, MC-ICP-MS is rarely suitable for environmental screening and health physics studies, where there is a high demand for the rapid processing of large numbers of samples. In these fields, SF-ICPMS is preferred because isotopic analysis can be performed despite significant and complex matrices. Health physicists have put efforts in developing methods to measure U isotopic ratios in biological samples such as blood (Todorov et al. 2009; Tolmachyov et al. 2004) and urine (Gray et al. 2012; Gwiazda et al. 2004; Pappas et al. 2003; Xiao et al. 2014). Because of the low sample preparation requirements, SF-ICPMS is also applied to environmental samples, such as soil and U-bearing particles (Boulyga and Becker 2001; Boulyga et al. 2001; Boulyga and Becker 2002; Shinonaga et al. 2008).

Other types of ICPMS are less commonly used for U isotopic analysis. Only a few studies evaluated the ability of quadrupole ICPMS (Ejnik et al. 2005; Lindahl et al. 2021; Oliveira and Sarkis 2002) and high-resolution (HR) ICPMS (Krystek and Ritsema 2002; Zhang et al. 2007) to provide fast U isotope data and test their relevance to the study of biological and particle samples.

In addition to liquid sample introduction, ICPMS can be combined with laser ablation (LA) systems, allowing for in-situ isotopic analysis of solid materials, which is especially beneficial for small size samples that lack adequate materials for solution-based measurement. Besides providing spatially resolved data, LA-ICPMS significantly reduces analysis time and does not generate radioactive waste, which are important in forensic studies. LA-ICPMS has thus proven a useful tool to characterize U isotopic compositions in single particles (Boulyga and Prohaska 2008; Claverie et al. 2016; Donard et al. 2017; Kappel et al. 2012, 2013; Pointurier et al. 2011, 2013; Ronzani et al. 2019; Varga et al. 2018; Varga 2008), highly radioactive materials (Guillong et al. 2007; Günther-Leopold et al. 2008; Stefánka et al. 2008) and biological samples (*e.g.,* flower leaves, Zoriy et al. 2005). In most natural materials, where U contents are low and isotopic variability is typically limited to sub-permil effects, LA-ICPMS provides insufficient precision to resolve U isotope variations. As a result, the use of laser ablation in geochemistry is still in its infancy, and, to our knowledge, only one recent study has successfully used LA-MC-ICP-MS, in combination with 10^{13} Ω amplifiers, to determine ^{238}U/^{235}U ratios in single zircon and titanite grains (Yamamoto et al. 2021).

SIMS is another type of in-situ technique for U isotopic determination (Kips et al.

2007; Lewis et al. 2015; Yomogida et al. 2017). SIMS analysis suffers from higher polyatomic interferences (Ranebo et al. 2009) than LA-ICPMS, but offers a better spatial resolution down to 1 μm (Boulyga et al. 2015). The higher spatial resolution allows for mapping U isotopic compositions in target samples. These maps can be used for preliminary screening in forensic particle analysis to locate and distinguish different types of particles (Betti et al. 1999; Peres et al. 2013; Ranebo et al. 2007; Tamborini et al. 1998). For larger samples like fuel pellets and big particles, SIMS maps are also valuable to detect spatial heterogeneity of U isotope ratios (Kips et al. 2019; Tamborini et al. 1998).

TIMS was the paramount technique for high-precision U isotope measurements before the advent of MC-ICP-MS. Although MC-ICP-MS plays a dominant role in geological and environmental investigations nowadays, TIMS still occupies an important place in studies requiring the determination of absolute U isotope ratios, such as geochronology (*e.g.,* Hiess et al. 2012), nuclear contamination (Sahoo et al. 2002, 2004; Taylor et al. 1998), solution-based single particle analysis (Kraiem et al. 2012; Shinonaga et al. 2008), as well as calibration of certified reference materials, commercially available compounds and reagents (Condon et al. 2010; Kraiem et al. 2013; Mathew et al. 2012; Peńkin et al. 2018; Richter et al. 1999b, 2005, 2006, 2010, 2018; Shibahara et al. 2016). A range of techniques for improving the performance of TIMS were developed, such as employing a cavity source to enhance ionization efficiency (Maden et al. 2018; Trinquier et al. 2019), optimizing evaporation protocols (Callis and Abernathey 1991; Fiedler 1995; Mathew et al. 2013; Richter and Goldberg 2003; Richter et al. 2011; Suzuki et al. 2010), enhancing ionization by porous ion emitter (Watrous and Delmore 2011), and leveraging higher resistance amplifiers or ion counter to improve electronic efficiency (Quemet et al. 2014, 2016), .

Other types of spectrometry for U isotope analysis are either preferred in early studies or confined within limited applications. Alpha spectrometry is a conventional technique to determine the activity ratio of U isotopes (Alamelu and Jagadish 2016; Boulyga et al. 2001; Duarte and Szeles 1994; Iturbe 1992; Kunzendorf 1968). Other techniques including ICP-OES (Zeiri et al., 2021), extractive electrospray ionization mass spectrometry (EESI-MS), passive gamma-ray spectrometry (Nir-El 2000), glow discharged OGS (Barshick et al. 1995), and neutron activation analysis (Ganapathy 1978) will not be described in detail here, because they are not commonly employed.

As predicted from counting statistics and Johnson Noise, the precision of U isotope analysis achievable with modern instrumentation is correlated with the total mass of U used for measurements (**Fig. 3.10**). For a given instrument (*i.e.,* analytical setup), precision can thus be improved by analyzing more U. The relationship shown in **Fig. 3.10** can be used a reference point to design analytical plans based on the available materials and desired precision in future studies.

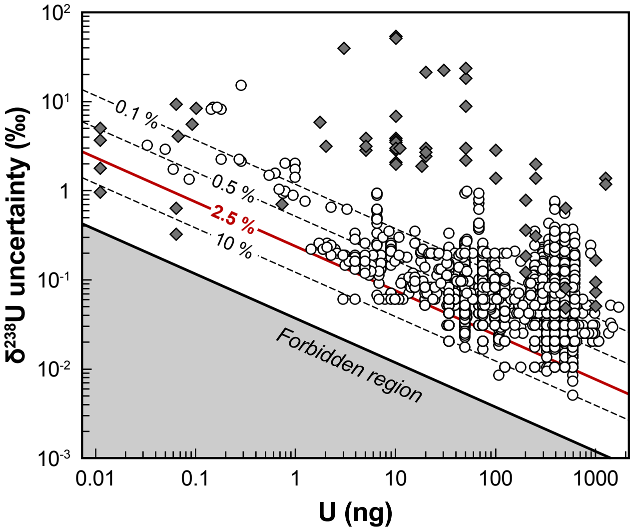

Figure 3.10: Relationship between δ^{238}U uncertainties and mass of U analyzed in nanograms. White circles and grey diamonds are uncertainties of NU samples obtained from MC-ICPMS and TIMS, respectively. Uncertainties are those reported in the original studies (2SD, 2SE or 95% CI depending on the study). When the exact mass of U for each sample is not reported, average masses reported in the study are used. Red solid curve and black dash curves represent reference theoretical 2SE (counting statistics and Johnson noise, see Eq. (2) in Tissot et al. (2019a), assuming 30 V signal on ^{238}U and use of $10^{11}\Omega$ amplifiers) with ion transmission of 2.5% (typical value for Neptune MC-ICPMS), 0.1%, 0.5%, 10%, respectively. Black curve shows precision limit, assuming 100% transmission.

Besides mass spectrometry, method developments also comprise chemical separation and purification. Chromatography based on the UTEVA resin is well-established nowadays, modified after Horwitz et al., 1992, Horwitz et al., 1993, with minor differences between labs (*e.g.,* Stirling et al. 2007; Tissot and Dauphas 2015; Weyer et al. 2008). Recent studies on U chemistry mainly focus on processing special samples, such as high-purity graphite (Metzger et al. 2021) and environmental swipe samples (Metzger et al. 2019), as well as measuring minor isotopes without spike addition (Rovan and Štrok 2019).

3.5.2.2 Oceanic paleoredox reconstruction

Reconstructing the oceanic redox history is important to understand the evolution of the Earth's surface conditions, and its interconnection with the appearance and evolution of life. In the past decade, U isotopes have received considerable attention as a paleoredox proxy of marine/seafloor anoxia (see review by Zhang et al. 2020c). Uranium is redox-sensitive and can hold two oxidation states in the terrestrial surface environment: insoluble U(IV) and soluble U(VI) (Langmuir 1978). In the modern (oxic) ocean, the long residence time of U (τ ~400 kyr, Dunk et al. 2002; Ku et al.

1977) results in both homogeneous salinity-normalized concentration (~3.2 ng/g for a salinity of 35 g/L, Chen et al. 1986) and isotopic composition (δ^{238}U = -0.379 ± 0.023 ‰, Kipp et al. 2022; Tissot and Dauphas 2015). As U inputs to the ocean are dominated by continental weathering, with an isotopic composition identical to that of the continental crust (-0.30 ± 0.04 ‰, Andersen et al. 2016; Tissot and Dauphas 2015), the δ^{238}U of seawater is thus primarily controlled by the isotopic fractionation associated with U removal into different oceanic sinks. The main process fractionating U isotopes during removal is reductive immobilization in anoxic/euxinic settings, which leads to ^{238}U enrichments in reduced sediments. As a result, in periods of expanded marine anoxia, the increased sequestration of U in reduced sediments, would result in lower U concentration and δ^{238}U value in seawater.

One key aspect when reconstructing past oceanic redox states with U isotopes is to work on a reliable seawater δ^{238}U archive. Carbonates are the most popular and straightforward archive to date since they tend to directly record the primary seawater δ^{238}U signal. U(VI) mainly exists as uranyl carbonate complexes $UO_2(CO_3)_3^{4-}$ in seawater, which is incorporated into marine carbonates with no significant isotopic fractionation. This conclusion is supported by both lab-controlled coprecipitation experiments (Chen et al. 2016) and comparison of primary carbonates and modern seawater (Kipp et al. 2022; Romaniello et al. 2013; Stirling et al. 2007; Tissot et al. 2018; Weyer et al. 2008). In just over a decade, more than 60 studies have placed constraints on oceanic anoxia using U isotopes in a variety of carbonates, including limestone, dolomite, biogenic carbonates, and carbonate-rich sediments (Andersen et al. 2014, 2018, 2020; Asael et al. 2013; Azmy et al. 2015; Bartlett et al. 2018; Brennecka et al. 2011a; Bruggmann et al. 2022; Brüske et al. 2020b; Bura-Nakić et al. 2020; Cao et al. 2020; Chen et al. 2022a; Chen et al. 2021a; Chen et al. 2018a,b, 2021b, 2022b; Cheng et al. 2020a; Cheng et al. 2020b; Cherry et al. 2022; Clarkson et al. 2018, 2020, 2021a,b; Dahl et al. 2014, 2017, 2019; Dang et al. 2022; Del Rey et al. 2022; Elrick et al. 2017, 2022; Gilleaudeau et al. 2019; Gothmann et al. 2019; Herrmann et al. 2018; Hood et al. 2016, 2018; Jost et al. 2017; Lau et al. 2016, 2017, 2022; Li et al. 2020; Liu et al. 2022; Livermore et al. 2020; Lu et al. 2020, 2023; Mänd et al. 2020; McDonald et al. 2022; Noordmann et al. 2016; Phan et al. 2018; Rey et al. 2020; Romaniello et al. 2013; Song et al. 2017; Tissot and Dauphas 2015; Tissot et al. 2018; Tostevin et al. 2019; Wang et al. 2022; Wei et al. 2018, 2021; White et al. 2018; Zhang et al. 2018a,b,c, 2019a,b, 2020a,b, 2022; Zhao et al. 2020). As recently discussed in Kipp and Tissot (2022), perhaps the main uncertainty affecting these reconstructions stems from the way diagenetic transformations alter the primary seawater signal. Studies of modern primary carbonates have shown that early diagenesis leads to non-negligible δ^{238}U offset between carbonates and seawater (from ~0 to +0.6 ‰; Romaniello et al. 2013; Tissot et al. 2018). Things become even more complicated when using ancient carbonates since the extent of diagenesis varies in different geological settings. In the absence, so far, of a proxy for δ^{238}U diagenetic offsets, the resulting uncertainty on anoxia reconstructions can have a substantial impact on data interpretations (Kipp and Tissot 2022).

Shales and organic-rich sediments are another set of widely used sedimentary archives for δ^{238}U seawater reconstructions (Abshire et al. 2020; Asael et al. 2013; Brüske et al. 2020a,b; Cheng et al. 2020b; Chiu et al. 2022; Cole et al. 2020; Dang et al. 2022; Dickson et al. 2021, 2022; Holmden et al. 2015; Kendall et al. 2013, 2015, 2020; Lau et al. 2022; Li et al. 2022; Lu et al. 2017, 2020; Montoya-Pino et al. 2010; Noordmann et al. 2015; Ostrander et al. 2022; Pan et al. 2021; Phan et al. 2018; Stockey et al. 2020; Wang et al. 2018, 2020; Weyer et al. 2008; Yang et al. 2017). In contrast to marine carbonates, which directly represent seawater, the shale signatures are highly fractionated away from the seawater composition, and the magnitude of the fractionation factor relative to seawater has been shown to depend on environmental controls such as the depositional environments (Andersen et al. 2014), organic carbon and sulfide burial rates (Cole et al. 2020) or the extent of oceanic anoxia (Chen et al. 2021a). Furthermore, shales and organic-rich sediments often consist of both authigenic and detrital components, and the two have to be teased apart, either physically/chemically prior to analysis or through corrections leveraging authigenic U enrichment proxies such as U/Al and U/Th ratios (Abshire et al. 2020; Asael et al. 2013; Brüske et al. 2020a,b; Cole et al. 2020; Kendall et al. 2020; Noordmann et al. 2015; Stockey et al. 2020; Yang et al. 2017). While these added uncertainties certainly complicate δ^{238}U seawater reconstructions, the record from shales and organic-rich sediments is nonetheless highly valuable, and study of the (co)variations with the carbonate record can provide complementary insights into the U oceanic cycle through time.

Fig. 3.11 presents the U isotopic data for carbonates and shales from 3500 Ma to the present (panels a and c), with emphasis on the Neoproterozoic and Phanerozoic (panels b and d). Even though there are thousands of data points available for various geological periods, this figure shows that almost all current paleo-redox studies are event-driven, with a particularly strong focus on catastrophic extinction events. Future U isotope studies targeting the current gaps in the record (*i.e.,* between geological events studied so far) will be extremely useful to develop a comprehensive understanding of the redox history through out Earth's history.

Two studies have investigated Fe-Mn crusts, where U is mostly adsorbed on the surface of the samples, as a potential record of seawater δ^{238}U value (Goto et al. 2014; Wang et al. 2016). In line with adsorption experiments (Brennecka et al. 2011b), these studies found Fe-Mn crusts, from modern back to 80 Myr ago, to be

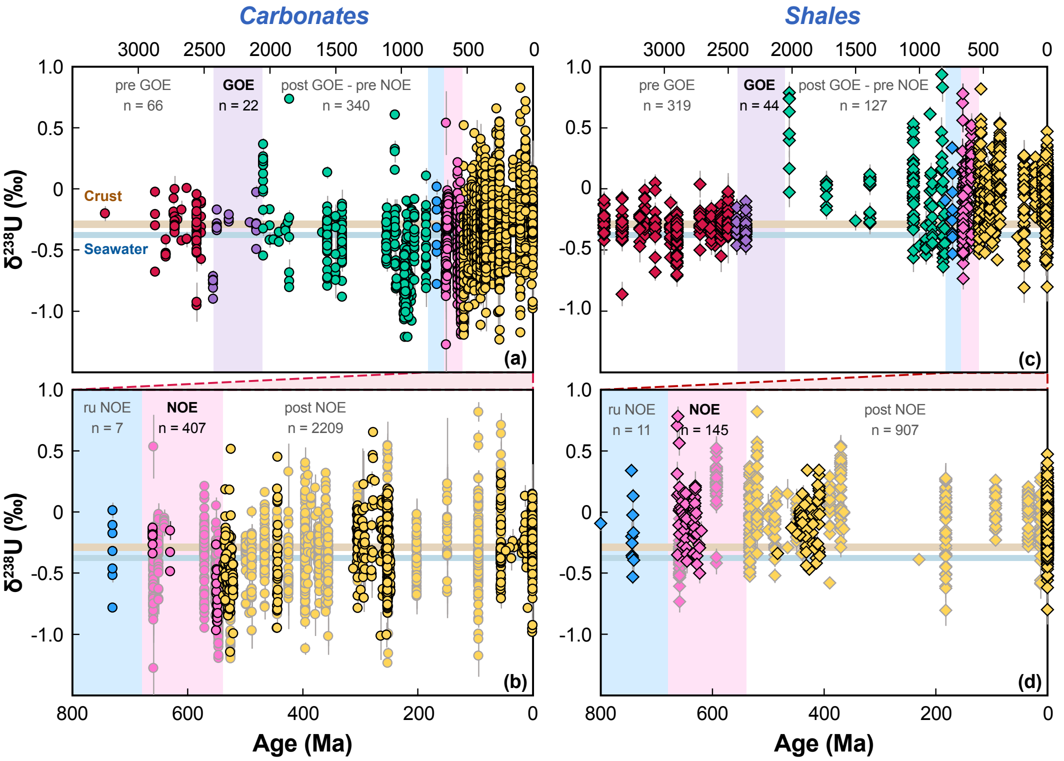

Figure 3.11: Compilation of δ^{238}U values in carbonates (a) from 3500 Ma to present (n = 3132), (b) from 800 Ma to present (n = 2704), and in shales (c) from 3500 Ma to present (n = 1553), (d) from 800 Ma to present (n = 1063). The brown and blue band show δ^{238}U of continental crust (-0.29 ± 0.03‰) and modern seawater (-0.379 ± 0.023‰), respectively (Kipp et al. 2022; Tissot and Dauphas 2015). The six geological intervals are pre GOE (3500–2430 Ma), GOE (2430–2060 Ma), post-GOE-pre-NOE (2060–800 Ma), ramp up (ru) NOE (800–680 Ma), NOE (680–540 Ma) and post-NOE (540 Ma–present). In panels (b) and (d), darker symbols denote numerical ages are reported in the original publications, while symbols greyed out denote ages are estimated by the geological periods.

offset from the modern seawater value by ∼0.24‰, which the authors interpreted as evidence of constant oxygen levels in the ocean during this time interval. The fact that the ^{234}U/^{238}U ratios in all samples are widely out of secular equilibrium, and, in many cases, offset towards the modern seawater value, suggests however constant U exchange and equilibration between the Fe-Mn crusts and seawater. This raises serious doubts about the reliability of Fe-Mn crusts as faithful recorders of past seawater δ^{238}U value and their usefulness in the study of oceanic paleoredox conditions.

It is essential to understand the terrestrial U cycling in paleoredox studies since this proxy is based on the rationale that δ^{238}U of seawater predominantly reflects the mass balance between riverine input and various sedimentary outputs such as anoxic sediments, euxinic sediments, and biogenic carbonates. While the U isotopic compositions of these sinks have been extensively characterized, those of seawater

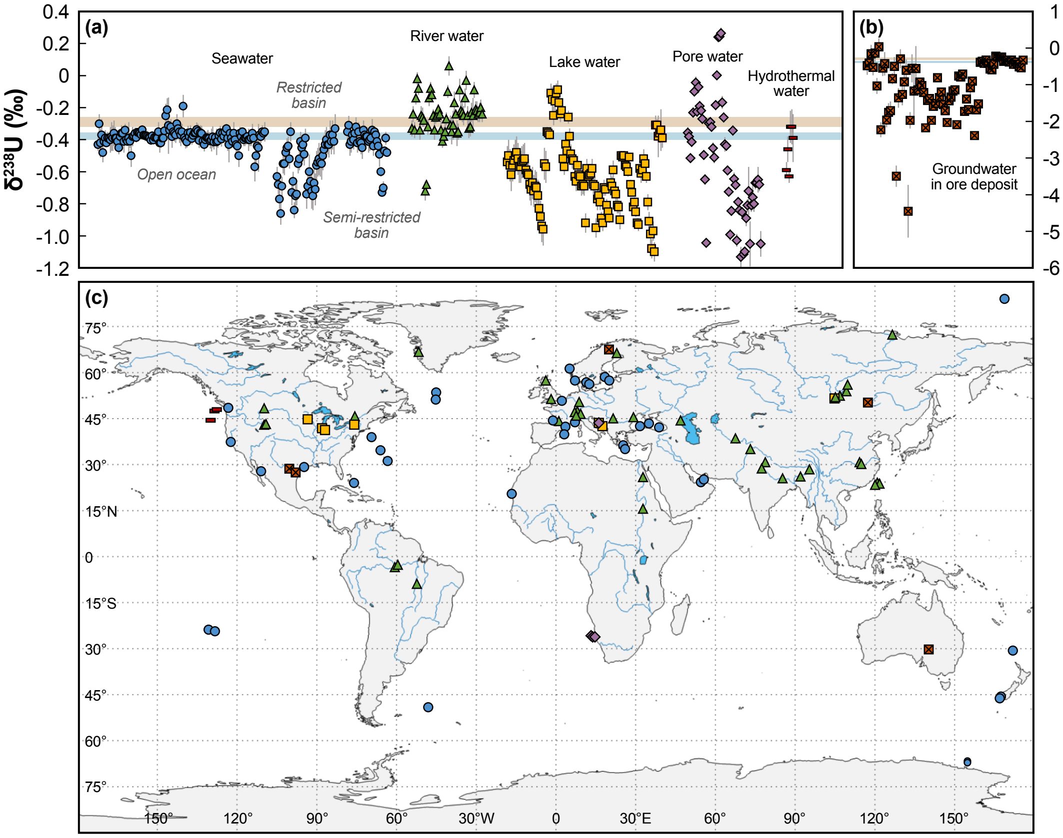

Figure 3.12: Compilation of δ^{238}U values in water samples and world map illustrating the water sample locations. (a–b) Compilation of δ^{238}U values in water samples. The symbol shapes denote sample type. The brown and blue band show δ^{238}U of continental crust (-0.29 ± 0.03 ‰) and modern seawater (-0.379 ± 0.023 ‰) respectively (Kipp et al. 2022; Tissot and Dauphas 2015). (c) World map illustrating the water sample locations. Symbols as in (a) and (b).

and rivers are less well constrained (**Fig. 3.12**, Andersen et al. 2016; Noordmann et al. 2016; Stirling et al. 2007). Recently, Kipp et al. (2022) partially addressed this issue by reevaluating the fundamental assumption of homogeneity of the marine U reservoir. They found that subtle δ^{238}U and δ^{238}U heterogeneity that correlate with U concentrations exist in modern seawater, and as a result proposed a new-salinity normalized global mean seawater for δ^{238}U of -0.379 ± 0.023‰ and $\delta^{234}U_{sec}$ of 145.55 ± 0.28‰.Previous research has shown that substantial variations exist between rivers from different regions, ranging from -0.72 to +0.06‰, and seasonality may affect the riverine δ^{238}U values (Andersen et al. 2016). In order to establish a tighter constraint on the U budget, an expanded riverine database, both in time and space, is required. Besides the uncertainty on the riverine value, **Fig. 3.12** also reveals other limitations in the data currently available. For instance, the U isotopic composition of groundwater (as an input to the ocean) has not been investigated since previous studies only measured groundwater contaminated by U mines. Furthermore, the

δ^{238}U record of lake water, pore water, and hydrothermal water are extremely limited (<5 sites for each category). Future characterization of the U isotopic compositions of these reservoirs will provide constraint on the U budget at a finer scale.

Another important issue in the context of the U budget is that U cycling can be dramatically different during expanded marine anoxia. Sparing dissolved U(VI) will significantly shorten the U residence time (*e.g.,* Li et al. 2013), invalidating the assumption of conservative behavior of uranium. This has the potential to shift U isotopic composition from a global to a regional redox indicator (Andersen et al. 2017), and can influence U isotopic fractionation (Chen et al. 2021a).

Finally, detailed studies establishing the reliability of current and future potential archives are needed. Carbonates, for example, frequently experience varying extents of diagenesis, which can significantly alter the primary isotopic composition. More efforts are needed to disentangle the diagenetic signal from the authigenic U composition. Possible directions include developing fine correction protocols for different diagenetic processes and identifying alternative archives that are less affected by and/or more resistant to these alterations. According to recent studies, brachiopod shells can be a promising proxy since they are less impacted by porewater diagenesis (Livermore et al. 2020; Rey et al. 2020). Finding more applicable archives can help us expand our toolbox when some samples are unavailable.

3.5.2.3 Igneous processes

High-precision U isotope investigations in igneous systems is a young but growing field. The discovery of δ^{238}U variations in felsic rocks (Telus et al. 2012), crustal materials (Andersen et al. 2015) and accessory minerals (Hiess et al. 2012), triggered interest in using U isotopes to shed light on high-temperature processes. Since then, several studies have started to explore in more details the potential of U isotopes as tracers of magmatic and other related processes such as crystallization, metasomatism, Soret diffusion, subduction, and sedimentary recycling (Andersen et al. 2015; Avanzinelli et al. 2018; Casalini 2018; Freymuth et al. 2019; Gaschnig et al. 2021; Livermore et al. 2018; Telus et al. 2012; Tissot et al. 2019a; Yamamoto et al. 2021).

Using the classical igneous (I-type) and sedimentary (S-type) granites from the Lachlan Fold Belt, Telus et al. (2012) found a spread in δ^{238}U from -0.50 ‰ to -0.21 ‰, but without any clear relationship to the nature of the protolith, or tracers of magmatic differentiation (*e.g.,* SiO_2). The lack of positive correlation between U, Fe and Mg isotope data in these samples showed nonetheless that thermal (Soret) diffusion was not the driver of isotope variations for these elements in these rocks.

After Andersen et al. (2015) found that samples from the Mariana arc had lighter U isotope composition than OIBs (by ~0.05 ‰), which were themselves lighter than

MORBs (also by ∼0.05 ‰), studies started investigating arc systems in more details. These revealed a general trend between δ^{238}U and Th/U ratios in arc lavas, consistent with the idea (Avanzinelli et al. 2012; Elliott et al. 1997) that the composition of the arc lavas is the result of mixing between low Th/U (and low δ^{238}U) slab-derived fluids and high Th/U (and δ^{238}U) recycled sediments melts into the source of the arc magmas (Andersen et al. 2015; Casalini 2018; Freymuth et al. 2019). A distinct trend observed in Mount Vesuvius lavas was interpreted to reflect an increase in carbonate sediment recycling, and thus increased CO_2 fluxes to the mantle source of these lavas during the more proactive phases of the volcano (Avanzinelli et al. 2018).

In a recent study of a differentiation sequence in the Kilauea Iki lava lake, Gaschnig et al. (2021) observed only a limited range of U isotope compositions (from -0.38 to -0.20 ‰), and no systematical variations with the extent of differentiation, ruling out this process as a major driver of isotopic variability in such tholeiitic systems. In contrast, correlations of δ^{238}U with REE patterns and mineral modes in angrites meteorites suggests that a change in the coordination environment of U during incorporation into pyroxene results in cpx-melt U isotope fractionation factor of ∼-0.25 ‰ (Tissot et al. 2017).

Some studies have also started exploring the U isotope systematics of pooled mineral fractions (Hiess et al. 2012; Livermore et al. 2018) and single-crystals (Tissot et al. 2019a; Yamamoto et al. 2021). We direct the reader to Section 3.5.2.5 (chronology) and Tissot and Ibañez-Mejia (2021) for more details on this topic.

While clear δ^{238}U variations have now been documented in igneous materials, the mechanisms underlying these fractionations at magmatic temperatures are still mostly unknown. The property of minerals incorporating U, temperature, the redox state of the melt, and the extent of crystallization are all potential drivers of isotopic fractionation. More work is needed to systematically assess the contribution as well as the direction and magnitude of U isotopic fractionation resulting from each of these mechanisms. As discussed in more details in Tissot and Ibañez-Mejia (2021), inter-crystal, inter-mineral and inter-rock ^{238}U/^{235}U variations could become powerful tools for studying magmatic evolution, provenance, redox, and/or composition. Exploiting the potential of this system will, however, require coordinated efforts to constrain the relationship between the characteristics of the host rock, host mineral, U crystal chemistry/bonding environments, and δ^{238}U of individual mineral grains, to build a robust interpretative framework for U isotope effects in natural accessory phases and bulk samples.

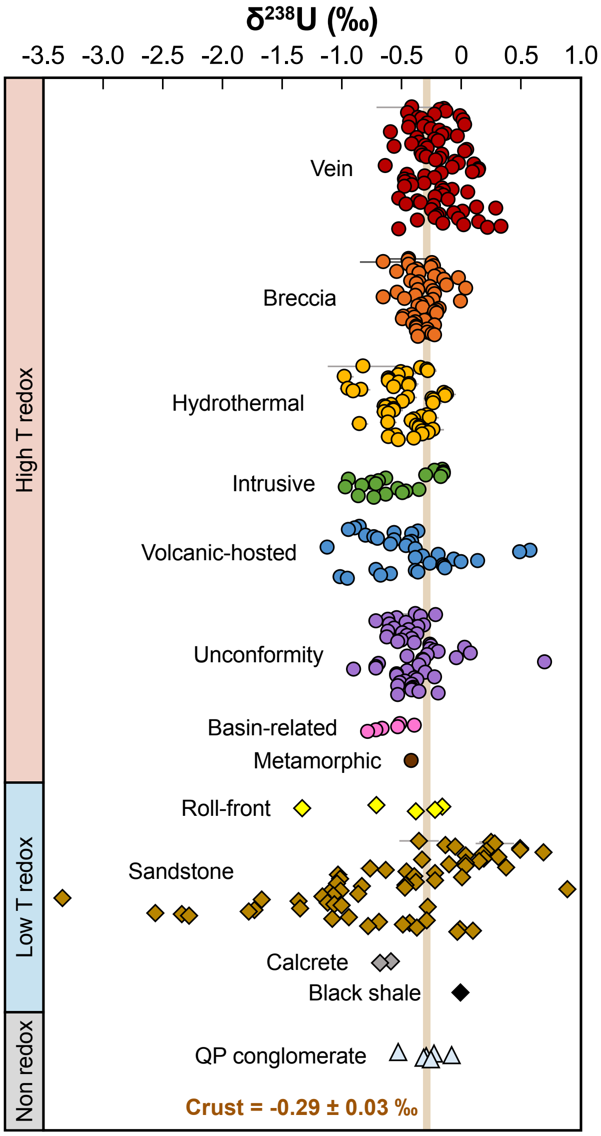

Figure 3.13: Compilation of δ^{238}U values in ore deposits. The symbol shapes represent the sample types: circle (high temperature redox sensitive), diamond (low temperature redox sensitive), and triangle (non-redox sensitive, QP = quartz-pebble). The brown band shows δ^{238}U value of continental crust (-0.29 ± 0.03 ‰, Tissot and Dauphas 2015).

3.5.2.4 Ore deposits

Due to their high U concentration, U ore deposits were the preferred target material for early U isotope studies (Hamer and Robbins 1960; Lounsbury 1956; Nier 1939; Rosholt et al. 1965; Rosholt et al. 1963; Senftle et al. 1957). The discovery in the early 70s of natural 'fossil' fission nuclear reactors with extremely high ^{238}U/^{235}U (due to ^{235}U burn-up) in Oklo (Gabon), led to a renewed interest for U isotope studies in ore deposits as a way to search for such reactors (Cowan and Adler 1976; Kirchenbaur et al. 2016; Richter et al. 1999a). A thorough review of observations and mechanisms of U isotope fractionation in ore deposits can be found in Andersen et al. (2017) and we only provide a brief overview below.

Extensive characterizations of U ore from various deposit types and locations revealed that ore deposits from different geological settings have distinct U isotopic compositions (**Fig. 3.13**), opening the possibility to utilize U isotopic composition as a "fingerprint" to distinguish and trace the origins of ore samples (Bopp et al. 2009; Brennecka et al. 2010b; Keatley et al. 2021; Keegan et al. 2008; Kirchenbaur et al. 2016; Placzek et al. 2016; Richter et al. 1999a; Spano et al. 2017; Uvarova et al. 2014). While the majority of U ore deposits studies focus on isotopic heterogeneity between mines, a few studies evaluate U isotopic variations at the smaller scales, such as samples collected from the same mine (Chernyshev et al. 2014; Kirchenbaur et al. 2016) or vein (Keatley et al. 2021), and even coexisting U minerals within single pitchblende (Chernyshev et al. 2014). Besides source fingerprinting, another important aim of U isotope investigations on ore deposits is to understand the mechanisms responsible for U isotopic fractionation in those environments, which are thought to be dominated by low-temperature reduction (Bopp et al. 2009; Brennecka et al. 2010b; Keatley et al. 2021; Murphy et al. 2014; Uvarova et al. 2014), and post-deposition aqueous alteration (Brennecka et al. 2010b; Keatley et al. 2021; Murphy et al. 2014). To confirm the validity of using U isotope to fingerprint the source of U in uranium ore concentrates (uranium oxide U_3O_8, an intermediate product of U ore after mining and chemical processing), a few studies have also investigated the impact of (i) small scale U isotope heterogeneity in the ore material and (ii) the manufacturing processes (Golubev et al. 2013; Keatley et al. 2021; Spano et al. 2017).

3.5.2.5 High precision chronology

Based on the decay of ^{235}U and ^{238}U to ^{207}Pb and ^{206}Pb with half-lives of 0.703 Gyr and 4.468 Gyr, respectively (Jaffey et al. 1971) the U-Pb/Pb–Pb system is the most widely used high-precision chronometer for dating terrestrial and extraterrestrial samples. Provided knowledge of the $^{238}\mathrm{U}/^{235}\mathrm{U}$ ratio at present, the dual decay system allows determination of a Pb–Pb age as:

$$\frac{^{207}\mathrm{Pb}^*}{^{206}\mathrm{Pb}^*} = \frac{^{235}\mathrm{U}}{^{238}\mathrm{U}} \times \frac{e^{\lambda_{235}t} - 1}{e^{\lambda_{238}t} - 1} \tag{3.28}$$

where * denotes radiogenic lead, λ_{235} and λ_{238} are decay constants for ^{235}U and ^{238}U, and t is the age of the sample.

For the sake of interlaboratory calibration, and in the absence of resolvable U isotope variations (beside Oklo) in natural materials, a $^{238}\mathrm{U}/^{235}\mathrm{U}$ consensus value of 137.88 was adopted in the late 70s for Pb–Pb dating (Steiger and Jäger 1977).

This important assumption was, however, overthrown by the discovery of resolvable U isotopic variations in natural samples (*e.g.,* Amelin et al. 2010; Bopp et al. 2009; Hiess et al. 2012; Stirling et al. 2007; Tissot and Dauphas 2015; Weyer et al. 2008). The impact of these variations on the accuracy of U-Pb and Pb–Pb ages has been extensively discussed (Hiess et al. 2012; Tissot and Dauphas 2015; Tissot et al. 2017, 2019a), and it is now accepted that both U and Pb isotopes need to be measured to obtain both precise and accurate dates.

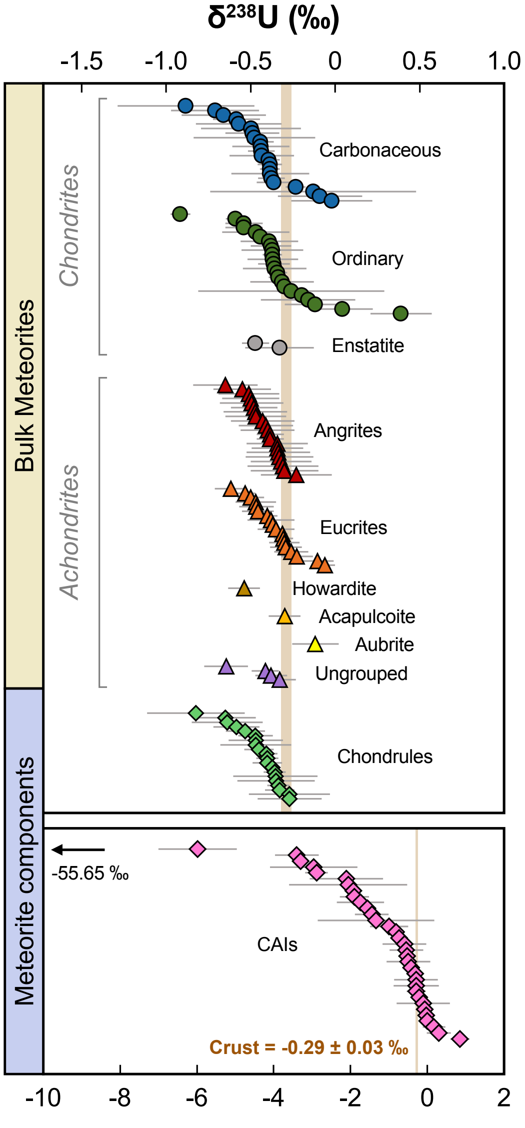

Figure 3.14: Compilation of δ^{238}U values iof extraterrestrial samples, including bulk meteorites and their components. The symbol shapes represent the sample types: circle (chondrites), triangle (achondrites), and diamond (meteorite components). The brown band shows δ^{238}U value of continental crust (-0.29 ± 0.03 ‰, Tissot and Dauphas 2015).

The impact of U isotope variations is particularly important in early solar system

(ESS) chronology, because (i) it took less than 10 Myr from the condensation of the Calcium, Aluminum-rich inclusions (CAIs: the first solids in the solar nebula) to the differentiation of asteroids (Connelly et al. 2017), (ii) the Pb–Pb system is the only high-precision absolute chronometer for such ancient ages, and (iii) small variations in ^{238}U/^{235}U results in relatively significant age offsets (∼0.15 Myr offset per 0.1‰ variation, Tissot and Dauphas 2015) compared to the achievable precision of Pb–Pb ages (∼0.2–0.5 Myr). Together with the long-lasting search for the short-lived radionuclide ^{247}Cm (Section 3.5.2.6), this has led to a wide characterization of U isotopes in extraterrestrial materials (**Fig. 3.14**), from bulk meteorites, including carbonaceous chondrite, ordinary chondrite, enstatite chondrite, achondrites (*e.g.,* angrite, acapulcoite, aubrite, eucrite, and howardite), and ungrouped meteorites (Amelin et al. 2010, 2011; Andersen et al. 2015; Bouvier et al. 2011a; Brennecka and Wadhwa 2012; Connelly et al. 2012; Goldmann et al. 2015; Iizuka et al. 2014; Larsen et al. 2011; Spivak-Birndorf et al. 2015; Stirling et al. 2005; Tissot et al. 2017), to meteorite components, such as CAIs, chondrules, mineral separates, and meteorite leachates (Amelin et al. 2010; Bollard et al. 2017; Bouvier et al. 2011a; Brennecka et al. 2010a; Brennecka and Wadhwa 2012; Brennecka et al. 2015; Connelly et al. 2012; Goldmann et al. 2015; Merle et al. 2020; Shollenberger et al. 2019; Stirling et al. 2006; Tissot et al. 2016). While variability can be resolved in most of these samples at the 0.1 to 0.5 ‰, the largest variations are observed in CAIs, with ^{235}U excesses reaching several ‰ (up to +59‰ in the Curious Marie CAI). The U-corrected Pb–Pb ages produced in some of these studies continue to refine the chronology and evolution history of the ESS, for instance establishing the age of the Solar System at ∼ 4.567–4.568 Gyr old (Amelin et al. 2010; Bouvier and Wadhwa 2010; Bouvier et al. 2011a; Connelly et al. 2012), and demonstrating that chondrule formation and reprocessing started contemporaneously with CAI formation and extended for ∼ 4 Myr after that (Bollard et al. 2017). In details, however, slight discrepancies between U-corrected Pb–Pb ages and chronometric constraints derived from short-lived chronometers, in particular the Al–Mg system, are the subject of much debate. Indeed, when combined U-Pb and Al–Mg isotopic investigations are conducted on the same CAI and chondrule samples, lower ESS ^{26}Al initials are recorded in chondrules than CAIs, and variable ^{26}Al initials are derived from different chondrules (Bollard et al. 2019). Understanding whether these variations (i) represent a true heterogeneous distribution of ^{26}Al in the ESS, (ii) have chronometric meaning, (iii) are the results of small systematic analytical biases (*e.g.,* isotopic fractionation during sample step leaching), or (iv) are a combination of the above, is a topic of intense research. Another issue in extraterrestrial samples is that the U isotope composition of some meteorite groups are not well-constrained, such as enstatite chondrites, howardites, acapulcoites, or aubrites (**Fig. 3.14**), and investigations on meteorite components are also limited to a few meteorites, primarily from the CV group.

Relevant to both extraterrestrial and terrestrial studies, ^{238}U/^{235}U variations also exist in the U-bearing minerals commonly used in U–Pb/Pb–Pb chronology, such as zircon, uraninite, apatite, monazite, xenotime, and baddeleyite (Hiess et al. 2012; Livermore et al. 2018). For zircon, the most widely used dating phase, variations have been observed in pooled fractions (100s to 1000s) of comagmatic grains (Hiess et al. 2012; Livermore et al. 2018) as well as in single crystals (Tissot et al. 2019a). Recently, variations from -3.5 ± 2.2 ‰ to 13.1 ± 3.4 ‰ have also been reported in single grains of titanite using LA-MC-ICP-MS and 1013 ohm amplifiers (Yamamoto et al. 2021). As discussed in Tissot and Ibañez-Mejia (2021), while these data clearly indicate the existence of significant mineral specific U isotope fractionations and, more likely for the largest effects, of kinetic isotope fractionations occurring at magmatic temperatures, the exact mecanisms driving U isotope fractionation in magmatic settings remain almost entirely unconstrained.

3.5.2.6 Search for ^{247}Cm

Curium-247 is short-lived radionuclide which decays into ^{235}U, with a half-life of 15.6 Myr (Tuli et al. 1995). Both U and Cm belong to the actinides, a group of heavy metal elements produced by the rapid neutron capture process (r-process), most likely during neutron-star merger events (Côté et al. 2021; Ji et al. 2016). If ^{247}Cm was present in the early solar system, the ^{247}Cm–^{235}U system would have the potential to serve as a short-lived r-process chronometer (Blake and Schramm 1973). Since ^{247}Cm is now extinct, the only evidence for the presence of live ^{247}Cm in the ESS would be ^{235}U excesses correlated with Cm/U ratios in ESS materials. An additional complication is that Cm has no stable isotope, and a proxy has to be used, most appropriately Nd (see Tissot et al. 2016 for details).

The findings of early investigations on ^{247}Cm are controversial due to analytical limitations: ^{235}U excesses or depletion up to several tens of percent were reported in meteorites, refractory inclusions and leachates (Arden 1977; Tatsumoto and Shimamura 1980). Follow up studies leveraging the “Lunatic I" digital TIMS and the double spike technique showed that lunar and meteoritic materials (and their inclusions) had no excess ^{235}U, within uncertainties, relative to the Earth (Chen 1988; Chen and Wasserburg 1981a,b,c). The search for the existence of ^{247}Cm ceased for approximately two decades, and only restarted after the advent of MC-ICP-MS, which achieved 1–2 orders of magnitude higher precision. Stirling et al. (2005, 2006) revisited the U isotopic compositions of bulk meteorites, mineral separates, and meteorite leachates. These initial searches did not find any well-resolved ^{235}U anomalies, but brought down the upper limit on the ESS ^{247}Cm/^{235}U ratio from ~4x10-3 (Chen and Wasserburg 1981a) to ~8×10^{-5}. In an investigation of CAIs, Brennecka et al. (2010a) found ^{235}U anomalies (up to ~3.5 permil) that correlated broadly with Nd/U and Th/U ratios. This study brought the first evidence of live ^{247}Cm in the ESS, suggesting an ESS ^{247}Cm/^{235}U ratio of (1.2 to 2.4)×10^{-4}. But the origin of these isotopic signatures was rapidly questioned as subsequent studies of CAIs found departure from the apparent correlation between ^{235}U excess and Nd/U ratios (Amelin et al. 2010; Connelly et al. 2012), and instead argued that the observed variations reflected mass-dependent fractionation during condensation of solid CAIs from nebular gas. By targeting fine-grained CAIs, which, due to their volatility-controlled origin, have large Nd/U (and thus Cm/U) ratios, Tissot et al. (2016) was able to find an extremely U-depleted CAI, Curious Marie, which also contained a ^{235}U excess (of +59‰) outside the range plausibly explained by evaporation/condensation processes. While more samples would be desirable to populate what is currently essentially a two-points isochron, the discovery of Curious Marie confirmed the presence of live ^{247}Cm in the ESS, with an initial ^{247}Cm/^{235}U of (5.6 ± 0.3)×10^{-5} (Tang et al. 2017; Tissot et al. 2016), a value that has become a key constraint to determine the astrophysical site of the r-process, and the timing of last injection of r-nuclides in the solar system's parental molecular cloud (Côté et al. 2021; Ji et al. 2016).

3.5.2.7 Experimental studies

NFS, as a mass-independent but volume-dependent effect, prompted a rethinking of equilibrium fractionation theory (Bigeleisen 1996; Knyazev and Myasoedov 2001; Schauble 2007; Yang and Liu 2016). As mass-dependent fractionation decreases with increasing mass, and NFS effects increase with electron density at the nucleus, NFS effects are most pronounced in heavy elements (*i.e.,* with large nuclei). Today, it is well accepted that NFS effects are the dominant driver of U isotope fractionations in natural materials. Indeed, NFS effect during U redox reactions at room temperature are 3× larger than mass-dependent effects (Abe et al. 2008; Bigeleisen 1996; Schauble 2007). Furthermore, while mass-dependent fractionation scales proportionally to 1/T^2, NFS effects scale as 1/T, which implies that their relative contribution to the total isotope fractionation increases in high-T (*e.g.,* igneous) environments, an observation supporting the potential of U isotopes as redox tracers in magmatic environments (Tissot and Ibañez-Mejia 2021). It is important to point out that NFS effects are equilibrium effects, and that it is not the reduction of U itself that promotes the isotopic fractionation, but the equilibration between oxidized and reduced U that allows the expression of these effects (see next section).

Redox experiments

Laboratory-based experiments are important approaches for quantifying the U fractionation associated with specific reaction pathways or environmental conditions. For U, redox reactions have been heavily studied, because of their potential for (i) understanding the role of redox transformation in U cycling near the Earth's surface and (ii) developing remediation methods to control contamination in aquifer systems.

Laboratory-controlled redox experiments have primarily focused on U reduction processes, which are further subdivided into biotic and abiotic reduction. There are two major pathways for U biotic reduction: those involving metal-reducing bacteria (Basu et al. 2014; Stylo et al. 2015b) and those involving sulfate-reducing bacteria (Basu et al. 2020; Dang et al. 2016; Rademacher et al. 2006; Stirling et al. 2015; Stylo et al. 2015a). Abiotically, U(VI) can be reduced by various natural reductants such as zerovalent metal, Fe(II)-based reductant, sulfide reductant, and reduced organic matter (Brown et al. 2018; Rademacher et al. 2006; Stirling et al. 2007; Stylo et al. 2015b). During biotic reduction, microbes preferentially incorporate ^{238}U and transfer it into the reduced phase, leading to a lower δ^{238}U (by ~-1‰) in the remaining U(VI) pool (Basu et al. 2014, 2020; Dang et al. 2016; Stirling et al. 2015; Stylo et al. 2015a,b). One early study reported slightly higher δ^{238}U (by ~+0.2 ‰) in the oxidized U phase during biotic reduction (Rademacher et al. 2006), but this result has since been revisited and attributed (by the same research group, Basu et al. 2014) to U(VI) adsorption onto the surface of bacteria cells overcompensating the U effect of reduction process during the U removal from the solution. In contrast, abiotic reduction experiments using zerovalent metals (Fe^0: Rademacher et al. 2006; Zn^0: Stirling et al. 2007) and organic species (peat: Stylo et al. 2015b) yielded no resolvable U isotopic fractionation. Adding to the initial confusion, most abiotic reduction reactions driven by Fe(II) and/or sulfide reductants, produced detectable U isotopic variations, but in the opposite direction of biotic reduction: ^{238}U is enriched in the remaining U(VI) pool (Stylo et al. 2015b). For a time, these results were interpreted as evidence that only biotic reduction results in significant NFS effects (*i.e.,* ^{238}U enrichments in the reduced phase), and the exciting possibility that U isotopes might be a specific tracer of bioreduction. This hypothesis was disproven by Brown et al. (2018), who showed that preferential sequestration of ^{238}U in the reduced U phases could occur even during abiotic reduction. This study was instrumental as it further showed that the seemingly conflicting literature results discussed above could be easily reconciled in a framework where ^{238}U/^{235}U fractionations reflects a balance between equilibrium (NFS) isotope effects and kinetic isotope fractionation. Indeed, during fast U removal, isotope fractionations are driven by kinetic (mass-dependent) effect, favoring precipitation in the reduced phase of the lighter ^{235}U isotope. In contrast, the expression of full blown NFS effects, with ^{238}U being enriched in the reduced phase, are only possible when U removal from the solution is slow enough that U(VI)-U(IV) isotope equilibration has time to take place. Because the pace of U removal (*i.e.,* reaction rate) is tied to the speciation of aqueous U, which itself depends on the water chemistry, this study also further supported the conclusion of Chen et al. (2017) that the fractionation factor associated with reductive U removal from the ocean (Δreduced-seawater) would likely change over geological times, as a function of the Ca/Mg, pCO_2, and pH of seawater.

In comparison to U reduction, there has been very little research done on U isotopic fractionation during U oxidation. Wang et al. (2015a) used dissolved oxygen to oxidize U(IV) and found a very limited enrichment of ^{238}U in the remaining reduced phase, likely due to a rind effect limiting the development of large isotope fractionations.

Well injection

Uranium contamination of groundwater and sediments during the mining and processing of U ores is a major public health concern and developing in-situ remediation techniques is the target of many environmental studies (Wall and Krumholz 2006). The main approach to mitigate U pollution and decrease [U] in the groundwater is to immobilize aqueous U as a solid phase in the aquifer by changing its mobility (*e.g.,* Ginder-Vogel et al. 2006; Hyun et al. 2009). Since the mobility of U is controlled by its oxidation state and aqueous speciation, the two main methods of U immobilization revolve around the injection of amended groundwater in contaminated sites that promotes either (i) reduction of soluble U(VI) to insoluble U(IV), or (ii) adsorption to the walls of the aquifer through changes in U(VI) speciation.

While the determination of U concentrations is the most common and straightforward approach for monitoring the efficiency of U-contamination remediation methods, it often cannot be used to identify the geochemical processes at play in the aquifer (Jemison et al. 2018). Being able to confirm that the low groundwater U concentrations are the results of the implemented remediation method (reduction vs adsorption) and not some other, non-controlled, parameter is crucial. Uranium isotope variations have emerged as a promising new tool to fingerprint these processes, inspired by the potential revealed by laboratory studies on U isotopic fractionation (Basu et al. 2014; Dang et al. 2016; Rademacher et al. 2006; Stylo et al. 2015a; Wang et al. 2015a,b). In line with the early findings of Brennecka et al. (2011b), recent field studies show that only limited $^{238}U/^{235}U$ fractionation is observed during the adsorption-desorption treatment, with ^{235}U being preferentially removed from solution ($\Delta_{\text{adsorbed–aqueous}}$ ~0 to -0.22 ‰, Dang et al. 2016; Jemison et al. 2016; Shiel et al. 2013). On the contrary, bioremediations that take advantage of metal-reducing bacteria lead to large and clearly resolvable fractionations of opposite direction ($\Delta_{\text{reduced-aqueous}}$ ~+0.5 to +1.0

‰; Bopp et al. 2010; Shiel et al. 2016), consistent with the permil effects observed in postmining natural reduction settings (Basu et al. 2015; Brown et al. 2016; Placzek et al. 2016). In a recent oxidation experiment designed to simulate the natural remobilization through U oxidation after remediation, Jemison et al. (2018) showed that a significant δ^{238}U change was observed, supporting the adequacy of using U isotopes as a monitor of natural redox reactions at mining sites. This conclusion is strengthened by recent reactive transport modeling efforts, which demonstrated that incorporating δ^{238}U data in the model allows for better interpretation of chemical reactions and groundwater transport processes influencing U cycling (Jemison et al. 2020).

Other experimental studies

In addition to redox reactions, lab-controlled experiments have investigated U isotopic fractionation during adsorption, coprecipitation, complexation, weathering, and biotic uptake. U(VI) adsorption onto Mn-oxyhydroxides (birnessite, Brennecka et al. 2011b) and Fe-hydroxides (goethite, Dang et al. 2016) under oxic conditions preferentially incorporate ^{235}U into adsorbed phases ($\Delta_{\text{adsorbed–aqueous}}$ ~-0.20 ‰). Similarly, nonreductive U uptake by freshwater plankton also enriches lighter U isotopes in the biomass ($\Delta_{\text{plankton–aqueous}}$ ~-0.23 ‰, Chen et al. 2020). As partly discussed above, the aqueous speciation of U, and thus the water chemistry and pH, as well as the nature of the mineral phase (*e.g.,* calcite vs aragonite) were also shown experimentally to influence the degree of isotope fractionation observed in carbonates (Brown et al. 2018; Chen et al. 2016, 2017).

A study investigating U(IV)-U(VI) exchange under near natural aqueous conditions also observed ^{235}U enrichment in U(VI) ($\Delta_{\text{U(VI)–U(IV)}}$ ~-1.64 ‰, Wang et al. 2015b), slightly larger than, but still broadly consistent with, the ~1.2–1.3 ‰ effects expected from NFS. Under anoxic conditions, a recent study showed that U(IV) can be remobilized by ligands in the near-surface environment, resulting in ^{238}U concentrating in mobilized materials, potentially complicating remediation monitoring or paleo-redox reconstructions (Roebbert et al. 2021).

A few leaching experiments have also been conducted to try to evaluate the influence of weathering and alteration on U isotopic fractionation, as well as to ensure that the minerals used for age determination behave as closed system with regards to U isotopes. The impact of leaching on U isotope fractionation remains, however, unclear. While a systematic enrichment of ^{235}U was observed in the leachates from euxenite (Stirling et al. 2007) and zircon (Hiess et al. 2012), other studies on zircon (Livermore et al. 2018; Stirling et al. 2007) and uraninite (Stirling et al. 2007) found no systematic offset between the leachates and bulk analyses. While the ^{235}U enrichment in successive leaching steps of euxenite and zircon have been interpreted as evidence of the preferential release of weakly bound ^{235}U from the crystal lattice during leaching, these effects could also simply reflect equilibrium U isotope fractionation between the oxidized (soluble) U in the leachates and reduced (insoluble) U in the minerals. More controlled experiments are needed to understand the isotopic impact of leaching on minerals.

Assuming U removal during U reaction experiments can be described as a Rayleigh distillation process, the U isotopic fractionation can be described as:

$$\delta^{238}\text{U} = \left(\delta^{238}\text{U}_0 + 1000\right)\left[\frac{c(t)}{c_0}\right]^{(\alpha-1)} - 1000 \tag{3.29}$$

where $\delta^{238}\text{U}_0$ and c_0 are the initial isotopic composition and concentration of aqueous U; δ^{238}U and c(t) are the isotopic composition and concentration at the sampling time t; and α is the U isotopic fractionation factor. Eq. 3.29 can be rewritten in the following format:

$$ln\left(\delta^{238}\text{U}_0 + 1000\right) = (\alpha - 1)ln\left[\frac{c(t)}{c_0}\right] + ln\left(\delta^{238}\text{U}_0 + 1000\right) \tag{3.30}$$

The α value can be determined by the slope of the linear regression between ln(δ^{238}U + 1000) and ln[c(t)/c_0]. Furthermore, in the case of a first-order reaction, the concentration and reaction time are related by the following equation:

$$ln\left[\frac{c(t)}{c_0}\right] = -kt \tag{3.31}$$

where k is the first-order rate constant, which can be obtained by linear fit between ln[c(t)/c_0] and time. The half-life ($\text{t}_{1/2}$) is expressed as:

$$t_{1/2} = \frac{ln(2)}{k} \tag{3.32}$$

Brown et al. (2018) investigated the relationship between the fractionation factor, α, and the aqueous U(VI) half-life in a series of abiotic reduction. This relationship revealed how the degree of U isotopic fractionation relates to the U removal rate. Using the UID, we expanded this framework to more U removal reactions (**Fig. 3.15**), including biotic and abiotic reduction, oxidation, complexation with ligand, biotic U uptake, and U coprecipitation with other mineral phases (Basu et al. 2014, 2020; Brown et al. 2018; Chen et al. 2016; Roebbert et al. 2021; Stylo et al. 2015a,b; Wang et al. 2015a). Only the experiments with first-order reactions rates are included in Fig. 15. We find that most abiotic reduction experiments and some of the biotic reduction and oxidation experiments follow the α–$\text{t}_{1/2}$ relationship defined in Brown et al. (2018), with no experiments plotting significantly to the left of this relationship. This observation further supports the proposal by Brown et al. (2018) that when the aqueous U(VI) half-life is short, the extent of isotopic fractionation represents a balance between equilibrium isotope fractionation (in this case, the mass-independent NFS) and kinetic isotope fractionation. Brown et al. (2018) further hypothesized the necessary half-life to achieve the predicted NFS fractionation of ~1.2 ‰ is ~65 hr. The plateau in isotope fractionation factors observed at ~1‰ in biotic reduction experiments with long aqueous U(VI) half-lives supports this proposal. It also reveals that the theoretical maximum NFS effects (~1.2 ‰, Bigeleisen 1996) is not expressed in any of the currently available experiments, indicating (i) that complete equilibrium between U(VI) and U(IV) is never attained, and/or (ii) in all experiments, another process imparts a small (~0.2‰) negative isotope fractionation. The same mechanism is likely to explain the similar offest to lower fractionation factors that is observed in many of the biotic reduction experiments with aqueous U(VI) half-life lower than 65 hr. More work is needed to further undertsand these effects.

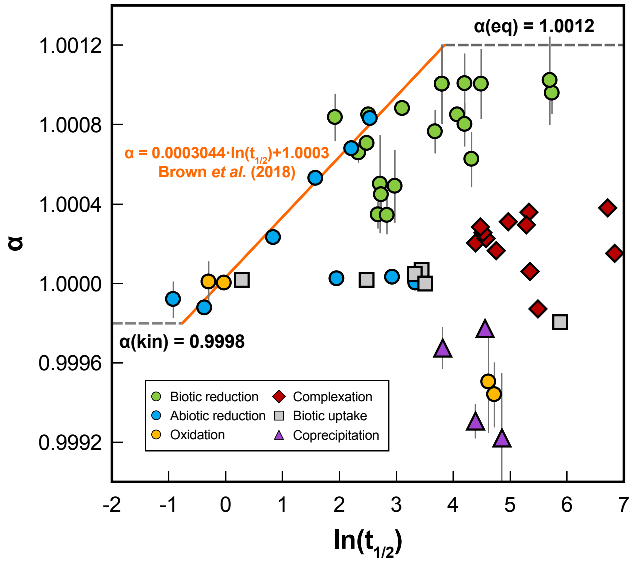

Figure 3.15: Relationship between the isotope fractionation factor (α) and half-life of aqueous U(VI) ($t_{1/2}$, in hours) for various U removal reactions. When available, fractionation factors and half-lives are plotted as reported in the original publication. Otherwise, α and $t_{1/2}$ are calculated based on Eqs. 3.29–3.32. The orange line represents the best fit between α and $t_{1/2}$ from a series of abiotic uranium reductions defined in Brown et al. (2018). The grey dash lines show the limit of kinetic fractionation (0.9998) and equilibrium fractionation (1.0012), respectively.

In clear contrast to the redox experiments, other U removal reactions are characterized by small, negigible or negative isotopic fractionations. This indicates that for these reactions, NFS effects are not the dominant driver of isotope fractionation. Instead, and as previous work have proposed, the fractionation factors retrieved from complexation, coprecipitation, and biotic uptake must reflect a stong control of vibrational mass-dependent effects (*e.g.*, during U adsorption) and/or kinetic effects, which both tend to enrich the product of the reaction in the lighter isotopes.

3.5.2.8 Forensic studies

Natural nuclear fission reactor

Under the right conditions, U-rich deposits formed before ∼1.8 Ga, when natural ^{235}U abundance was >∼3%, could have reached criticality. The only location where such sustained spontaneous fission chain reactions are known to have naturally occurred is in the mine of Oklo, in the Republic of Gabon. These reactors are a series of sandstone-hosted U ore deposits discovered in the 1970's near Oklo and Bangombè, where natural fission events occurred at ∼ 1.78 Ga (Bodu et al. 1972; Neuilly et al. 1972; Roth 1977). Compared with other types of U deposits (see Section 3.5.2.4), natural nuclear reactors display unusually high ^{238}U/^{235}U ratios due to ^{235}U burn-up during self-sustained fission. As a result, U isotopic compositions in Oklo's bulk ore samples or their mineral components are widely used to examine nuclear fission activities (Bros et al. 1993, 1996; Bros et al. 2003; Curtis et al. 1989; De Laeter et al. 1980; Fernández-Dıaz et al. 2000; Gauthier-Lafaye et al. 1996; Hidaka and Holliger 1998; Hidaka et al. 1999; Hidaka and Gauthier-Lafaye 2000; Holliger and Devillers 1981; Horie et al. 2004; Kikuchi and Hidaka 2009; Lancelot et al. 1975; Loss et al. 1989). Natural fission reactors are important for assessing the long-term effects of nuclear waste disposal in geological settings because they are considered as analogues of disposal sites to understand the behavior of radionuclides in natural environment over geological timescales. Hence, numerous isotopic investigations have studied the presence and migration of fissiogenic radionuclides in Oklo's natural nuclear reactors (*e.g.,* Mo, Ru, Pd, Ag, Cd, Sn, Te, Cs, Ba, Tc, Rh and rare earth elements, Gauthier-Lafaye et al. 1996).

Health physics

Depleted uranium, which is predominantly a by-product of nuclear enrichment efforts, has numerous civilian and military applications, including in aeronautics, the shipbuilding industry, radiological protection, chemical manufacturing and armor-piercing ammunitions, due to its high density, hardness, and melting point (Bleise et al. 2003). Internal exposure to DU is a major health concern in humans, especially soldiers, who can be exposed to DU via inhalation of airborne particles from weapon combustion, ingestion of contaminated food and water, penetration by embedded shrapnel, and/or contact on wounds (Bleise et al. 2003). Given that DU has a U isotopic composition significantly different from that of NU (*i.e.,* it is depleted in ^{234}U and ^{235}U), isotopic compositions of urine or blood can be effective diagnostic tools for tracing the source of U exposure. U in urine is the primary focus of isotopic studies on DU exposure since it has historically been used in biomonitoring (Duarte and Szeles 1994; Ejnik et al. 2005; Ejnik et al. 2000; Gray et al. 2012; Gwiazda et al. 2004; Horan et al. 2002; Krystek and Ritsema 2002; Pappas et al. 2003; Parrish et al. 2006; Xiao et al. 2014), while only a few pioneering studies have investigated U isotopes in blood specimen (Todorov et al. 2009; Tolmachyov et al. 2004). These studies successfully identified DU exposure in patients by detecting lower ^{235}U/^{238}U ratios urine or blood samples than NU.

Nuclear contamination

U isotopes are a useful tool for tracking environmental contaminations produced by anthropogenic nuclear activities such as weapon explosions, power plant accidents, and other contaminations associated with mining or nuclear fuel processing.

Military contamination can cause ^{238}U/^{235}U ratios in environmental samples to fluctuate in opposing directions depending on the source of contamination. Contamination from DU munitions causes higher ^{238}U/^{235}U ratios in war-zone soils or sediments (Al.-Zamel et al. 2005; Boulyga et al. 2001; Danesi et al. 2003a,b; Lloyd et al. 2009). Nuclear weapons and related tests, on the other hand, employed enriched uranium, resulting in lower ^{238}U/^{235}U ratios in atmospheric deposits or fallouts (Fujikawa et al. 2003; Kikawada et al. 2015; Lewis et al. 2015; Taylor et al. 1998). Establishing full records of ^{238}U/^{235}U in environmental samples over time is thus an efficient method for investigating the existence, sources, or transit of radioactive contamination (Warneke et al. 2002).

Forensic investigations into power plant accidents have focused on the two most catastrophic nuclear energy disasters: the 1986 Chernobyl nuclear power plant accident (Barescut et al. 2009; Boulyga et al. 2000; Boulyga and Becker 2001, 2002; Boulyga and Prohaska 2008; Pazukhin and Rudya 2002; Pöml et al. 2013; Sahoo et al. 2002, 2004; Sobotovich and Bondarenko 2001) and the 2011 Fukushima Daiichi nuclear power plant accident (Mishra et al. 2019; Shibahara et al. 2016; Veerasamy et al. 2020). Direct measurement of the nuclear fuel from power plant accident reveals enrichment in ^{235}U versus NU (Pöml et al. 2013). When fallout radionuclides from power plants migrated and deposited in neighboring regions, soil samples from polluted areas inherited lower ^{238}U/^{235}U ratios than NU (Barescut et al. 2009; Boulyga et al. 2000; Boulyga and Becker 2001, 2002; Boulyga and Prohaska 2008; Pazukhin and Rudya 2002; Sahoo et al. 2002, 2004; Sobotovich and Bondarenko 2001), while those that avoided contamination from the accidents preserved indistinguishable ^{238}U/^{235}U compositions relative to NU (Mishra et al. 2019; Shibahara et al. 2016; Veerasamy et al. 2020).

Other nuclear contamination studies are based on the same principle of detecting anomalous ^{238}U/^{235}U in sedimentary or water samples near nuclear facilities that produce and process EU (Christensen et al. 2004; Hamilton and Stevens 1985; Howe et al. 2002; Meyers et al. 2014; Rodríguez-Alvarez and Sanchez 1995; Sahoo et al. 2002;

Yamamoto et al. 2002). And similar investigations have been conducted near mines (Awudu and Darko 2011) or river systems (Joshi et al. 1983) that were potentially contaminated by radionuclides.

Nuclear safeguard

The rapid and precise isotopic characterization of particulate uranium materials is critical for nuclear safeguard applications, such as identifying illicit radioactive material trafficking and detecting the usage of unapproved nuclear materials in nuclear facilities. In-situ characterization of solid nuclear samples is a useful approach for determining the presence and provenance of nuclear materials because U particles have distinct U isotopic fingerprints that are influenced by source materials and manufacturing procedures (Betti et al. 1999; Claverie et al. 2016; Hubert et al. 2014; Kips et al. 2019; Krachler et al. 2018; Marin et al. 2013b; Ronzani et al. 2019; Stebelkov et al. 2018; Tamborini 2004; Varga et al. 2018; Varga 2008; Yomogida et al. 2017). Aside from direct measurement of U particles (Betti et al. 1999; Hubert et al. 2014; Ronzani et al. 2019; Varga 2008; Yomogida et al. 2017), fuel pellets (Kips et al. 2019; Krachler et al. 2018) and confiscated illicit U samples (Krachler et al. 2018), some of the nuclear safeguard studies have developed techniques to discover U particles in the mixture of other materials in swipe samples from the environment (Tamborini 2004) or the surface of nuclear packaging materials (Stebelkov et al. 2018), as a means to identify and prevent undeclared nuclear activities without time-consuming procedures.

3.6 Conclusions

This work introduces the UID, a comprehensive, freely accessible, updatable, and internally consistent uranium isotope database. At this writing, the UID contains more than 14,000 data points from approximately 320 publications. We provided a detailed description of our data collection procedure, all additional information entered in the UID, and their coverage as well as the normalization procedure carried out on the data. We took the highest care to make all data coherent, comparable, and back trackable, as well as all adjustments transparent. Adequate metadata are also provided to allow users to select data that are suitable for a particular type of study. The UID will be regularly updated to incorporate newly published uranium isotopes data. With constructive feedback from the community, we expect that the UID can become a reliable resource for the U isotope community, as well as the broader geochemical community.

In the long-term, we hope to see the UID grow from the simple database presented here into a more extensive tool. This includes the development of an online and interactive searchable database with built-in visualization capabilities, as well as a streamlined protocol for data submission, review, and incorporation into the UID. With constructive feedback and involvement from the community, we expect that the UID can become a more community-involved resource, maintained for and by the community, and whose impact will reach far into the broader geochemical community.

Chapter 4

URANIUM ISOTOPES AS A PALEO-REDOX PROXY: EXPLORE NEW ARCHIVE AND CALIBRATE SEAWATER COMPOSITION

Part of this chapter has been published in:

Li, H., Kipp, M.A., Kim, S.L., Kast, E.R., Eberle, J.J., and Tissot, F.L.H. (2024). Exploring uranium isotopes in shark teeth as a paleo-redox proxy. *Geochimica et Cosmochimica Acta* **365**, 158–173

Kipp, M.A., **Li, H.**, Ellwood, M.J., John, S.G., Middag, R., Adkins, J.F., and Tissot, F.L.H. (2022). ^{238}U, ^{235}U and ^{234}U in seawater and deep-sea corals: A high-precision reappraisal. *Geochimica et Cosmochimica Acta* **336**, 231–248

Reconstructing the oceanic redox history is fundamental to understanding the evolution of the Earth's surface conditions and its interconnection with the appearance and evolution of life. In the past decade, U isotopes have received considerable attention as a paleoredox proxy of marine/seafloor anoxia. Carbonate sediments are the most popular archive used in such reconstructions as they are abundant in the geologic record, contain ample U, and tend to record the seawater δ^{238}U signature upon precipitation. The utility of the U isotope proxy in carbonate archives relies on this faithful archiving of ambient seawater signatures. However, carbonates are subject to syndepositional and post-depositional diagenetic alterations, which can overprint the original δ^{238}U signatures, posing a significant challenge for this archive (Chen et al. 2018b; Livermore et al. 2020; Romaniello et al. 2013; Tissot et al. 2018. This diagenetic overprinting complicates quantitative paleoredox reconstructions (Kipp and Tissot 2022), undermining the utility of carbonates as a U isotope archive. The shortcoming of carbonates raises the need to seek alternative archives, which are more resistant to secondary alterations. While such diagenetic modifications also commonly exist in bioapatite, shark teeth enameloid is nevertheless thought to be more resistant to post-depositional alteration than carbonate. To address this issue, the first part of this chapter explores the potential of shark teeth as a novel archive of seawater δ^{238}U, leveraging the diagenetic stability of apatite over carbonate. The usefulness of the U isotopes as a global redox indicator also requires the assumption of the homogeneity of the seawater U isotope composition, which enables samples to be leveraged as the entire ocean. To further justify this important assumption, the second part of this chapter re-calibrated the U isotope composition of the seawater based on the measurements of multiple sites from the Pacific and Atlantic.

4.1 Exploring uranium isotopes in shark teeth as a paleo-redox proxy

4.1.1 Motivation

Biogenic phosphates are regarded as a valuable geochemical archive offering insight into a wide range of paleoceanographic conditions and processes, such as temperature, salinity, and water mass circulation (*e.g.,* Fischer et al. 2013; Huck et al. 2016; Kohn and Cerling 2002; Kolodny et al. 1983; Longinelli 1966; Martin and Scher 2004; Ounis et al. 2008; Reynard et al. 1999). Shark teeth are among the most extensively studied marine biogenic phosphates due to their ability to record and retain geochemical signatures on geological timescales. Sharks have existed on Earth for over 400 Myr, and the oldest shark fossils date from the early Devonian (Miller et al. 2003), with continuous records to the present and wide spatial distribution (Ginter et al. 2010). Because sharks are Chondrichthyes (cartilaginous fish), shark skeletons largely decompose before fossilization, making shark teeth their most abundant fossil record. With lifelong continuous tooth replacement, sharks can produce thousands of teeth throughout their lifetime (Botella et al. 2009). Once shark teeth are lost from their bodies, they interact with ambient water and incorporate elements from the surrounding environment. Due to the rapid mineralization process on daily to weekly timescales, shark teeth can even capture local geochemical snapshots of the sites where they formed (Dera et al. 2009; Fischer et al. 2012; Kim et al. 2014, 2020; Kocsis et al. 2009; Kolodny et al. 1991; Lécuyer et al. 2003; Martin and Scher 2004; Picard et al. 1998; Pucéat et al. 2003; Vennemann et al. 2001).

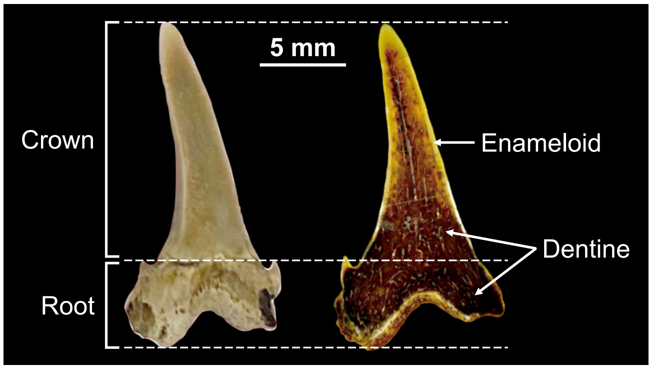

Figure 4.1: Histology of shark tooth. Photo (left) and transmitted light microscope image of polished cross section (right) of a *Striatolamia macrota* shark tooth from the Banks Island in the Arctic. Enameloid forms a thin translucent layer covering the crown, while dentine forms the crown base and the root of the tooth. The junction between enameloid and dentine is clear, and the dentine is more porous than enameloid.

Shark teeth enameloid tissues are primarily composed of fluorapatite (Enax et al. 2012), a calcium phosphate with extremely low solubility (Moreno et al. 1974), making them more resistant to post-depositional alterations than other popular paleoceanographic archives such as carbonates (Iacumin et al. 1996; Kolodny et al. 1983;

Kolodny and Raab 1988; Lécuyer et al. 2013; Shemesh et al. 1983; Zazzo et al. 2004b). Shark teeth are composed of two types of tissue (**Fig. 4.1**): enameloid (enamel-like outer layer) and dentine (mineralized but organic-rich inner core). Enameloid is considered to be a more robust archive for geochemical proxies because of its higher apatite content, fluorapatite mineralogy, lower water and organic matter content, and more compact structure with larger phosphate crystallites (Enax et al. 2012; Kohn et al. 1999; Kohn and Cerling 2002; Sharp et al. 2000; Zazzo et al. 2004a). These characteristics have led to the successful application of geochemical tracers in shark teeth to understand paleo-environmental conditions and the behavior of sharks.

Several isotopic tracers have been well-studied in the enameloid of shark teeth. Oxygen isotopes are the most widely-studied system, being frequently used to track paleotemperature and paleosalinity (Dera et al. 2009; Fischer et al. 2012, 2013; Hättig et al. 2019; Kim et al. 2014, 2020; Kocsis et al. 2009, 2014; Kolodny and Raab 1988; Kolodny et al. 1991; Lécuyer et al. 1993, 2003; Ounis et al. 2008; Picard et al. 1998; Pucéat et al. 2003; Sharp et al. 2000; Vennemann and Hegner 1998; Vennemann et al. 2001). Strontium isotopes are used for chemostratigraphic dating of shark teeth, as well as for understanding freshwater or brackish habitat preference and migration history (Barrat et al. 2000; Becker et al. 2008; Bosio et al. 2020; Fischer et al. 2012, 2013; Kocsis et al. 2007, 2009, 2013; Martin and Haley 2000; Schmitz et al. 1991, 1997; Tütken et al. 2020; Vennemann and Hegner 1998; Vennemann et al. 2001). Additionally, the neodymium isotope composition of shark teeth is extensively used as a paleocirculation tracer (Huck et al. 2016; Kim et al. 2020; Kocsis et al. 2007, 2009; Martin and Haley 2000; Shaw and Wasserburg 1985; Vennemann and Hegner 1998; Vennemann et al. 2001). These broad applications of shark teeth motivated our exploration of this archive to track the extent of marine anoxia in deep time.

The redox history of surface environments is of interest in paleoenvironmental studies because of its cause-effect relationships with the evolution of life on Earth. In recent years, uranium (U) isotopes (^{238}U/^{235}U, expressed in delta notation as (δ^{238}U) have become one of the most powerful quantitative tools for reconstructing marine redox variations (*e.g.,* Zhang et al. 2020c, and references therein). U has two oxidation states in the terrestrial surface environment: insoluble U(IV) and soluble U(VI) (Langmuir 1978). The U input to the ocean is dominated by riverine U(VI) input from weathering, which is isotopically indistinguishable from continental crust (δ^{238}U = -0.29 ± 0.03 ‰, Andersen et al. 2016; Tissot and Dauphas 2015). In anoxic/euxinic settings, U(VI) is efficiently removed from the water column via reductive precipitation as U(IV) in uraninite by abiotic and/or biotic reductions (Langmuir 1978). During the U(VI) removal processes, ^{238}U (relative to ^{235}U) is preferentially incorporated into the sediments (Andersen et al. 2017). As a result, in periods of expanded marine anoxia the rate of U burial increases, causing seawater to shift toward lower U concentration and δ^{238}U value.

Importantly, U isotopes are considered a proxy for the global extent of marine anoxia. In the well-oxygenated modern ocean, the long residence time of U (τ ~400 kyr, Dunk et al. 2002; Ku et al. 1977), much longer than global ocean mixing time (~1 kyr, Broecker and Peng 1982) results in both homogeneous salinity-normalized concentration (~3.2 ng/g for a salinity of 35 g/L, Chen et al. 1986; Owens et al. 2011) and isotopic composition (δ^{238}U = -0.379 ± 0.023 ‰, Kipp et al. 2022; Tissot and Dauphas 2015). Thus, any geological archive that faithfully records the ambient seawater δ^{238}U value can be used to infer the global extent of marine anoxia in deep time.

Carbonate sediments are the most popular archive used in such reconstructions to-date as they are abundant in the geologic record, contain ample U, and tend to record the seawater δ^{238}U signature upon precipitation (Chen et al. 2016, 2018b; Kipp et al. 2022; Romaniello et al. 2013; Stirling et al. 2007; Tissot and Dauphas 2015; Tissot et al. 2018; Weyer et al. 2008). However, carbonates are subject to syndepositional and post-depositional diagenetic alterations, which can overprint the original δ^{238}U signatures, posing a significant challenge for this archive (Chen et al. 2018b; Livermore et al. 2020; Romaniello et al. 2013; Tissot et al. 2018. This diagenetic overprinting complicates quantitative paleoredox reconstructions (Kipp and Tissot 2022), undermining the utility of carbonates as a U isotope archive. While such diagenetic modifications also commonly exist in bioapatite (Toyoda and Tokonami 1990; Tütken et al. 2011, shark teeth enameloid is nevertheless thought to be more resistant to post-depositional alteration than carbonate (Zazzo et al. 2004a).

The objective of this study is to explore shark teeth as a novel archive of seawater δ^{238}U, leveraging the diagenetic stability of apatite over carbonate. We first report U isotope compositions of a variety of modern and fossil shark teeth (from both enameloid and dentine tissues) and the sediments in which they are embedded. Bulk U and Th concentrations, in-situ U concentration transition profiles, and phosphate δ^{18}O values are then used to understand the diagenetic history of these shark teeth and assess the corresponding implications for their promise as a seawater U isotope archive.

4.1.2 Methods

4.1.2.1 Geological settings and materials

In this work, 39 fossil shark teeth, 6 modern teeth, and 7 sediment samples were analyzed (**Table 4.1**). Fossil shark teeth were mainly selected from three locations: Banks Island, the Gulf of Mexico, and the Pisco Basin (called the Arctic, GOM, and Peru hereafter, respectively, **Fig. 4.2**). The Arctic shark teeth housed at the

Canadian Museum of Nature belong to *Striatolamia macrota*, and were recovered as float on unconsolidated sands in the Cyclic Member of the Eureka Sound Formation (Aulavik National Park, northern Banks Island, Northwest Territories, Canada, ca. 74° N, Padilla et al. 2014).

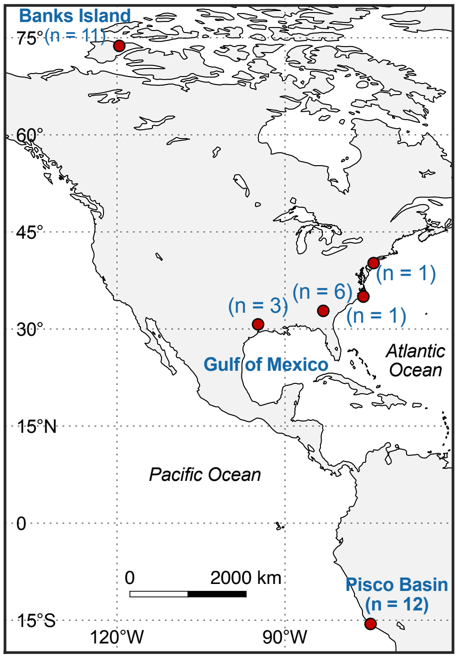

Figure 4.2: Map showing the localities of the fossil shark teeth and sediments used in this study. The samples are primarily from 3 locations: Banks Island (Arctic), the Gulf of Mexico (GOM), and Pisco Basin (Peru), with a few others scattered on the east coast of the US.

Shark teeth from this locality were deposited in a shallow coastal marine delta front environment (Miall 1979), with a stratigraphic age of early Eocene (ca. 51–53 Ma) based on palynology (Sweet 2012). The GOM shark teeth are *Carcharias hopei*, which were collected from the Eocene Jackson Group in Polk County, Texas, USA, and the late Eocene Clinchfield Formation in Gordon, Wilkinson County, Georgia, USA (specimens are from the Texas Vertebrate Paleontology Collection at the University of Texas, Austin). Peruvian shark teeth are from *Cosmopolitodus hastalis*, which were recovered as float on unconsolidated sandstone from the Pisco Formation in the Province of Caravelí, Peru, whose depositional environment is shallow marine spanning protected coastal to offshore shelf habitats (Ehret et al. 2012; Ochoa et al. 2021) with a stratigraphic age of Late Miocene. Prior work (Gothmann et al. 2019; Wang et al. 2016) has suggested that there was little change in the seawater δ^{238}U value over the Cenozoic, meaning well-preserved primary signatures should resemble the modern value. For modern shark teeth, the sources include collections from Gordon Hubbel and Lisa Natanson, purchase from eBay.

Table 4.1: Summary of locality, formation, age, U isotope compositions, U and Th concentrations, U/Th ratios, and O isotope composition of shark teeth and sediments measured in this study.

Sample	Locality	Formation	Age	δ^{238}U (‰)	95% CI	δ^{234}U (‰)	95% CI	U (ng)	n	[U] (ppm)	[Th] (ppm)	U/Th	δ^{18}O (‰)	±SD
Enameloid														
Banks Island (Arctic)														
2004-31-01	Banks Island, BC, Canada	Eureka	Eocene	-0.41	0.07	753.7	0.4	108	6	3.96	36.78	0.108	16.1	0.4
2004-31-02	Banks Island, BC, Canada	Eureka	Eocene	-0.38	0.05	444.2	0.5	162	9	10.25	53.12	0.193	11.6	0.6
2004-31-03	Banks Island, BC, Canada	Eureka	Eocene	-0.68	0.05	197.1	0.5	162	9	8.76	32.07	0.273	10.4	0.2
2004-31-04	Banks Island, BC, Canada	Eureka	Eocene	-0.56	0.05	226.4	0.5	162	9	17.50	63.63	0.275	10.4	0.2
2004-31-05	Banks Island, BC, Canada	Eureka	Eocene	-0.39	0.06	668.0	0.6	108	6	4.44	38.89	0.114		
2004-31-06	Banks Island, BC, Canada	Eureka	Eocene	-0.43	0.05	143.1	0.5	162	9	27.64	101.27	0.273	11.0	0.9
SLK2004-13-4	Banks Island, BC, Canada	Eureka	Eocene	-0.32	0.07	814.8	0.4	108	6	5.54	54.62	0.101	10.9	0.3
SLK2004-13-3	Banks Island, BC, Canada	Eureka	Eocene	-0.44	0.07	310.9	0.4	108	6	5.46	36.08	0.151	9.1	0.1
SLK2004-13-1	Banks Island, BC, Canada	Eureka	Eocene	-0.57	0.08	969.7	0.4	90	5	2.61	25.25	0.103	18.5	0.1
BKS04-19	Banks Island, BC, Canada	Eureka	Eocene	-0.66	0.11	925.3	1.0	36	2	2.16	15.49	0.139		
BKS2004-31	Banks Island, BC, Canada	Eureka	Eocene	-0.42	0.06	450.3	0.5	126	7	3.32	28.77	0.115		
Gulf of Mexico (GOM)														
TxVP 43390-2.102	Wilkinson Co., GA, USA	Clinchfield	late Eocene	0.03	0.07	-30.6	0.4	108	6	2.09	3.09	0.678	21.5	0.7
TxVP 43390-2.201	Wilkinson Co., GA, USA	Clinchfield	late Eocene	0.21	0.11	-40.0	0.5	54	3	320.30	50.09	6.394	21.5	0.5
TxVP 43390-2.85	Wilkinson Co., GA, USA	Clinchfield	late Eocene	0.17	0.07	-126.3	0.4	108	6	17.53	4.78	3.669	22.1	0.2
TxVP 43390-2.252	Wilkinson Co., GA, USA	Clinchfield	late Eocene	-0.04	0.06	-14.2	0.3	162	9	3.16	1.95	1.617	21.8	0.1
TxVP 43390-2.218	Wilkinson Co., GA, USA	Clinchfield	late Eocene	0.04	0.07	-133.8	0.4	108	6	6.87	3.31	2.077	21.8	0.2
TxVP 43390-2.235	Wilkinson Co., GA, USA	Clinchfield	late Eocene	0.27	0.07	-162.1	0.4	108	6	14.17	5.29	2.677	22.5	0.1
TxVP 40278-1-01	Polk Co., TX, USA	Jackson	Eocene	-0.44	0.06	243.5	0.3	198	11	11.60	15.51	0.748	19.5	0.3
TxVP 40278-1-02	Polk Co., TX, USA	Jackson	Eocene	0.50	0.05	-11.5	0.5	162	9	31.07	1.62	19.12	19.8	0.2
TxVP 40278-1-BB	Polk Co., TX, USA	Jackson	Eocene	-0.37	0.05	292.5	0.5	144	8	28.39	14.49	1.959	19.2	0.4
TxVP 45995-1-01	GA, USA	Clinchfield	late Eocene	0.27	0.11	-48.1	0.5	54	3	32.15	1.30	24.75	24.0	0.8
TxVP 45995-1-02	GA, USA	Clinchfield	late Eocene	-0.53	0.05	448.6	0.5	162	9	20.66	9.32	2.216	23.3	0.2
TxVP 45995-1-03	GA, USA	Clinchfield	late Eocene	0.57	0.05	-17.7	0.5	162	9	45.09	2.00	22.51	23.4	0.1
Pisco Basin (Peru)														
P1007-01	Bella Unión, Caravelí, Peru	Pisco	Late Miocene	-0.26	0.06	15.5	0.3	144	8	3.16	1.26	2.517	23.2	0.1
P1007-02	Bella Unión, Caravelí, Peru	Pisco	Late Miocene	-0.03	0.06	8.5	0.6	108	6	4.08	3.92	1.039	22.5	0.1
P1007-03	Bella Unión, Caravelí, Peru	Pisco	Late Miocene	-0.05	0.06	-4.5	0.6	108	6	4.72	8.21	0.574	22.2	0.1
P1007-04	Bella Unión, Caravelí, Peru	Pisco	Late Miocene	-0.72	0.09	151.4	0.8	54	3	2.56	0.43	6.002	20.2	0.5
LMS001-05	Bella Unión, Caravelí, Peru	Pisco	Late Miocene	-0.05	0.07	86.5	0.4	108	6	6.23	11.95	0.521		
LMS001-08	Bella Unión, Caravelí, Peru	Pisco	Late Miocene	-0.28	0.11	-16.1	0.5	54	3	67.32	4.08	16.50	21.2	0.1
JAH001-02	Bella Unión, Caravelí, Peru	Pisco	Late Miocene	-0.16	0.07	63.2	0.4	108	6	23.21	0.18	129.5	21.6	0.3
JAH001-03	Bella Unión, Caravelí, Peru	Pisco	Late Miocene	-0.23	0.07	517.7	0.4	108	6	3.82	0.02	160.5	22.3	0.5
SS001-04	Bella Unión, Caravelí, Peru	Pisco	Late Miocene	-0.41	0.13	44.9	0.7	36	2	1.22	1.39	0.882	21.0	0.4
SCM001-05	Bella Unión, Caravelí, Peru	Pisco	Late Miocene	-0.08	0.05	5.1	0.3	216	12	8.34	1.62	5.154	22.2	0.2
SCM001-06	Bella Unión, Caravelí, Peru	Pisco	Late Miocene	-0.04	0.07	-31.7	0.4	108	6	5.16	7.54	0.685	22.1	0.2

Table 4.1 continued from previous page

Sample	Locality	Formation	Age	δ^{238}U (‰)	95% CI	δ^{234}U (‰)	95% CI	U (ng)	n	[U] (ppm)	[Th] (ppm)	U/Th	δ^{18}O (‰)	±SD
CMTR001-04	Bella Unión, Caravelí, Peru	Pisco	Late Miocene	-0.29	0.11	-6.8	0.5	54	3	38.39	1.77	21.69	21.8	0.2
Other fossil teeth														
279414	Lee Creek Mine, NC, USA	Yorktown	Pliocene	-0.12	0.04	-84.6	0.2	82	7	16.60	0.02	689.1		
444242-2	Howell Park, NJ, USA	Kirkwood	Miocene	-0.52	0.04	26.6	0.8	23	2	1.23	0.08	15.13		
FT-2e	Ramenessin Brook, NJ, USA		Cretaceous*	-0.38	0.03	-1.1	0.2	105	9	59.70	2.33	25.67		
EK digest1	North Carolina, USA*		Pliocene*	-0.32	0.02	0.8	0.3	152	13	115.40	0.15	772.9		
EK digest2	North Carolina, USA*		Pliocene*	-0.32	0.02	0.9	0.3	140	12	105.50	0.14	780.7		
EK digest3	North Carolina, USA*		Pliocene*	-0.30	0.02	0.8	0.3	129	11	100.90	0.13	774.3	22.4	0.4
EK digest4	North Carolina, USA*		Pliocene*	-0.29	0.03	1.6	0.2	105	9	97.60	1.82	53.6	22.7	0.4
EK average				-0.31	0.01	1.2	0.1							
Dentine														
P1007-01	Bella Unión, Caravelí, Peru	Pisco	Late Miocene	-0.41	0.05	51.4	0.5	162	9	65.38	0.04	1839.1		
LMS001-08	Bella Unión, Caravelí, Peru	Pisco	Late Miocene	-0.29	0.05	-30.3	0.5	144	8	145.45	3.98	36.50		
SS001-04	Bella Unión, Caravelí, Peru	Pisco	Late Miocene	-0.37	0.05	180.3	0.5	144	8	106.10	0.62	171.0		
SCM001-06 Dc	Bella Unión, Caravelí, Peru	Pisco	Late Miocene	-0.20	0.05	-53.6	0.5	162	9	48.30	17.97	2.688		
SCM001-06 Dr	Bella Unión, Caravelí, Peru	Pisco	Late Miocene	-0.25	0.05	-71.5	0.5	144	8	149.85	42.81	3.500		
TMM40278-1-BB	Polk Co., TX, USA	Jackson	Eocene	-0.36	0.05	287.5	0.5	162	9	64.55	8.81	7.323		
Sediments														
BKS04-19_sed	Banks Island, BC, Canada	Eureka	Eocene	-0.56	0.04	101.1	0.3	288	16	1.71	1.67	1.023		
BKS2004-31_sed	Banks Island, BC, Canada	Eureka	Eocene	-0.27	0.04	-2.9	0.4	234	13	0.98	2.46	0.399		
JAH010_sed	Bella Unión, Caravelí, Peru	Pisco	Late Miocene	-0.24	0.04	128.1	0.3	306	17	2.50	5.67	0.441		
JBL002_sed	Bella Unión, Caravelí, Peru	Pisco	Late Miocene	1.38	0.04	457.8	0.3	306	17	13.51	4.56	2.965		
SS003_sed	Bella Unión, Caravelí, Peru	Pisco	Late Miocene	-0.45	0.04	142.2	0.3	306	17	3.36	1.47	2.296		
SCM002_sed	Bella Unión, Caravelí, Peru	Pisco	Late Miocene	-0.06	0.04	64.4	0.3	288	16	20.25	5.84	3.466		
P1002_sed	Bella Unión, Caravelí, Peru	Pisco	Late Miocene	-0.16	0.04	22.3	0.3	288	16	1.09	4.11	0.264		
Geostandard														
BCR-2 digest1				-0.21	0.05	-0.1	1.3	162	9					
BCR-2 digest2				-0.25	0.04	0.6	0.4	198	11					
BCR-2 digest3				-0.21	0.07	0.3	0.6	90	5					
BCR-2 digest4				-0.26	0.06	0.3	0.6	108	6					
BCR-2 digest5				-0.25	0.09	0.4	0.8	54	3					
BCR-2 average				-0.236	0.028	0.32	0.25							

The shark teeth investigated here show the same histology as described in previous literature, which consists of two tissues: enameloid and dentine (**Fig. 4.1**). The highly crystalline enameloid forms a thin compact outer layer covering the crown of the tooth, whereas the less crystalline and more porous dentine comprises the pulp cavity and the root structure of the shark tooth.

4.1.2.2 Sample preparation

For the fossil shark teeth from the Arctic, GOM, and Peru, enameloid was carefully abraded from each fossil shark tooth with a clean razor blade to avoid contamination from other tissues. Small chunks of dentine and sediments were also extracted and individually ground with pestle and agate mortar for isotopic analysis. All tools used in the extraction were cleaned with ethanol before and after sampling each tooth and sediments sample. For other fossil teeth from New Jersey and North Carolina, either enameloid chips were taken from the teeth with any dentine on the inside surface removed with a Dremel tool, or the enameloid powder was directly drilled from the surface of the teeth.

Wet chemistry and isotopic measurements were performed at the Isotoparium. All digestions and dilutions used trace-metal-clean acids (purified via two rounds of sub-boiling distillation) and acid-cleaned PFA beakers. Enameloid (10–40 mg), dentine (5–70 mg), and sediments (160–200 mg) were weighed in clean 7 mL PFA beakers, and then dissolved by consecutive acid attack: 5 mL concentrated 3:1(v/v) HF:HNO_3 at 130 °C for 24 h followed by 5 mL concentrated aqua regia at 140 °C for 24 h. Between the two acid attacks, 100 μL concentrated $HClO_4$ were added to dried samples to dissolve residual fluorides, and then the $HClO_4$ was removed by heating at 165 °C for several hours. These steps were repeated to ensure complete dissolution. After digestion, samples were dried and redissolved into concentrated HNO_3, then brought up in 5 mL of 3 M HNO_3. A 2–3 % aliquot was taken from the digest for concentration analysis on an iCAP RQ ICPMS (ThermoFisher). Based on [U] data, samples were spiked with IRMM-3636 to obtain U_{spike}/U_{sample} ratios of 3–5 % (Tissot et al. 2019a). The spiked solutions were dried completely and taken back into 1 mL concentrated HNO_3. The samples were refluxed on a hotplate at 130 °C to ensure the sample and spike were well equilibrated and then diluted to 5 mL 3 M HNO_3 for column chemistry. To monitor long-term external reproducibility, several powder aliquots of geostandard BCR-2 were digested in parallel to the shark teeth and sediment samples.

Uranium purification was performed on pre-packed 2 mL U-TEVA cartridges (Eichrom) following established methods (Tissot and Dauphas 2015; Tissot et al. 2016, 2017). In brief, the resin was cleaned with 40 mL 0.05 M HCl, and then conditioned with 10 mL 3 M HNO_3. Samples were loaded onto the resin in 5 mL 3 M HNO_3, and matrix elements were eluted in 12 mL 3 M HNO_3. The resin was then converted with 5 mL 10 M HCl, followed by Th removal in 8 mL 5 M HCl. U was finally eluted in 20 mL 0.05 M HCl and collected in cleaned 30 mL beakers. The U cut was evaporated to dryness, and 0.25 mL H_2O_2 and 0.20 mL concentrated HNO_3 were added to oxidize any organic matter released from the resin. After refluxing overnight at 120 °C, the mixture was completely dried and taken back into 3 M HNO_3. The column chemistry was repeated a second time to ensure precise and accurate measurements of $^{234}\mathrm{U}/^{238}\mathrm{U}$ (Tissot et al. 2018). Uranium procedural blank ∼13 pg (<0.04 % of U in sample) and are therefore negligible. The final U cuts were evaporated to dryness before being redissolved in concentrated HNO_3. Samples were then evaporated to near dryness, and ultimately diluted to 3 vol% HNO_3 for isotopic measurements.

4.1.2.3 Mass spectrometry

All U isotope analyses were performed on a NeptunePlus (ThermoFisher) multiple collector inductively coupled plasma mass spectrometer (MC-ICPMS) at Caltech, following established methods (Kipp et al. 2022; Tissot and Dauphas 2015). The Jet sample and X-skimmer cones were used in combination with an Aridus3 or Apex Omega HF desolvating nebulizer. The measurements were conducted in low-resolution mode using a static cup configuration. Each analysis consisted of 50 cycles of 4.194 s integration time. The sample measurements were bracketed by the CRM-112a standard spiked with IRMM-3636 at a similar $\mathrm{U}_{spike}/\mathrm{U}_{sample}$ ratio as the samples. Instrumental mass fractionation was corrected by standard-sample-bracketing and double spike deconvolution. Amplifier gain calibrations were performed daily. The $^{234}\mathrm{U}$ signal was measured with a secondary electron multiplier (SEM) on the axial mass. The SEM-Faraday cup gain was calibrated manually with replicate analyses of the CRM-112a standard solution in both SEM and Faraday mode at the beginning and end of each analytical sequence (Kipp et al. 2022).

The $^{238}\mathrm{U}/^{235}\mathrm{U}$ ratios are reported in δ-notation relative to the standard CRM-112a (CRM-145 for the solution form, $^{238}\mathrm{U}/^{235}\mathrm{U} = 137.837$, Richter et al. 2010), which is defined as:

$$\delta^{238}\mathrm{U} = \left(\frac{^{238}\mathrm{U}/^{235}\mathrm{U}_{\mathrm{smp}}}{^{238}\mathrm{U}/^{235}\mathrm{U}_{\mathrm{CRM\text{-}112a}}} - 1 \right) \times 1000 \tag{4.1}$$

The $^{234}\mathrm{U}/^{238}\mathrm{U}$ ratios are reported as $\delta^{234}\mathrm{U}_{\mathrm{sec}}$, relative to secular equilibrium as:

$$\delta^{234}\mathrm{U}_{\mathrm{sec}} = \left(\frac{^{234}\mathrm{U}/^{238}\mathrm{U}_{\mathrm{smp}}}{^{234}\mathrm{U}/^{238}\mathrm{U}_{\mathrm{Sec.\ Eq}}} - 1 \right) \times 1000 \tag{4.2}$$

where $^{234}\mathrm{U}/^{238}\mathrm{U}_{Sec.Eq}$ denotes the atomic ratio at secular equilibrium, which is the ratio of the decay constants of $^{238}\mathrm{U}$ and $^{234}\mathrm{U}$, $\lambda_{238}/\lambda_{234} = (1.55125\times10^{-10})/(2.8220\times$

$10^{-6}) = 5.4970 \times 10^{-5}$ (Cheng et al. 2013).Uncertainties are reported as 2SE (95% CI) and calculated using the daily external reproducibility of the CRM-112a standard (2SD) divided by the square root of the number of replicate measure-ments for a given sample (*i.e.,* $2\text{SE} = 2\text{SD}_{External}/\sqrt{n}$). Depending on the available material, each sample was analyzed 3 to 17 times. Replicate measurements of the BCR-2 basalt geostandard gave an average δ^{238}U of -0.236 ± 0.026 ‰ and $\delta^{234}\text{U}_{\text{sec}}$ of 0.32 ± 0.25 ‰ ($\text{n}_{digests} = 5$, $\text{n}_{analyses} = 34$), within the uncertainty of the recommend δ^{238}U value of -0.262 ± 0.004 ‰, calculated using all previously published high-precision data (data from the uranium isotope database, Li and Tissot 2023).

4.1.2.4 LA-ICPMS

Elemental concentration profiles across shark teeth sections were measured *in-situ* by laser ablation inductively coupled plasma mass spectrometry (LA-ICPMS) at the Isotoparium. Selected shark teeth samples were mounted in 1 inch of epoxy and polished prior to analysis. Concentrations were measured using an iCAP RQ ICPMS coupled with a NWRfemto laser ablation system (Elemental Scientific). Laser sampling was conducted at $\lambda = 257$ nm, with 30 % energy output. The spot size and repetition rate were set to 40 μm and 20 Hz, respectively. The measurements were conducted in linear scan mode, with a scan speed of 10 μm/s. Data reduction followed the method in Longerich et al. (1996), and the uranium concentrations were calculated as:

$$[\text{U}]_{smp} = \frac{n(\text{U})_{\text{smp}}}{\frac{n(\text{U})_{\text{NIST616}}}{[\text{U}]_{\text{NIST616}}} \times (\frac{n(\text{Ca})_{\text{smp}}}{n(\text{Ca})_{\text{NIST616}}} \times \frac{[\text{Ca}]_{\text{NIST616}}}{[\text{Ca}]_{\text{smp}}})} \tag{4.3}$$

where n is the background corrected count rate, with units of counts per second (cps). The international glass reference material NIST616 was used for external calibration, assuming a CaO content of 12 wt% (Kane 1998) and U concentration of 0.0721 ppm. Calcium was used as the internal standard to correct the variations in mass ablation yield, assuming shark teeth with an average apatite CaO value of 53 wt% (Trotter and Eggins 2006).

4.1.2.5 O isotopes

The enameloid powder was gently abraded from each tooth using a razor blade. The sampling tools were cleaned with ethanol before each sample collection. To analyze the phosphate oxygen isotope composition, we followed the rapid, small volume preparation methodology of Mine et al. (2017). Briefly, ∼1 mg of enameloid powder was weighed and dissolved in 50 μL 2 M HNO_3 overnight. Then, 30 μL of 2.9 M HF and 50 μL of 2 M NaOH were added to precipitate CaF_2 and supernatant removed to a separate vial. The CaF_2 pellet was rinsed with 50 μL 0.1 M NaF and this second aliquot of supernatant was added to the separate vial. Before precipitating the Ag_3PO_4, the pH was adjusted to 4.5 with 2 M HNO_3 ($\sim$30 μL), then 180 μL of Ag ammine solution (1.09 M NH_4OH and 0.37 M $AgNO_3$; pH of 5.5–6.5 after addition of Ag-ammine solution) was added; crystals precipitated and settled for 5–7 min. Finally, we centrifuged samples to pellet the silver phosphate crystals and rinsed the samples five times with deionized water. Samples were dried overnight at 60 °C and weighed in triplicate to 300 ± 100 μg into silver capsules for isotopic analysis. The measurements were performed at the Stable Isotope Ecosystem Laboratory of University of California, Merced (SIELO) using a Temperature Conversion Elemental Analyzer (TC/EA) coupled with a Conflo IV to a Thermo Scientific Delta V continuous flow isotope ratio mass spectrometer (CF-IRMS). The O isotope compositions ($\delta^{18}O_{PO4}$) are reported relative to the standard V-SMOW using silver phosphate standards USGS 80 (n = 15; $1\sigma = 0.4$) and USGS 81 (n = 14; $1\sigma = 0.5$) for normalization, drift, and linearity corrections. A preparation check standard (IAEA 601) resulted in $\delta^{18}O$ values = +23.0 ± 0.2 ‰ and analytical corrections were checked with an in house Ag_3PO_4 reference material (Alfa Aesar; n = 2, $\Delta = 0.2$). Each sample was measured three times, with uncertainty reported as the standard deviation of the triplicate analyses.

4.1.3 Results

4.1.3.1 U concentration

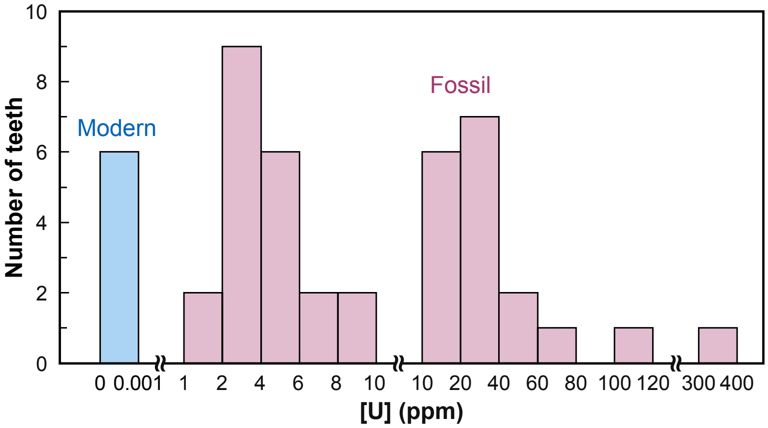

Figure 4.3: Histogram of U concentrations in enameloid of modern and fossil shark teeth.

Considering first the U concentrations of enameloid tissues only, the data show that modern and fossil shark teeth define two populations (**Fig. 4.3**). Modern teeth are characterized by low U concentrations (in the ppb range), whereas the 43 fossil shark teeth display values at or above the ppm level, at least four orders of magnitude higher than modern teeth. The U concentrations in enameloid tissues of fossil teeth are highly variable (1.2–320 ppm), and no clear trend in U concentrations is observed with sample age or locality.

In fossil teeth, U concentrations of enameloid and dentine tissues were determined by both bulk solution (n = 5; **Fig. 4.3a**) and in-situ methods (n = 2; **Fig. 4.3b**). Bulk measurements conducted on 5 shark teeth show that [U] of enameloid range from 1.2 to 67 ppm, and dentine from 48 to 150 ppm. In the same tooth, U concentrations are always lower in the enameloid compared to dentine, in agreement with previous literature (Kohn et al. 1999; Tütken et al. 2020). The U concentration variations also exist between different segments of the same tissue, as shown by the lower concentration seen in the crown dentine than in the root dentine.

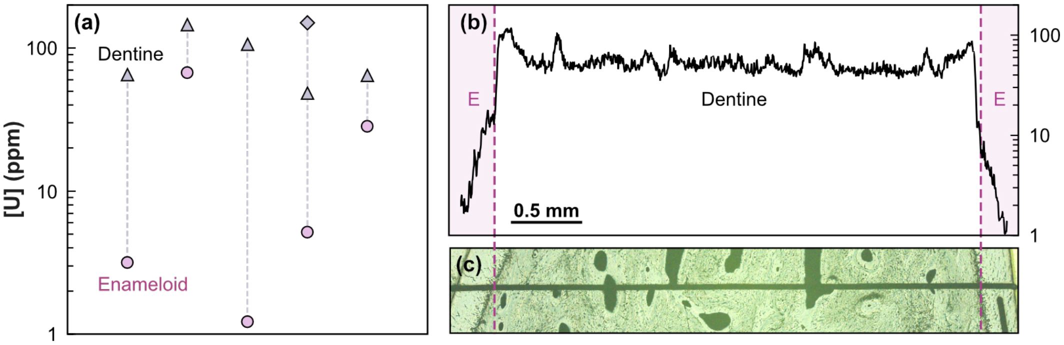

Figure 4.4: U concentration trends across tissues. (a) Bulk U concentrations of enameloid and dentine from 5 fossil shark teeth. The dentine is shown in grey (triangle: crown, diamond: root) and enameloid samples are shown in pink circles. The vertical grey dash line connects the tissues from the same tooth. (b) Representative LA-ICPMS U concentration profile through the middle of a fossil tooth crown (2004–31-05). (c) Reflected light microscope image of the ablated cross section.

In-situ measurements corroborate the results of the bulk analyses. The U concentration profile based on LA-ICPMS through the cross-section of fossil shark teeth crown varies and delineates differences between the enameloid and dentine (**Fig. 4.4b, S2b**). Dentine is enriched in U compared to the enameloid, and compositional variations within the same tissue are also observed. The [U] profile in the dentine is noisy, with concentrations ranging from ∼40 to 120 ppm, while values in enameloid decrease from the inner side (contact with dentine) to the outer side.

4.1.3.2 U isotopes

Shark teeth enameloid and sediments

The U isotope compositions of fossil shark teeth tissues and sediments are shown in **Table 4.1** and **Fig. 4.5**. Owing to the extremely low U content of modern teeth, isotopic analyses were not possible on these samples. To test the if U isotope heterogeneity exists in enameloid tissues, four aliquots were taken from a large *Otodus megalodon* tooth (EK) and digested separately for isotopic analyses. The δ^{238}U values of the replicated digests are indistinguishable within the uncertainty (**Table 4.1** and **Fig A.3**). Small variabilities (<1 ‰) are observed in $\delta^{234}U_{sec}$ values, but this intra-tooth variability is much smaller than those among different shark teeth.

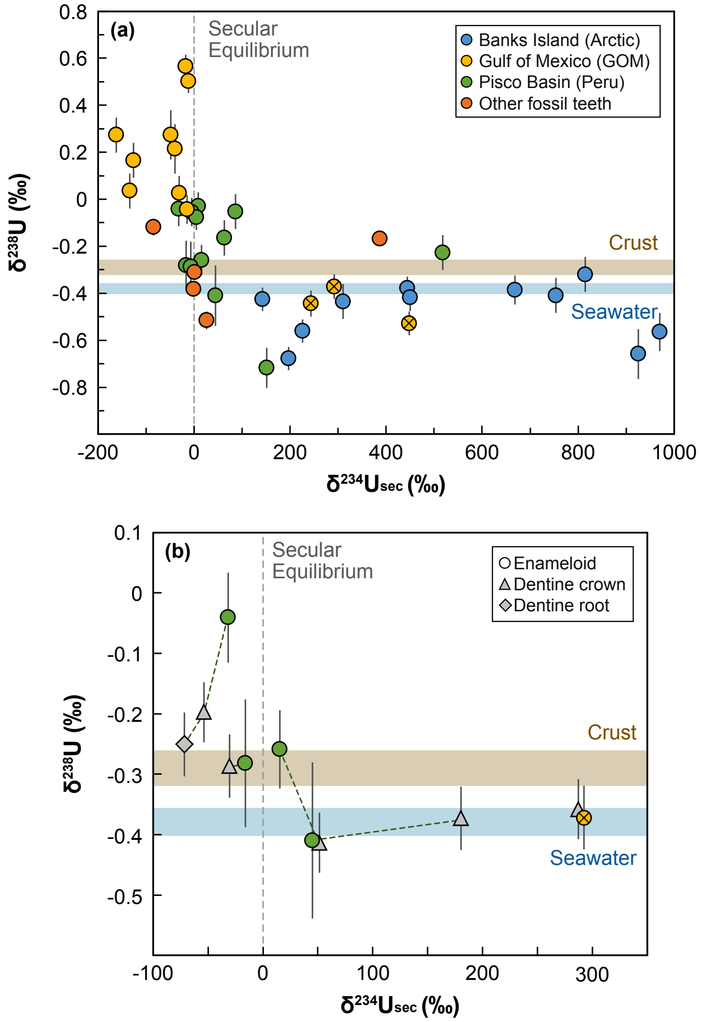

Figure 4.5: $\delta^{238}U$ vs. $\delta^{234}U_{sec}$ in (a) the shark teeth enameloid from different localities, and (b) different tissues (*i.e.,* enameloid and dentine). The color of enameloid symbols indicate localities, same as panel (a). Samples from the GOM are categorized into two groups based on their evolution history. Yellow ⊗ represents the first group with elevated $\delta^{234}U_{sec}$ values and $\delta^{238}U$ near modern seawater. Dashed lines connect different tissues from the same tooth. The brown and blue horizontal band show $\delta^{238}U$ of continental crust (-0.29 ± 0.03 ‰) and modern seawater (-0.379 ± 0.023 ‰), respectively (Andersen et al. 2016; Kipp et al. 2022; Tissot and Dauphas 2015). The vertical grey dash line denotes the secular equilibrium $\delta^{234}U_{sec}$.

The $\delta^{238}U$ values of enameloid from fossil shark teeth vary from -0.72 to +0.57 ‰, a range comparable to that observed in Cenozoic carbonates (Bura-Nakić et al. 2018; Chen et al. 2018a,b, 2021b; Gothmann et al. 2019; Livermore et al. 2020; Romaniello et al. 2013; Tissot and Dauphas 2015; Tissot et al. 2018). The $\delta^{234}U_{sec}$ values cover a very wide range, from -162.1 to +969.7 ‰, showing departures both below and (far) above secular equilibrium, which testify to recent open-system behavior and exchange of ^{234}U.

In the Arctic, δ^{238}U values range from -0.68 to -0.32 ‰, showing limited variation near the modern seawater value. The $\delta^{234}U_{sec}$ values of these samples range from +143.1 to +969.7 ‰, displaying the largest range among the three studied localities. For two of these teeth (BKS04-19 and BKS2004-31), the embedding sediments were analyzed. The shark teeth enameloid and embedding sediments show similar δ^{238}U values within analytical uncertainties ($\Delta_{\text{enamel-sed}} < 0.15$ ‰). In contrast, the sediments have $\delta^{234}U_{sec}$ values of -2.9 to +101.1 ‰, much lower than that of the shark teeth they surround.

Shark teeth from Peru have δ^{238}U and $\delta^{234}U_{sec}$ values ranging from -0.72 to -0.03 ‰ and -31.7 to +517.4 ‰, respectively. Most sediments from Peru cover similar ranges of both δ^{238}U and $\delta^{234}U_{sec}$, with one exception, sediment JBL002-sed, which is characterized by the highest δ^{238}U value measured in this study of +1.38 ‰.

Samples from GOM have a larger range of δ^{238}U values, from -0.53 to +0.57 ‰ and have $\delta^{234}U_{sec}$ between -162.1 and +448.6 ‰. For this locality, no sediments were available for comparative analysis. The remaining fossil shark teeth, which originated from North Carolina and New Jersey, USA (orange symbols in **Fig. 4.5a**), show more limited variations in δ^{238}U and $\delta^{234}U_{sec}$.

Enameloid and dentine

Similar to U concentration, U isotopes also show heterogeneity between different tissues from the same tooth. The δ^{238}U and $\delta^{234}U_{sec}$ data of enameloid and dentine from 5 fossil shark teeth from two localities indicate the differences between tissue substrates (**Fig. 4.5b**). Generally, dentine samples have similar or lower δ^{238}U values than enameloid and $\delta^{234}U_{sec}$ values that deviate more from secular equilibrium. The magnitude of U isotope offsets between the enameloid and dentine varies among these samples ($\Delta_{\text{enamel–dentine}} =$ -0.04–0.21 ‰).

4.1.3.3 O isotopes

The O isotope compositions of fossil shark teeth are presented in **Table 4.1** and their relationships between the U isotope compositions are shown in **Fig. 4.6**. Compared to modern shark teeth, which show typical $\delta^{18}O_{PO4}$ values between 22 and 26 ‰ (mainly reflects the temperature and the O isotope composition of ambient water, Vennemann et al. 2001), enameloid $\delta^{18}O_{PO4}$ values in the fossil teeth studied here vary between 9.1 and 24.0 ‰ and define two main clusters. The Arctic shark teeth have lower $\delta^{18}O_{PO4}$ values (<19 ‰) and range of compositions (9.1–18.5 ‰). A correlation between δ^{238}U and $\delta^{18}O_{PO4}$ is not observed, while $\delta^{234}U_{sec}$ is positively correlated with $\delta^{18}O_{PO4}$. In contrast, samples from Peru and GOM have higher $\delta^{18}O_{PO4}$ (>19 ‰) and have a smaller range of compositions (19.2–24.0 ‰).

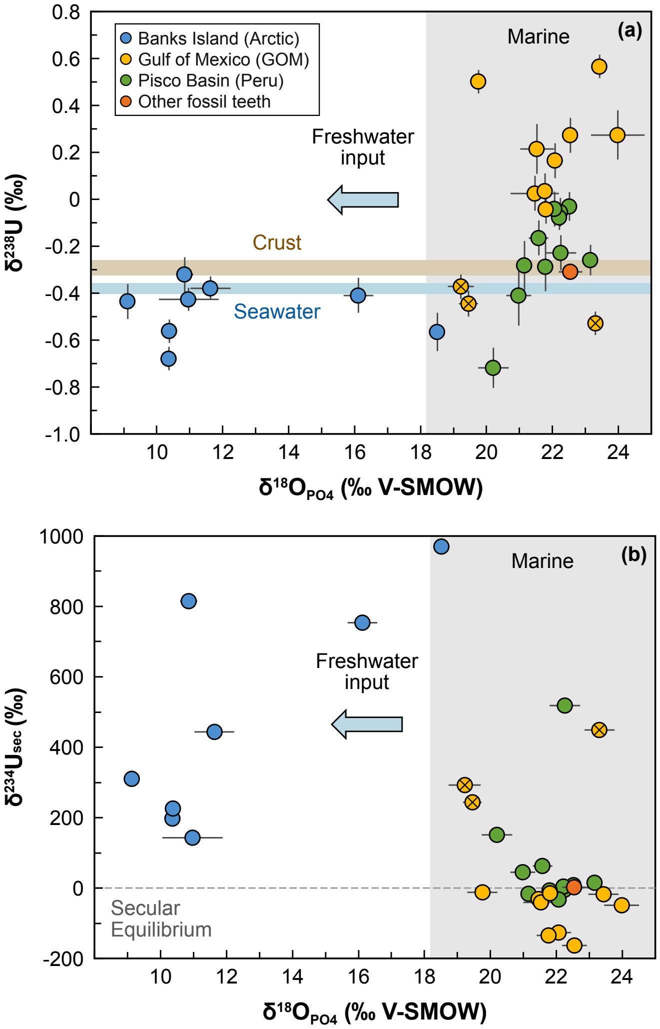

Figure 4.6: Uranium and oxygen isotopes in the enameloid of fossil shark teeth (a) $\delta^{238}U$ vs. $\delta^{18}O_{PO4}$ and (b) $\delta^{234}U_{sec}$ vs. $\delta^{18}O_{PO4}$ in enameloid tissues of fossil shark teeth. Symbols as in Fig. 4.5. The vertical light grey band denotes the expected $\delta^{18}O_{PO4}$ range (Fischer et al. 2013; Klug et al. 2010) for marine sharks.

4.1.4 Discussion

4.1.4.1 Timing of U incorporation in shark teeth

Uranium concentrations are high in fossil shark teeth but negligible in modern teeth, indicating that U in fossil teeth derives from postmortem incorporation. Uranium isotope records in fossil shark teeth are therefore not impacted by in-vivo factors (*i.e.*, lack vital effects), which could be an advantage for using shark teeth as a geochemical archive, in comparison to biological carbonates that can have variable vital effects (0–0.09 ‰, Chen et al. 2018a).

While the absence of vital effects is a strength of fossil shark teeth as a U isotope archive, postmortem acquisition of U means that burial conditions can considerably impact the degree to which tooth-hosted U isotope signatures resemble those of primary seawater. Thus, for robust application of the U isotope redox proxy in fossil shark teeth, we need to first understand the timescale and mechanism of U uptake. Here, it is helpful to consider the uptake of not just U, but also other elements with similar behavior in biogenic apatite.

A disparity in concentration between modern and fossil teeth is in fact observed for a variety of trace elements (*e.g.,* U, Th and rare earth elements, REEs) in conodonts and fish teeth (Kohn et al. 1999; Martin and Haley 2000; Shaw and Wasserburg 1985; Staudigel et al. 1985; Trotter and Eggins 2006; Trueman and Tuross 2002; Vennemann et al. 2001), which may imply similar uptake timescale(s) and mechanism(s) for these elements. For example, Nd – one of the most extensively-studied systems – is thought to be rapidly incorporated into shark teeth with other REEs during the fossilization from apatite to hydroxyfluorapatite, early in the burial process in surface sediments (Huck et al. 2016; Kim et al. 2020; Martin and Haley 2000; Martin and Scher 2004; Shaw and Wasserburg 1985; Staudigel et al. 1985). This process is similar to U uptake models for mammal teeth, which predict that U incorporation would reach equilibrium on as short as $\sim$ kyr timescales (Pike and Hedges 2001). The similarity in U and REE uptake in bioapatite is supported by their strong co-variance in fossil teeth (Li et al. 2023). If true, early uptake of U into teeth could mean that U isotope signatures record early porewater conditions, with the signatures then preserved on geologic (Myr) timescales.

The timescales of U uptake in fossil teeth are also reflected by intra-sample spatial concentration patterns. For instance, we can consider diffusion-adsorption (DA) models, which are widely used to describe U uptake in teeth. These models state that U diffuses into the teeth as uranyl ion and then adsorbs onto the mineral surface (Millard and Hedges 1996; Pike and Hedges 2001). In these models, the spatial distribution of U in teeth is controlled by the diffusion and the partition coefficient of uranyl between aqueous fluids and apatite. The differing concentrations of U in enameloid and dentine (Kohn et al. 1999; Trotter and Eggins 2006; Tütken et al. 2020; this study **Fig. 4.4**) can therefore be explained by their porosity difference. The higher porosity of dentine gives higher diffusion coefficient, resulting in higher U concentrations and a shorter time to reach equilibrium (Pike and Hedges 2001).

Looking at the LA-ICPMS concentration profile across a representative shark tooth (2004–31-05, **Fig. 4.4b**), the relative history of U uptake can be reconstructed. First, higher [U] in dentine than enameloid reflects faster U diffusion into dentine and quicker accumulation of U from porewaters (*e.g.,* entering via the exposed root tissue).

The U-rich dentine would then become a U source to the enameloid. Diffusion of U from dentine to enameloid is observed in the strong [U] gradient in enameloid, with concentrations steeply declining away from the junction with dentine. In other words, this process implies that formerly dentine-hosted U likely represents more of the enameloid U pool than the U that entered enameloid directly from porewater. In principle, the U concentration profiles in the teeth could provide a constraint on absolute timescales of U uptake, insofar as [U] is not homogenous in either enameloid or dentine, meaning that equilibrium was not achieved (or was recently disturbed). If equilibrium was not reached, it would imply a recrystallization timescale less than that required for [U] equilibration across tissues; in the models presented above, this timing could range from kyr to perhaps Myr timescales (Li et al. 2023; Millard and Hedges 1996; Pike and Hedges 2001; Trueman and Tuross 2002). The U distribution may also be influenced by mineralogy, such as the presence of amorphous silica has a high U affinity and leads to high U concentration. In practice, without knowledge of the sedimentary conditions (*e.g.,* [U] in sediments and porewater), it is difficult to precisely constrain the timescale of U incorporation with concentration data alone.

Beyond the early U uptake, our data also provide insights into whether recent U addition or loss occurred. Here, we use $\delta^{234}\mathrm{U}_{\mathrm{sec}}$ as a tracer of recent U mobility. An intermediate product of the $^{238}\mathrm{U}$ decay chain, $^{234}\mathrm{U}$ has a half-life ($t_{1/2}$) of ∼245 kyr (Cheng et al. 2013) and in a sample behaving as a closed-system the $^{234}\mathrm{U}/^{238}\mathrm{U}$ ratio will reach secular equilibrium after ∼2 Myr (*i.e.,* ∼8 half-lives). Given that the age of the fossil shark teeth investigated here are much older (all >5 Myr), if they had behaved as closed systems following early diagenesis, their $\delta^{234}\mathrm{U}_{\mathrm{sec}}$ values should all be 0. However, most samples have $\delta^{234}\mathrm{U}_{\mathrm{sec}}$ values that deviate significantly from secular equilibrium (**Fig. 4.5a**), indicating that they experienced recent U open-system episodes. For the four out of five samples on which $\delta^{234}\mathrm{U}_{\mathrm{sec}}$ was measured in both enameloid and dentine, dentine tended to deviate more from secular equilibrium (**Fig. 4.5b**), implying that recent U mobilization is more pronounced in dentine than enameloid. This interpretation is consistent with the slow diffusion of U from dentine to enameloid tissues, and the idea that enameloid tissues are a more robust phase to target for paleo-environmental reconstructions (Becker et al. 2008; Kohn et al. 1999; McCormack et al. 2022; Sharp et al. 2000; Thomas et al. 2011).

In summary, U uptake in fossil shark teeth appears to have proceeded via rapid (kyr to Myr timescale) accumulation of U in the dentine followed by slow diffusion of U into enameloid tissues. Concentration gradients suggest that [U] did not reach equilibrium in the fossil teeth systems. Furthermore, $\delta^{234}\mathrm{U}_{\mathrm{sec}}$ variations suggest that recent U mobilization has occurred in the last 2 Myr. Collectively, these observations depict a complicated history of U uptake in fossil shark teeth.

4.1.4.2 Shark teeth do not uniquely record the seawater δ^{238}U

We now consider the ability of shark teeth to record ancient seawater U isotope ratios. The δ^{238}U values of shark teeth display considerable variability around the plausible seawater composition (**Fig. 4.5**), assuming that Cenozoic seawater was isotopically indistinguishable from modern seawater (Wang et al. 2016). Even allowing for moderate variation in seawater δ^{238}U, many shark teeth display values exceeding those of the riverine input (>-0.3 ‰) (Andersen et al. 2016; Noordmann et al. 2016), which likely reflect diagenetic ^{238}U enrichment (*e.g.,* Bura-Nakić et al. 2018; Chen et al. 2018b; Clarkson et al. 2021a; Hood et al. 2018; Rey et al. 2020; Romaniello et al. 2013; Tissot et al. 2018; White et al. 2018; Zhang et al. 2019a). To first order, this means that for U isotopes, shark teeth do not directly preserve a snapshot of coeval seawater during the fossilization process.

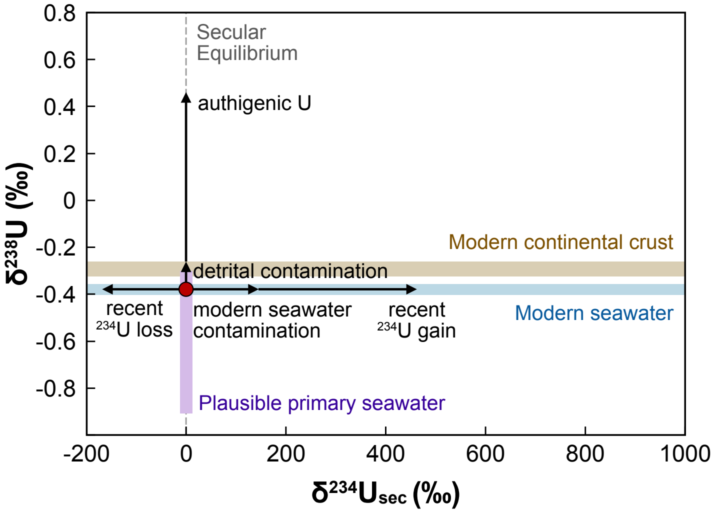

Figure 4.7: Schematic impact of various processes on U isotope composition. The red circle represents the present archive values assuming preservation of primary seawater compositions and closed-system behavior since sample formation (*i.e.,* ^{234}U/^{238}U ratio at secular equilibrium). The light purple band indicates the plausible primary seawater δ^{238}U values (from -0.90 to -0.30 ‰) in the geological past, based on the model in (Kipp and Tissot 2022). The brown and blue horizontal bands show δ^{238}U of continental crust (-0.29 ± 0.03 ‰) and modern seawater (-0.379 ± 0.023 ‰), respectively (Andersen et al. 2016; Kipp et al. 2022; Tissot and Dauphas 2015), and the vertical grey dash line shows $\delta^{234}U_{sec}$ value at secular equilibrium. For δ^{238}U, detrital contamination can only generate elevated δ^{238}U values up to the value of continental crust, while the authigenic input of reduced U can lead to larger magnitude of δ^{238}U. For $\delta^{234}U_{sec}$, the incorporation of modern seawater can only lead to $^{234}U_{sec}$ excess up to the modern seawater level (+145.55 ‰, Kipp et al. 2022), while recent (<2 Myr) ^{234}U gain (loss) relative to ^{238}U can result in larger $\delta^{234}U_{sec}$ variability. The U isotope compositions of shark teeth typically reflected a combination of these processes.

If U isotopes in fossil shark teeth are not uniquely representative of the seawater composition, what are the processes that contribute to the observed isotopic variability? Diagenesis is known to significantly impact many geochemical proxies in sedimentary archives, including the δ^{238}U proxy in the most popular archives, carbonates and shales (Asael et al. 2013; Chen et al. 2018b; Phan et al. 2018; Romaniello et al. 2013; Tissot et al. 2018). The same is true for δ^{18}O values in conodonts and fish teeth (Chen et al. 2015; Iacumin et al. 1996; Kohn et al. 1999; Sharp et al. 2000; Zazzo et al. 2004a). Hence, it is likely that the U isotope compositions of the shark teeth studied here have strayed from the seawater value during diagenetic transformations. Below, we consider several syn- and post-depositional processes that may shape the U isotope composition of shark teeth (**Fig. 4.7**). These can be broken into four main categories:

(i) detrital contamination,
(ii) isotope fractionation during U incorporation into the teeth,
(iii) assimilation of porewater U with isotope ratio deviating from that of seawater,
(iv) recent U gain/loss.

Detrital contamination

Some of the U isotope variability observed in the fossil shark teeth could be due to incorporation of detrital components. For instance, cavities can serve as reservoirs for detritus after the loss of basal body postmortem (Schmitz et al. 1991; Trotter and Eggins 2006). Here we tracked detrital contributions to the tooth signatures with U/Th ratios (**Fig. 4.8, 4.9**). Detrital inputs are characterized by high Th contents (*i.e.,* low U/Th ratios) and a crustal δ^{238}U value of -0.30 ± 0.04 ‰ (Andersen et al. 2016; Tissot and Dauphas 2015). Previous work has shown that detrital inputs can modify both [U] and δ^{238}U in sedimentary archives (Asael et al. 2013; Kendall et al. 2020; Lau et al. 2016; Noordmann et al. 2015; Tarhan et al. 2018). The impact of detrital inputs on shark teeth has also been observed for other geochemical tracers (Chen et al. 2015; Ehret et al. 2012; Elderfield and Pagett 1986; Kocsis et al. 2009; Lécuyer et al. 2004), suggesting it could be important for U as well. If detrital U is present in shark teeth, correlations between U isotope compositions and U/Th ratios would be expected, which would represent the mixing of authigenic and detrital components. The relationship between U isotope composition and U/Th does not define a unique relationship for all fossil shark teeth (**Fig. 4.8**). However, when considering each location independently, some correlations are observed, specifically in the δ^{238}U vs. U/Th diagram of GOM and the $\delta^{234}\mathrm{U}_{\mathrm{sec}}$ vs. U/Th diagram of the Arctic (**Fig. 4.9c, d**). While these trends could suggest a control of detrital contamination, in neither case is detrital mixing able to explain trends in both δ^{238}U and $\delta^{234}\mathrm{U}_{\mathrm{sec}}$. Furthermore, most of these teeth have far higher [U] (several to several hundred ppm) than detrital material (2.7 ppm, Rudnick and Gao 2014), meaning nuggets of detritus should only have a small impact on the bulk sample composition. Thus, we conclude that detrital contamination has a negligible impact on U isotopes in the fossil shark teeth studied here.

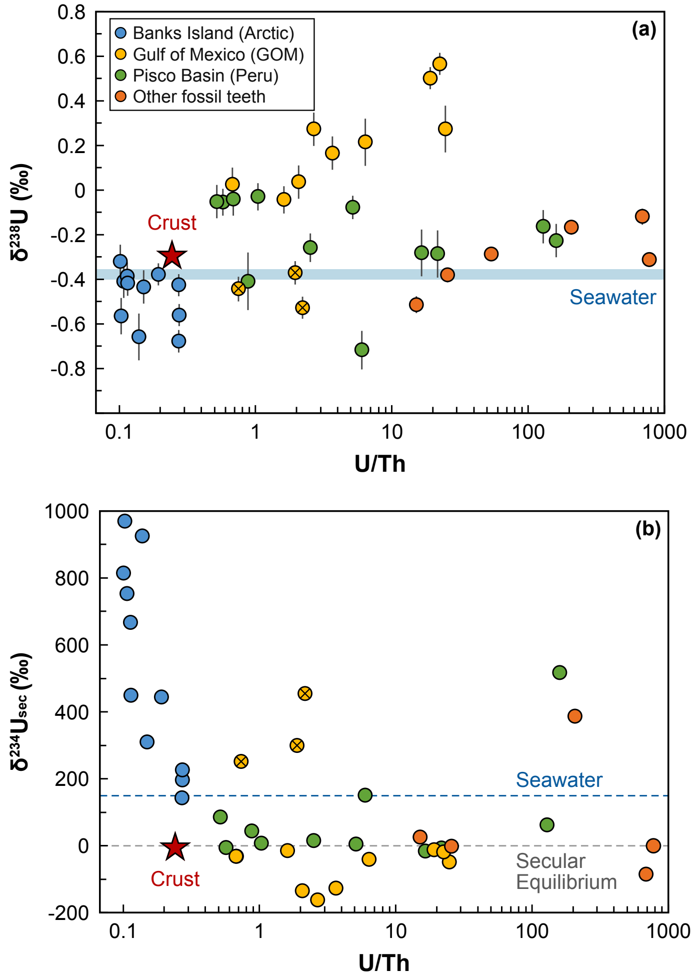

Figure 4.8: Uranium isotopes and U/Th ratios in the enameloid fossil shark teeth. (a) δ^{238}U vs. U/Th and (b) δ^{234}U$_{\text{sec}}$ vs. U/Th in enameloid tissues of fossil shark teeth. The red star represents the composition of continental crust, with δ^{238}U value of -0.29 ‰ (Andersen et al. 2016; Tissot and Dauphas 2015), and U/Th ratio of 0.257 (Rudnick and Gao 2014). The blue dash line represents the δ^{234}U$_{\text{sec}}$ value of modern seawater (+145.55 ‰, Kipp et al. 2022). Other symbols as in **Fig. 4.5**.

Isotopic fractionation during U incorporation into teeth

In theory, the uptake process itself could lead to isotope fractionation. Incorporation of U in teeth is thought to occur via diffusion of uranyl ions from surrounding water followed by adsorption on bioapatite (Millard and Hedges 1996; Pike and Hedges 2001). Since these processes do not involve a change in valence state, which is the mechanism generating the largest low-temperature U isotope fractionation in surface environments (Bigeleisen 1996; Brown et al. 2018), the diffusion and adsorption are unlikely to be the cause of the large U isotopes variations observed in this study. Nevertheless, U adsorption on iron-manganese oxides is well-known to result in preferential incorporation of light U isotopes in the adsorbed phases, by ~0.20 ‰

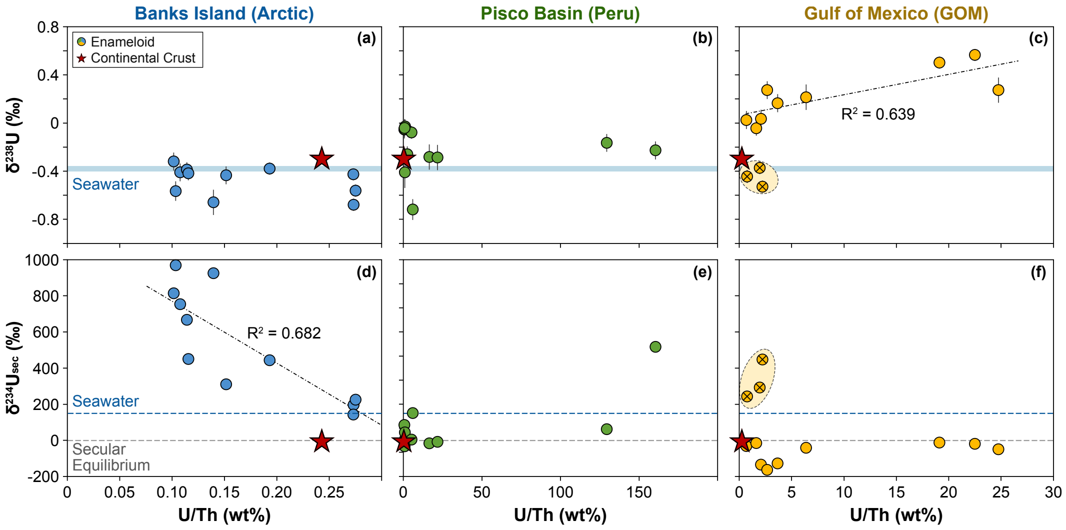

Figure 4.9: U isotope trends vs. U/Th concentration ratios in enameloid tissues of fossil shark teeth. Symbols as in **Fig. 4.8**. The light yellow ellipses highlight the first group of fossil shark teeth from GOM.

(Brennecka et al. 2011b; Wang et al. 2016). Assuming a similar isotopic fractionation during adsorption on apatite in the teeth could explain the lower δ^{238}U observed in some teeth (but not the higher δ^{238}U values).

Alternatively, uptake processes involving U reduction could result in significant U isotope fractionation. For instance, interaction between the organic matter in the teeth and the pore fluid could result in locally reducing conditions and U incorporation occurring via U reduction. In this case, the addition of authigenic U would manifest as a coincident increase in [U] and δ^{238}U. Here, such a [U] versus δ^{238}U correlation is observed at one site (GOM, **Fig. 4.10c**). These are among the most ^{238}U-enriched samples in the entire dataset, consistent with a role of U reduction in supplying extra U to the system. In summary, incorporation of authigenic reduced U is capable of generating the magnitude of observed isotopic fractionation.

Porewater U isotope ratios deviating from seawater

In another end-member scenario, the variations in δ^{238}U in shark teeth would not result from fractionation during U incorporation into the teeth, but simply record the composition of the surrounding porewaters. In this scenario, porewaters that start with a seawater δ^{238}U value could drift toward different compositions if U is added or removed with associated isotopic effects, and this altered composition could then become recorded in teeth upon U uptake.

The dominant process generating δ^{238}U variability in marine sediments is U(VI) reduction to U(IV) (*e.g.,* Stirling et al. 2007; Weyer et al. 2008). If this process were to occur in sediments hosting shark teeth, it would progressively decrease [U] and

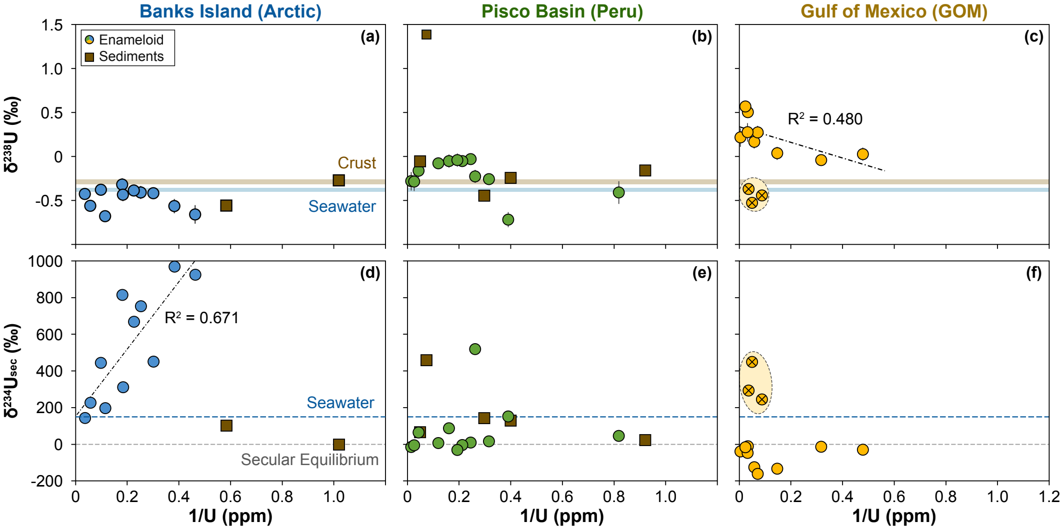

Figure 4.10: U isotope vs. U concentration in sediments and the enameloid of fossil shark teeth. Symbols as in **Fig. 4.5**.

δ^{238}U in porewaters. There is perhaps evidence of this in the lower δ^{238}U values in the Arctic data (**Fig. 4.10a**). Conversely, if U reduction occurred and sequestered isotopically heavy U(IV) in sediments, and the sediments were then flushed with oxidizing porewaters, a large release of ^{238}U-enriched U would occur, which could potentially become sequestered in shark teeth. The elevated δ^{238}U values in GOM data can support this possibility (**Fig. 4.10c**). These scenarios are not mutually exclusive, and it is quite possible that a given depositional environment oscillated between both conditions for multiple times before lithification.

To disambiguate between these possibilities, we can consider the δ^{238}U values of sediments hosting the fossil shark teeth. The first scenario, with isotopic distillation of porewaters due to U reduction, would predict low δ^{238}U in teeth and high δ^{238}U in sediments. The second scenario, with release of isotopically-modified authigenic U, would predict similar δ^{238}U in teeth and sediments (because sediments supplied U to the teeth). In both the Arctic and Peru datasets, a similarity in sediments and teeth δ^{238}U values favors the latter scenario. The isotopically-fractionated sediments may have become enriched in U via reductive immobilization and subsequent interaction with oxidizing porewaters may have liberated some U, a fraction of which ultimately became sequestered in the shark teeth. Importantly, δ^{238}U signatures in these two localities have both higher and lower values than the continental crust, meaning that the U isotope signatures in shark teeth is not dominated by detrital U contamination. Besides the incorporation of porewater with low δ^{238}U values due to local reduction, U adsorption on ferromanganese oxides is another process that could explain lower than seawater δ^{238}U values. Absorbed U on Fe-Mn oxides is isotopically lighter than aqueous U by ∼0.22 ‰ (Brennecka et al. 2011b), which is comparable to the magnitude of δ^{238}U offsets observed in these samples. This hypothesis is further supported by the elevated Fe and Mn concentrations in the enameloid of fossil teeth compared to modern teeth (**Table A.1** and Kohn et al. 1999).

Another way to alter pore fluid composition is to introduce meteoric fluids with isotopically-fractionated U (Polyak et al. 2023). Meteoric fluid can be identified using δ^{18}O values, since Rayleigh distillation depletes ^{18}O in rainfall, giving meteoritic fluid a lower δ^{18}O values than seawater (Dansgaard 1964; LeGrande and Schmidt 2006). In this view, the input of freshwater will lower $\delta^{18}O_{PO4}$ values in shark teeth (Fischer et al. 2013; Klug et al. 2010; Kocsis et al. 2007). If all fossil shark teeth are considered as a single group, no systematic correlations between U isotope compositions and $\delta^{18}O_{PO4}$ are observed (**Fig. 4.6**). However, at least in the Arctic, low δ^{18}O values point to freshwater input (Kim et al. 2014). Thus, while meteoric fluids may have played a role in shaping δ^{18}O patterns, it is an unlikely explanation for the large U isotope fractionations observed in these samples.

In summary, while meteoric diagenesis likely does not account for the observed trends, a contribution of sediment-hosted authigenic U to the tooth-hosted U pool could have generated much or all of the observed δ^{238}U variability.

U isotope fractionation during U gain/loss

The large range of $\delta^{234}U_{sec}$ values in shark teeth (**Fig. 4.5**) testifies to recent U mobilization (<2 Myr ago). If these shark teeth incorporated only modern seawater, they would record a $\delta^{234}U_{sec}$ value of +145.55 ‰ (**Fig. 4.7**, Andersen et al. 2010; Chen et al. 1986; Kipp et al. 2022). In contrast, the samples present ^{234}U excesses of up to ∼ +1000 ‰, reminiscent of the highly variable and elevated $\delta^{234}U_{sec}$ values observed in rivers and groundwaters, which can reach over +1000 ‰ (Andersen et al. 2007, 2016; Chabaux et al. 2001, 2003; Robinson et al. 2004). The same phenomenon responsible for the elevated $\delta^{234}U_{sec}$ of rivers waters, alpha recoil, can readily explain the ^{234}U systematics of shark teeth. During alpha decay of ^{238}U, a fraction of the daughter nuclide ^{234}Th can be expelled as a result of the recoil effect into the surrounding porewater and rapidly decay into ^{234}U, leading to a ^{234}U excess at a few thousand permil scale (Henderson et al. 1999). The direct incorporation of porewater with ^{234}U excess can result in high $\delta^{234}U_{sec}$ values that are comparable to those measured in this study. On the other hand, alpha-recoil of the apatite-hosted U can explain the lower $\delta^{234}U_{sec}$ values observed in the samples. Indeed, the recoil-produced ^{234}U, even if not directly expelled from the mineral, can be preferentially mobilized out of damaged lattice site during aqueous leaching, compared to the lattice-bond ^{238}U (Kigoshi 1971). Both U loss by leaching and/or alpha recoil would be consistent with the [U] profile in **Fig. 4.4**. To assess the impact of alpha recoil on ^{234}U excesses, the $\delta^{234}U_{sec}$ of porewater is plotted against the grain radius (**Fig. 4.11**) using the established model in Henderson et al. (1999).

During the alpha recoil process, the ^{234}Th is expelled from the mineral grain into the porewater and rapidly decays into ^{234}U. The excesses of ^{234}U can further decay and decrease ^{234}U in the porewater. Porewaters can eventually reach a steady state, in which the rate of ^{234}U gain from 234Th ejection equals the rate of ^{234}U loss from decay. The ^{234}U activity ratio (^{234}U/^{238}U) at the steady state is given by:

$$\left(\frac{^{234}\mathrm{U}}{^{238}\mathrm{U}}\right)_{\mathrm{SS}} = \frac{r^3-(r-\alpha)^3}{4r^3} \times \frac{[\mathrm{U}]_{\mathrm{sed}}}{[\mathrm{U}]_{\mathrm{pw}}} \times \frac{\rho_{\mathrm{sed}}}{\rho_{\mathrm{pw}}} \times \frac{1-\phi}{\phi} + 1 \tag{4.4}$$

where the ^{234}U activity ratio is defined as:

$$\left(\frac{^{234}\mathrm{U}}{^{238}\mathrm{U}}\right) = \frac{^{234}\mathrm{U}/^{238}\mathrm{U}_{\mathrm{smp}}}{^{234}\mathrm{U}/^{238}\mathrm{U}_{\mathrm{Sec.Eq.}}} \tag{4.5}$$

When porewater evolves towards the steady state, the (^{234}U/^{238}U) at time t is given by:

$$\left(\frac{^{234}\mathrm{U}}{^{238}\mathrm{U}}\right)_t = \left[\left(\frac{^{234}\mathrm{U}}{^{238}\mathrm{U}}\right)_{\mathrm{SS}} - \left(\frac{^{234}\mathrm{U}}{^{238}\mathrm{U}}\right)_0\right] \times \left(1-e^{-\lambda_{234}t}\right) + \left(\frac{^{234}\mathrm{U}}{^{238}\mathrm{U}}\right)_0 \tag{4.6}$$

The $\delta^{234}\mathrm{U}_{\mathrm{sec}}$ at time t is:

$$\delta^{234}\mathrm{U}_{\mathrm{sec}}(t) = \left[\left(\frac{^{234}\mathrm{U}}{^{238}\mathrm{U}}\right)_t - 1\right] \times 1000 \tag{4.7}$$

The parameters and their values used in this model are defined in **Table 4.2** below.

Table 4.2: Parameters in alpha recoil model in porewater system

Parameter	Definition	Value	Comments
r	Grain radius	1–1000 μm	
α	Alpha recoil distance	550 Å[a]	
$[\mathrm{U}]_{sed}$	U concentration in sediments	6 ppm[b]	
$[\mathrm{U}]_{pw}$	U concentration in porewater	8 ppb[a]	
ρ_{sed}	Density of sediments	2.42 g/cm^3	Density of sandstone
ρ_{pw}	Density of porewater	1 g/cm^3	Density of water
ϕ	Porosity of sediments	0.25	Porosity of sandstone
$\left(\frac{^{234}U}{^{238}U}\right)_0$	Initial activity ratio of porewater	1.1455[c]	Modern seawater value
λ_{234}	Decay constants of ^{234}U	0.0028[d]	
t	Time of porewater evolution	0–1000 kyr	

[a] Henderson et al. (1999)
[b] This study, average U concentration of sediments
[c] Kipp et al. (2022)
[d] Cheng et al. (2013)

Fig. 4.11 shows the maximum ^{234}U excesses that can be generated by alpha recoil process are larger than the observed $\delta^{234}\mathrm{U}_{\mathrm{sec}}$ values in shark teeth, which strengthen the interpretation that alpha-recoil in porewater can lead to the ^{234}U excesses in shark teeth.

We note that while alpha recoil can readily account for the variations of $\delta^{234}\mathrm{U}_{\mathrm{sec}}$ in shark teeth, both the riverine and modern seawater inputs may also contribute to the ^{234}U budget in the samples. Given that these mechanisms are not necessarily correlated to other proxies (*i.e.,* [U] and δ^{238}U), we are not able to disentangle their relative impacts on the compositions of the samples.

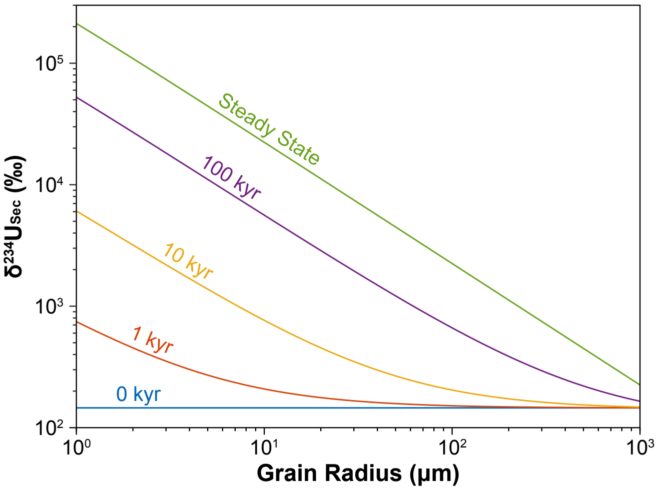

Figure 4.11: Predicted $\delta^{234}U_{sec}$ vs. grain radius in porewater-sediments system from the model in Henderson et al. (1999). The curve of steady state indicates the upper limit of $\delta^{234}U_{sec}$ can be generated in porewater system.

4.1.4.3 Evaluation of U uptake and isotopic alteration history at each site

Shark teeth from the 3 localities in this study have distinct characteristics in the variability of δ^{238}U and $\delta^{234}U_{sec}$ as well as their relationships with diagenetic tracers, indicating that U uptake and isotopic fractionation is controlled by local environmental conditions. Here, we look at the history of U incorporation and isotopic alteration at each site, considering the implications for the use of shark teeth as an archive of ancient seawater U isotope ratios.

Banks Island (Arctic)

In the Arctic shark teeth, the range of δ^{238}U is relatively limited around the modern seawater value (-0.48 ± 0.12 ‰, ±1 SD). On the other hand, $\delta^{234}U_{sec}$ values are highly variable, and all exhibit ^{234}U excess, most likely caused by the alpha-recoil in the porewater system. Correlations of $\delta^{234}U_{sec}$ vs. δ^{18}O, U/Th, and 1/U are observed (**Fig. 4.6b, 4.9d, 4.10d**), and provide clues to understand the geological processes that controlled the U isotope fractionation in this location. Shark teeth from the Eocene Arctic are significantly depleted in ^{18}O relative to the other locations, reflecting freshwater inputs into the Arctic during the early Eocene (Kim et al. 2014), such as meteoric water and rivers. In this framework, the low [U] and high $\delta^{234}U_{sec}$ values of river water (Andersen et al. 2007, 2016; Chabaux et al. 2001, 2003;

Robinson et al. 2004), are consistent with initial uptake of riverine U in the teeth. The estimated salinity of northern Banks Island during the Eocene is 12.7 PSU (Kim et al. 2014), which is substantially lower than the central Arctic Ocean during the Eocene (21–25 PSU, Waddell and Moore 2008), and the modern Arctic Ocean (32–35 PSU, Boyer et al. 2009), implying the U mass balance in the Banks Island region was not dominated by open ocean. Subsequent uptake of seawater U in the teeth would then readily explain the positive correlation between $\delta^{234}U_{sec}$ and 1/U (R_2 = 0.671, **Fig. 4.10d**), and the convergence towards a seawater like $\delta^{234}U_{sec}$ value in the samples with the highest [U].

The limited $\delta^{238}U$ variability around a seawater-like value in the Arctic teeth samples could reflect either (i) preservation of the original $\delta^{238}U$ of seawater during the early Eocene with a similar composition as modern seawater or (ii) incorporation of U from modern seawater during recent reworking. For the most U-rich samples, the evidence points to a predominant control of the U budget by recent U addition (*i.e.,* seawater-like $\delta^{238}U$ and $\delta^{234}U_{sec}$, and a clear correlation between $\delta^{234}U_{sec}$ and 1/U). In the most U-depleted samples, the elevated $\delta^{234}U_{sec}$ values preclude addition of seawater U in the last 2 Myr, but the available information is insufficient to determine if the $\delta^{238}U$ values in these samples preserve the seawater composition at the time of burial (Eocene), or a more recent U addition (prior to 2 Myr ago).

Gulf of Mexico (GOM)

Based on their U isotope compositions, Eocene shark teeth from GOM can be grouped into subsets that are likely to have had different evolution histories. The first group (yellow ⊗), similar to the Arctic samples, display elevated $\delta^{234}U_{sec}$ values (>+200 ‰), $\delta^{238}U$ around the modern seawater value and higher Fe and Mn contents, which are most readily explained by exchange with pore fluids and incorporation of contemporary seawater. The second group shows $\delta^{234}U_{sec}$ near secular equilibrium and elevated $\delta^{238}U$ values. Limited deviations of $\delta^{234}U_{sec}$ from secular equilibrium imply that these teeth did not experience recent resetting, Examination of a $\delta^{238}U$ vs. U/Th plot (**Fig. 4.9c**) shows that the spread in $\delta^{238}U$ of the samples is not primarily controlled by incorporation of a detrital component. Since large $\delta^{238}U$ variations reflecting globally expanded marine anoxia/oxygenation were not observed during the Cenozoic (Gothmann et al. 2019; Goto et al. 2014; Wang et al. 2016), the higher $\delta^{238}U$ values of the second group from GOM are best explained by the locally reducing conditions driving U isotope fractionation during early U uptake in the samples.

Pisco Basin (Peru)

Most Miocene shark teeth from Peru show moderate enrichment in ^{238}U relative to the modern seawater (<+0.4 ‰). This range of δ^{238}U values is similar to the one observed in the surrounding sediments, suggesting that the addition of reduced isotopically heavy U may contribute to the δ^{238}U observed in shark teeth. The lack of correlation between δ^{238}U and 1/[U] reveals however a more complicated U evolution history than for the samples from GOM, whereby the addition of heavy U only influenced but did not dominate the U isotope signals in shark teeth. It is notable that one sediment sample has an extremely high δ^{238}U value (+1.38 ‰), which is much higher than the δ^{238}U signatures of the sediments from the representative anoxic setting – the Black Sea (Andersen et al. 2014; Brüske et al. 2020a; Montoya-Pino et al. 2010; Rolison et al. 2017). This observation reflects that ^{238}U can be preferentially scavenged into sediments under local reducing conditions, which also results in a decrease in the seawater δ^{238}U value. The incorporation of such seawater can explain why some shark teeth from Peru have δ^{238}U values much lower than modern seawater. Sediments from the Pisco Basin show large variations in δ^{238}U values (-0.45–+1.38 ‰), indicating potential spatial–temporal changes in the redox state of the local burial environment. In most of the samples, the secular equilibrium δ^{234}U$_{\text{sec}}$ values indicate that the incorporation of U happened more than ~2 Myr ago. In a small subset of the samples, modern seawater δ^{234}U$_{\text{sec}}$ values, indicating the recent exchange with the seawater.

4.1.4.4 Outlook for U isotopes in fossil fish teeth as a paleoredox proxy

Our results demonstrate that shark teeth were affected by post-depositional processes, which modified their primary U isotope signatures to varying degrees. Given that such sample alteration is common in paleoenvironmental reconstructions, and keeping in mind the relatively small data set for fossil shark teeth, we conduct a preliminary evaluation of the robustness of the teeth paleoredox proxy against other widely used archives, including corals (Chen et al. 2018a,b; Gothmann et al. 2019; Kipp et al. 2022; Romaniello et al. 2013), marine carbonate sediments (Bura-Nakić et al. 2018; Chen et al. 2018b, 2021b, 2022b; Clarkson et al. 2021b; Lau et al. 2022; Martin et al. 2023; Noordmann et al. 2016; Romaniello et al. 2013; Tissot et al. 2018; Zhang et al. 2023), and ferromanganese crusts (Goto et al. 2014; Wang et al. 2016).

The spread of U isotopes in Cenozoic samples from these 4 types of archives are shown in **Fig. 4.12** and **Table 4.3**. Previous studies suggested indistinguishable seawater δ^{238}U throughout the Cenozoic (Gothmann et al. 2019; Wang et al. 2016). If correct, this means that a faithful U isotope archive preserving the primary seawater signature should have δ^{238}U resembling modern seawater and δ^{234}U$_{\text{sec}}$ near secular equilibrium. As is well-known (*e.g.,* Kipp et al. 2022), corals can preserve superbly the original seawater signals, showing very limited variations in both δ^{238}U and δ^{234}U$_{\text{sec}}$, as well as δ^{238}U values concentrated around the modern seawater composition. Iron-manganese crusts also show limited variations in δ^{238}U centered around the seawater value, but serious doubts have been raised regarding the primary nature of these signatures (Li and Tissot 2023). Indeed, Fe-Mn crusts have ^{234}U/^{238}U ratios widely out of secular equilibrium, and, in many cases, offset towards the modern seawater value, suggesting recent U exchange and equilibration between the Fe-Mn crusts and seawater. Compared to corals, fossil shark teeth and carbonates display much larger U isotope variations, indicating a more complicated U incorporation history, and thus redox inferences that are bound to be more uncertain.

The limited data on fossil shark teeth samples prevents a proper statistical analysis. Taken at face value, fossil shark teeth have an average δ^{238}U value (-0.22 ‰) closer to modern seawater (-0.379 ‰) than carbonate sediments, which are biased towards higher values (-0.16 ‰, as noted in Chen et al. 2018b; Tissot et al. 2018). On the other hand, the fossil shark teeth data display slightly larger δ^{238}U variations (±0.31 ‰, 1SD) compared to carbonates (±0.22 ‰, 1SD). While the performance of fossil shark teeth as recorder of seawater U isotope composition can appear to roughly match that of carbonates, we emphasize that this conclusion is only a first-order assessment and is likely to be biased by (i) the different sample sizes ($n_{shark_{t}eeth}$ = 39, $n_{carb_{s}ed}$ = 458), and (ii) the clear evidence for recent addition of seawater U in the Arctic samples. Furthermore, diagenetic alterations are common in fossil shark teeth (*e.g.,* Toyoda and Tokonami 1990; Tütken et al. 2011), and the local scale diagenesis can be unique for each investigated location, complicating inferences of global anoxia with this archive. A full assessment of the potential of U isotopes in fossil shark teeth as a paleoredox proxy will benefit from future work that:

(i) explore geological settings less prone to diagenetic overprinting (*e.g.,* pelagic open ocean).

(ii) use prescreening of well-preserved samples (*e.g.,* appearance and in-situ [U] profiles).

(iii) Implement diagenetic and/or detrital corrections (*e.g.,* δ^{18}O, Mn/Sr/Fe contents,

Table 4.3: Summary of U isotopes in paleoredox archives in Cenozoic (up to 66 Ma): shark teeth (this study), marine carbonate sediments (Bura-Nakić et al. 2018; Chen et al. 2018b, 2021b, 2022b; Clarkson et al. 2021b; Lau et al. 2022; Martin et al. 2023; Noordmann et al. 2016; Romaniello et al. 2013; Tissot et al. 2018; Zhang et al. 2023), coral (Chen et al. 2018a,b; Gothmann et al. 2019; Kipp et al. 2022; Romaniello et al. 2013), Fe-Mn crust (Goto et al. 2014; Wang et al. 2016).

Sample Type	δ^{238}U (‰)					$\delta^{234}U_{sec}$ (‰)				
	min	max	mean	±SD	n	min	max	mean	±SD	n
Shark Teeth	-0.72	0.57	-0.22	0.31	39	-162.1	969.7	181.5	304.5	39
Carbonates	-0.98	0.71	-0.16	0.22	458	-234.0	2669.0	150.9	357.8	310
Fe-Mn Crust	-0.49	-0.30	-0.40	0.04	85	-95.6	117.0	-13.4	41.6	85
Coral	-0.45	-0.07	-0.34	0.07	58	-41.0	580.0	112.4	95.4	46

U/Th, Mn/Sr, Mg/Ca, Sr/Ca, and TOC) to understand if such methods can reliably avoid the pitfalls associated with diagenetic overprints.

Based on the current dataset, we provisionally conclude that shark teeth might have the potential to become a complementary archive for the U proxy, but do not have advantages over carbonate sediments and other more established archives.

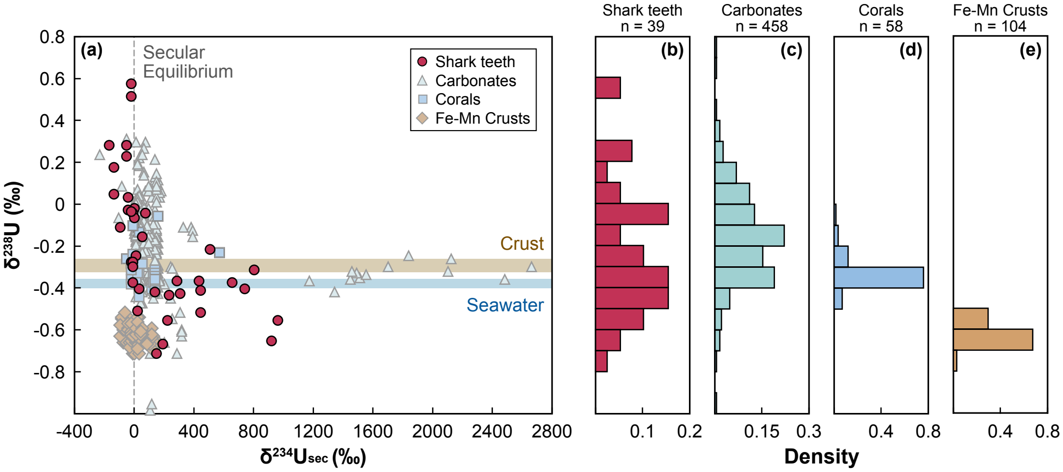

Figure 4.12: U isotopes variations in Cenozoic (up to 66 Ma) shark teeth and various archives used for paleoredox reconstructions. (a) δ^{238}U vs. δ^{234}U$_{\text{sec}}$ (b)–(e) Histogram of δ^{238}U in fossil shark teeth (this study), sedimentary carbonates (Bura-Nakić et al. 2018; Chen et al. 2018b, 2021b, 2022b; Clarkson et al. 2021b; Lau et al. 2022; Martin et al. 2023; Noordmann et al. 2016; Romaniello et al. 2013; Tissot et al. 2018; Zhang et al. 2023), coral (Chen et al. 2018a,b; Gothmann et al. 2019; Kipp et al. 2022; Romaniello et al. 2013), Fe-Mn crust (Goto et al. 2014; Wang et al. 2016). Shark teeth show larger deviations in both δ^{238}U (away from modern seawater) and δ^{234}U$_{\text{sec}}$ (away from secular equilibrium) than Fe-Mn crusts and fossil corals, as well as slightly smaller deviations than carbonates, suggesting that diagenesis, recent U loss/uptake and/or intra-sample U diffusion leads to large offsets between tooth-hosted U isotope ratios and those of coeval seawater. In panel (a), only data for which both δ^{238}U and δ^{234}U$_{\text{sec}}$ are available are shown, while the full dataset is included in panel (b)–(e).

4.1.5 Conclusion

The potential of bioapatite as a novel archive of past seawater δ^{238}U values was tested using fossil shark teeth from three localities (Arctic, GOM, and Peru) and ranging in age from early Eocene to the Miocene. Uranium concentrations in modern and fossil shark teeth differ significantly. Uranium contents are negligible in modern shark teeth (<ppb) but substantially higher and more variable in fossil samples (a few to a few hundred ppm), demonstrating that U was incorporated into shark teeth postmortem during burial. Fossil shark teeth δ^{238}U values range from -0.72 to +0.57 ‰, which is comparable to the variability observed in marine carbonate sediments. The U isotope composition of fossil shark teeth is influenced by local redox conditions and depositional environments. The impacts of these parameters

notably complicate the interpretation of U isotope data in shark teeth. For future applications of δ^{238}U in shark teeth as a paleoredox proxy, screening and correction methods are recommended to overcome the effects of such secondary processes.

4.2 High-precision reappraisal of U isotope composition in modern seawater and deep-sea corals

4.2.1 Motivation

Reconstructing paleo-redox conditions with U isotopes requires archives that record the primary seawater composition, previous work has demonstrated that stony corals provide faithful records (Chen et al. 2018a; Tissot et al. 2018). An essential advantage of the U isotopes over other redox indicators is that it is a global proxy for marine anoxia, so the utility of the U isotope proxy in biogenic carbonate archives relies on the homogeneity of the seawater U isotope composition, which enables samples to be leveraged as a proxy for the entire ocean. While the U isotope composition has been calibrated in modern seawater and biological archives (Chen et al. 1986; Chen et al. 2018a; Cheng et al. 2000; Tissot and Dauphas 2015; Tissot et al. 2018), no study has thoroughly revisited these calibrations with high-precision methods for U isotope analysis. Thus, while the U proxy has been successfully used to track episodes of widespread marine anoxia in the distant past, it has to date not been utilized with sufficient precision to resolve subtle redox changes in more recent geologic history. Such applications could be particularly useful in studying climate evolution in the Quaternary. This work targeted deep-sea scleractinian corals of the taxon *Desmophyllum dianthus* (*D. disnthus* in short), which has been used as an archive of geochemical properties in paleoceanographic studies (*e.g.,* Hines et al. 2015; Robinson et al. 2005; Wang et al. 2017). Individual D. dianthus corals have a lifespan of decades, while populations of D. dianthus corals can persist in habitat for millennia (Thiagarajan et al. 2013) and thus have considerable utility as an archive of Quaternary seawater chemistry.

4.2.2 Sample

Here, 45 seawater and 26 modern deep-sea corals are used for high-precision U isotope measurements. Coral samples were collected from Tasmanian seamounts during cruise TN-228, which are identified as modern samples due to the presence of organic matter. Seawater was sampled from GEOTRACES stations, including cruises GA03, GA02, and GP13 in the North Atlantic, South Atlantic, and South Pacific at depths close to the coral specimens. The locations of seawater and samples are illustrated in **Fig. 4.13**.

4.2.3 Results

Seawater samples analyzed show subtle heterogeneity in δ^{238}U, and to a lesser extent in $\delta^{234}\mathrm{U}_{\mathrm{sec}}$ along depth profiles. Individual seawater samples from the North Atlantic (GA02 and GA03) display a ~0.1 ‰ range in measured δ^{238}U values. The salinity-normalized global mean seawater values for δ^{238}U (-0.379 ± 0.023 ‰) and $\delta^{234}\mathrm{U}_{\mathrm{sec}}$ (+145.55 ± 0.28 ‰). The results demonstrate that these corals record seawater U isotope ratios extremely well within analytical uncertainty. Furthermore, there appear to be subtle differences in both $^{238}\mathrm{U}/^{235}\mathrm{U}$ and $^{234}\mathrm{U}/^{238}\mathrm{U}$ across ocean basins. These findings collectively support the utility of deep-sea corals as archives of ambient seawater U isotope ratios in the past, but highlight the importance of utilizing multiple sample sites, as even in the modern ocean there is observable heterogeneity that could influence paleo-proxy interpretations.

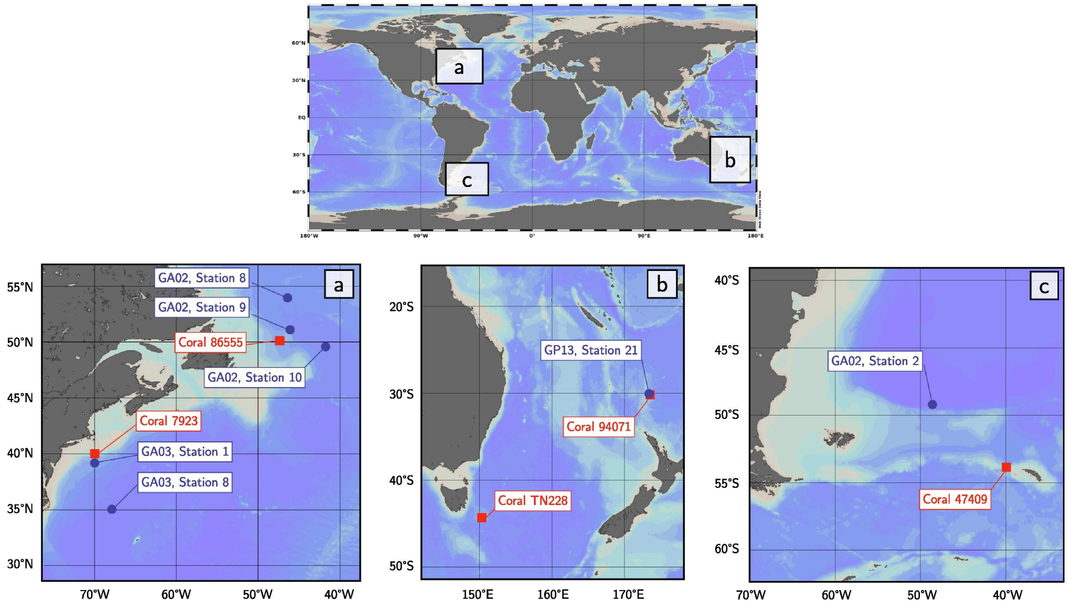

Figure 4.13: Locations of seawater and coral samples. GEOTRACES stations marked with blue circles; coral sites marked with red squares.

Table 4.4: Uranium isotope data of modern seawater and deep-sea corals

Sample	Lat	Long	depth (m)	δ^{238}U	2SE	$\delta^{234}\text{U}_{\text{sec}}$	2SE	salinity	U (ppb)	n
North Atlantic										
GEOTRACES										
GA03	35.418	293.474	235.7	-0.387	0.036	145.73	0.35	36.60	3.02	8
GA03	39.686	290.187	420	-0.400	0.054	145.56	0.33	35.10	3.04	9
GA03	35.418	293.474	422.5	-0.414	0.036	145.75	0.35	36.51	3.04	8
GA03	39.686	290.187	475	-0.358	0.045	146.22	0.43	35.07	3.05	5
GA03	39.686	290.187	526	-0.380	0.044	144.98	0.23	35.05	2.98	13
GA03	35.418	293.474	552.3	-0.355	0.046	145.27	0.27	36.21	3.14	13
GA03	39.686	290.197	600	-0.392	0.038	145.65	0.32	35.02	2.99	8
GA03	39.686	290.197	665	-0.373	0.038	145.63	0.32	34.99	2.93	8
GA03	35.418	293.474	803.6	-0.358	0.046	145.33	0.27	35.34	2.99	13
GA03	39.686	290.197	825	-0.355	0.040	146.15	0.28	34.96	2.89	11
GA02	49.722	317.552	1012	-0.337	0.045	145.71	0.25	34.94	2.83	7
GA02	51.820	314.268	1014	-0.347	0.046	145.57	0.27	34.89	2.93	13
GA02	51.820	314.268	1258	-0.405	0.047	145.57	0.28	34.90	3.05	12
GA02	49.722	317.552	1262	-0.357	0.048	145.65	0.27	34.91	3.05	6
GA03	39.686	290.197	1501	-0.361	0.048	145.74	0.30	34.96	2.91	11
GA02	49.722	317.552	1517	-0.407	0.040	145.91	0.26	34.92	2.91	7
GA02	51.820	314.268	1521	-0.431	0.042	145.40	0.21	34.91	3.04	14
GA02	54.063	314.165	1521	-0.400	0.051	145.95	0.31	34.91	3.04	10
GA03	39.686	290.197	1671	-0.386	0.037	145.58	0.23	34.95	3.01	7
GA02	54.063	314.165	1758	-0.390	0.052	145.76	0.31	34.91	3.06	10
GA02	49.722	317.552	1771	-0.392	0.040	145.90	0.26	34.92	3.02	7
GA02	51.820	314.268	1773	-0.407	0.047	145.22	0.17	34.91	2.91	14
GA03	39.686	290.197	1800	-0.402	0.071	145.74	0.52	34.96	3.00	8
GA03	39.686	290.197	2000	-0.382	0.067	145.06	0.52	34.95	3.00	8
GA02	51.820	314.268	2003	-0.413	0.047	145.49	0.17	34.91	2.89	14
GA02	49.722	317.552	2024	-0.386	0.035	146.12	0.23	34.92	3.01	9
GA03	39.686	290.197	2050	-0.413	0.083	145.49	0.38	34.95	2.97	3
D. dianthus										
7923	39.725	290.617	1953–2220	-0.395	0.042	141.33	0.29		3.51	9
78461	38.488	286.973	1990–2175	-0.366	0.041	145.19	0.21		3.91	21
62306	39.775	290.262	1675	-0.386	0.064	141.56	0.26		4.22	6
62309	40.379	292.344	430–613	-0.404	0.030	145.78	0.31		3.39	15
South Atlantic										
GEOTRACES										
GA02	-48.968	311.121	301	-0.407	0.043	145.37	0.30	34.05	3.03	9
GA02	-48.968	311.121	404	-0.374	0.024	145.08	0.37	34.11	2.87	9
GA02	-48.968	311.121	502	-0.356	0.044	144.90	0.39	34.21	2.97	9
GA02	-48.968	311.121	750	-0.396	0.046	145.66	0.16	34.37	3.64	10
GA02	-48.968	311.121	1014	-0.358	0.045	145.52	0.40	34.51	2.99	8
GA03	-48.968	311.121	1267	-0.379	0.042	145.54	0.26	34.63	3.00	7
D. dianthus										
47409	-54.483	320.633	659–686	-0.366	0.034	145.10	0.23		4.71	21
South Pacific										
GEOTRACES										
GP13	-29.999	173.000	15	-0.376	0.036	145.37	0.30	35.64	2.92	21
GP13	-29.999	173.000	30	-0.361	0.038	145.29	0.23	35.64	3.01	25
GP13	-29.999	173.000	50	-0.387	0.029	145.27	0.21	35.64	3.01	21
GP13	-29.999	173.000	75	-0.354	0.027	145.43	0.23	35.64	3.05	25
GP13	-29.999	173.000	100	-0.357	0.030	145.48	0.25	35.64	3.03	21
GP13	-29.999	173.000	150	-0.360	0.028	145.43	0.35	35.60	3.07	21
GP13	-29.999	173.000	200	-0.369	0.026	145.15	0.40	35.56	2.99	23
GP13	-29.999	173.000	300	-0.338	0.030	145.21	0.20	35.43	3.08	21
GP13	-29.999	173.000	500	-0.372	0.027	145.51	0.31	35.00	2.97	20
GP13	-29.999	173.000	750	-0.374	0.033	145.63	0.30	34.64	2.94	19
GP13	-29.999	173.000	1000	-0.375	0.024	145.34	0.31	34.43	2.90	20

Table 4.4: Uranium isotope data of modern seawater and deep-sea corals

Sample	Lat	Long	depth (m)	δ^{238}U	2SE	$\delta^{234}\mathrm{U}_{\mathrm{sec}}$	2SE	salinity	U (ppb)	n
GP13	-29.999	173.000	1450	-0.379	0.026	145.76	0.32	34.55	2.86	19
D. dianthus										
94071	-30.717	173.28	590–640	-0.370	0.031	145.44	0.34		3.71	9
TN228	-44.8	150.3	2395	-0.331	0.044	145.31	0.42		5.75	13
TN228	-44.8	150.3	2395	-0.361	0.073	145.21	0.41		5.67	11
TN228	-44.8	150.3	2395	-0.385	0.053	145.20	0.28		5.28	12
TN228	-44.8	150.3	2395	-0.380	0.074	145.11	0.34		5.34	9
TN228	-44.8	150.3	2395	-0.402	0.069	145.06	0.35		5.33	9
TN228	-44.8	150.3	2395	-0.324	0.034	145.20	0.40		5.23	8
TN228	-44.8	150.3	2395	-0.338	0.067	145.10	0.36		5.34	9
TN228	-44.8	150.3	2395	-0.366	0.050	145.34	0.31		5.08	12
TN228	-44.8	150.3	2395	-0.425	0.058	144.03	0.34		5.12	9
TN228	-44.8	150.3	2395	-0.361	0.061	145.26	0.23		4.92	9
TN228	-44.8	150.3	2395	-0.355	0.083	144.70	0.30		4.67	8
TN228	-44.8	150.3	2395	-0.373	0.045	145.37	0.35		4.68	8
TN228	-44.8	150.3	2395	-0.374	0.051	144.75	0.38		4.66	9
TN228	-44.8	150.3	2395	-0.344	0.045	144.89	0.40		4.69	8
TN228	-44.8	150.3	2395	-0.377	0.041	144.58	0.40		4.73	9
TN228	-44.8	150.3	2395	-0.365	0.051	145.70	0.35		4.47	8
TN228	-44.8	150.3	2395	-0.400	0.060	145.41	0.26		4.56	9
TN228	-44.8	150.3	2395	-0.371	0.038	145.50	0.20		4.64	8
TN228	-44.8	150.3	2395	-0.375	0.075	145.25	0.22		4.58	10
TN228	-44.8	150.3	2395	-0.373	0.079	144.94	0.33		4.63	9
Geostandard										
BCR-2	-0.291	0.047	0.41	0.31					1.63	9
BCR-2	-0.226	0.036	0.66	0.55					1.61	4
BCR-2	-0.229	0.032	0.53	0.67					1.71	4
BCR-2	-0.235	0.060	0.84	0.38					1.74	8
BCR-2	-0.277	0.034	0.71	0.15					1.59	19
BCR-2	-0.264	0.025	0.65	0.21					1.59	16
BCR-2	-0.243	0.025	0.52	0.16					1.59	21
BCR-2	-0.299	0.040	0.59	0.20					1.59	14
BCR-2	-0.269	0.022	0.65	0.16					1.59	25
BCR-2	-0.265	0.036	0.75	0.18					1.58	11
BCR-2	-0.263	0.036	0.70	0.29					1.58	11

Appendix A

Figure A.1: Photos of shark teeth investigated in this study.

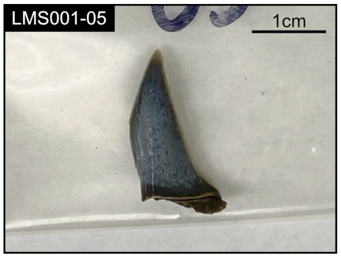
LMS001-05


LMS001-08


JAH001-2

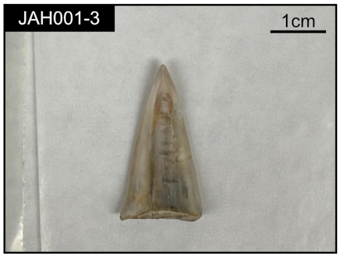
JAH001-3


SS001-04

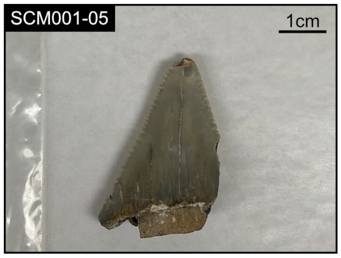
SCM001-05


SCM001-08


CMTR001-04


SLK-UC-102

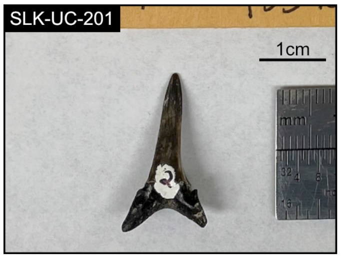
SLK-UC-201

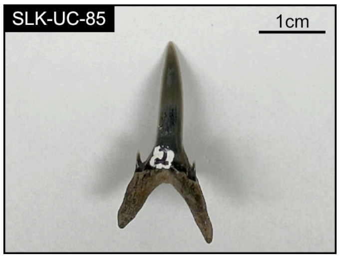
SLK-UC-85

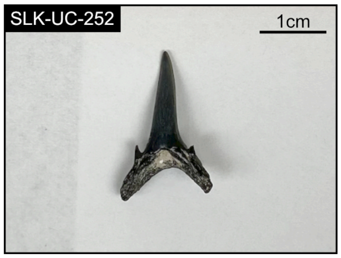
SLK-UC-252


SLK-UC-218

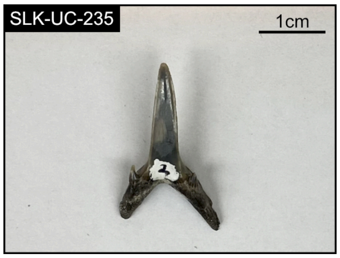
SLK-UC-235


TMM40278-1-01


TMM40278-1-02


TMM40278-1-BB


TMM45995-1-01

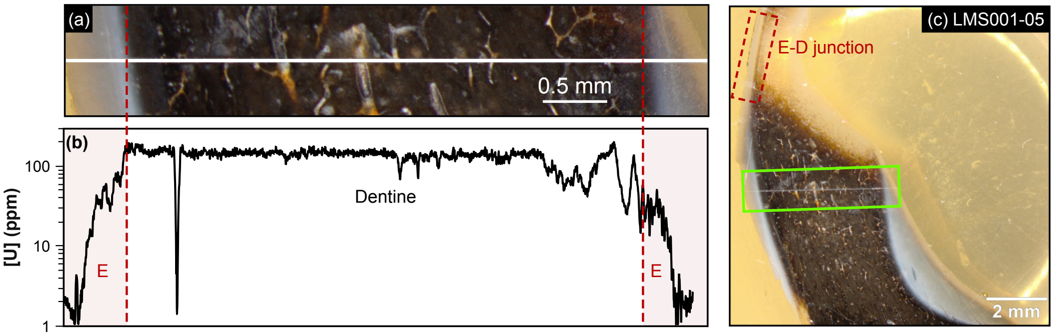

Figure A.2: U concentration trends across fossil shark tooth LMS001-05 from the Pisco Basin. (a) Microscope image (transmitted) of a laser ablated cross section through the . (b) LA-ICPMS U concentration profile. The significant drops and fluctuations of [U] in the dentine are due to the dental pulps and cracks. (c) Microscope image of the epoxy mount of the investigated fossil shark tooth. The red dash line rectangle high-lights the enameloid-dentine junction, with a clear boundary between the two tissues, and the green rectangle shows the location of the ablated area in panel (a).

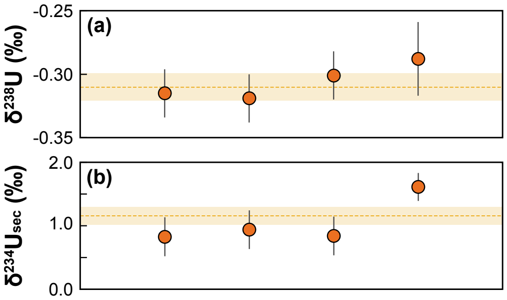

Figure A.3: Replicate measurements of (a) δ^{238}U and (b) δ^{234}U$_{\text{sec}}$ in enameloid of a *Otodus megalodon* tooth (EK). Enameloid was chipped off the shark tooth and then ground with a mortar and pestle. The 4 replicates were sub-sampled from the enameloid powder. The orange dash lines and bands show the average values and uncertainties of these 4 replicates.

Table A.1: Major and trace element concentrations (in ppm) of shark teeth and sediments measured in this study.

Sample	**Al**	**Ti**	**V**	**Mn**	**Fe**	**Y**	**La**	**Ce**	**Pr**	**Nd**	**Sm**	**Eu**	**Gd**	**Tb**	**Dy**	**Ho**	**Er**	**Tm**	**Yb**	**Lu**
2004-31-01	515.1	1559.6	4.95	188.3	4531.7	67.63	29.47	72.58	12.26	52.50	14.24	3.57	15.16	2.52	14.21	4.59	7.46	0.97	5.81	0.79
2004-31-02	477.1	1742.4	6.11	149.3	3743.4	113.43	30.16	93.69	13.43	55.53	16.78	4.38	18.59	3.32	19.38	3.68	10.59	1.41	8.76	1.17
2004-31-03	747.5	1708.7	11.12	249.7	5365.6	551.73	33.58	142.16	27.64	151.10	49.49	12.68	58.72	10.58	66.87	14.64	42.60	5.68	33.00	4.79
2004-31-04	1259.9	1630.6	12.94	268.0	5260.5	336.88	27.34	117.54	21.74	112.95	37.16	9.79	43.48	7.98	49.51	10.33	30.08	4.01	23.80	3.40
2004-31-05	1165.4	1632.5	7.36	176.9	4400.9	158.64	15.14	62.62	10.96	56.08	17.80	4.62	19.85	3.50	20.87	4.35	12.44	1.63	9.62	1.38
2004-31-06	673.0	2333.5	7.68	139.3	3571.4	216.45	35.19	123.84	19.69	92.15	30.75	8.84	35.88	6.44	38.49	7.45	21.05	2.82	17.10	2.32
SLK2004-13-4	173.1	1593.2	5.21	137.9	3467.6	122.10	47.27	144.22	22.24	97.37	27.71	6.77	30.60	5.11	28.71	6.88	14.18	1.75	9.92	1.35
SLK2004-13-3	237.4	1606.5	5.80	116.6	3826.1	141.86	52.61	161.91	24.92	107.12	30.03	7.23	33.59	5.75	32.65	6.47	16.86	2.07	12.04	1.64
SLK2004-13-1	212.4	1667.2	4.67	70.4	3270.2	48.39	12.51	45.95	6.84	30.75	9.89	2.58	11.10	2.01	11.80	4.27	5.95	0.77	4.41	0.60
BKS04-19	285.0	721.7	4.69	111.8	2725.9	68.76	17.52	61.65	9.43	42.38	12.15	3.06	13.92	2.45	14.56	2.83	8.02	0.99	5.64	0.81
BKS2004-31	388.3	792.7	2.84	95.0	2306.4	42.77	7.57	25.20	4.18	19.70	6.72	1.95	7.81	1.44	8.90	1.76	5.06	0.67	3.98	0.57
SLK-UC-102	133.2	1671.5	3.39	157.0	2317.9	29.73	26.29	46.85	7.12	29.49	7.24	1.63	7.79	1.14	6.27	4.22	3.38	0.43	2.51	0.36
SLK-UC-201	157.5	1885.0	11.20	360.0	1415.8	1061.36	666.01	1363.52	176.87	729.28	204.48	47.57	250.87	39.22	210.72	43.18	116.35	14.67	86.86	12.25
SLK-UC-85	117.1	2722.9	3.13	170.5	648.3	46.30	36.26	80.21	11.17	46.64	12.27	2.73	12.99	1.85	10.05	2.70	5.10	0.63	3.86	0.53
SLK-UC-252	168.5	1480.6	5.75	108.1	1820.5	31.56	25.95	51.59	6.81	28.63	7.01	1.58	7.77	1.12	6.26	3.17	3.39	0.43	2.56	0.37
SLK-UC-218	31.5	1612.4	2.88	184.6	563.9	47.13	28.90	70.65	9.67	41.01	11.90	2.72	13.14	1.93	10.15	5.38	4.98	0.63	3.74	0.51
SLK-UC-235	125.6	1963.1	3.53	132.1	839.5	57.68	52.00	96.93	14.56	59.70	15.10	3.30	15.80	2.23	12.22	3.59	6.48	0.82	5.02	0.70
TMM40278-1-01	1661.3	1649.1	5.57	222.4	1977.5	688.16	379.89	527.84	81.75	306.04	82.14	14.43	92.84	16.07	103.48	23.48	76.76	11.82	85.32	13.11
TMM40278-1-02	61.7	1580.8	7.22	14.6	234.6	27.76	19.42	46.21	5.20	20.15	4.21	1.01	4.43	0.64	3.61	0.72	2.09	0.27	1.72	0.24
TMM40278-1-BB	3977.0	1545.6	5.27	355.6	4122.8	1579.48	1198.30	2562.05	354.52	1205.06	310.68	51.39	285.21	48.45	287.11	54.04	164.19	27.97	201.16	29.55
TMM45995-1-01	116.3	1689.5	5.21	20.7	440.3	15.14	15.59	36.86	3.96	15.50	3.07	0.74	3.26	0.48	2.73	2.60	1.64	0.22	1.37	0.19
TMM45995-1-02	1679.4	1621.4	8.17	608.9	1778.1	804.97	436.72	421.28	65.34	247.78	53.44	9.84	76.98	12.84	89.53	22.56	77.99	11.91	81.06	13.70
TMM45995-1-03	41.6	1652.2	7.27	23.2	294.5	24.84	23.08	60.47	6.36	24.85	5.16	1.25	5.31	0.78	4.34	0.87	2.46	0.32	1.99	0.28
P1007-01	638.5	1655.4	5.25	120.9	846.0	10.92	17.77	36.58	4.08	14.31	2.60	0.30	2.52	0.34	1.75	1.31	0.91	0.11	0.63	0.09
P1007-02	317.3	1703.8	6.64	74.3	420.1	28.23	34.13	70.40	8.26	29.51	5.44	0.62	5.32	0.68	3.53	0.68	1.88	0.22	1.26	0.17
P1007-03	234.1	1769.2	5.47	73.0	619.7	19.73	18.29	44.35	5.13	18.78	3.84	0.49	3.63	0.50	2.55	0.49	1.32	0.17	0.97	0.13
P1007-04	420.6	1684.2	6.37	121.2	794.3	4.13	3.29	7.32	0.85	3.18	0.62	0.10	0.64	0.09	0.48	0.09	0.28	0.04	0.22	0.03
LMS001-05	81.2	1595.0	3.28	219.9	332.6	113.44	72.49	126.97	17.98	71.87	17.51	1.69	20.00	3.03	16.55	3.88	9.00	1.11	6.47	0.91
LMS001-08	2377.3	1548.3	11.47	515.3	1601.1	655.10	216.98	796.29	146.26	670.36	187.19	16.60	165.67	23.75	114.75	17.35	50.45	6.14	36.44	4.92
JAH001-02	2897.9	1468.6	13.87	356.8	985.8	105.01	29.93	112.52	19.70	101.01	27.09	4.12	25.36	3.63	18.47	4.28	8.85	1.07	6.27	0.86
JAH001-03	136.4	1565.7	7.86	112.4	772.3	5.89	11.75	7.22	1.64	5.98	0.92	0.15	0.98	0.12	0.66	1.31	0.41	0.05	0.30	0.05
SS001-04	245.5	1813.9	5.92	89.4	741.4	6.78	10.14	22.14	2.75	10.33	2.03	0.31	1.92	0.26	1.32	4.99	0.69	0.09	0.53	0.08
SCM001-05	447.8	1535.5	6.19	66.7	578.9	9.84	6.94	17.10	1.80	6.98	1.37	0.28	1.49	0.21	1.29	1.00	0.89	0.12	0.74	0.11
SCM001-06	552.6	1605.2	5.17	75.3	454.7	11.91	15.13	37.34	4.06	14.73	2.78	0.52	2.69	0.37	2.08	2.12	1.28	0.17	1.10	0.16
CMTR001-04	3412.4	1565.0	8.53	260.2	2107.5	914.06	73.36	393.30	104.85	702.95	258.58	30.59	249.04	38.50	187.69	32.25	85.33	10.80	66.14	8.60
P1007-01_D	142.1	1409.2	13.50	1533.6	929.0	3.40	0.73	2.02	0.36	1.71	0.42	0.07	0.53	0.08	0.41	0.08	0.23	0.03	0.17	0.03
LMS001-08_D	3830.0	1566.5	30.28	605.6	3167.5	2499.26	360.44	1239.88	239.70	1267.35	315.66	32.08	407.02	57.56	297.93	59.43	158.30	18.76	104.21	15.67
SS001-04_D	1370.1	1882.4	44.12	2791.8	10063.5	77.25	133.41	134.71	14.47	49.93	7.35	1.22	9.48	1.28	7.68	1.73	5.58	0.77	5.29	0.86
SCM001-06_Dc	804.8	1720.2	26.54	756.0	1470.1	70.15	62.84	126.10	14.51	52.83	9.89	1.98	10.21	1.50	8.94	1.90	6.03	0.87	5.58	0.84
SCM001-06_Dr	2546.1	2033.6	44.96	605.2	5607.1	112.37	118.92	218.14	26.53	94.34	16.83	3.30	17.74	2.58	15.47	3.37	10.81	1.53	10.13	1.55
TMM40278-1-BB_D	11346.9	1584.1	16.04	1511.8	17096.1	3246.34	2843.76	5925.37	851.27	2883.53	710.31	119.02	686.02	121.13	716.23	137.00	422.78	69.79	506.16	72.36
BKS04-19_sed	10629.2	499.9	85.79	638.0	77651.0	28.38	13.02	30.20	4.14	17.14	4.19	1.12	5.01	0.83	4.96	1.04	3.02	0.40	2.42	0.36
BKS2004-31_sed	15828.5	603.2	64.94	2087.3	62056.5	8.02	9.36	18.94	2.29	8.42	1.79	0.49	1.86	0.28	1.61	0.31	0.95	0.13	0.88	0.13
JAH010_sed	29172.5	3032.9	80.83	452.2	24035.2	10.88	15.20	31.16	3.99	14.78	2.89	0.63	2.69	0.39	2.11	0.42	1.25	0.17	1.12	0.17
JBL002_sed	30081.1	3542.4	116.73	487.1	33583.9	14.34	17.52	42.17	5.75	21.08	4.43	0.77	3.82	0.56	2.99	0.56	1.71	0.23	1.54	0.22
SS003_sed	12549.2	1053.9	18.38	827.7	4858.0	6.68	8.25	16.47	2.00	7.15	1.36	0.26	1.32	0.20	1.12	0.23	0.70	0.10	0.61	0.09
SCM002_sed	27646.8	1327.6	25.74	112.2	6120.5	10.90	13.99	28.86	3.49	12.38	2.27	0.53	2.16	0.31	1.75	0.37	1.13	0.16	1.02	0.15
P1002_sed	26182.9	1340.0	25.65	499.0	8668.0	10.89	15.66	32.33	3.69	12.81	2.39	0.46	2.33	0.35	1.98	0.41	1.23	0.17	1.12	0.16

Chapter 5

CONTINUOUSLY HETEROGENEOUS INFALL OF THE EARLY SOLAR SYSTEM FROM MAGNESIUM ISOTOPES IN REFRACTORY INCLUSIONS

5.1 Motivation

Calcium-aluminum-rich inclusions (CAIs) are the oldest dated solids (4567.2 Ma, Amelin et al. 2010; Connelly et al. 2012) in the Solar System (SS), with refractory mineralogy closely resembling the first phases to condense from the solar nebula predicted by thermodynamic calculations (Grossman 1972). CAIs are thought to form from the early infalling materials from the SS's parental molecular cloud in a hot protoplanetary disk region most likely near the protosun (Burkhardt et al. 2019; Jacquet et al. 2019; Jansen et al. 2024; Nanne et al. 2019). After the formation in the inner SS, CAIs were transported outwards to the outer SS where carbonaceous chondrites accreted (*e.g.,* Yang and Ciesla 2012). As a result, CAIs can provide unique insights into the properties of the materials infalling onto the nascent Sun, as well as disk dynamics in the early SS. A powerful approach to explore the infalling materials composition is isotopic variations of CAIs, especially nucleosynthetic anomalies, which are not susceptible to subsequent processing (*e.g.,* evaporation, condensation, and secondary alterations) and transport of material in the solar nebula that can modify the primary signatures. Previous studies have demonstrated that CAIs have significantly distinct isotopic compositions compared with late-formed materials in the SS (see Dauphas and Schauble 2016 for review). However, the extent and distribution of isotopic variations among CAIs are still not well constrained, and thus, whether CAIs only captured a transient snapshot or a series of evolving records of the primordial SS remains an open question.

Short-lived ^{26}Al–^{26}Mg systematic is particularly interesting for investigating CAI precursors that reflect the composition of infalling materials. The former presence of radionuclide ^{26}Al ($t_{1/2} = 0.72$ Myr) in the majority of CAIs results in ^{26}Mg excesses that are positively correlated with ^{27}Al/^{24}Mg ratio, indicating the ingrowth of ^{26}Mg by the decay of ^{26}Al. While the internal ^{26}Al–^{26}Mg isochrons obtained from different phases typically acts as a relative chronometer of the last melting event, the isochron inferred from bulk analyses characterized the reservoir that CAIs condensed from: the slope (initial ^{26}Al abundance: ^{26}Al/^{27}Al) dates the formation of CAI precursors, and the intercept (initial ^{26}Mg/^{24}Mg composition: $\delta^{26}\mathrm{Mg}^*_0$) constrains the Mg isotope composition of CAI precursor materials before the decay of ^{26}Al.

Early studies on high-precision Mg isotope of bulk CAIs from CV3 chondrite define a single isochron with slope of canonical $^{26}\mathrm{Al}/^{27}\mathrm{Al}$ value of $(5.30 \pm 0.06) \times 10^{-5}$, and intercept of -0.028 ‰ (Jacobsen et al. 2008; Larsen et al. 2011). Numerous in-situ $^{26}\mathrm{Al}$–$^{26}\mathrm{Mg}$ analyses have found some slightly variable $\delta^{26}\mathrm{Mg}_0^*$ in CAIs. While the elevated $\delta^{26}\mathrm{Mg}_0^*$ can be explained as the later remelting and $^{26}\mathrm{Al}$ decay in the solar nebula, the large negative values suggest resolvable Mg isotope heterogeneity during the CAI formation epoch (*e.g.,* MacPherson et al. 2017; Wasserburg et al. 2012) and lead to the question how representative the canonical bulk isochron reflects the known CAI population. Recently, the observation of two parallel bulk isochrons defined by CAIs from CV and CR chondrites, respectively, further confirmed the presence of Mg isotope heterogeneity among CAIs and was interpreted as evidence for episodic formation of CAIs in the early SS (Larsen et al. 2020). However, this finding is contrary to the observation of other isotope systems that CAIs show a gradual transition covering a wide range of isotopic composition. This discrepancy may be due to a general scarcity of the bulk Mg isotope data and all CAIs of the CV group are from Allende and Efremovka. Here, we addressed this question by determining the Mg isotope composition for 19 various types of CAIs from multiple carbonaceous chondrites (CV3 group: $\mathrm{CV_{ox}}$: Allende, Axtell, and NWA 3118; $\mathrm{CV_{red}}$: Efremovka and Leoville) that cover a broad representation of the known CAI population. We combine these bulk Mg measurements with the in-situ $^{26}\mathrm{Al}$–$^{26}\mathrm{Mg}$ analyses of 11 CAIs from the same batch of samples (see materials and method section in supplementary for details).

5.2 Materials and method

5.2.1 Sample selection

In this work, 19 CAIs are selected to obtain a broad representation of the known CAI population, which are from different types of host meteorites ($\mathrm{CV_{ox}}$: Allende, Axtell, and NWA 3118; $\mathrm{CV_{red}}$: Efremovka and Leoville). The CAIs used in this study comprise fine-grained (fg), fluffy Type A (FTA), compact Type A (CTA), Type B, and forsterite-bearing Type B (FoB). This sample set was previously investigated in Budde et al. (2023) and Tissot et al. (2019b) for other isotopic systems. Given the collection name can be long, a shorter name is assigned for each CAI in these two studies. Samples with short name started with CG*ft* and AVLIN (a.k.a TS-45) are from Tissot et al. (2019b), and those started with CT are from Budde et al. (2023).

5.2.2 Sample preparation

These CAIs were cut out of their host meteorites using a diamond saw, and carefully extracted from the matrix materials using dental tool to minimize the contamination. Then, the surface of CAI fragments was cleaned using SiC sandpaper and/or gently broke into small pieces in a precleaned agate mortar. For most of CAIs

(CG*ft*-4–8, 10–13, CT23, 24, 41), a small piece of each CAI was mounted in epoxy and carbon coated for petrological characterization and in-situ ^{26}Al-^{26}Mg analyses. The remaining CAI materials were cleaned by sonicating in dilute HNO_3, MQ and ethanol, and then ground with clean pestle and agate mortar for the solution work.

Sample digestions and dilutions used trace-metal-clean acids (purified via two rounds of sub-boiling distillation) and acid-cleaned PFA beakers. CAI powders were dissolved by consecutive acid attacks by slightly different method. For CAIs from Tissot et al. (2019b), ∼200 mg was digested in concentrated HF-HNO_3-$HClO_4$ (2:1:0.05 by volume) at 150 °C for 9 days. The digests were used for non-spiked W chemistry, and the matrix cuts were preserved for Mg isotope analyses. For CAIs from Budde et al. (2023), samples were digested using HF-HNO_3-$HClO_4$ and HNO_3-HCl mixtures on hotplate. To monitor long-term external reproducibility, several powder aliquots of geostandards BCR-2, BHVO-2 and DTS-2 were digested in parallel to CAIs. The following Mg wet chemistry and isotope analyses are all performed at the Isotoparium (Caltech).

5.2.3 Petrological characterization

Five CAIs of this study were described in previous studies: CT36(49E), 38(16N), and 39(9bN) in Ivanova et al. (2015), ALVIN in Bullock et al. (2012) and CT37(4N) in MacPherson et al. (2017). For the newly investigated CAIs, the mineralogy and petrology were characterized using a JEOL JSM-5900LV scanning electron microscope (SEM) at University of Hawaii at Manoa (CG*ft*-4–8, 10–13) or a ZEISS 1550VP Field Emission SEM at Caltech (CT23, 24, 41). Backscattered electron (BSE) and combined X-ray elemental (Ca, Al, and Mg) maps of these CAIs are obtained by using 15 keV accelerating voltage, 100 nA beam current, and beam sizes of 2–10 μm depending on the size of the CAI.

5.2.4 Mg isotope analyses

After the digestion, small aliquots were taken for concentration measurements on an iCAP RQ ICPMS (ThermoFisher). Based on Mg concentration data, aliquots containing 5–10 μg were taken for Mg purification and isotopic analyses. Then, the aliquots were completely dried down and redissolved in 0.5 M HCl for chemistry. The Mg column chemistry and mass spectrometry followed the protocols described in **Section 2.3**. Each CAI was measured at least 9 times, and geostandards ranged from 6–26 times. Replicate measurements of geostandards were used to monitor the accuracy of Mg isotope data: BCR-2 gave δ^{25}Mg = -0.151 ± 0.013 ‰, δ^{26}Mg = -0.322 ± 0.024 ‰, and δ^{26}Mg* = -0.044 ± 0.008 ‰ (n = 12); BHVO-2 gave δ^{25}Mg = -0.136 ± 0.011 ‰, δ^{26}Mg = -0.270 ± 0.021 ‰, and δ^{26}Mg* = -0.019 ± 0.007 ‰ (n = 12); DTS-2 gave δ^{25}Mg = -0.178 ± 0.010 ‰, δ^{26}Mg = -0.354 ± 0.019 ‰, and

$\delta^{26}Mg^*$ = -0.027 ± 0.05 ‰ (n = 26), which are consistent with previously reported values (Huang et al. 2009; Teng et al. 2007, 2015).

To determine $^{27}Al/^{24}Mg$ ratios, concentration standard (50 ppb Mg, 150 ppb Al) was prepared by diluting SPEX CertiPrep ICP-MS single-element standards. The Al/Mg ratio of the prepared concentration standard was calibrated as 3.042 by the gravimetric method. The $^{27}Al/^{24}Mg$ ratios ratios were measured on MC-ICPMS using the same setting up as Mg isotopes. Sample standard bracketing method was applied, and all data were collected in 10 cycles of 4.194 s integration time.

5.2.5 In-situ Al-Mg analyses

In-situ ^{26}Al-^{26}Mg isotope analyses were performed on CAMECA IMS 1270-E7 and IMS 1280-HR2 at CRPG following the method described in previous studies (Luu et al. 2013; Piralla et al. 2023; Villeneuve et al. 2009). Measurements were conducted in multicollection mode on 4 Faraday cups (FC): ^{24}Mg on L1 equipped with a 10^{11} Ω resistor, ^{25}Mg and ^{26}Mg on C and H1 equipped with 10^{12} Ω resistors and ^{27}Al on H'2 equipped with a 10^{11} Ω resistor. Mass resolution was set to 2500 (*i.e.,* exit slit 1 on multicollection trolleys) to separate the doubly charged interference $^{48}Ca^{2+}$ and $^{48}Ti^{2+}$. Selected spots were bombarded with a <10 μm, 5 nA O_2^- primary ion beam generated by a Hyperion-II oxygen plasma source accelerated at 13 keV. The instrumental mass fractionation (IMF) was calibrated by a series of international and in-house standards, including San Carlos olivine, Burma spineal, CLDR01 MORB glass, gold enstatite, and Allende melilite (Mel-1) glass. To precisely determine the $^{27}Al/^{24}Mg$ ratios for isochron, the measured values were corrected using the relative sensitivity factor (RSF) for different mineral phases, given that Al and Mg have slightly different ion yields during SIMS analyses. The $^{27}Al/^{24}Mg$ ratios of analyzed CAI minerals, including melilite, spinel, anorthite, and hibonite were calibrated by RSFs determined by Mel-1, 2 glass, Burma spinel, An-2 glass, Al-rich pyroxene glass, and Hib-A-00, respectively.

5.3 Results

5.3.1 Description of CAIs

Petrology and mineralogy characterization of CAIs categorized the type of the newly analyzed samples, including 2 FTA, 8 CTA, and 3 Type B CAIs. Combined elemental and BSE maps of analyzed CAIs are shown in **Figs. 5.1–5.9**).

CG*ft*-7 and 8 are FTA CAIs with highly irregular shapes and mineralogy that includes gehlenitic melilite and spinel. CG*ft*-8 shows the aggregate structure comprised of melilite nodules enclosed spinel. Some nodules are surrounded by Al-diopside rims, and secondary veins fill the interstitial space between nodules. CG*ft*-7 contains large spinel grains (a few hundred μm) and minor perovskite compared with CG*ft*-8.

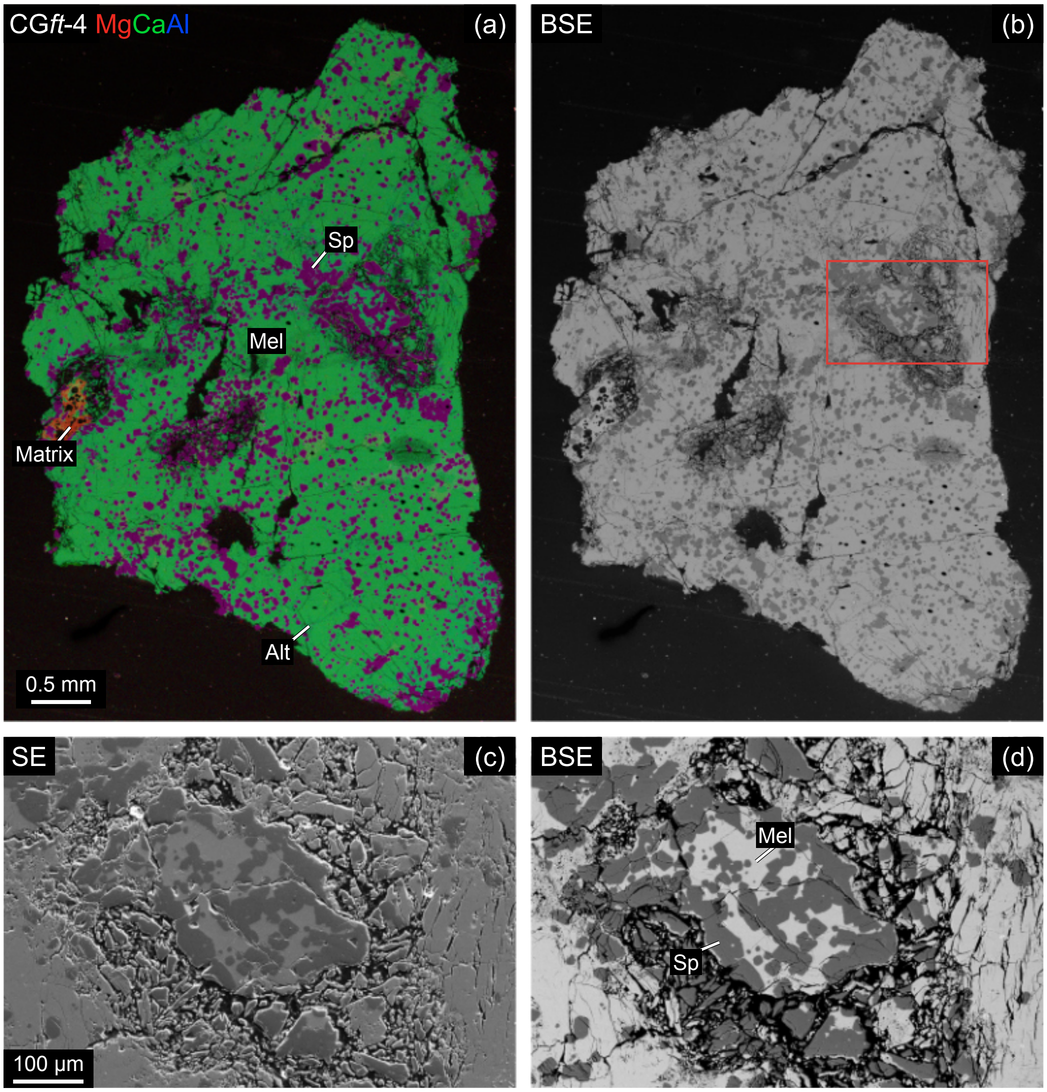

Figure 5.1: Petrography of CG*ft*-4, which is a CTA CAI from Allende. (a) Combined elemental map (Mg–red, Ca–green, Al–blue), and (b) BSE map of CG*ft*-4. The red rectangular highlights a representative area of the CAI, whose SE and BSE images are shown in panels (c) and (d). Mel = melilite; Sp = spinel; Alt = alteration.

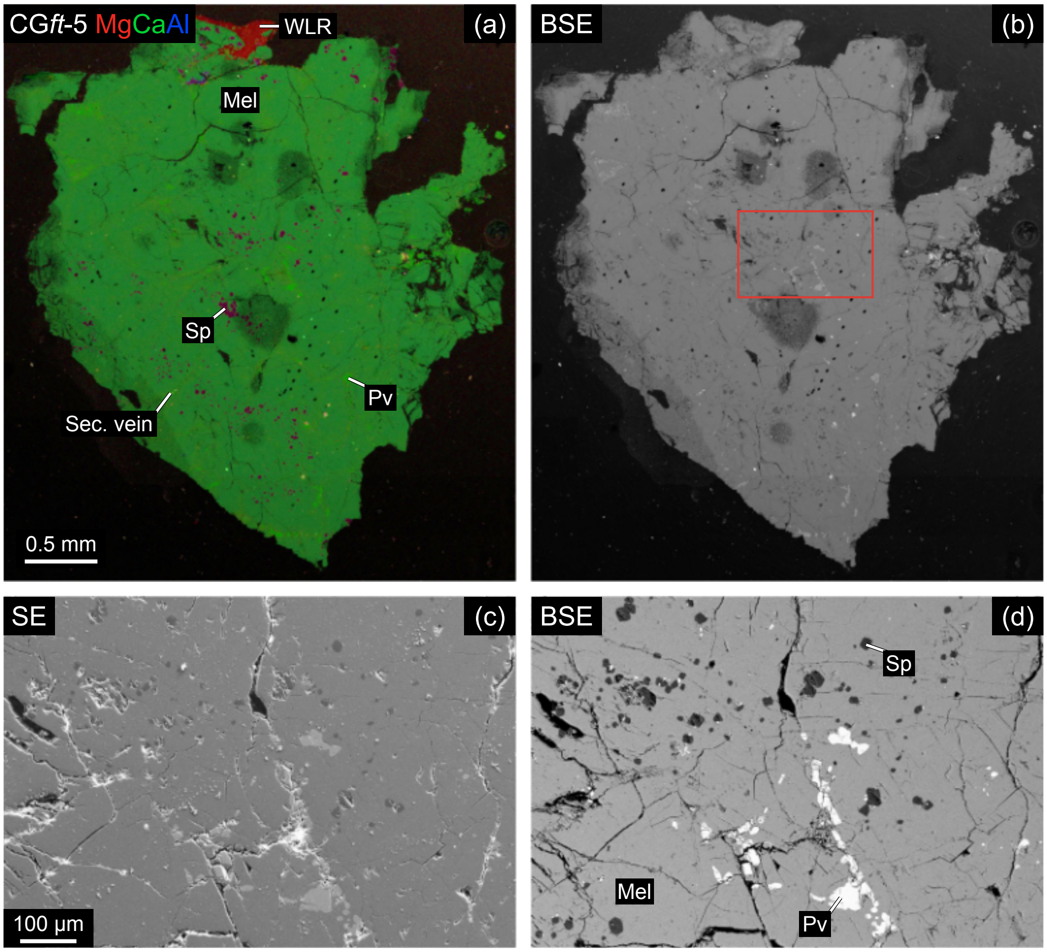

Figure 5.2: Petrography of CG*ft*-5, which is a CTA CAI from Allende. (a) Combined elemental map (Mg–red, Ca–green, Al–blue), and (b) BSE map of CG*ft*-5. The red rectangular highlights a representative area of the CAI, whose SE and BSE images are shown in panels (c) and (d). Mel = melilite; Sp = spinel; Pv = perovskite; Sec. vein = secondary vein; WRL = Wark-Lovering rims.

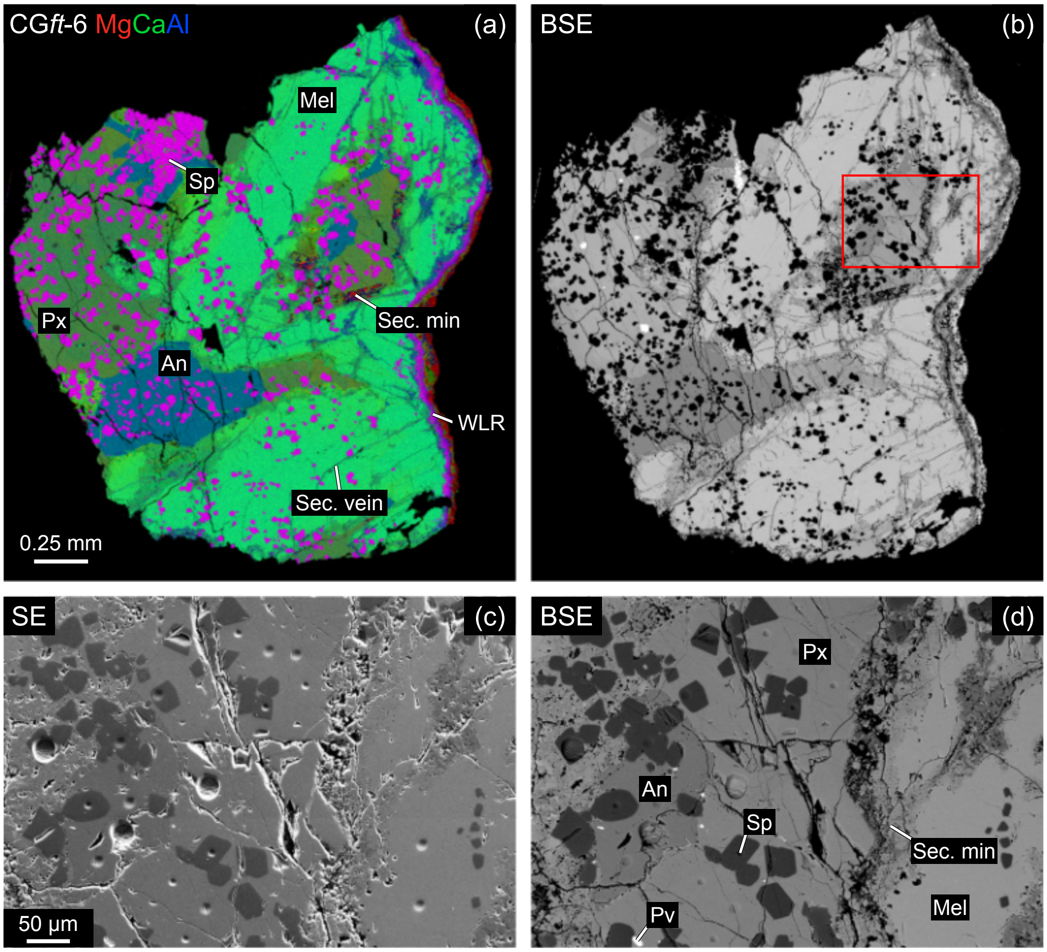

Figure 5.3: Petrography of CG*ft*-6, which is a Type B CAI from Allende. (a) Combined elemental map (Mg–red, Ca–green, Al–blue), and (b) BSE map of CG*ft*-6. The red rectangular highlights a representative area of the CAI, whose SE and BSE images are shown in panels (c) and (d). Mel = melilite; Sp = spinel; An = anorthite; Px = pyroxene; Pv = perovskite; Sec. min = secondary mineral; Sec. vein = secondary vein; WRL =Wark-Lovering rims.

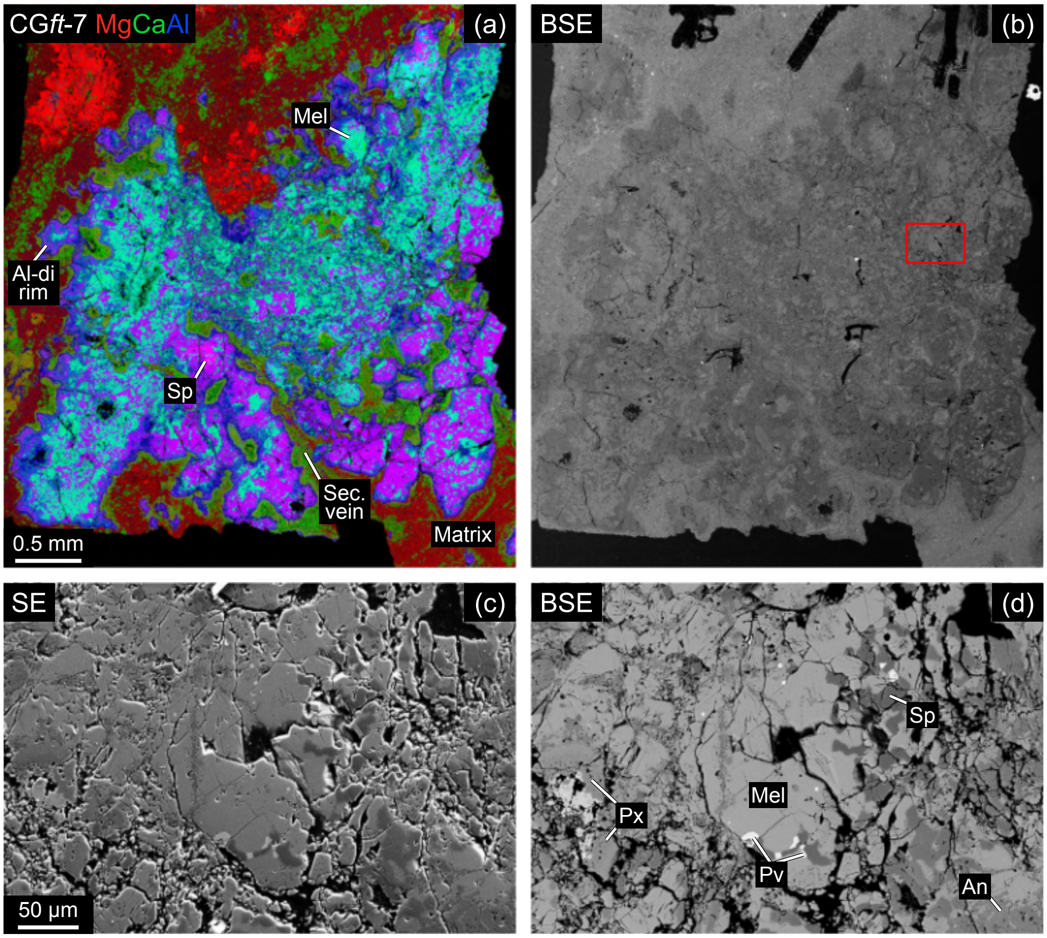

Figure 5.4: Petrography of CG*ft*-7, which is a FTA(or CTA?) CAI from Allende. (a) Combined elemental map (Mg–red, Ca–green, Al–blue), and (b) BSE map of CG*ft*-7. The red rectangular highlights a representative area of the CAI, whose SE and BSE images are shown in panels (c) and (d). The pyroxene and anorthite are secondary phases. Mel = melilite; Sp = spinel; An = anorthite; Px = pyroxene; Pv = perovskite; Sec. vein = secondary vein; Al-di rim = Al-diopside rim.

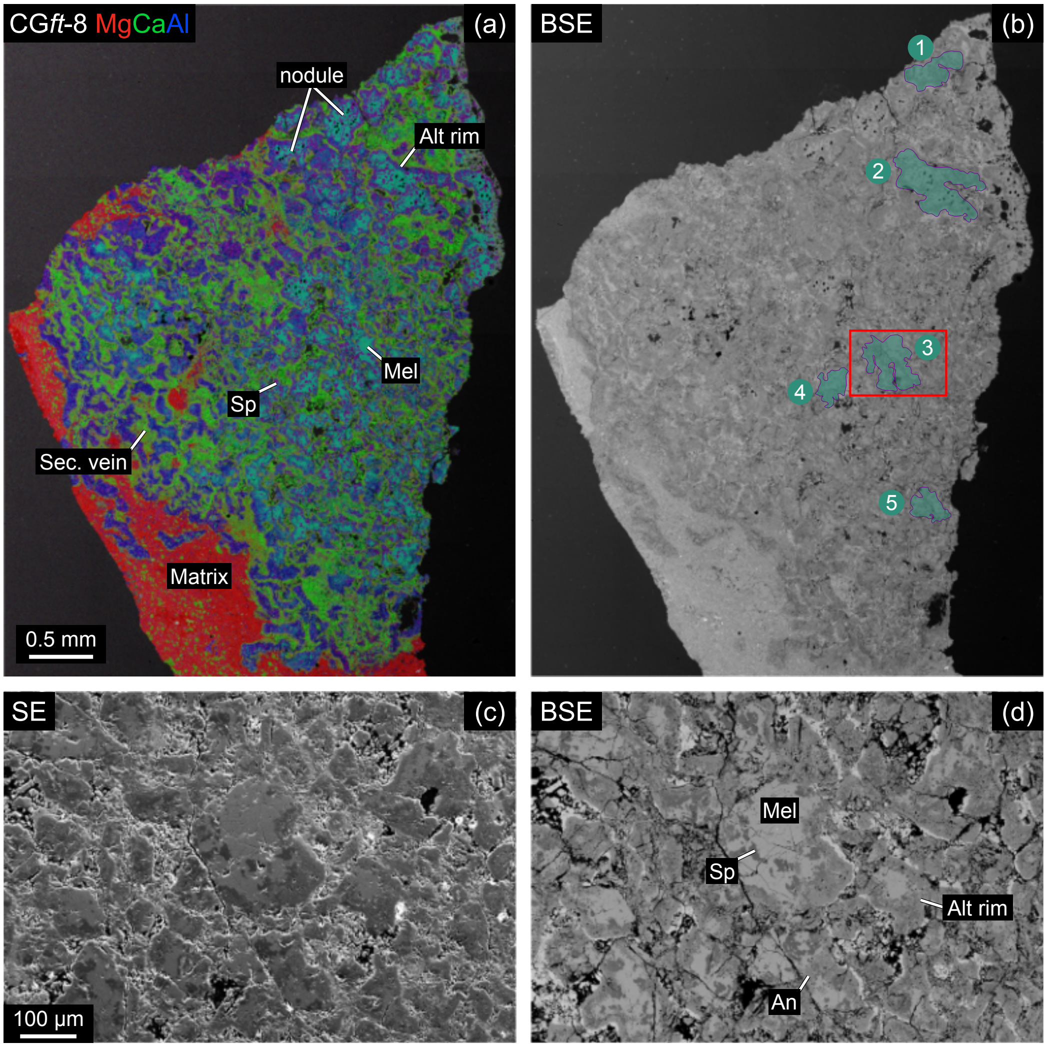

Figure 5.5: Petrography of CG*ft*-8, which is a FTA CAI from Allende. (a) Combined elemental map (Mg–red, Ca–green, Al–blue), and (b) BSE map of CG*ft*-8. The CAI consist of a number of nodules with mineralogy of melilite and spinel. The blue shaded areas with purple border represent the 5 nodules used for in-situ ^{26}Al-^{26}Mg analyses. The red rectangular highlights a representative area of the CAI, whose SE and BSE images are shown in panels (c) and (d). Mel = melilite; Sp = spinel; An = anorthite; Sec. vein = secondary vein; Alt rim = Alteration rim.

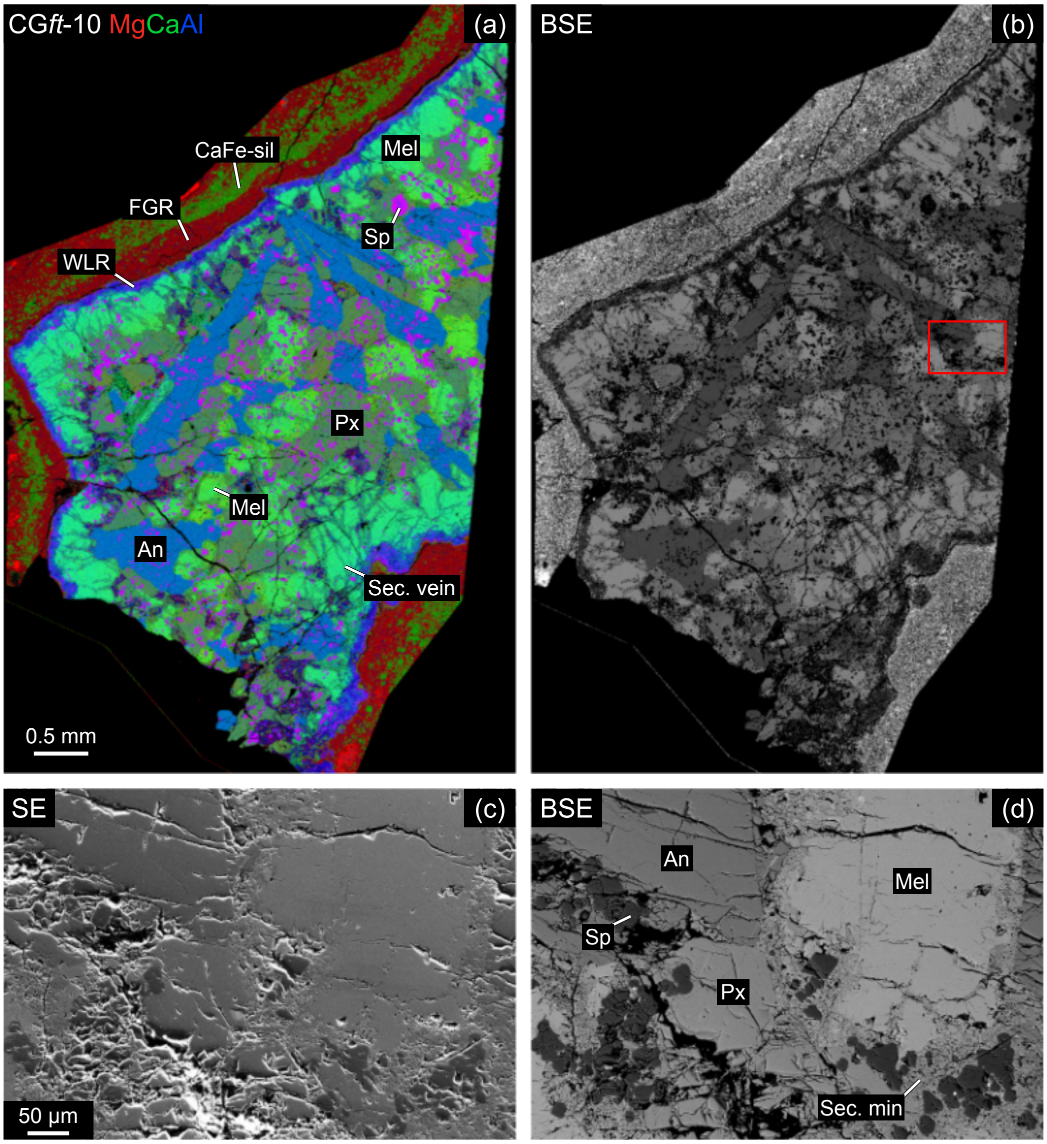

Figure 5.6: Petrography of CG*ft*-10, which is a Type B CAI from Allende. (a) Combined elemental map (Mg–red, Ca–green, Al–blue), and (b) BSE map of CG*ft*-10. The red rectangular highlights a representative area of the CAI, whose SE and BSE images are shown in panels (c) and (d). Mel = melilite; Sp = spinel; An = anorthite; Px = pyroxene; Sec. min = secondary mineral; Sec. vein = secondary vein; WRL =Wark-Lovering rims; FGR = fine-grained matrix-like rim; CaFe-sil = Ca, Fe-rich silicate layer.

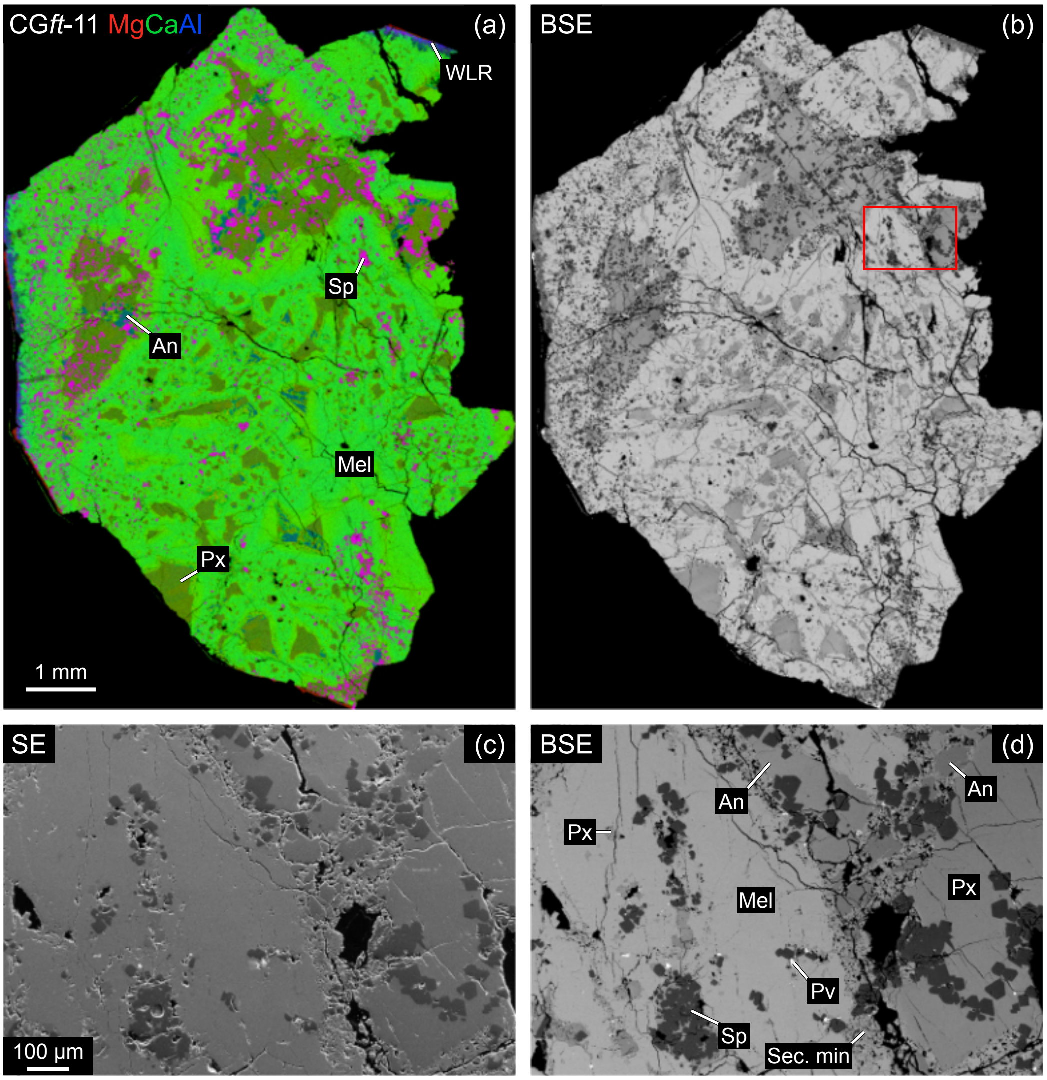

Figure 5.7: Petrography of CG*ft*-11, which is a Type B CAI from Allende. (a) Combined elemental map (Mg–red, Ca–green, Al–blue), and (b) BSE map of CG*ft*-11. The red rectangular highlights a representative area of the CAI, whose SE and BSE images are shown in panels (c) and (d). Mel = melilite; Sp = spinel; An = anorthite; Px = pyroxene; Pv = perovskite; Sec. min = secondary mineral; WRL =Wark-Lovering rims.

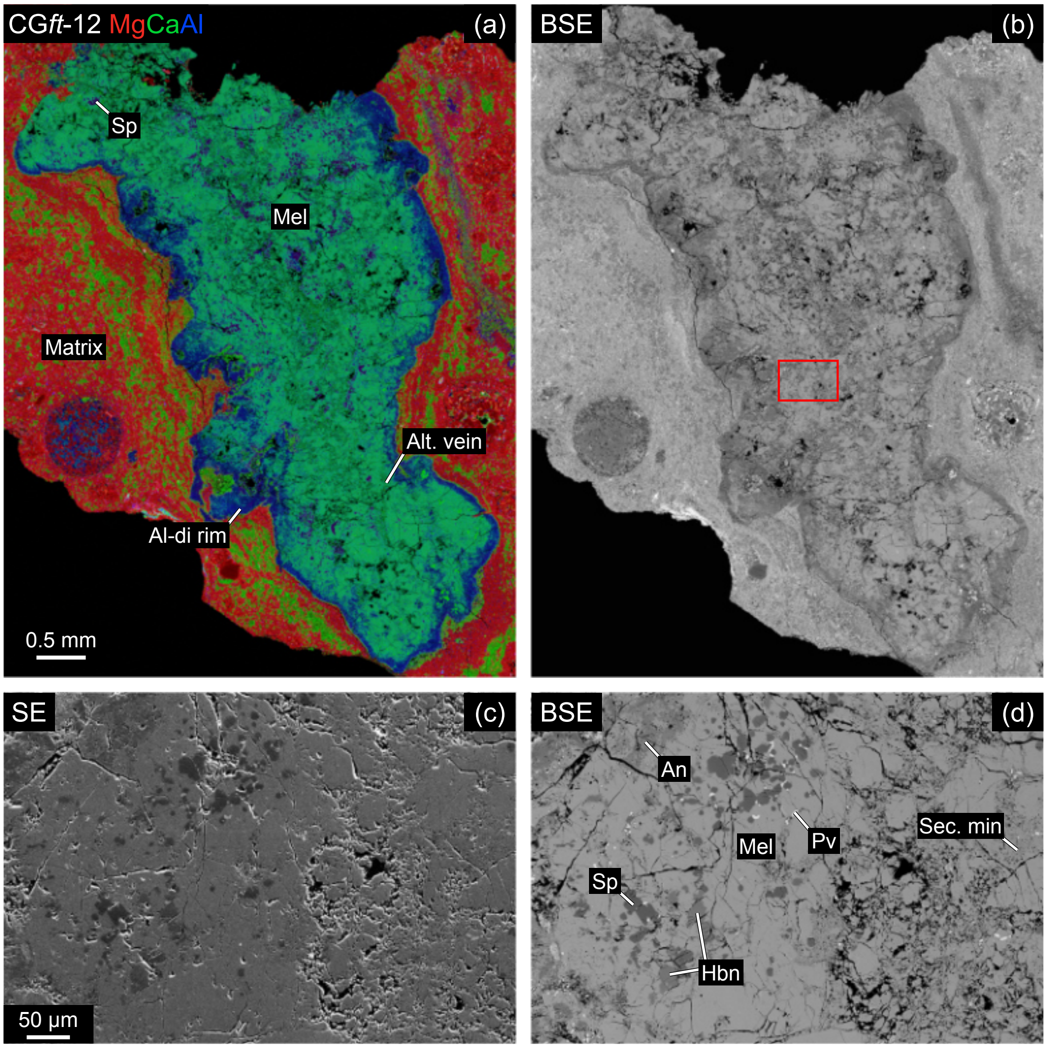

Figure 5.8: Petrography of CG*ft*-12, which is a CTA CAI from Allende. (a) Combined elemental map (Mg–red, Ca–green, Al–blue), and (b) BSE map of CG*ft*-12. The red rectangular highlights a representative area of the CAI, whose SE and BSE images are shown in panels (c) and (d). Mel = melilite; Sp = spinel; An = anorthite; Pv = perovskite; Hbn = hibonite; Sec. min = secondary mineral; Al-di rim = Al-diopside rim; Alt vein = Alteration vein.

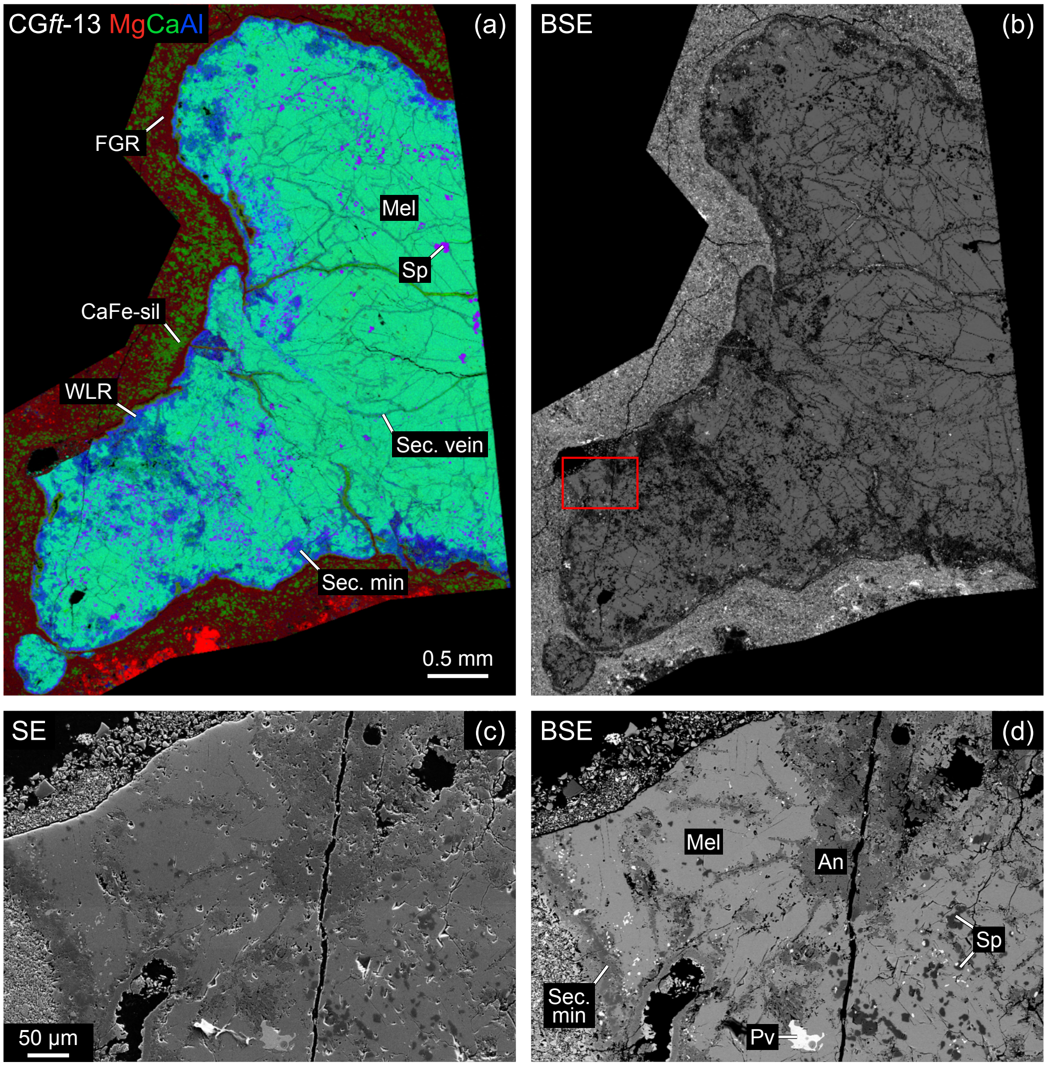

Figure 5.9: Petrography of CG*ft*-13, which is a CTA CAI from Allende. (a) Combined elemental map (Mg–red, Ca–green, Al–blue), and (b) BSE map of CG*ft*-13. The red rectangular highlights a representative area of the CAI, whose SE and BSE images are shown in panels (c) and (d). Mel = melilite; Sp = spinel; An = anorthite; Pv = perovskite; Hbn = hibonite; Sec. min = secondary mineral; Sec. vein = secondary vein; WRL =Wark-Lovering rims; FGR = fine-grained matrix-like rim; CaFe-sil = Ca, Fe-rich silicate layer.

CG*ft*-4, 5, 12, 13, CT23(ME2628-12), 24(W285-429), 41(ME2628-13) are CTA CAIs, which are mostly composed of melilite (more Mg-rich than FTA), spinel, and varying amount of perovskite and hibonite phases. CG*ft*-5, CT23, and 41 have less abundant spinel (a few percent) and frequently occurred perovskite. These 3 CAIs show limited secondary alterations, indicating they are relatively pristine. CG*ft*12, 13, CT24 are surrounded by discontinuous coarse-grained Al-diopside accretionary rims. They experienced more common alterations, given that melilite was crosscut by veins and replaced by secondary minerals. CG*ft*-4 is characterized by more abundant spinel and presence of Al,Ti-rich pyroxene at wt% level, indicating the transition from Type A to Type B CAI.

CG*ft*-6, 10, and 11 are Type B CAIs composed of melilite, Al,Ti-rich pyroxene, anorthite; all poikilitically enclose spinel grains. Melilite ($Åk_{10–75}$) and pyroxene (∼2–10 wt% TiO_2, 12–21 wt% Al_2O_3) show normal igneous zoning, with åkermanite content in melilite increasing towards the CAI core. These CAIs are surrounded by Wark-Lovering rims that consist of spinel and Al,Ti-diopside.

5.3.2 Mg isotopes of bulk CAIs

The bulk Mg isotope data of CAIs are reported in **Table 5.1**. A positive correlation between ^{26}Mg excesses and ^{27}Al/^{24}Mg ratios is observed in all 19 CAIs, corresponding to a slope that is generally consistent with the canonical value, which is in agreement with a homogeneous distribution of ^{26}Al in the forming region(s) of the majority of CAIs (Jacobsen et al. 2008; Kita et al. 2013; Larsen et al. 2011;

Table 5.1: Mg isotope and ^{27}Al/^{24}Mg data for bulk CAIs

Sample ID	Collection	Meteorite	Type	δ^{25}Mg	2SE	δ^{26}Mg	2SE	δ^{26}Mg*	2SE	n	^{27}Al/^{24}Mg	2SE
CG*ft*-5	ME	Allende	CTA	7.640	0.013	16.413	0.023	1.376	0.013	9	3.805	0.027
CG*ft*-6	ME2629-4.73	Allende	B	4.395	0.012	9.703	0.022	1.058	0.011	9	3.240	0.102
CG*ft*-7	ME	Allende	CTA	0.345	0.012	2.397	0.023	1.702	0.007	9	5.123	0.028
CG*ft*-8	ME	Allende	FTA	-0.437	0.012	0.106	0.023	0.941	0.013	9	2.827	0.014
CG*ft*-10	ME2639-3.1	Allende	B	4.403	0.014	9.638	0.026	0.976	0.013	9	2.790	0.006
CG*ft*-11	ME2639-13.1	Allende	B	5.226	0.021	11.153	0.040	0.872	0.013	9	2.486	0.003
CG*ft*-12	ME	Allende	CTA	5.886	0.021	14.394	0.040	2.813	0.013	9	7.540	0.015
CG*ft*-13	ME2639-49.6	Allende	CTA	5.966	0.023	12.872	0.042	1.135	0.010	9	3.184	0.006
TS45	ME2629-4.109	Allende	FoB	-0.855	0.023	-1.491	0.042	0.162	0.011	9	0.872	0.002
CT23	ME2628-12	Leoville	CTA	6.256	0.012	15.266	0.022	2.958	0.009	9	7.838	0.031
CT24	W(285)429	Allende	CTA	-0.719	0.013	2.691	0.023	4.080	0.009	9	11.362	0.057
CT34	3203-14	Axtell	fg	-2.281	0.012	-3.238	0.022	1.204	0.012	9	3.195	0.017
CT35	45E	Efremovka	B	4.247	0.014	9.327	0.026	0.972	0.010	9	3.499	0.016
CT36	49E	Efremovka	B	4.436	0.014	9.696	0.026	0.970	0.011	9	3.433	0.012
CT37	4N	NWA 3118	FoB	0.249	0.011	1.017	0.020	0.510	0.008	18	1.490	0.006
CT38	16N	NWA 3118	CTA	5.940	0.012	13.428	0.023	1.743	0.010	9	4.958	0.019
CT39	9bN	NWA 3118	CTA	6.082	0.021	13.302	0.040	1.335	0.009	9	3.849	0.022
CT40	CG*ft*-4	Allende	CTA	7.968	0.021	17.392	0.040	1.707	0.014	9	4.711	0.017
CT41	ME2628-13	Leoville	CTA	0.599	0.023	3.284	0.042	2.090	0.012	9	5.662	0.019
Geostandards												
BCR-2				-0.151	0.013	-0.322	0.024	-0.044	0.008	12	3.739	0.007
BHVO-2				-0.136	0.011	-0.270	0.021	-0.019	0.007	12	1.875	0.003
DTS-02				-0.178	0.010	-0.354	0.019	-0.027	0.005	26		
Concentration standard												
SPEX Mg				-0.705	0.017	-1.366	0.031	-0.003	0.003	13		

MacPherson et al. 2012; Mishra and Chaussidon 2014). A number of the CAIs plot resolvable below the canonical CV CAI isochron and show variable extent ^{26}Mg deficits. To quantify this Mg heterogeneity in the CAI forming region before the ^{26}Al decay, the notation Δ_0^{26} is introduced and defined as: $\Delta_0^{26} = \delta^{26}\text{Mg}^*–(0.380\times{}^{27}\text{Al}/^{24}\text{Mg}–0.028)$, which describes the derivation from the canonical isochron of individual CAI. It is typically to quantify the pre-^{26}Al decay Mg heterogeneity is constraining the intercept of linear regression on a set of CAIs formed in the same reservoir (*i.e.,* the reservoir has a homogeneous initial Mg isotope composition). Given the variable extent of Mg heterogeneity observed in CAIs, the traditional method is not applicable because the continuous transition of initial Mg isotope composition impedes to selection of a subset of the CAIs used for regression. In this context, we introduce the notation Δ_0^{26} to describe the pre-^{26}Al decay Mg heterogeneity in the CAI forming region, which is defined as the vertical derivation of the measured δ^{26}Mg* from the canonical CV CAI isochron. The rationale of this approach is assuming the initial ^{26}Al/^{27}Al ratio of the large CAI forming region is homogeneous and well characterized with the canonical value, and thus it is possible to evaluate pre-^{26}Al decay Mg isotope composition of CAIs by subtracting the ^{26}Mg excesses resulting from the decay. The canonical CV CAI isochron in this work considers the high-precision Mg isotope measurements of bulk CAIs from CV chondrites (Allende and Efremovka) from widely accepted previous studies (Jacobsen et al. 2008; Larsen et al. 2011). The regressions for bulk isochron from these two works are consistent with each other. It is noticeable that Jacobsen et al. (2008) solely included the CAI data, while Larsen et al. (2011) also combined Amoeboid olivine aggregates (AOAs) data. Provided the debate on whether AOA should be considered together with CAIs to determine δ^{26}Mg*, we only used the 11 CAIs data (A33, A39, A43, A44A, AJEF, AM10-21 CAI-1, 31E, 22E, E104, E48(1) and E48(2)) to determine the canonical CV CAI isochron, which yields a slope of 0.380 ± 0.008 (corresponding to a intial ^{26}Al/^{27}Al ratio of $(5.30 \pm 0.12) \times 10^{-5}$), and a intercept of -0.028 ± 0.024. Then Δ_0^{26} is calculated as:

$$\Delta_0^{26} = \delta^{26}\text{Mg}^* - (0.380 \times^{27} \text{Al}/^{24}\text{Mg} - 0.028) \tag{5.1}$$

where δ^{26}Mg* and ^{27}Al/^{24}Mg are the measured ^{26}Mg excesses and ^{27}Al/^{24}Mg ratio of the CAI. It is noticeable that the importance of determining the canonical CV CAI isochron is to obtain the ^{26}Al/^{27}Al ratio, while the intercept $\delta^{26}\text{Mg}_0^*$ can be considered as a reference point to quantify the offsets of initial Mg isotope composition between samples.

The Δ_0^{26} values of newly analyzed CAIs range from 0.017 to -0.330 ‰, which cover a similar range of CR CAIs and expand the previously observed heterogeneity in CV CAIs by ~70 % (**Fig. 5.10**). The probability density distribution of the Δ_0^{26}

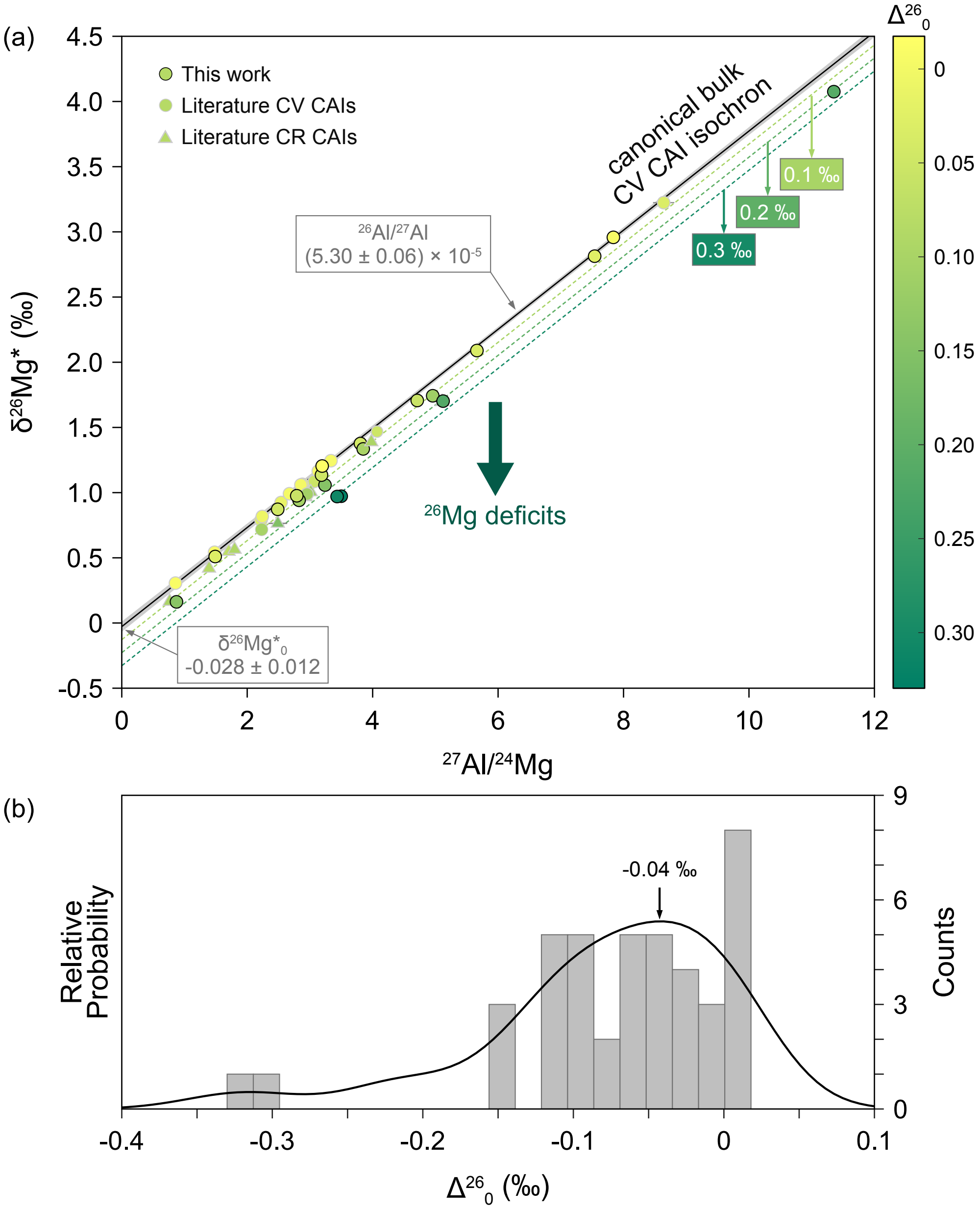

Figure 5.10: ^{26}Al-^{26}Mg isochron diagram and probability density plot of Δ^{26}_0 for bulk CAIs. (a) ^{26}Al-^{26}Mg isochron diagram for bulk CAIs showing variable extent of pre-^{26}Al decay Mg heterogeneity during the CAI forming epoch. Symbols with black and grey borders represent the CAIs measured in this work and complied from the literature (Jacobsen et al. 2008; Larsen et al. 2011, 2020; Wasserburg et al. 2012), while circle and triangular denote the CAIs from CV and CR chondrites, respectively. The filled color of the symbols indicates the Δ^{26}_0 of the sample corresponding to the color bar on the right. The black line shows the canonical bulk CV CAI isochron, and the grey shaded area is the 95 % confidence interval of the isochron. The green dashed lines represent the bulk isochron with 0.1, 0.2, and 0.3 ‰ deficits compared with the canonical isochron. (b) Histogram and probability density plot for bulk CAIs, including all the samples shown in panel (a). The probability density plot (black line) uses kernel density estimation, which yields a peak at -0.040 ‰.

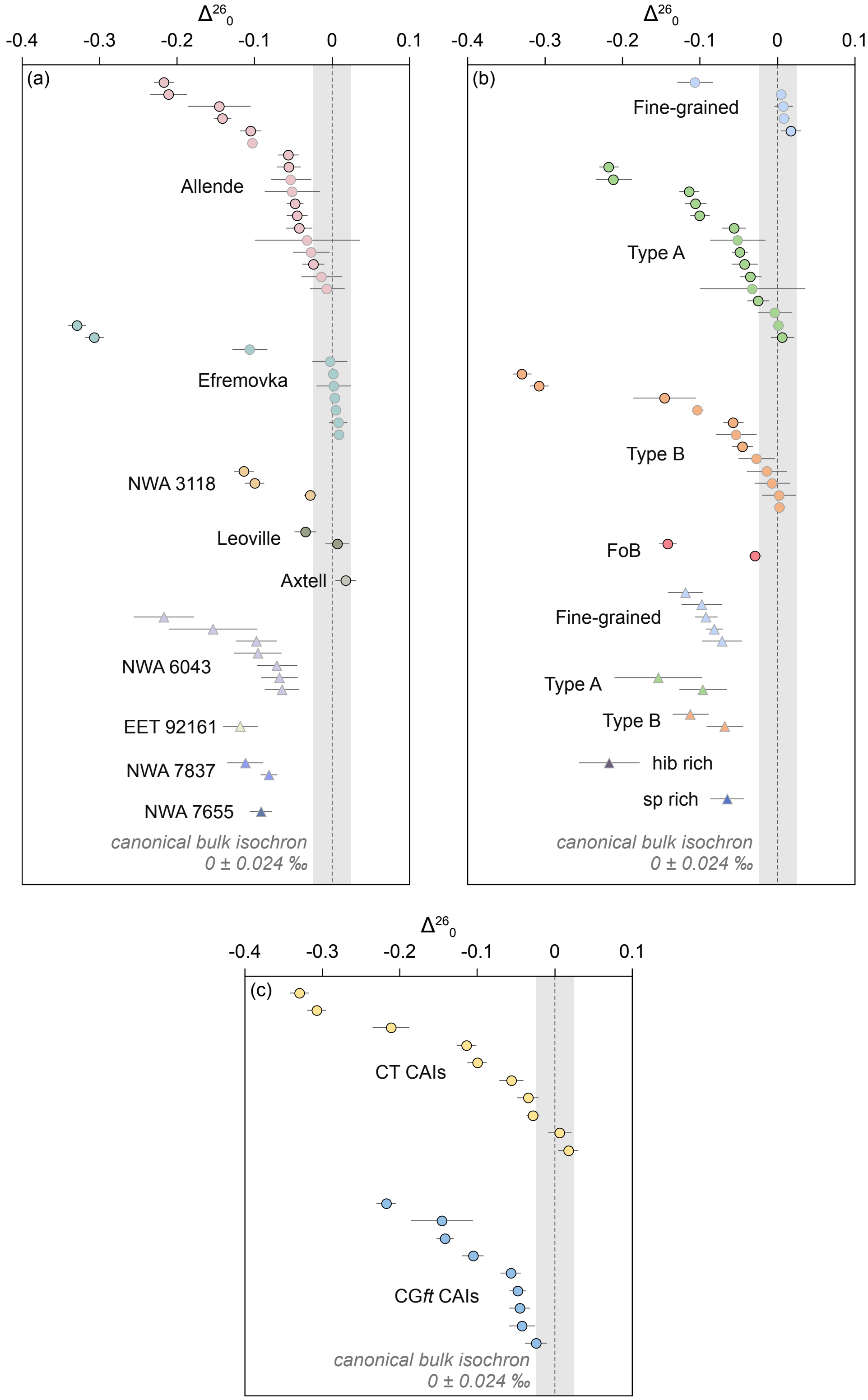

Figure 5.11: Summary of Δ_0^{26} for CAIs categorized by (a) hosting chondrites, (b) CAI types, and (c) batch of analyses. Symbols with black and grey borders represent the CAIs measured in this work and complied from the literature, while circle and triangular denote the CAIs from CV and CR chondrites, respectively. The grey band indicate the Δ_0^{26} range for the canonical bulk CV CAI isochron.

revealed a major peak at -0.040 ‰, which explains initial Mg isotope composition of -0.028 ± 0.012 ‰ defined by the canonical isochron of bulk CV CAIs. Furthermore, the Δ_0^{26} values do not appear to be related with the type of the CAIs or the hosting chondrites (**Fig. 5.11**), which indicates these factors did not control the initial Mg heterogeneity observed in CAIs. It is particularly noteworthy that bulk CAI isochron is more robust to subsequent thermal processing and secondary alterations, and thus can largely retain their original signatures. The lack of systematic difference of Δ_0^{26} between CAIs from $\mathrm{CV_{ox}}$ and $\mathrm{CV_{red}}$ also justify the parent body processing did not have noticeable impact on the these CAIs.

5.3.3 Internal Al-Mg isochrons

Internal ^{26}Al-^{26}Mg isochrons of all analyzed CAIs also show a positive correlation similar to bulk isochron, indicating the in-situ decay of ^{26}Al (**Table 5.2, Fig. S15–25**). Inferred $^{26}\mathrm{Al}/^{27}\mathrm{Al}$ ratios, calculated from York regression (Model 1 fit in IsoplotR), span a range from $(4.48 \pm 0.05) \times 10^{-5}$ to $(5.06 \pm 0.13) \times 10^{-5}$, which either similar to or below the solar system initial defined by the bulk CAI isochron, implying late formation or reprocessing of these CAIs. Most of the analyzed CAIs show elevated $\delta^{26}\mathrm{Mg}_i^*$ values ranging from -0.099 to 0.367 ‰, which generally tend to increase with the decrease of $^{26}\mathrm{Al}/^{27}\mathrm{Al}$, suggesting Mg isotope evolution in the solar nebula due to ^{26}Al decay.

Evidence of disturbance in CAIs

Reprocessing and secondary alterations are common in CAIs and could lead to extra scattering in internal isochrons and lower initial $^{26}\mathrm{Al}/^{27}\mathrm{Al}$ ratios (*i.e.*, younger ages). The impacts of these subsequent processes are supported by two pieces of evidence: Firstly, anorthite in CAIs L2628-13-AM and CG*ft*-11 are observed to have lost radiogenic ^{26}Mg and plotted significantly below the isochron. Secondly, the spinel enclosed in anorthite is plotted above the isochron (CG*ft*-6). This observation demonstrates the Mg isotope exchange between spinel and anorthite, reflecting the fast Mg diffusion speed of spinel (MacPherson et al. 2012).

Consistency of multiple measurements on the same CAI

Most of the CAIs analyzed in this work are measured twice at CRPG and UCLA, respectively. The isochrons obtained by these two sessions are consistent with each other for the majority of CAIs (CG*ft*-5, 6, 8, and 13). The sampling bias can lead to the discrepant isochrons from two sessions for some CAIs: the first possibility is that the two different measurements covered various ranges of $^{27}\mathrm{Al}/^{24}\mathrm{Mg}$ ratios (CG*ft*-4, 11(X)); the second possibility is the local resetting that the ^{26}Mg excesses redistributed among the mineral phases, and selective analyses of these reset phases would result in the discrepancy of calculated regressions (CG*ft*-7, 11(3)). For CAI

CG*ft*-11, two epoxy mounts were measured, and the two reasons discussed above can also explain the discrepancy between these two mounts. Meanwhile, Mount X consists of more pyroxene than Mount 3, indicating the uneven distribution of minerals, and the local alterations can also be different.

Difference in MSWD between measurements conducted at CRPG and UCLA

The Mean Square of the Weighted Deviates (MSWD) is widely used in isochrons to assess the goodness of fit of the linear regression and measured values. However, the MSWD values for the isochrons measured at CRPG are generally larger than those of UCLA. This situation is not due to extra scattering from CRPG measurements but differences in uncertainties of these two sets of measurements. The large MSWD values reflect the observed scatter less than that predicted by the analytical uncertainties and can be explained by the smaller uncertainties from the CRPG measurements.

Multi-isochrons of the same CAI defined by different mineral combination

We notice that the analyzed minerals may define more than one isochron characterized by distinct ^{26}Al/^{27}Al ratios. The most common situation is that the anorthite defined an isochron with a shallower slope (*e.g.,* L2628-13-AM and CG*ft*-11(X)). There are two possible explanations for this observation: (i) primary anorthite condensed later at a slightly lower temperature than other refractory phases in CAI, and ^{26}Al/^{27}Al reflected this later formation time. (ii) anorthite is more easily to be altered and lost radiogenic ^{26}Mg during the open system processing (diluted by normal Mg). The second interpretation is more ubiquitous, and it can also overprint the later formation signature from the primary condensation. Another example is CG*ft*-10, the analyzed minerals with low ^{27}Al/^{24}Mg ratios (< 3, spinel, pyroxene, high Åk melilite) define a isochron with ^{26}Al/^{27}Al of $(7.40 \pm 0.32) \times 10^{-5}$ and $\delta^{26}\mathrm{Mg}_0^*$ of -0.352 ± 0.049 ‰, while the minerals with high ^{27}Al/^{24}Mg ratios (> 3, relatively low Åk melilite) define a a isochron with ^{26}Al/^{27}Al of $(5.06 \pm 0.40) \times 10^{-5}$ and $\delta^{26}\mathrm{Mg}_0^*$ of 0.046 ± 0.165 ‰. This discrepancy may be due to the different evolution histories of these two mineral sets (*e.g.,* thermal processing, alteration) leading to the difference in closing time. However, the supercanonical slope for minerals with low ^{27}Al/^{24}Mg ratios is not very likely to be real and may be due to the loss of radiogenic ^{26}Mg for some low ^{27}Al/^{24}Mg phases in this region. The isochron defined by minerals with high ^{27}Al/^{24}Mg ratios probably reflect a more primary isochron of this CAI.

Isochrons of individual nodules in the FTA CAI CG*ft*-8

CAI CG*ft*-8 consists of multiple nodules with the mineralogy of melilite and spinels. Several nodules were measured independently to understand if these nodules condensed from the solar nebula at the same time. The isochrons have ^{26}Al/^{27}Al range from $(4.52 \pm 0.12) \times 10^{-5}$ to $(5.00 \pm 0.10) \times 10^{-5}$ and $\delta^{26}\mathrm{Mg}_0^*$ range from 0.055

± 0.028 ‰ to 2.45 ± 0.031 ‰. The isochrons of nodules 2–4 have isochrons consistent with each other, while nodules 1 and 5 were affected by secondary processing. The results suggest the nodules condensed from the solar nebula simultaneously, which is consistent with the primary condensation origin of this CAI indicated by the slight negative δ^{25}Mg.

Table 5.2: Internal ^{26}Al-^{26}Mg isochron of CAIs. Inferred ^{26}Al/^{27}Al ratios, $\delta^{26}\text{Mg}^*_0$, goodness of fit, and number of point analyses used for regression.

Sample	^{26}Al/^{27}Al (± 2SE)	$\delta^{26}\text{Mg}^*_0$ (± 2SE)	MSWD	n
Data obtained at CRPG				
W(285)429	$(5.84 \pm 0.05) \times 10^{-5}$	0.040 ± 0.023	135.1	26
2628-12-AM	$(4.84 \pm 0.09) \times 10^{-5}$	0.367 ± 0.029	10.95	19
2628-13-AM	$(4.95 \pm 0.09) \times 10^{-5}$	0.131 ± 0.025	11.89	22
CG*ft*-4	$(4.77 \pm 0.08) \times 10^{-5}$	0.076 ± 0.020	9.877	31
CG*ft*-5	$(4.67 \pm 0.12) \times 10^{-5}$	0.152 ± 0.027	5.566	30
CG*ft*-6	$(4.84 \pm 0.09) \times 10^{-5}$	-0.048 ± 0.024	8.627	32
CG*ft*-7	$(4.60 \pm 0.04) \times 10^{-5}$	-0.003 ± 0.014	54.58	35
CG*ft*-8	$(4.80 \pm 0.04) \times 10^{-5}$	0.159 ± 0.015	18.66	49
Nodule 1	$(4.52 \pm 0.12) \times 10^{-5}$	0.189 ± 0.043	32.37	10
Nodule 2	$(4.99 \pm 0.08) \times 10^{-5}$	0.055 ± 0.028	9.905	10
Nodule 3	$(5.00 \pm 0.10) \times 10^{-5}$	0.155 ± 0.036	38.06	8
Nodule 4	$(4.72 \pm 0.11) \times 10^{-5}$	0.197 ± 0.034	7.033	9
Nodule 5	$(4.63 \pm 0.09) \times 10^{-5}$	0.245 ± 0.031	11.22	12
CG*ft*-10	$(5.60 \pm 0.13) \times 10^{-5}$	-0.099 ± 0.026	11.33	36
CG*ft*-11(3)	$(4.54 \pm 0.11) \times 10^{-5}$	0.121 ± 0.022	8.328	36
CG*ft*-11(X)	$(4.91 \pm 0.09) \times 10^{-5}$	0.060 ± 0.021	11.44	50
with An	$(4.48 \pm 0.05) \times 10^{-5}$	0.125 ± 0.012	13.76	56
CG*ft*-13	$(4.61 \pm 0.07) \times 10^{-5}$	0.311 ± 0.021	10.56	35
Data obtained at UCLA				
CG*ft*-4	$(4.25 \pm 0.19) \times 10^{-5}$	0.236 ± 0.051	1.523	20
CG*ft*-5	$(4.78 \pm 0.26) \times 10^{-5}$	0.249 ± 0.089	1.667	15
CG*ft*-6	$(4.82 \pm 0.19) \times 10^{-5}$	0.035 ± 0.052	2.959	31
CG*ft*-7	$(4.28 \pm 0.12) \times 10^{-5}$	0.209 ± 0.032	3.480	22
CG*ft*-8	$(4.68 \pm 0.10) \times 10^{-5}$	0.239 ± 0.030	3.956	34
CG*ft*-10	$(5.21 \pm 0.54) \times 10^{-5}$	0.046 ± 0.100	1.888	19
CG*ft*-11(3)	$(3.84 \pm 0.55) \times 10^{-5}$	0.330 ± 0.127	1.922	12
CG*ft*-11(X)[a]	$(3.76 \pm 0.65) \times 10^{-5}$	0.286 ± 0.124	3.092	14
CG*ft*-13	$(4.61 \pm 0.35) \times 10^{-5}$	0.254 ± 0.111	2.998	10

[a] CG*ft*-11(3) and (X) are two pieces extracted from the same CAI. The two epoxy mounts are both measured to compare the consistency of internal-isochrons obtained from different parts of the same CAI.

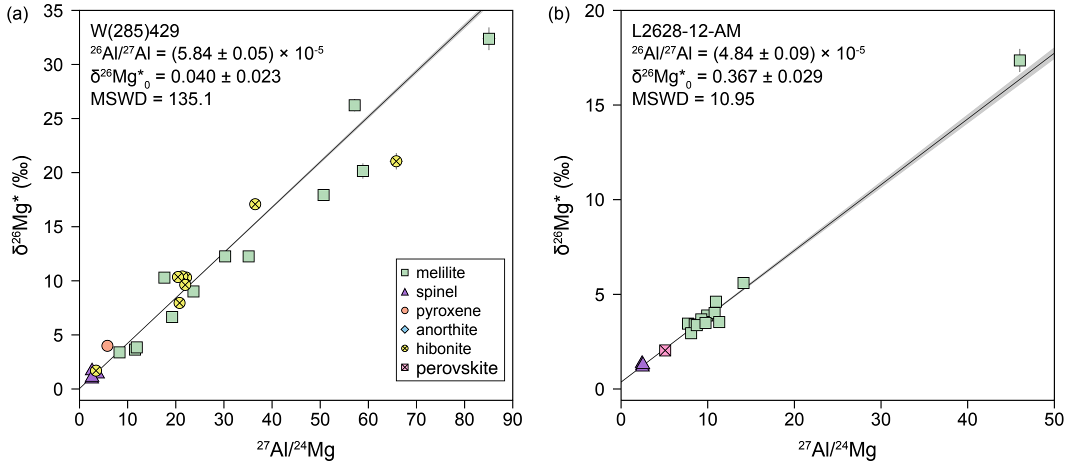

Figure 5.12: ^{26}Al-^{26}Mg isochron diagrams for CAIs (a) W(285)429 and (b) L2628-12-AM. The isochron of W(285)429 shows significantly resolvable scatter from the linear regression, indicating the alteration disturbance of the ^{26}Al-^{26}Mg system. Symbols are the same for all following isochrons.

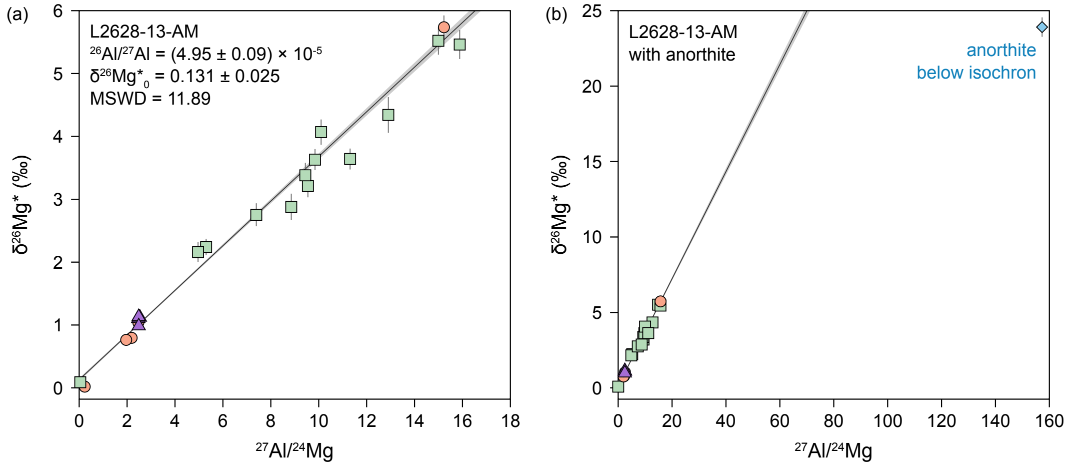

Figure 5.13: ^{26}Al-^{26}Mg isochron diagrams for L2628-13-AM (a) without anorthite and (b) with anorthite. Anorthite in L2628-13-AM has lost excess ^{26}Mg and falls below the linear regression.

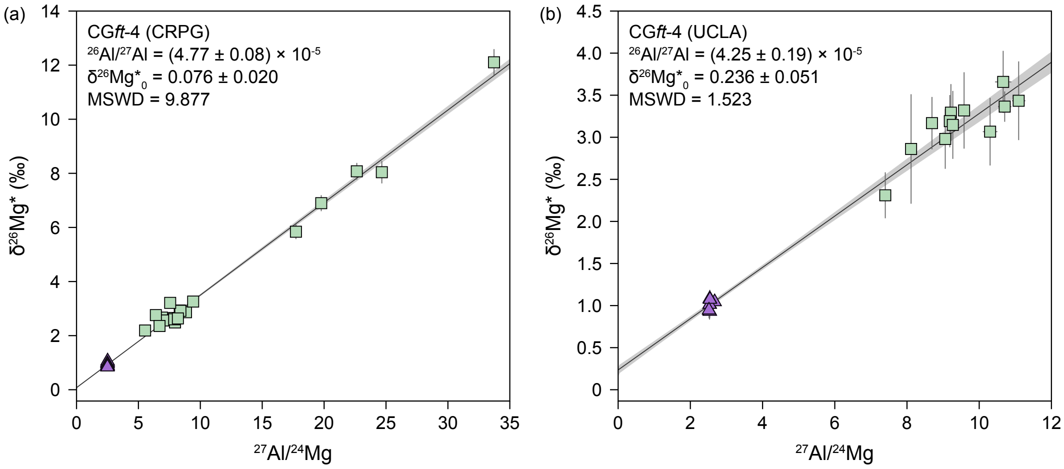

Figure 5.14: ^{26}Al-^{26}Mg isochron diagrams for CG*ft*-4 measured at (a) CRPG and (b) UCLA.

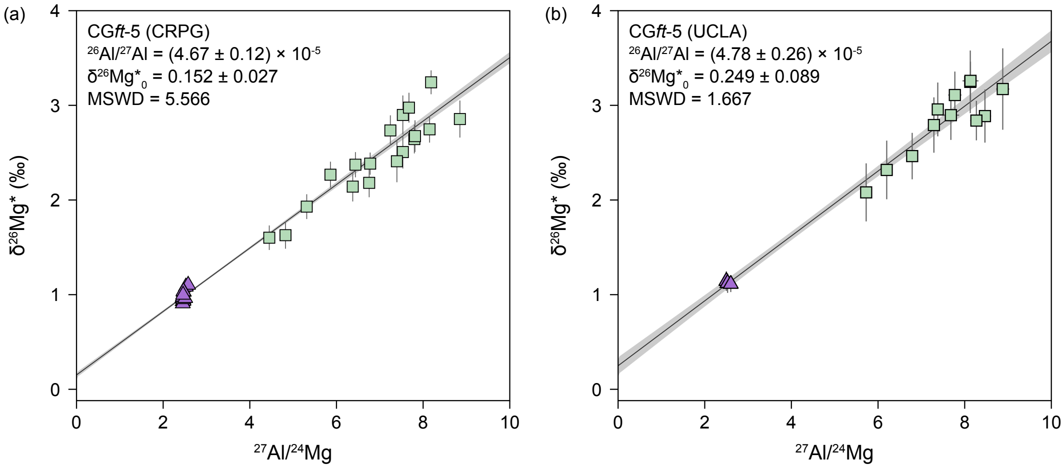

Figure 5.15: ^{26}Al-^{26}Mg isochron diagrams for CG*ft*-5 measured at (a) CRPG and (b) UCLA.

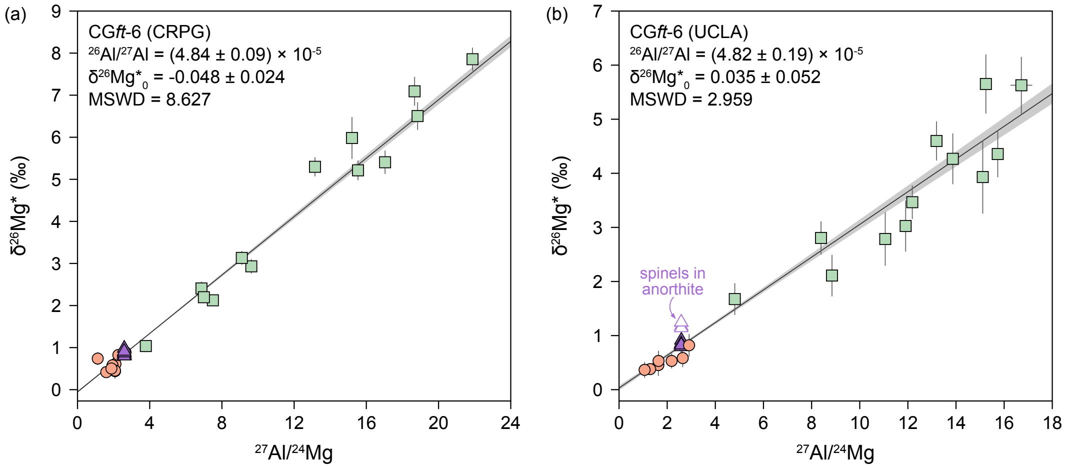

Figure 5.16: ^{26}Al-^{26}Mg isochron diagrams for CG*ft*-6 measured at (a) CRPG and (b) UCLA. The open purple triangular represents the spinels embedded in anorthite.

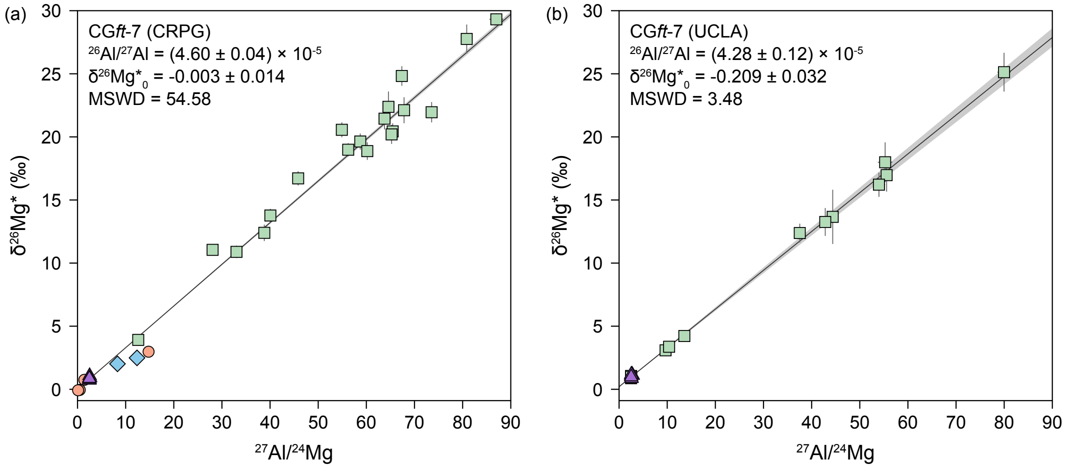

Figure 5.17: ^{26}Al-^{26}Mg isochron diagrams for CG*ft*-7 measured at (a) CRPG and (b) UCLA.

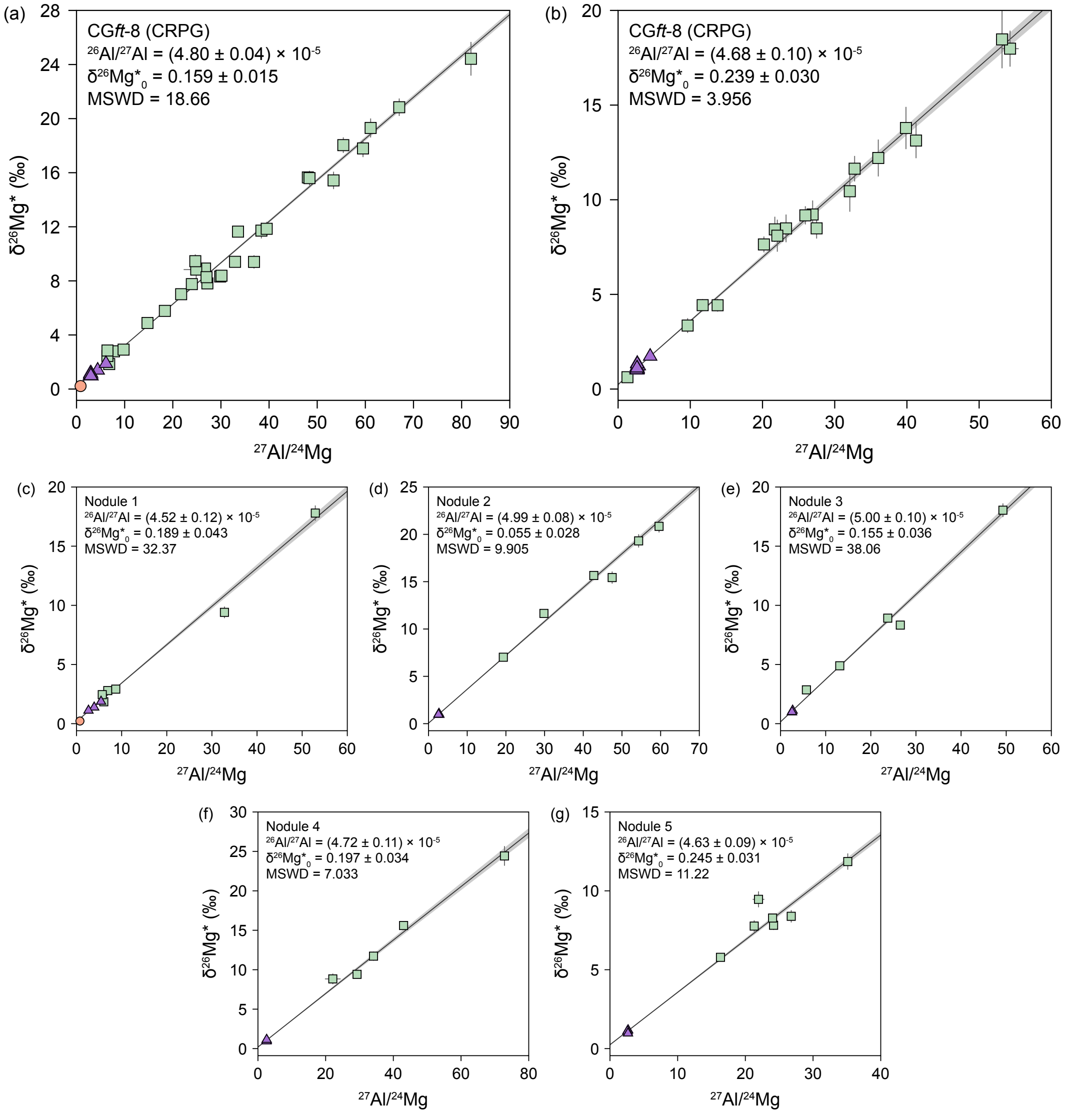

Figure 5.18: ^{26}Al-^{26}Mg isochron diagrams for CG*ft*-8 measured at (a) CRPG and (b) UCLA; melilite + spinel nodules (c)–(g).

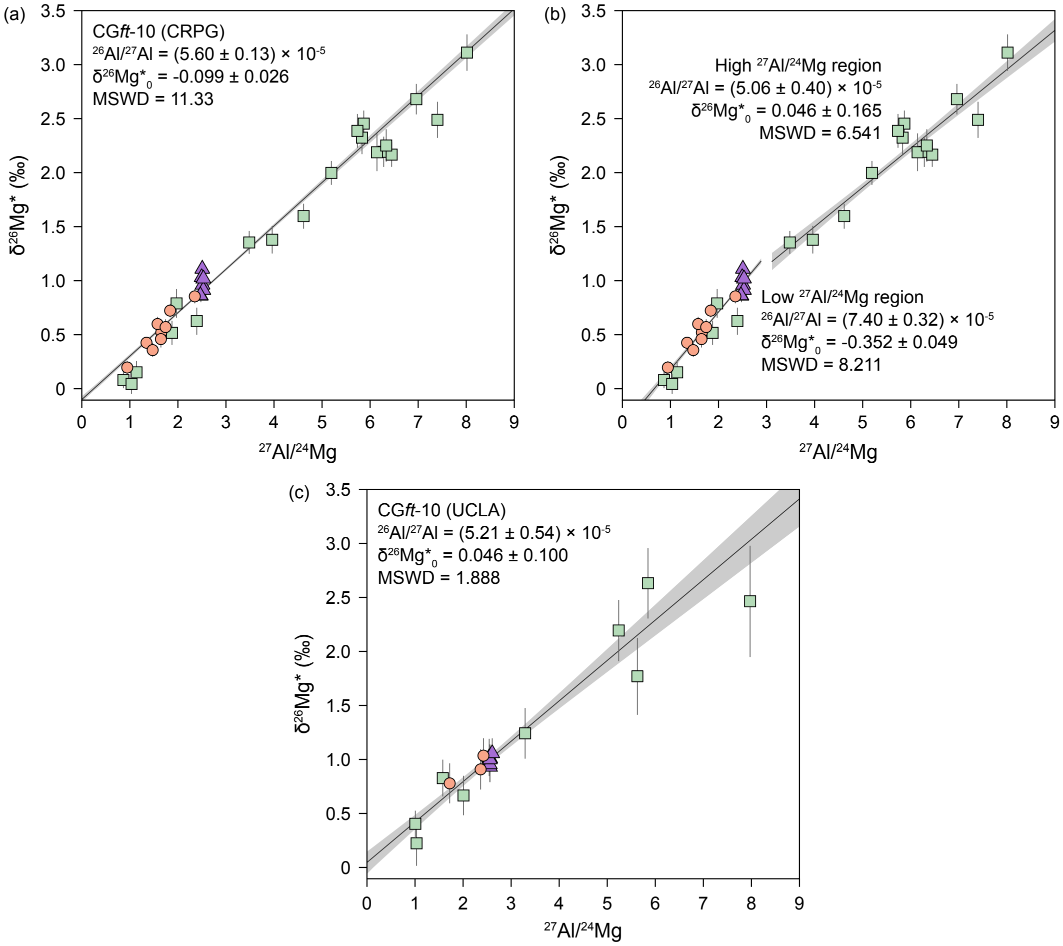

Figure 5.19: ^{26}Al-^{26}Mg isochron diagrams for CG*ft*-10 measured at (a, b) CRPG and (c) UCLA. In panel (b), the mineral phases with low (< 3) and high (> 3) ^{27}Al/^{24}Mg phases define two isochrons with different slopes.

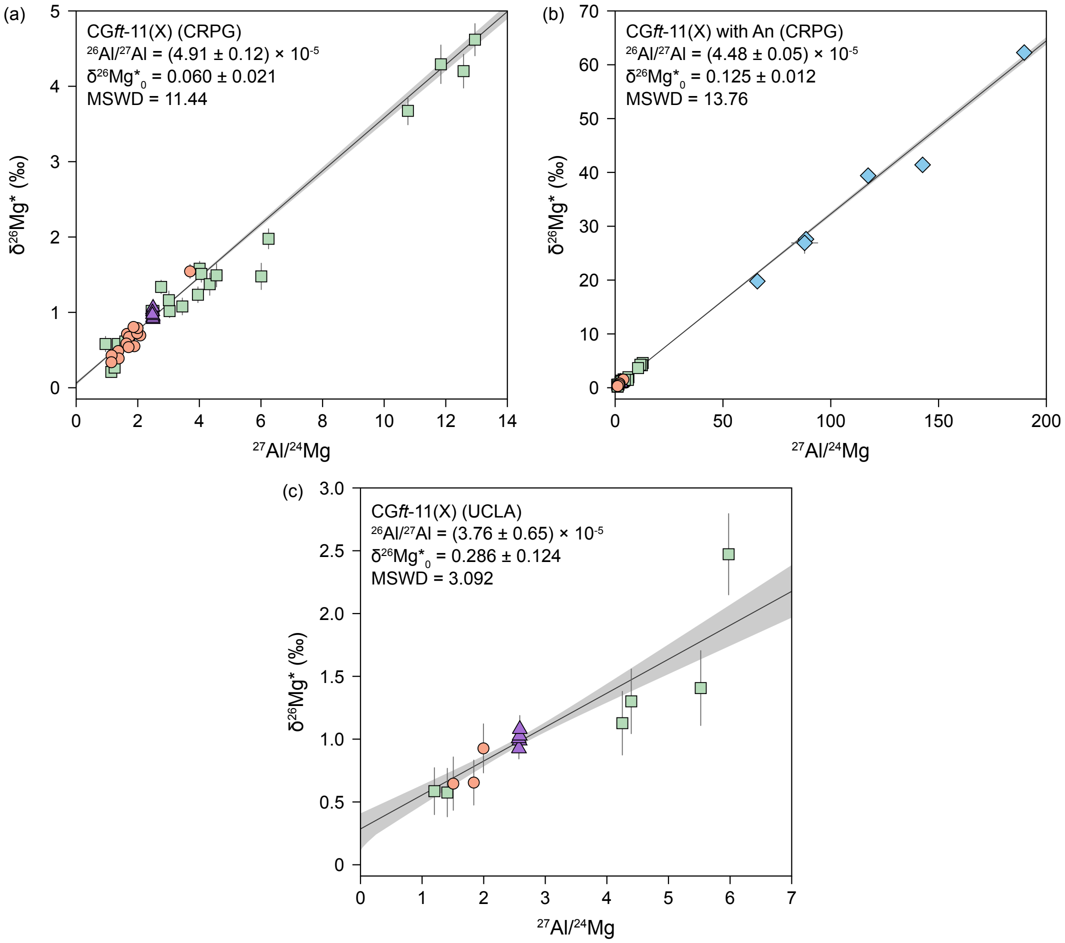

Figure 5.20: ^{26}Al-^{26}Mg isochron diagrams for CG*ft*-11 Epoxy mount X measured at (a, b) CRPG and (c) UCLA. Panel (b) shows the linear regression including the anorthite.

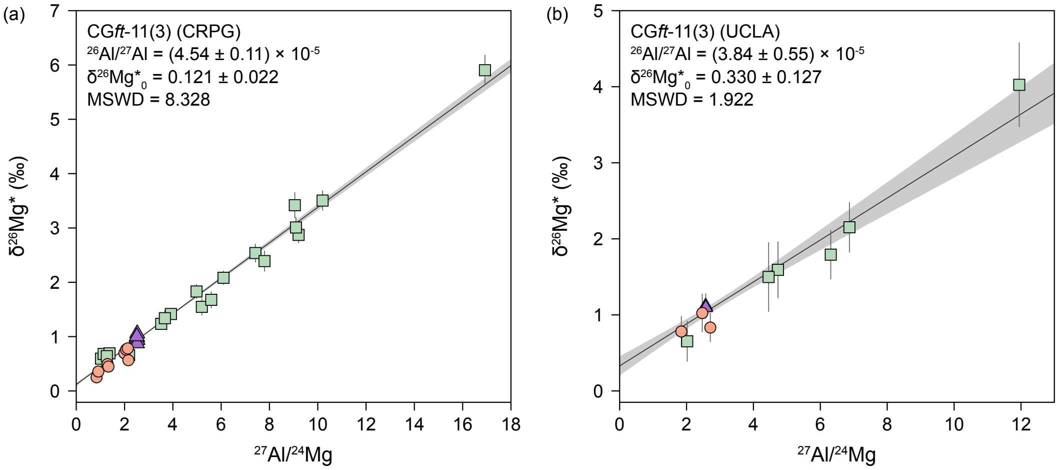

Figure 5.21: ^{26}Al-^{26}Mg isochron diagrams for CG*ft*-11 Epoxy mount X measured at (a) CRPG and (b) UCLA.

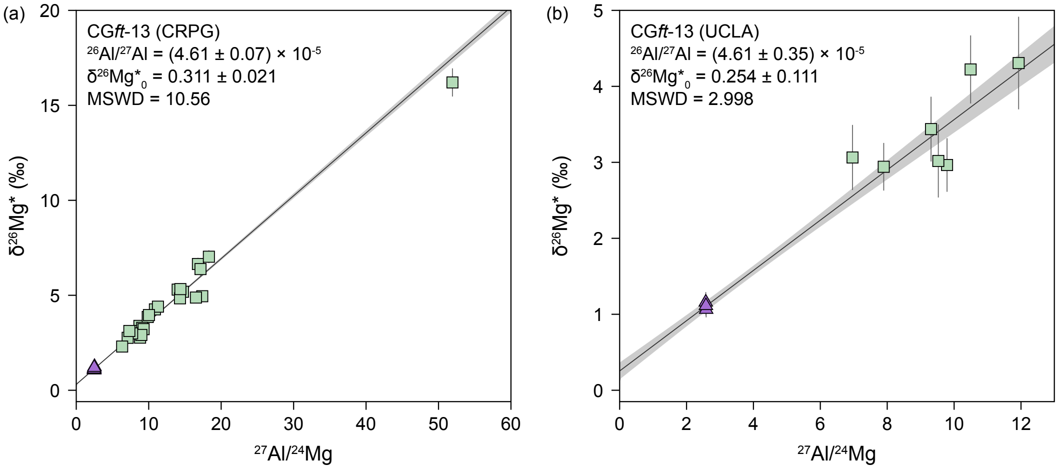

Figure 5.22: ^{26}Al-^{26}Mg isochron diagrams for CG*ft*-13 measured at (a) CRPG and (b) UCLA.

5.4 Discussion

5.4.1 Initial Mg isotope composition of CAIs

The variable extent of ^{26}Mg deficits resolved in the high-precision bulk CAI isochron cannot be explained by a simple scenario that all CAIs evolved from a single reservoir with homogeneous Al and Mg isotope composition and thus point to ubiquitous heterogeneity in the initial (*i.e.,* pre-^{26}Al decay) Mg isotope composition of CAIs precursors. Our results demonstrate a continuous gradient of $\delta^{26}\text{Mg}_0^*$ heterogeneity that covered a wide range (in the Δ_0^{26} range from 0 to -300 ppm) was present in the CAI forming region(s) when $^{26}\text{Al}/^{27}\text{Al}$ was homogeneous at the canonical value, which is in contrast to the proposal that CAI formed from a few reservoirs/episodes with characteristic $\delta^{26}\text{Mg}_0^*$ compositions (Larsen et al. 2020).

This heterogeneity can also be tested by modeling the Mg isotope evolution using the internal ^{26}Al-^{26}Mg isochrons. For the CAIs analyzed in this work, the increase in $\delta^{26}\text{Mg}_0^*$ values is typically accompanied by the decrease in $^{26}\text{Al}/^{27}\text{Al}$, reflecting the growth of radiogenic ^{26}Mg due to the decay of ^{26}Al in the solar nebula. The magnitude of ^{26}Mg excesses is a linear function of the bulk CAI $^{27}\text{Al}/^{24}\text{Mg}$ ratio and is associated with the initial Al and Mg isotope composition of the CAI precursors. Hence, extrapolation of the slope and intercept of internal isochrons of multiple CAIs can provide key constrain on the initial composition of the CAI precursors.

To derive the function between $\delta^{26}\text{Mg}_0^*$ and $^{26}\text{Al}/^{27}\text{Al}$, we consider the Mg isotopes evolution in a closed system first. For a given CAI, the amount of ^{26}Mg when it formed (represented by t_0, *i.e.,* the time for the last melting event that Al-Mg system closed) is composed by two components: the initial ^{26}Mg of the CAI precursor that CAI evolved from at t_i and the ^{26}Mg from the decay of ^{26}Al from t_i to t_0:

$$^{26}\text{Mg}_0 = ^{26}\text{Mg}_i + (^{26}\text{Al}_i - ^{26}\text{Al}_0) \tag{5.2}$$

where $^{26}\text{Mg}_0$ and $^{26}\text{Al}_0$ is the amount of ^{26}Mg and ^{26}Al when CAI formed, respectively; $^{26}\text{Mg}_i$ and $^{26}\text{Al}_i$ is the initial ^{26}Mg and ^{26}Al of the CAI precursor; and thus ($^{26}\text{Al}_i$-$^{26}\text{Al}_0$) represents the amount of ^{26}Mg from the decay of ^{26}Al. In order to connect the ^{26}Mg to measured Mg isotope, we divide ^{24}Mg on the both side of the equation:

$$\left(\frac{^{26}\text{Mg}}{^{24}\text{Mg}}\right)_0 = \left(\frac{^{26}\text{Mg}}{^{24}\text{Mg}}\right)_i + \frac{1}{^{24}\text{Mg}} \times \left(^{26}\text{Al}_i - ^{26}\text{Al}_0\right) \tag{5.3}$$

For the decay component from ^{26}Al, we add ^{27}Al to both numerator and denominator, and the equation can be rewritten as:

$$\left(\frac{^{26}\text{Mg}}{^{24}\text{Mg}}\right)_0 = \left(\frac{^{26}\text{Mg}}{^{24}\text{Mg}}\right)_i + \frac{^{27}\text{Al}}{^{24}\text{Mg}} \times \left[\left(\frac{^{26}\text{Al}}{^{27}\text{Al}}\right)_i - \left(\frac{^{26}\text{Al}}{^{27}\text{Al}}\right)_0\right] \tag{5.4}$$

where $^{27}\text{Al}/^{24}\text{Mg}$ is the bulk $^{27}\text{Al}/^{24}\text{Mg}$ ratio of the CAI that measured today; $(^{26}\text{Al}/^{27}\text{Al})_i$ and $(^{26}\text{Al}/^{27}\text{Al})_0$ are $(^{26}\text{Al}/^{27}\text{Al})$ ratio of the initial CAI precursor and when CAI formed. Since ^{27}Al is a stable isotope, we assume the abundance of ^{27}Al remained as a constant through the time. If we move the Mg isotope to the left hand side:

$$\left(\frac{^{26}\mathrm{Mg}}{^{24}\mathrm{Mg}}\right)_0 - \left(\frac{^{26}\mathrm{Mg}}{^{24}\mathrm{Mg}}\right)_i = \frac{^{27}\mathrm{Al}}{^{24}\mathrm{Mg}} \times \left[\left(\frac{^{26}\mathrm{Al}}{^{27}\mathrm{Al}}\right)_i - \left(\frac{^{26}\mathrm{Al}}{^{27}\mathrm{Al}}\right)_0\right] \tag{5.5}$$

It is noteworthy that the ^{26}Mg/^{24}Mg is not measured ^{26}Mg/^{24}Mg ratio because the mass dependent fractionation of Mg isotopes can influence the ^{26}Mg/^{24}Mg. To make the ^{26}Mg/^{24}Mg comparable between different samples, we use the unfractionated ^{26}Mg/^{24}Mg ratio (*i.e.,* $(^{26}\mathrm{Mg}/^{24}\mathrm{Mg})_{\mathrm{uf}}$)defined in Davis et al. (2015) by normalizing ^{25}Mg/^{24}Mg to the chondritic value of 0.126896 (Bizzarro et al. 2011) and correct the mass dependent ^{26}Mg/^{24}Mg fraction using the mass dependent fractionation law used in Eq. 2.18. To obtain the relationship between $\delta^{26}\mathrm{Mg}^*$ and ^{26}Al/^{27}Al, we need to derive the relationship between $\delta^{26}\mathrm{Mg}^*$ and $(^{26}\mathrm{Mg}/^{24}\mathrm{Mg})_{\mathrm{uf}}$:

$$\delta^{26}\mathrm{Mg}^* = \delta^{26}\mathrm{Mg}_{\mathrm{m}} - \left[\left(1 + \frac{\delta^{25}\mathrm{Mg}_{\mathrm{m}}}{1000}\right)^{\frac{1}{\beta}} - 1\right] \times 1000 \tag{5.6}$$

where m represents the measured value Substituting Eq. 2.17 into Eq. 5.6 leads to:

$$\delta^{26}\mathrm{Mg}^* = \left[\left(\frac{^{26}\mathrm{Mg}/^{24}\mathrm{Mg}_{\text{smp-m}}}{^{26}\mathrm{Mg}/^{24}\mathrm{Mg}_{\text{std-m}}}\right) - 1\right] \times 1000 - \left[\left(\frac{^{25}\mathrm{Mg}/^{24}\mathrm{Mg}_{\text{smp-m}}}{^{25}\mathrm{Mg}/^{24}\mathrm{Mg}_{\text{std-m}}}\right)^{\frac{1}{\beta}} - 1\right] \times 1000 \tag{5.7}$$

which can be simplified to:

$$\delta^{26}\mathrm{Mg}^* = \left[\frac{^{26}\mathrm{Mg}/^{24}\mathrm{Mg}_{\text{smp-m}}}{^{26}\mathrm{Mg}/^{24}\mathrm{Mg}_{\text{std-m}}} - \left(\frac{^{25}\mathrm{Mg}/^{24}\mathrm{Mg}_{\text{smp-m}}}{^{25}\mathrm{Mg}/^{24}\mathrm{Mg}_{\text{std-m}}}\right)^{\frac{1}{\beta}}\right] \times 1000 \tag{5.8}$$

if we use $\delta^{26}\mathrm{Mg}^*$ to express ^{26}Mg/^{24}Mg:

$$\left(\frac{^{26}\mathrm{Mg}}{^{24}\mathrm{Mg}}\right)_{\text{smp-m}} = \left[\frac{\delta^{26}\mathrm{Mg}^*}{1000} + \left(\frac{^{25}\mathrm{Mg}/^{24}\mathrm{Mg}_{\text{smp-m}}}{^{25}\mathrm{Mg}/^{24}\mathrm{Mg}_{\text{std-m}}}\right)^{\frac{1}{\beta}}\right] \times \left(\frac{^{26}\mathrm{Mg}}{^{24}\mathrm{Mg}}\right)_{\text{std-m}} \tag{5.9}$$

applying the normalization method for unfractionated ^{26}Mg/^{24}Mg ratio to 5.9:

$$\left(\frac{^{26}\mathrm{Mg}}{^{24}\mathrm{Mg}}\right)_{\mathrm{uf}} = \left[\frac{\delta^{26}\mathrm{Mg}^*}{1000} + \left(\frac{^{25}\mathrm{Mg}/^{24}\mathrm{Mg}_{\mathrm{chond}}}{^{25}\mathrm{Mg}/^{24}\mathrm{Mg}_{\mathrm{std}}}\right)^{\frac{1}{\beta}}\right] \times \left(\frac{^{26}\mathrm{Mg}}{^{24}\mathrm{Mg}}\right)_{\mathrm{std}} \tag{5.10}$$

where $^{26}\mathrm{Mg}/^{24}\mathrm{Mg}_{\mathrm{std}}$ represents the true ^{26}Mg/^{24}Mg ratio of the standard. Then, we can write the similar equations for both $(^{26}\mathrm{Mg}/^{24}\mathrm{Mg})_{\mathrm{uf(0)}}$ and $(^{26}\mathrm{Mg}/^{24}\mathrm{Mg})_{\mathrm{uf(i)}}$:

$$\left(\frac{^{26}\mathrm{Mg}}{^{24}\mathrm{Mg}}\right)_{\mathrm{uf(0)}} = \left[\frac{\delta^{26}\mathrm{Mg}_0^*}{1000} + \left(\frac{^{25}\mathrm{Mg}/^{24}\mathrm{Mg}_{\mathrm{chond}}}{^{25}\mathrm{Mg}/^{24}\mathrm{Mg}_{\mathrm{std}}}\right)^{\frac{1}{\beta}}\right] \times \left(\frac{^{26}\mathrm{Mg}}{^{24}\mathrm{Mg}}\right)_{\mathrm{std}} \tag{5.11}$$

$$\left(\frac{^{26}\mathrm{Mg}}{^{24}\mathrm{Mg}}\right)_{\mathrm{uf(i)}} = \left[\frac{\delta^{26}\mathrm{Mg}_i^*}{1000} + \left(\frac{^{25}\mathrm{Mg}/^{24}\mathrm{Mg}_{\mathrm{chond}}}{^{25}\mathrm{Mg}/^{24}\mathrm{Mg}_{\mathrm{std}}}\right)^{\frac{1}{\beta}}\right] \times \left(\frac{^{26}\mathrm{Mg}}{^{24}\mathrm{Mg}}\right)_{\mathrm{std}} \tag{5.12}$$

using Eq. 5.11 minus Eq. 5.12:

$$\left(\frac{^{26}\mathrm{Mg}}{^{24}\mathrm{Mg}}\right)_{\mathrm{uf(0)}} - \left(\frac{^{26}\mathrm{Mg}}{^{24}\mathrm{Mg}}\right)_{\mathrm{uf(i)}} = \frac{1}{1000} \times \left(\delta^{26}\mathrm{Mg}_i^* - \delta^{26}\mathrm{Mg}_0^*\right) \times \left(\frac{^{26}\mathrm{Mg}}{^{24}\mathrm{Mg}}\right)_{\mathrm{std}} \tag{5.13}$$

Then, the Eq. 5.5 can be expressed as:

$$\delta^{26}\mathrm{Mg}_0^* - \delta^{26}\mathrm{Mg}_i^* = -\frac{^{27}\mathrm{Al}}{^{24}\mathrm{Mg}} \Big/ \frac{^{26}\mathrm{Mg}}{^{24}\mathrm{Mg}}_{\mathrm{std}} \times \left[\left(\frac{^{26}\mathrm{Al}}{^{27}\mathrm{Al}}\right)_0 - \left(\frac{^{26}\mathrm{Al}}{^{27}\mathrm{Al}}\right)_i\right] \times 1000 \tag{5.14}$$

For a given CAI (named sample A), the slope and intercept obtained from the internal ^{26}Al-^{26}Mg isochron is ($^{27}\mathrm{Al}/^{26}\mathrm{Al}_{\mathrm{A}}$, $\delta^{26}\mathrm{Mg}^*_{0(A)}$), the function is:

$$\delta^{26}\mathrm{Mg}_0^* = -\frac{^{27}\mathrm{Al}}{^{24}\mathrm{Mg}} \Big/ \frac{^{26}\mathrm{Mg}}{^{24}\mathrm{Mg}}_{std} \times \left(\frac{^{26}\mathrm{Al}}{^{27}\mathrm{Al}_0} - \frac{^{26}\mathrm{Al}}{^{27}\mathrm{Al}_{\mathrm{A}}}\right) \times 1000 + \delta^{26}\mathrm{Mg}^*_{0(\mathrm{A})} \tag{5.15}$$

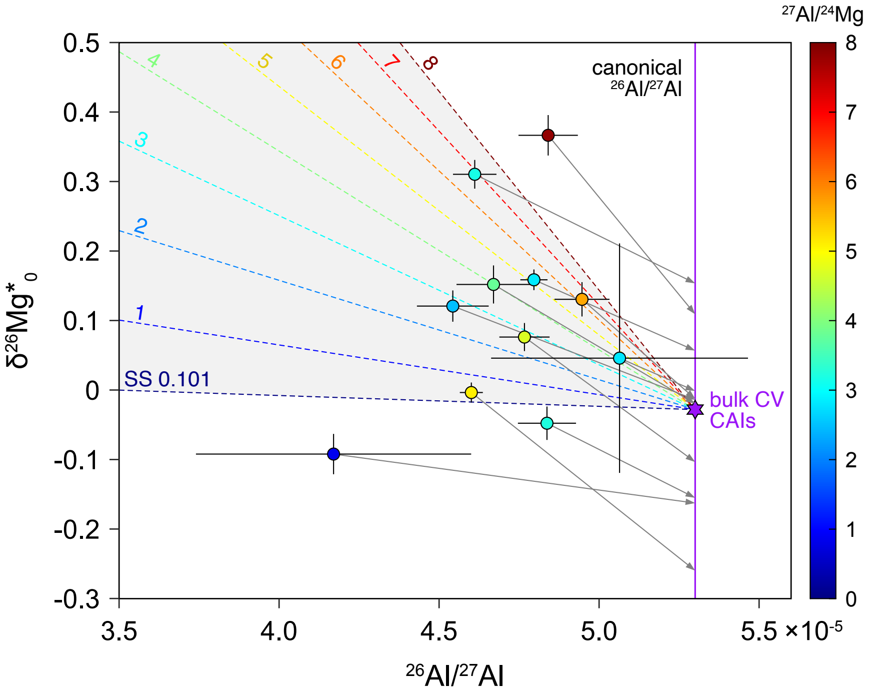

Figure 5.23: $\delta^{26}\mathrm{Mg}_0^*$ vs. $^{26}\mathrm{Al}/^{27}\mathrm{Al}$ obtained from internal isochrons, representing the Mg isotope evolution in CAIs. The purple hexagram denotes the canonical bulk CV CAI isochron, with $^{26}\mathrm{Al}/^{27}\mathrm{Al}$ of 5.30 × 10^{-5} and $\delta^{26}\mathrm{Mg}_0^*$ of -0.028 ‰. Circles represent the CAIs analyzed in this work, and the dashed lines show the projected Mg isotope evolution trajectory from the canonical bulk isochron with corresponding certain bulk $^{27}\mathrm{Al}/^{24}\mathrm{Mg}$ labeled beside the line. The color of the circles and dash lines indicates the present bulk $^{27}\mathrm{Al}/^{24}\mathrm{Mg}$ ratios of CAIs, corresponding to the color bar on the right. The grey-shaded area represents the plausible range that could evolve from the canonical CAI reservoir. The grey arrow is drawn for each CAI to show the Mg isotope evolution trajectory, and the intersection to the purple vertical line with canonical $^{26}\mathrm{Al}/^{27}\mathrm{Al}$ value represent the pre-^{26}Al decay Mg isotope composition.

In the Mg isotope evolution diagram, we only used 10 CAIs having the same or lower ^{26}Al/^{27}Al ratios than the canonical value. CAIs W(285)429 and CG*ft*-10 with ^{26}Al/^{27}Al ratios of $(5.84 \pm 0.05) \times 10^{-5}$ and $(5.60 \pm 0.13) \times 10^{-5}$, respectively, are not included. These supercanonical ^{26}Al/^{27}Al ratios are not due to early formation than the majority of CAIs and most likely reflect the scattering in the internal isochron resulting from the disturbance created artifact for the slope regression. The back-calculated pre-^{26}Al decay Mg isotope composition in $\delta^{26}\mathrm{Mg}_0^*$–^{26}Al/^{27}Al space (**Fig. 5.23**, intersection of the Mg evolution trajectory and canonical ^{26}Al/^{27}Al, noted as $\delta^{26}\mathrm{Mg}^*_{0,i}$) span a range from -0.259 to 0.154 ‰, which is broadly consistent with the Δ^{26}_0 values obtained from bulk isochron (**Fig. 5.24**). The inferred $\delta^{26}\mathrm{Mg}^*_{0,i}$ values also support a variable extent of heterogeneous initial Mg isotope composition in the CAI forming region(s).

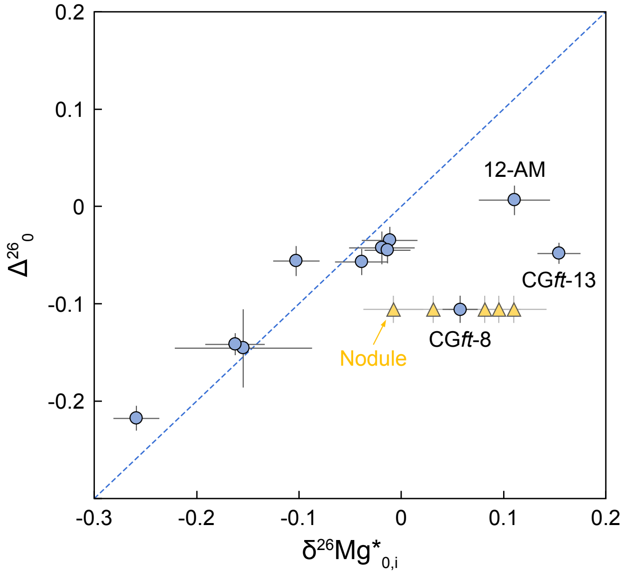

Figure 5.24: Comparison of initial Mg isotope composition of CAIs: Δ^{26}_0 vs. $\delta^{26}\mathrm{Mg}_{0,i}$. Δ^{26}_0 and $\delta^{26}\mathrm{Mg}_{0,i}$ are calculated from bulk isochron and extrapolated from internal isochron, respectively. The grey dash line represents the 1:1 line. Most of CAIs fall around the 1:1 line within the uncertainty, with three outliers CG*ft*-8, 13 and 2628-12-AM, which may due to the scatter in internal isochron.

Subsequent reprocessing and alteration after the condensation could potentially lead to disturbance in bulk and/or internal isochrons, and overprint the initial isotopic compositions. Below, we examine these processes and argue none of them can account for the observed Mg isotope variations (**Fig. B.1–B.4**):

(i) Closed system processing: CAI remains as closed system during most remelting or reprocessing (MacPherson et al. 2012). Closed system processing did not shift the Mg isotope composition and ^{27}Al/^{24}Mg ratio of the CAI in bulk ^{26}Al-^{26}Mg isochron. For the internal isochron, Mg isotope evolution in closed-system follows the lever rule with the bulk CAI as the fulcrum of the lever and the upward shift in $\delta^{26}\mathrm{Mg}^*_0$

accompanied by downward shift in ^{26}Al/^{27}Al ratio, whose effect can be corrected when extrapolation in the δ^{26}Mg$^*_0$-^{26}Al/^{27}Al relationship to obtain the true initial δ^{26}Mg$^*_{0,i}$ values.

(ii) Open system processing: The potential effects of open system resetting are more complex. We examined the two most typical open system processing scenarios: the interaction with ambient nebula gas and partial evaporation. The exchange with nebula gas can be further classified based on whether the CAI re-equilibrated with the gas during the last melting event. If the equilibration was achieved, the reset CAI would reflect mixing between the original CAI and solar nebula gas, and δ^{26}Mg$^*_{0,i}$ calculated back-extrapolation would not be affected (Mishra and Chaussidon 2014). When the surrounding environment is abundant with non-radiogenic Mg, the reset would result in ^{26}Mg deficits. This situation can be tested by comparing the δ^{26}Mg$^*_0$ with chondritic values (Simon and Young 2011) since this type of resetting could only lead to a decrease in δ^{26}Mg$^*_0$ approaching chondritic values (-0.030 ± 0.006 ‰, Luu et al. 2019) but not those below chondritic values observed in CAIs analyzed in this work. Partial evaporation can fractionation Al/Mg ratio in CAIs, and the loss of Mg would increase the ^{27}Al/^{24}Mg ratio without shifting the δ^{26}Mg$^*_0$ values. The extent of partial evaporation can be evaluated by the stable Mg isotope composition (δ^{25}Mg). CAIs analyzed in this work show only several permil of δ^{25}Mg variation, representing Mg losses less than 30 % (Richter et al. 2007). Meanwhile, the variable extent of ^{26}Mg deficits observed in CAIs that experienced limited evaporation (characterized by near zero or slightly negative δ^{25}Mg values) demonstrates the existence of initial Mg heterogeneity in CAIs.

Re-equilibration of CAI with nebula gas

In this situation, the CAI admixed with the nebula gas that followed the Solar System initial evolution line (^{27}Al/^{24}Mg ratio of 0.101). On the bulk isochron, both the δ^{26}Mg* and ^{27}Al/^{24}Mg are shifted downwards along the canonical bulk isochron. The reason is that the nebula gas evolves from the same composition of CAI precursor, just with a lower ^{27}Al/^{24}Mg ratio. Given the ^{26}Al/^{27}Al ratios in the nebula gas and CAI were the same, the slope of the internal isochron remains the same, and the whole isochron shifts downwards, leading to a lower δ^{26}Mg$^*_0$. On the Mg evolution diagram, the reset CAI reflects a mixing process between the original and solar evolution functions, which falls on the evolution line from the same precursor with the reset ^{27}Al/^{24}Mg ratio and thus would not change the back-extrapolated δ^{26}Mg$^*_{0,i}$.

Exchange with nebula gas but equilibrium not achieved

This scenario is proposed by Simon and Young (2011), which assumed the surrounding gas had significant partial pressure of Mg (*i.e.,* the ambient environment was abundant with non-radiogenic Mg). In this situation, the normal Mg would keep diluting the radiogenic Mg in the CAI, so the bulk $^{27}\mathrm{Al}/^{24}\mathrm{Mg}$ isochron will not change, but the $\delta^{26}\mathrm{Mg}^{*}_{0}$ would decrease. On the bulk isochron, the bulk composition moves vertically downwards. On the internal isochron, the flattened slope represents the last reset time that the system closed, and the $\delta^{26}\mathrm{Mg}^{*}_{0}$ would also move downwards due to the dilution of normal Mg. The extreme situation of this scenario is that $\delta^{26}\mathrm{Mg}^{*}$ in all mineral phases and whole rock may never increase and match the chondritic value. However, this type of open system resetting can only lead to $\delta^{26}\mathrm{Mg}^{*}_{0}$ approaching the chondritic value, but not those below the chondritic value, and thus cannot explain the $^{26}\mathrm{Mg}$ deficits observed in CAIs.

Partial evaporation

This scenario is discussed in MacPherson et al. (2012). The direct result of the partial evaporation is Mg loss and thus elevated $^{27}\mathrm{Al}/^{24}\mathrm{Mg}$. The time of the evaporation can influence the extrapolation of the CAI on the Mg isotope evolution diagram: (a) evaporation happened when the CAI precursor formed (*i.e.,* the $^{27}\mathrm{Al}/^{24}\mathrm{Mg}$ ratio was developed after condensation from the precursor). In this case, the extrapolation would not be impacted and still can be used to precisely examine the $\delta^{26}\mathrm{Mg}^{*}_{0,i}$. Previous studies (MacPherson et al. 2012; Mishra and Chaussidon 2014) demonstrate this case applied to most of CAIs. (b) evaporation happened during the last melting event. In this case, given the amount of $^{26}\mathrm{Al}$ was not modified, the $^{26}\mathrm{Mg}$ excesses are the same as the original CAI, but the $^{27}\mathrm{Al}/^{24}\mathrm{Mg}$ is higher due to the Mg loss, so the bulk isochron is moved to the right. On the internal isochron, the isochron is parallel to the original isochron but moves downwards. For the Mg evolution diagram, the CAI evolved through an evolution line with a lower $^{27}\mathrm{Al}/^{24}\mathrm{Mg}$ ratio. However, when extrapolating the $\delta^{26}\mathrm{Mg}^{*}_{0}$ and $^{26}\mathrm{Al}/^{27}\mathrm{Al}$, we used a higher $^{27}\mathrm{Al}/^{24}\mathrm{Mg}$ value (*i.e.,* through a steeper line), and would lead to artifact of lower $\delta^{26}\mathrm{Mg}^{*}_{0}$. (c) evaporation happened between the precursor formed and the last melting event. This case is similar to the second case, and the only difference is that it evolved from the evolution line with an original $^{27}\mathrm{Al}/^{24}\mathrm{Mg}$ ratio at the beginning and then follows a steeper line with a higher $^{27}\mathrm{Al}/^{24}\mathrm{Mg}$ ratio. In this case, the back-calculation would also lead to a lower $\delta^{26}\mathrm{Mg}^{*}_{0}$. The best approach to evaluate the evaporation is stable Mg isotopes ($\delta^{25}\mathrm{Mg}$). CAIs solely with a condensation origin typically have near zero or negative $\delta^{25}\mathrm{Mg}$ values, while that experienced evaporation would result in heavier $\delta^{25}\mathrm{Mg}$. In the analyzed samples, several CAIs with condensation origin also show variable extent of $^{26}\mathrm{Mg}$ deficits, supporting that these heterogeneity are not the artifacts from the extrapolation due to the partial evaporation.

(iii) Secondary alterations: Secondary alterations in the solar nebula and/or parent body can cause scattering in bulk and internal isochrons. However, these disturbances are challenging to quantitatively constrain. Previous analysis on one highly altered CAI (identified by almost absence of primary mineral phases) shows Δ_0^{26} ~-0.27 ‰ (Jacobsen et al. 2008). CAIs selected in this work are much more pristine than the highly altered CAI, so the impact of secondary alterations should be negligible compared with the initial Mg heterogeneity observed.

Although subsequent processes after the condensation may modify the Mg isotope compositions in some CAIs, they cannot account for most of the Δ_0^{26} values observed in this work. Consequently, the variable extent of ^{26}Mg variations reflect the true initial Mg isotope heterogeneity in the CAI forming region(s) rather than the interferences from subsequent processes.

5.4.2 Heterogeneous infalling materials during the CAI formation epoch

The existence of the pre-^{26}decay Mg isotope variations motivated the investigation of the origin of such heterogeneity observed among CAIs. The origin of isotopic variations in CAIs remains under debate, with two competing models proposed: selective thermal processing of presolar phases with distinct isotopic compositions in the protoplanetary disk (Paton et al. 2013; Schiller et al. 2015b, 2018; Trinquier et al. 2009) or inheritance of the SS's parental molecular cloud reflecting the earliest infalling materials (Burkhardt et al. 2019; Jacquet et al. 2019; Jansen et al. 2024; Nanne et al. 2019). The first model is used to interpret the Mg isotope variations in CAIs, which result from the thermal processing of presolar carrier characterized by enriched-^{26}Al and solar non-radiogenic δ^{26}Mg* (Larsen et al. 2011). The observation of the distinct $\delta^{26}\mathrm{Mg}_0^*$ values of CV and CR CAIs in Larsen et al. (2020) was explained by episodic transient heating events disproportionately admixed two presolar dust components: a ^{26}Al-rich with solar Mg isotope composition component and a ^{26}Mg deficit component. However, our finding of a gradual transition of variable Mg isotope heterogeneity with homogeneous ^{26}Al in CAIs does not support a few episodic formations of CAIs and is also hard to reconcile with a thermal processing origin. It would need the ^{26}Al-enriched presolar component to be completely evaporated and homogeneously distributed in the CAI forming region with the ^{26}Mg deficit presolar dust gradually evaporated and mixed with the first component. This scenario requires specific thermal properties of these isotopically distinct presolar components, and the high temperature in the CAI-forming region leaves little room for such selective processing.

Alternatively, the variable extent of initial Mg isotope heterogeneity in the CAI forming region can be easily explained by the infalling model. We interpret the gradual transition of Δ_0^{26} values as a continuous formation of CAIs from infalling materials with isotopically evolving compositions in the CAI forming region, after ^{26}Al had been injected and homogenized in the solar nebula (**Fig. 5.25a**). The scenario depicted here refers to the formation of majority CAIs, and we notice that

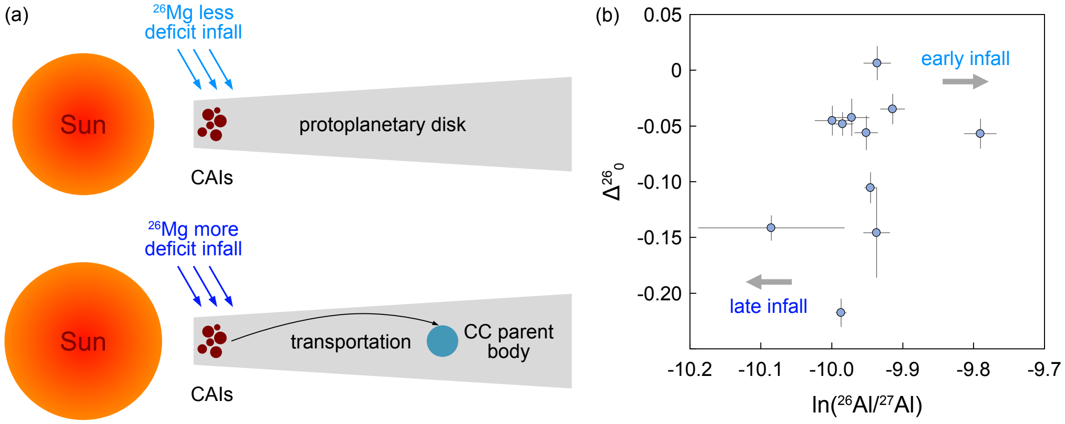

Figure 5.25: Mechanism of CAI formation process inferred from Mg isotopes. (a) Schematic diagram of CAI formation process. The heterogeneous initial Mg isotope compositions in CAIs reflected the temporal isotopic composition change of the infalling materials (b) Δ_0^{26} vs. $\ln(^{26}\mathrm{Al}/^{27}\mathrm{Al})$ reflecting the evolution of Mg isotope composition of infalling materials through the time.

small refractory inclusions (*e.g.,* hibonite, spinel grains, SHIBs, PLACs) and FUN CAIs could have distinct evolution history (Kööp et al. 2016a,b, 2018; Liu et al. 2012). This heterogeneous infall model inferred from Mg isotopes is consistent with the evidence form Mo isotope anomalies in CAIs (Budde et al. 2023), and disentangle that CAI reservoir captured a series of evolving records rather than a transient snapshot of the nascent SS, which is proposed in Burkhardt et al. (2019). The range of initial Mg isotope variations in CAIs could be explained by temporal or spatial differences of the infalling materials during the CAI formation. We tested the hypothesis of temporal evolution by evaluating the relationship between the initial Mg heterogeneity and the CAI formation time constrained by the internal isochron. In the Δ_0^{26}–$\ln(^{26}\mathrm{Al}/^{27}\mathrm{Al})$ space (the natural logarithm scale is used because it is linearly correlated with time), a weak negative correlation can be virtually identified, implying the increasing extent of ^{26}Mg deficits from the early to late infalling materials. The reasons for the poorly constrained trend could be: (i) CAIs experienced remelting, and $^{26}\mathrm{Al}/^{27}\mathrm{Al}$ did not record the time of infalling materials incorporation; (ii) heterogeneity in infalling materials did not solely reflected the temporal differences; (iii) the lack of CAI data that both bulk and internal isochrons are determined, and more work is needed.

The Mg isotope composition of bulk CAIs shows variable extent of ^{26}Mg deficits compared with normal CAIs that fall on the canonical CV CAI isochron, suggesting the existence of initial Mg isotope heterogeneity in the CAI forming region before the decay of ^{26}Al. The new finding suggests that CAI forming is a continuous process recording the evolution of the isotopic composition of the infalling materials, which reflects a temporal shift from slightly to highly ^{26}Mg deficits. The high-precision Mg isotope data suggests that CAIs can not only reflect a snapshot of the nascent SS but also can be used to understand the fine-scale evolution history of the SS.

Appendix B

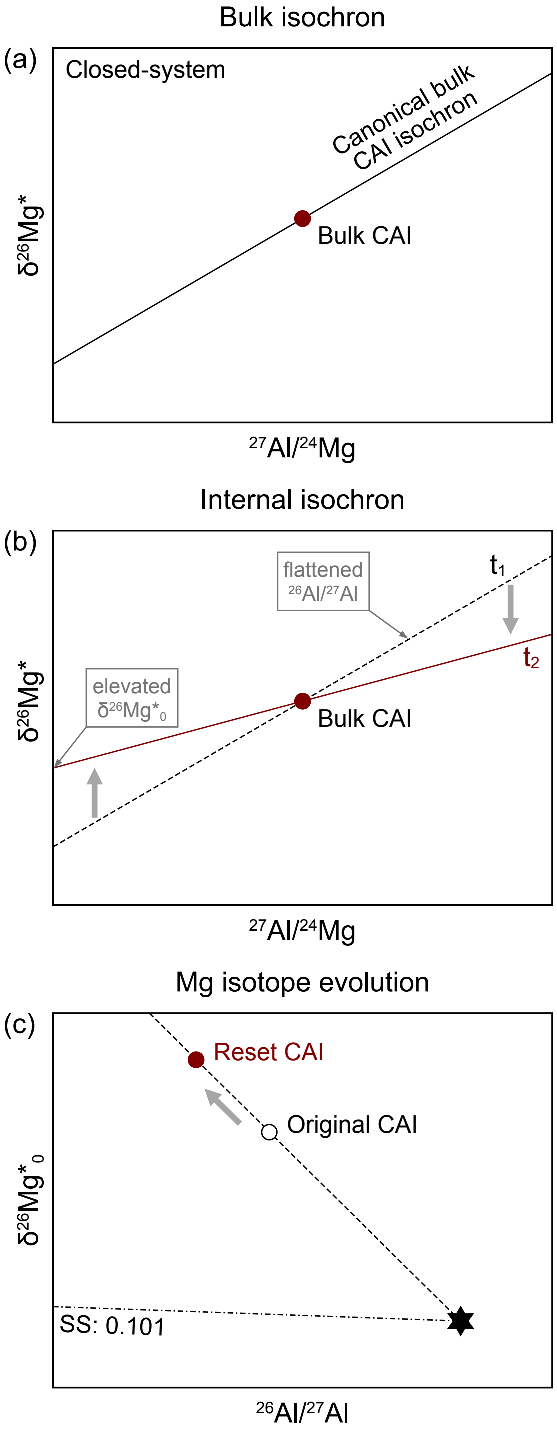

Figure B.1: Schematic bulk isochron, internal isochron, and Mg evolution diagrams showing the impact of closed system processing.

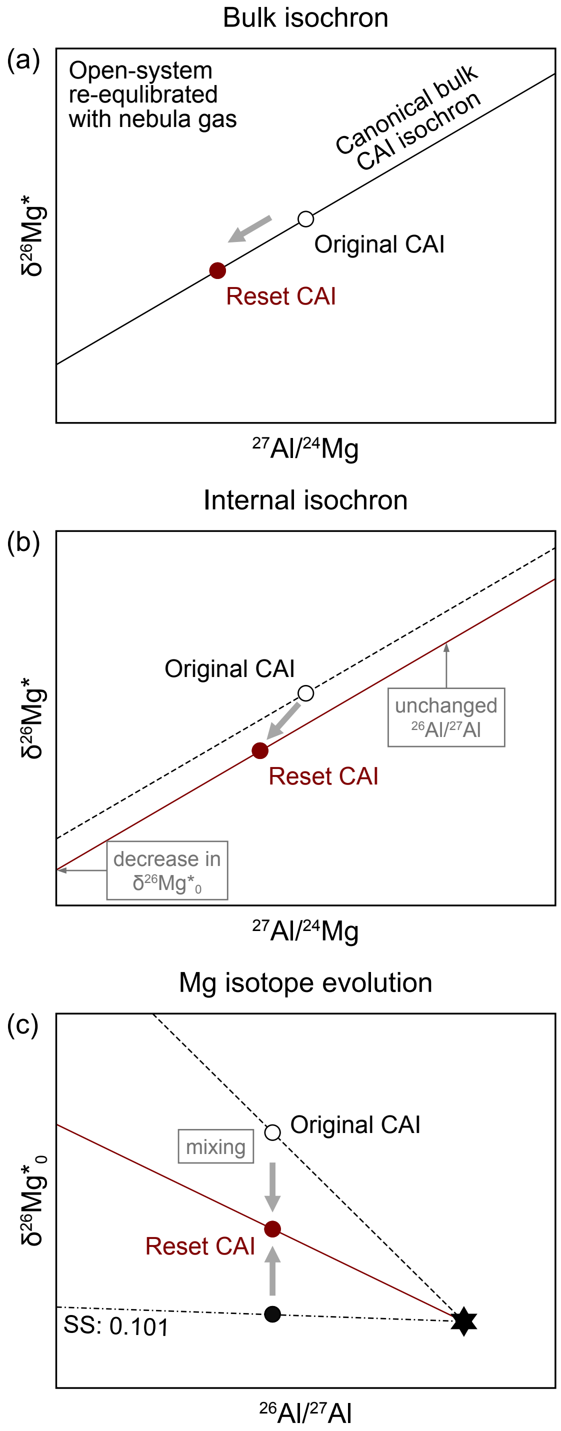

Figure B.2: Schematic bulk isochron, internal isochron, and Mg evolution diagrams showing the impact of open system processing that CAI re-equilibrated with the nebula gas.

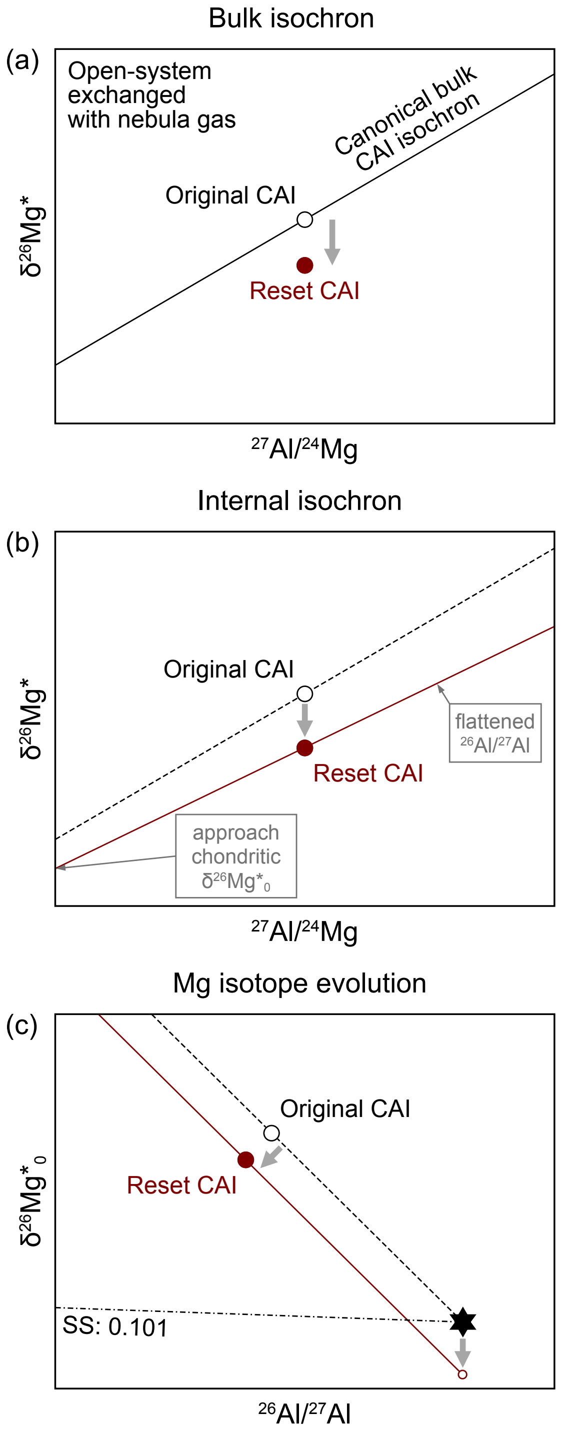

Figure B.3: Schematic bulk isochron, internal isochron, and Mg evolution diagrams showing the impact of open system processing that CAI exchanged with the nebula gas but not reach equilibrium.

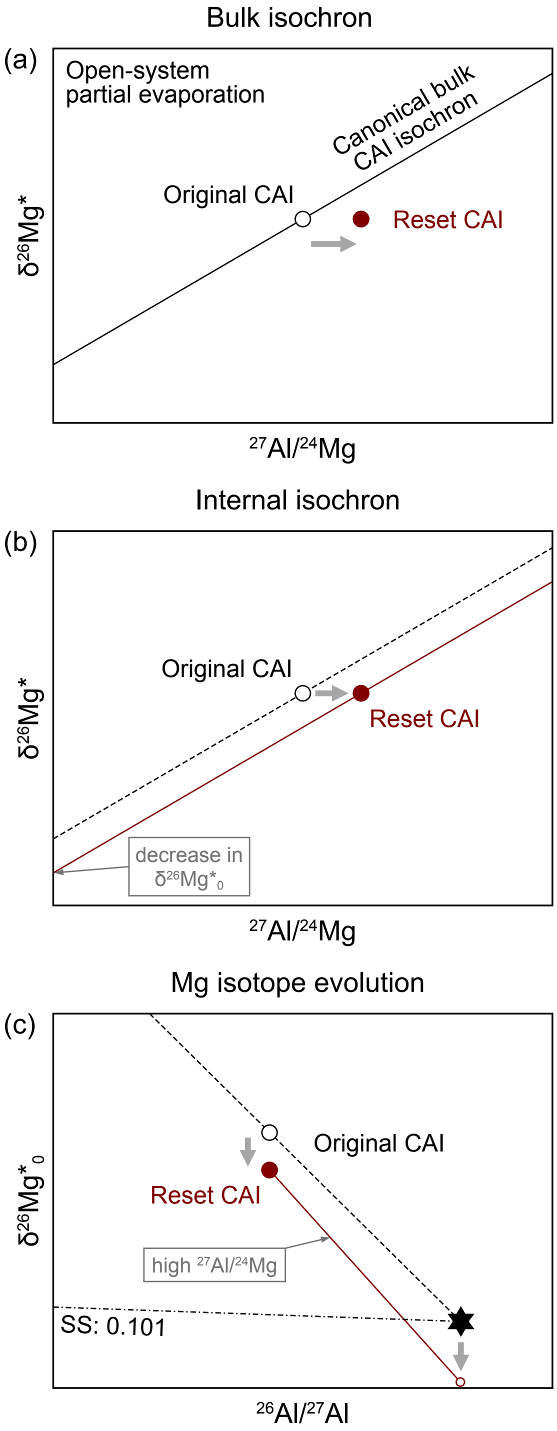

Figure B.4: Schematic bulk isochron, internal isochron, and Mg evolution diagrams showing the impact of partial evaporation.

Chapter 6

DECOUPLED RESETTING OF Pb-Pb AND Al-Mg CHRONOMETERS IN CAIS CHALLENGES THE STARTING POINT OF THE SOLAR SYSTEM

6.1 Motivation

Chronology of the Early Solar System (ESS) is fundamental to understanding its evolution history, given that this epoch covered the SS's evolution stages from the collapse of the parental molecular cloud to accretion and differentiation of planetary bodies (*e.g.,* Connelly et al. 2017; Davis 2022). Calcium-aluminum-rich inclusions (CAIs) play a critical role in the ESS chronology due to their nature of the oldest solids condensed in the solar nebula (Amelin et al. 2010; Connelly et al. 2012; Gray et al. 1973) and are therefore used to functionally define the starting point of the ESS (t_0). Deriving the value of t_0 is best done by determining CAIs age using the absolute Pb-Pb chronometer, while obtaining information on age differences between CAIs and other Solar System materials can be done using either the Pb-Pb chronometer or the relative ^{26}Al-^{26}Mg chronometer.

Over the last decade, high-precision chronological data has revealed a number of discrepancies and issues in the construction of a fine-scale ESS chronology (**Fig. 6.1**). Firstly, the two Pb-Pb ages proposed for the oldest CAIs do not agree within uncertainty: 4567.23 ± 0.15 Myr (average of 4 CAIs whose ages are consistent with each other: SJ101, 22E, 31E, and 32E, Amelin et al. 2010; Connelly et al. 2012) versus 4567.94 ± 0.31 Myr (B4, Bouvier et al. 2011a). However, the initial ^{26}Al/^{27}Al ratios of SJ101 and C4 are determined as $(5.20 \pm 0.53) \times 10^{-5}$ (MacPherson et al. 2017) and $(4.90 \pm 0.05) \times 10^{-5}$ (Wadhwa et al. 2014), respectively, which apparently do not match the age differences obtained from the absolute chronometer. On the other hand, the resolvable Pb-Pb age difference also conflicts with the short formation interval (∼20 kyr) of primary CAIs (characterized by ^{26}Al/^{27}Al ratio close to canonical value) derived from ^{26}Al-^{26}Mg systematics (MacPherson et al. 2012). Secondly, discrepancies between these two clocks also exist on subsequently formed solids in the SS, with the debate focusing on the discrepant estimates of the chondrule and achondrites ages. For chondrules, Pb-Pb ages suggested a protracted chondrule formation that started contemporaneously with CAIs (Bollard et al. 2017; Connelly et al. 2012) while the ^{26}Al-^{26}Mg systematics revealed an age gap of ∼1 Myr between CAI and chondrule formation (Fukuda et al. 2022; Pape et al. 2019; Siron et al. 2021; Villeneuve et al. 2009). For achondrites, Pb-Pb ages of quenched angrites, another type of common anchor in the ESS chronology, are found to be older than ^{26}Al-^{26}Mg ages when anchoring the determined ^{26}Al/^{27}Al ratios to CAIs.

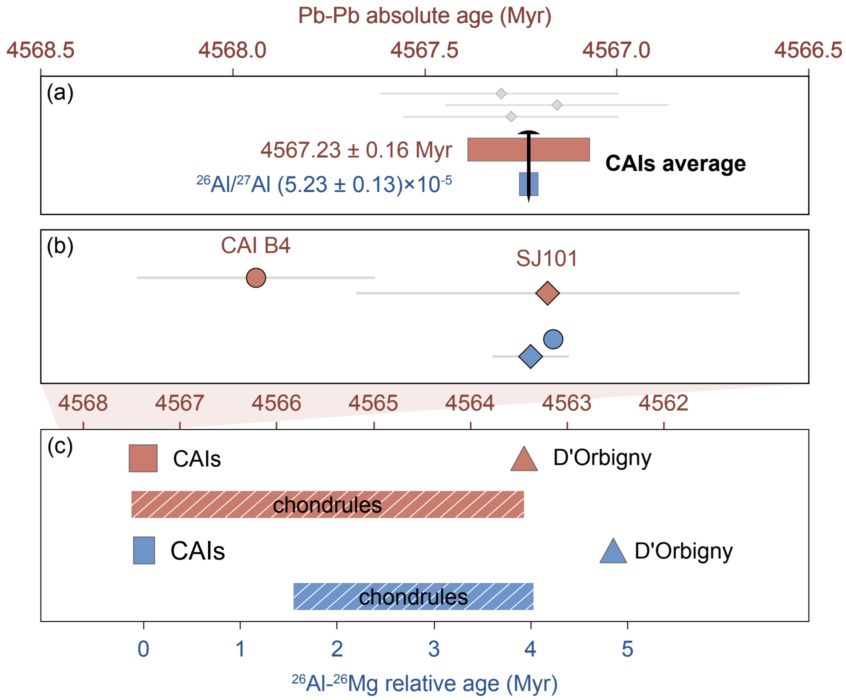

Figure 6.1: Discrepancies between Pb-Pb ages and ^{26}Al-^{26}Mg ages in the ESS chronology. (a) CAIs anchoring the Pb-Pb and ^{26}Al-^{26}Mg chronometers. The CAIs average Pb-Pb age is based on three Efremovka CAIs (Connelly et al. 2012), which is anchored to ^{26}Al/^{27}Al ratio of $(5.23 \pm 0.13)\times10^{-5}$ defined by the bulk CV CAIs isochron (Jacobsen et al. 2008).(b) Two different Solar System ages have been proposed based on CAI U-corrected Pb-Pb ages. The resolvable age difference conflicts with the short formation interval of CAIs (MacPherson et al. 2012). The CAI SJ101 from Allende (Amelin et al. 2010) is consistent with the anchoring approach described in panel (a), while the CAI B4 from NWA6991 is featured by much older Pb-Pb age and near canonical ^{26}Al/^{27}Al ratio. (c) Pb-Pb and ^{26}Al-^{26}Mg chronologies of the ESS, which yield discrepant estimates on the ages of chondrules and achondrites. For chondrules, Pb-Pb ages reflect a contemporaneous formation with CAIs, while ^{26}Al-^{26}Mg ages suggest a gap between chondrules and CAIs.

The cause of these discrepancies remains unknown but poses the question of the uniformity of different chronometers. For the first issue, the difference between the two oldest CAIs could be due to the method used to correct the uranium isotope composition while calculating Pb-Pb ages. The discovery of resolvable U isotope variations in natural samples has led to a significant revolution in Pb-Pb chronology (Stirling et al. 2007; Weyer et al. 2008), which overthrew the long-standing assumption of a constant ^{238}U/^{235}U (Steiger and Jäger 1977), and thus U isotopes are supposed to be determined to obtain accurate Pb-Pb ages. For CAIs in particular, ages are derived using step leaching approaches that have the benefit of removing non-radiogenic Pb in the early leachates. The final leachates and residues, typically comprised of pyroxene, are the most radiogenic and control the age determination. Recent studies of igneous samples suggest that U isotopes can fractionate during magmatic processes, and in particular during incorporation into specific minerals (Hiess et al. 2012; Livermore et al. 2018; Tissot et al. 2017, 2019a). As such, intermineral U isotope variations could be expected in CAIs and therefore, result in age offsets. Although U isotopes in CAIs are typically measured in bulk fractions only (Amelin et al. 2010; Brennecka et al. 2010a; Connelly et al. 2012; Tissot et al. 2016), only very limited data exits for U isotope on mineral separates of CAIs (Cooke et al. 2013; Shollenberger et al. 2019). This hypothesis can be tested by comparing U isotope composition in mineral separates and bulk samples, especially on large CAIs that have abundant U to perform high-precision measurement.

For the second issue, several hypotheses are proposed to explain the discrepancies between CAIs and chondrules/achondrites. A popular interpretation for the disagreement is that ^{26}Al/^{27}Al ratios in CAI forming regions were significantly higher than those of chondrules and achondrites by order of magnitude at most (Bollard et al. 2017, 2019; Krestianinov et al. 2023; Schiller et al. 2015a). However, such a significant degree of ^{26}Al/^{27}Al heterogeneous distribution did not accord with the prediction of astrophysical models since isotopic variations that existed in the molecular cloud would be mixed and homogenized during the collapse process (Kuffmeier et al. 2017; Pan et al. 2012; Pignatale et al. 2018). As a result, alternative theories are investigated to reconcile the inconsistencies under the framework of a homogeneous ^{26}Al/^{27}Al distribution in the protoplanetary disk. For example, CAIs and chondrules may consist of precursors from various origins, and therefore Pb-Pb ages could partially represent the mixing processes rather than the pure age information of formation (Blichert-Toft et al. 2020). Subsequent processes in the solar nebula or parent bodies (*e.g.,* aqueous alterations, thermal metamorphism) could reset ^{26}Al-^{26}Mg and Pb-Pb ages to different extents, and thus result in the inconsistency between the two chronometers (Lewis and Jones 2019; Siron et al. 2021; Van Orman et al. 2014). Recent studies proposed that this discrepancy of CAIs and achondrites can be resolved if the CAIs define a t_0 of 4568.7 Myr (Desch et al. 2023; Piralla et al. 2023), based on the assumption that Pb-Pb system of CAIs could be reset without affecting ^{26}Al-^{26}Mg ages. However, this much older age of CAIs and the assumption of decoupled resetting of these two chronometers have not been justified by direct Pb-Pb dating yet. Furthermore, the current widely accepted age of CAIs is obtained by averaging the ages of only 4 CAIs (Amelin et al. 2010; Connelly et al. 2012). The most direct approach to address these problems and limitations requires the determination of both ^{26}Al-^{26}Mg and Pb-Pb ages on a same set of CAIs.

This work seeks to revisit the proposed origins of these two essential inconsistencies in the ESS chronology. To test the impact of subsequent processes on these two chronometers, we determined both ^{26}Al-^{26}Mg and U-corrected Pb-Pb ages of a set of 5 CAIs with various extent of alterations. We also measured U isotopes of mineral fractions and bulk material for one large coarse-grained CAI to investigate whether the potential intermineral U isotope variations can reconcile the age discrepancy between CAIs.

6.2 Sample and method

6.2.1 Sample preparation

In this work, seven CAIs from CV chondrites were selected, and analyses performed on each sample are illustrated in **Table 6.1**. CAIs CG*ft*-6, 10, 11, 13, 15, and ALVIN were previously studied for combined Ti, W, and Mo isotopes (Tissot et al. 2019b). This set of 6 CAIs were used for comprehensive investigations, including petrology characterization, bulk U isotopes, Pb-Pb dating, and in-situ ^{26}Al-^{26}Mg analyses. These CAIs were cut out of their host meteorites using a diamond saw, and then the sample surface was cleaned using SiC sandpaper and/or gently broke into small pieces in a precleaned agate mortar.

Table 6.1: Sample information of CAIs investigated in this study, and analyses conducted on each sample.

Collection ID	Short Name	CAI Type	Meteorite	Petrology characterization	Bulk U isotopes	Pb-Pb dating	Al-Mg analyses	Mineral Separates
ME2629-4.73	CG-*ft*-6	Type B	Allende	●	●	●	●	
ME2639-3.1	CG-*ft*-10	Type B	Allende	●	●	●	●	
ME2639-13.1	CG-*ft*-11	Type B	Allende	●	●	●	●	
ME2639-49.6[a]	CG-*ft*-13	CTA	Allende	●	●	●	●	
	CG-*ft*-15	CTA	Allende			●		
ME2629-4.109	ALVIN	FoB	Allende	○[b]	●	●	○[c]	
Check YD	3529-49	Type B	Allende	●	●	●		
Check GBU	AI01	Type B	NWA6870	○[d]	●		○[d]	●

* Notes: ● represents analyses conducted in this work; ○ represents data from literature.
[a] CG-*ft*-13 and CG-*ft*-15 are two sub-domains (alteration-poor and alteration-rich) of the same CTA CAI.
[b] Bullock et al. (2012)
[c] MacPherson et al. (2017)
[d] Budde et al. (2019)

A small chip was picked and mounted in epoxy for mineralogy and petrology characterization. The epoxy mount was polished and carbon coated for mapping and secondary ion mass spectrometry (SIMS) analyses. A bulk fragment (∼50 mg) was set aside and used for Pb-Pb work. The remainder of the CAI was digested in concentrated HF-HNO$_3$-HClO$_4$ (2:1:0.05 by volume) at 150 °C for 9 days. Along with CAI samples, several geostandards (BCR-2 and BHVO-2) as well as bulk Allende chondrite were processed parallel as quality control. The digested solution was spilt into three aliquots for multi-elemental and isotopic investigation. One of the aliquots was used for non-spiked W chemistry, and the matrix cut is preserved for following bulk U isotope analyses.

3529-49 is an additional CAI used for U-corrected Pb-Pb dating. The sample is located in an Allende slab with dark matrix materials surrounding the light CAI material. The CAI was extracted from the matrix using dental tools under a binocular microscope and cleaned with acetone. Then, the sample was crushed using a boron carbide mortar and separated into two fractions: a ∼50 mg fraction used for bulk digestion and U isotopes, while another ∼60 mg fraction for Pb-Pb analyses.

AI01 is an exceptionally large CAI, which is ideal for investigating the intermineral U isotope variations. Extracted CAI fragments were gently crushed with a pestle and agate mortar and sieved through nylon mesh from coarse to fine in sequence. The CAI grains were separated into 5 fractions based on mineralogy and magnetic susceptibility: melilite, fassaite (Ti-Al-rich calcic pyroxene), magnetic, non-magnetic, and fines. Magnetic and non-magnetic fractions were separated by hand magnets. Melilite and fassaite were distinguished according to appearance and separated by hand-picking. Melilite is typically transparent or white, while fassaite can range from dark grey to black, which reflects the spinel abundance in these minerals. Anorthite and spinel are minor (rel. to mel and fas) phases in the CAI, which are difficult to separate from other phases: anorthite is white and thus hard to recognize from melilite; spinel grains are small and poikilitically embedded in other mineral phases. Several representative grains of each fraction were selected to check mineralogy under a scanning electron microscope (SEM) using Energy Dispersive Spectroscopy (EDS) analyses. The bulk and mineral fractions AI01, as well as its host NWA6870, were digested using similar consecutive acid attacks for following W chemistry (Budde et al. 2019), and the matrix cut was used for U chemistry.

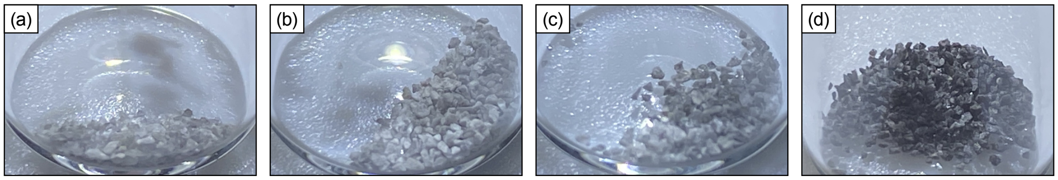

Figure 6.2: Minerals separated from CAI. (a) transparent, (b) white, (c) grey, and (d) black fractions. The diameter of the bottle is ∼ 2 cm.

6.2.2 Mineralogy and petrology characterization

The mineralogy and petrology of CAIs were characterized using a JEOL JSM-5900LV scanning electron microscopy at University of Hawaii at Manoa. Backscattered electron (BSE) and combined X-ray elemental maps (Ca, Al, Mg, Ti, Si, Cl, and Na) are obtained with the SEM coupled with energy dispersive X-ray spectroscopy (EDS) using 15 keV accelerating voltage, 100 nA beam current, and a beam size of 2 μm. The major elemental compositions of primary and secondary mineral phases were determined by electron microprobe.

6.2.3 U isotope analyses

Before U purification, a ∼1 % aliquot was taken from the digest for concentration determination on a Thermo Fisher iCAP RQ ICP-MS. The sample solutions were evaporated to dryness and taken back into 5 mL 3 M HNO_3, that are ready for loading on the column.

Uranium chemistry was performed on pre-packed 2 mL U-TEVA cartridges (Eichrom) following established methods (Tissot et al. 2016, 2017) modified for low U samples using a vacuum box. In brief, samples were loaded in 2.5-10 mL 3 M HNO_3 onto the resin pre-cleaned by 40 mL 0.05 M HCl and conditioned by 10 mL 3 M HNO_3. After loading, 30 mL of 3 M HNO_3, 5 mL of 10 M HCl, and 12 mL of 5 M HCl were used in sequence to elute matrix elements and Th. The U was finally eluted in 32 mL 0.05 M HCl at the end. After the first round of chemistry, each sample was spiked with IRMM-3636 to obtain a U_{spike}/U_{sample} ratio of ∼10 % based on the U concentration obtained from iCAP measurements. The spiked U cut was dried completely, and 0.25 mL H_2O_2 and 0.20 mL concentrated HNO_3 were added to oxidize any organic matter released from the resin. After refluxing overnight at 120 °C, the mixture was completely dried and taken back into 3 M HNO_3. The column chemistry was repeated to ensure the complete removal of matrix elements. The final U cuts were evaporated to dryness before being redissolved in concentrated HNO_3. Samples were then evaporated to near dryness and ultimately diluted to 1mL 3 vol% HNO_3 for isotopic measurements. For 3529-49, a three-step protocol was used for U separation, as described in in Di (2023). The solution was passed through the Bio-rad AG50W-X8 to separate U and high-field strength elements from matrix. The pre-concentrated cut with U was spiked with IRMM-3636 and then loaded onto a Teflon column ($\varnothing$ = 3.5 mm, length = 30 mm) filled with 0.2 mL pre-cleaned Bio-rad AG1-X8 resin (200-400 mesh) on top of 0.1 mL Eichrom Pre-filter resin, followed by the final U purification step using 50 μL of UTEVA resin using 3 M HNO_3.

Uranium isotope analyses were performed on a Neptune*Plus* (ThermoFisher) multiple collector inductively coupled plasma mass spectrometer (MC-ICPMS) at Caltech, using a cone combination of Jet sample and X-skimmer cones coupled with an Aridus3 desolvating nebulizer. The measurements were conducted in low-resolution mode using a static cup configuration. A small aliquot (10 μL, ∼1 % of the total sample) was taken from the purified solution to determine recovered U after chemistry. The amount of U in bulk CAIs ranged from 3.1 to 11.5 ng. The sample concentrations were adjusted to 8–13 ppb, corresponding to volumes of 0.40–0.88 mL, which allowed for one high-precision measurement. For CAI AI01, given the large size of this sample, the quantity of U in mineral separates and bulk fraction was larger than other CAIs (3.7–33.0 ng). The U concentrations were adjusted to 11–18 ppb, corresponding to volumes of 0.53–1.8 mL, which allowed for 1–3 times of measurements. To avoid wasting samples, the take-up time was reduced to 36 s (minimal time to achieve stable signal), and each analysis consisted of 40–60 cycles of 4.194 s integration time depending on the available sample masses. The sample measurements were bracketed by the CRM-112a standard spiked with IRMM-3636 at a similar U_{spike}/U_{sample} ratio as the samples. Geostandards BCR-2 or BHVO-2 were measured between CAIs to monitor the accuracy and precision of the U isotope analyses.

6.2.4 U-Pb isotope analyses

The U-Pb systematics were analyzed at the Australian National University. The CAI chips were ultrasonically cleaned with ethanol for 60 min and weighed for their masses. After weighing, samples are washed down with ∼2 ml of MQ water. Cleaned CAIs were crushed in a boron carbide mortar and fragments were separated into 4 mineral fractions by handpicking under a binocular microscope: melilite, pyroxene, intergrown coarse, and bulk medium-fine. All picked fractions were ultrasonically cleaned with ethanol for 30 min, followed by rinsing with distilled acetone for 3 times. After drying in the air, the cleaned fragments were transferred into precleaned Savillex vials for digestion. The step dissolution procedure produced 4 fractions: W1 (MQ H_2O, 0.3 M HBr, and 0.5 M HNO_3), W2a (3 M HNO_3 at 110 °C), W2b (6 M HCl at 110 °C), Residue (30 M HF at 110 °C). Residues and washes of CAIs were spiked with ^{202}Pb-^{205}Pb-^{232}Th-^{233}U-^{236}U tracer, then converted to bromide form, and finally reconstituted into 1 M HBr for chemistry. Lead purification was performed using 0.05 mL AG1-X8 anion exchange resin, with Pb eluted in 0.5 M HNO_3 after matrix removal in 0.3 M HBr + 2.5 M HCl. The chemistry was repeated once to ensure complete removal of matrix elements. Lead isotope measurements were preformed on a MAT 261 thermal ionization mass spectrometer (TIMS). The Pb fraction were loaded on refined rhenium filaments with silica gel, and then measured in static multi-collector mode using Faraday cups or peak jumping mode using secondary electron multiplier (SEM).

6.2.5 In-situ Al-Mg analyses

In-situ ^{26}Al-^{26}Mg isotope analyses were performed on CAMECA IMS 1270-E7 and IMS 1280-HR2 at CRPG following the method described in previous studies (Luu et al. 2013; Piralla et al. 2023; Villeneuve et al. 2009). Measurements were conducted in multicollection mode on 4 Faraday cups (FC): ^{24}Mg on L1 equipped with a 10^{11} Ω resistor, ^{25}Mg and ^{26}Mg on C and H1 equipped with 10^{12} Ω resistors and ^{27}Al on H'2 equipped with a 10^{11} Ω resistor. Mass resolution was set to 2500 (*i.e.,* exit slit 1 on multicollection trolleys) to separate the doubly charged interference $^{48}Ca^{2+}$ and $^{48}Ti^{2+}$. Selected spots were bombarded with a <10 μm, 5 nA O_2^- primary ion beam generated by a Hyperion-II oxygen plasma source accelerated at 13 keV. Each spot analysis had a 45 s sputtering and 30 cycles (10 s/cycle) of acquisition. The instrumental mass fractionation (IMF) was calibrated by a series of international and in-house standards, including San Carlos olivine, Burma spineal, CLDR01 MORB glass, gold enstatite, and Allende melilite (Mel-1) glass. To precisely determine the

^{27}Al/^{24}Mg ratios for isochron, the measured values were corrected using the relative sensitivity factor (RSF) for different mineral phases, given that Al and Mg have slightly different ion yields during SIMS analyses. The ^{27}Al/^{24}Mg ratios of analyzed CAI minerals, including melilite, spinel, anorthite, and hibonite were calibrated by RSFs determined by Mel-1, 2 glass, Burma spinel, An-2 glass, Al-rich pyroxene glass, and Hib-A-00, respectively.

6.3 Results

6.3.1 Brief description of CAIs

The combined Ca-Mg-Al elemental and BSE maps of the investigated CAIs are shown in **Section 5.3.1**, and detailed characterization for each CAI is described here. CG-*ft*-6 is a Type B CAI, composed of melilite ($\text{Åk}_{13\text{–}75}$), fassaite (5–10 wt% TiO_2, 19 wt% Al_2O_3), and anorthite, all poikilitically enclose spinel grains. Melilite and fassaite show normal igneous zoning. Åkermanite content in melilite increase towards the CAI core. Melilite is crosscut by veins and replaced by secondary minerals, while fassaite, spinel, and perovskite show no evidence for alteration. The CAI is surrounded by a Wark-Lovering rim.

CG-*ft*-10 is a Type B CAI, composed of melilite ($\text{Åk}_{10\text{–}74}$), fassaite (3.6–8.1 wt% TiO_2, 12.4–20.4 wt% Al_2O_3), anorthite; all poikilitically enclose spinel grains. Melilite and fassaite show normal igneous zoning. Åkermanite content in melilite increase towards the core. Melilite is crosscut by veins and replaced by secondary minerals, while coarse-grained anorthite, fassaite, and spinel are largely unaltered. The CAI is surrounded by a Wark-Lovering rim, a fine-grained matrix-like rim, and a layer of Ca, Fe-rich silicates. Spinel and Al, Ti-diopside in the Wark-Lovering rims show enrichment in FeO.

CG-*ft*-11 is a Type B CAI, composed of melilite, anorthite, and igneously-zoned fassaite (~2–10 wt% TiO_2, ~13–21 wt% Al_2O_3), all poikilitically enclosing abundant spinel grains. Melilite in the central part is åkermanite-rich ($\text{Åk}_{46\text{–}70}$). There are several relatively fine-grained regions in this fragment composed of anorthite, highly-åkermanitic melilite and low-Ti fassaite, whose textures and mineralogy suggest they represent eutectic melts from which these three minerals co-crystallized. Melilite in these regions is almost completely replaced by secondary secondary minerals. Anorthite grains contain abundant submicron silicate inclusions and are only slightly corroded by Na-melilite and grossular. Fassaite shows no evidence for alteration.

CG-*ft*-13 is a compact Type A (CTA) CAI, composed of gehlenitic melilite ($\text{Åk}_{3\text{–}32}$), spinel, and minor hibonite, perovskite, and fassaite (~9–14 wt% TiO_2, ~20–21 wt% Al_2O_3), whic is surrounded by a Wark-Lovering rim, a discontinuous coarse-grained accretionary rim, a fine-grained matrix-like rim, and a layer of Ca, Fe-rich silicates. The CAI experienced extensively open-system metasomatic alteration, with Ca and some Al removed. Melilite in the CAI mantle and core is crosscut by veins apparently of multiple generations.

ALVIN (a.k.a. TS-45) is a forsterite-bearing Type B (FoB) CAI, which is previously characterized in Bullock et al. (2012). ALVIN is predominately composed of Al,Ti-rich pyroxene that poikilitically enclosing abundant forsterite and spinel grains. This CAI is featured with numerous vesicles, which are filed with needles of wollastonite. 3529-49 from Allende is a Type B CAI composed of melilite (Åk$_{55\text{-}65}$), pyroxene, spinel, and minor anorthite. AI01 from NWA6870 is a Type B CAI composed of melilite, pyroxene, spinel, and anorthite.

6.3.2 U isotopes

Uranium isotopes are reported in delta notation relative to CRM-112a standard ($^{238}\mathrm{U}/^{235}\mathrm{U} = 137.837$, Richter et al. 2010), which is expressed as:

$$\delta^{238}\mathrm{U} = \left(\frac{^{238}\mathrm{U}/^{235}\mathrm{U}_{\mathrm{smp}}}{^{238}\mathrm{U}/^{235}\mathrm{U}_{\mathrm{CRM\text{-}112a}}} - 1 \right) \times 1000 \tag{6.1}$$

Uncertainties are reported as 2SE (95 % CI) and calculated using the daily external reproducibility of the CRM-112a standard (2SD) divided by the square root of the number of replicate measurements for a given sample (*i.e.*, $2\mathrm{SE} = 2\mathrm{SD}_{\mathrm{External}}/\sqrt{n}$).

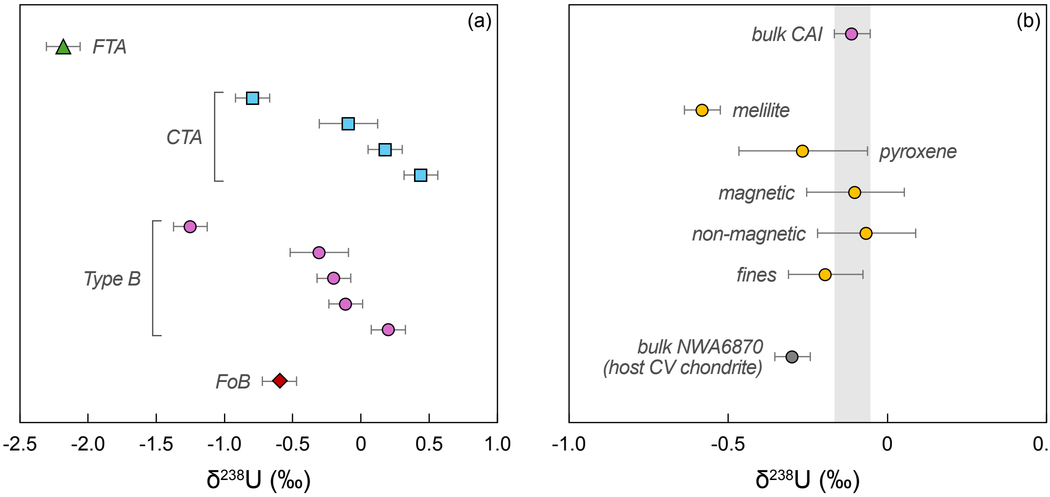

Figure 6.3: U isotope composition of (a) bulk CAIs; The symbols represents the type of CAIs: green triangular–FTA, blue square–CTA, pink circle–Type B, red diamond–FoB; (b) mineral separates and bulk CAI 'AI01', as well as the host CV chondrite NWA6870. The grey band indicates the δ^{238}U of the bulk CAI 'AI01'. The δ^{238}U values are normalized to CRM-112a, assuming a $^{238}\mathrm{U}/^{235}\mathrm{U}$ value of 137.837 (Richter et al. 2010).

The U isotope data of bulk CAIs and mineral separates of AI01 are shown in **Table 6.2** and **Fig. 6.3**. The 11 newly investigated CAIs from Allende show U isotope variations ranging from -2.88 ‰ to +0.44 ‰, consistent with the wide presence of U isotope variations in CAIs from CV chondrites (Amelin et al. 2010; Brennecka et al. 2010a; Connelly et al. 2012; Tissot et al. 2016). The FTA CG*ft*-8 shows the largest U isotope fractionation, while the CTA and Type B CAIs cover a similar range of U isotope variations. For CAI AI01, despite the low amounts of U available for analysis, uranium isotopic variations are observed between the melilite fraction and the bulk CAI, with the melilite being 0.47 ± 0.21 ‰. This difference is larger than those observed in a previous study (Cooke et al. 2013; Shollenberger et al. 2019). For pyroxene, the δ^{238}U difference is not resolved at the current level of analytical precision. However, if taking the composition at face value, the pyroxene is lighter than the bulk CAI by ~0.15 ‰. For a CAI (*i.e.,* a sample formed about 4565 Myr ago), this difference would translate in an age corrections of 0.22 Myr in the Pb-Pb absolute age. The magnitude of this age offset is unlikely to reconcile the discrepancy of the age difference between the two oldest known CAIs.

Table 6.2: U isotope composition of bulk CAIs, CAI mineral separates, and bulk chondrite.

Short Name	Type	Meteorite	Material	Mass (mg)	δ^{238}U	2SE	n	U (ng)
CAI								
CG*ft*-5	CTA	Allende	bulk CAI	~200	-0.09	0.12	1	10.3
CG*ft*-6	Type B	Allende	bulk CAI	~200	-0.31	0.12	1	10.8
CG*ft*-7	CTA	Allende	bulk CAI	~200	-0.79	0.21	1	3.0
CG*ft*-8	FTA	Allende	bulk CAI	~200	-2.18	0.12	1	7.1
CG*ft*-10	Type B	Allende	bulk CAI	~200	-0.20	0.12	1	12.0
CG*ft*-11	Type B	Allende	bulk CAI	~200	0.20	0.12	1	8.5
CG*ft*-12	CTA	Allende	bulk CAI	~200	0.18	0.12	1	9.9
CG*ft*-13	CTA	Allende	bulk CAI	~200	0.44	0.12	1	8.3
ALVIN	FoB	Allende	bulk CAI	~200	-0.60	0.12	1	9.5
3529-49	Type B	Allende	bulk CAI	55.8	-1.25	0.21	1	x
AI01	Type B	NWA6870	bulk CAI	289	-0.11	0.06	3	46
Mineral separates								
AI01 mel	Type B	NWA6870	melilite	90	-0.58	0.20	1	4
AI01 fas	Type B	NWA6870	fassaite	74	-0.26	0.15	1	10
AI01 mag	Type B	NWA6870	magnetic	59	-0.10	0.15	1	8
AI01 non-mag	Type B	NWA6870	non-magnetic	189	-0.07	0.12	3	28
AI01 fines	Type B	NWA6870	fines	170	-0.19	0.12	3	29
Bulk chondrite								
NWA6870	CV3	NWA6870	bulk chond	536	-0.30	0.06	3	34
Allende dig1	CV3	Allende	bulk chond	~500	-0.41	0.12	1	6.4
Allende dig2	CV3	Allende	bulk chond	~501	-0.29	0.12	1	6.7
Geostandards								
BCR-2					-0.26	0.07	34	546
BHVO-2					-0.31	0.10	14	122

6.3.3 Pb isotopes and Pb-Pb ages

The age corrections caused by U variability is given by the following equation (Tissot and Dauphas 2015; Tissot et al. 2017):

$$\Delta t = \frac{\Delta \mathrm{U}\left(e^{\lambda_{238}t}-1\right)\left(e^{\lambda_{235}t}-1\right)}{1000\left[\lambda_{238}e^{\lambda_{238}t}-\lambda_{235}e^{\lambda_{235}t}+(\lambda_{235}-\lambda_{238})e^{(\lambda_{238}+\lambda_{235})t}\right]} \tag{6.2}$$

where ΔU is the difference between the actual and assumed U isotope composition of the sample; λ_{238} and λ_{235} are decay constants of ^{238}U and ^{235}U, respectively; t is the Pb-Pb age of the sample obtained using an assumed U isotope composition. The U-corrected Pb-Pb ages of 6 CAIs range from 4565.86 ± 0.35 Myr to 4567.10 ± 0.30 Myr (**Fig. 6.5**). The observed U isotope variations result in age corrections ranging from -0.66 Myr to +0.84 Myr. The correction reduced the range of CAI ages from 2.35 Myr to 1.25 Myr. The addition of these high-precision absolute ages to the existing CAI age dataset emphasizes the importance of measuring the U isotope composition of each individual CAI for high-precision Pb-Pb dating.

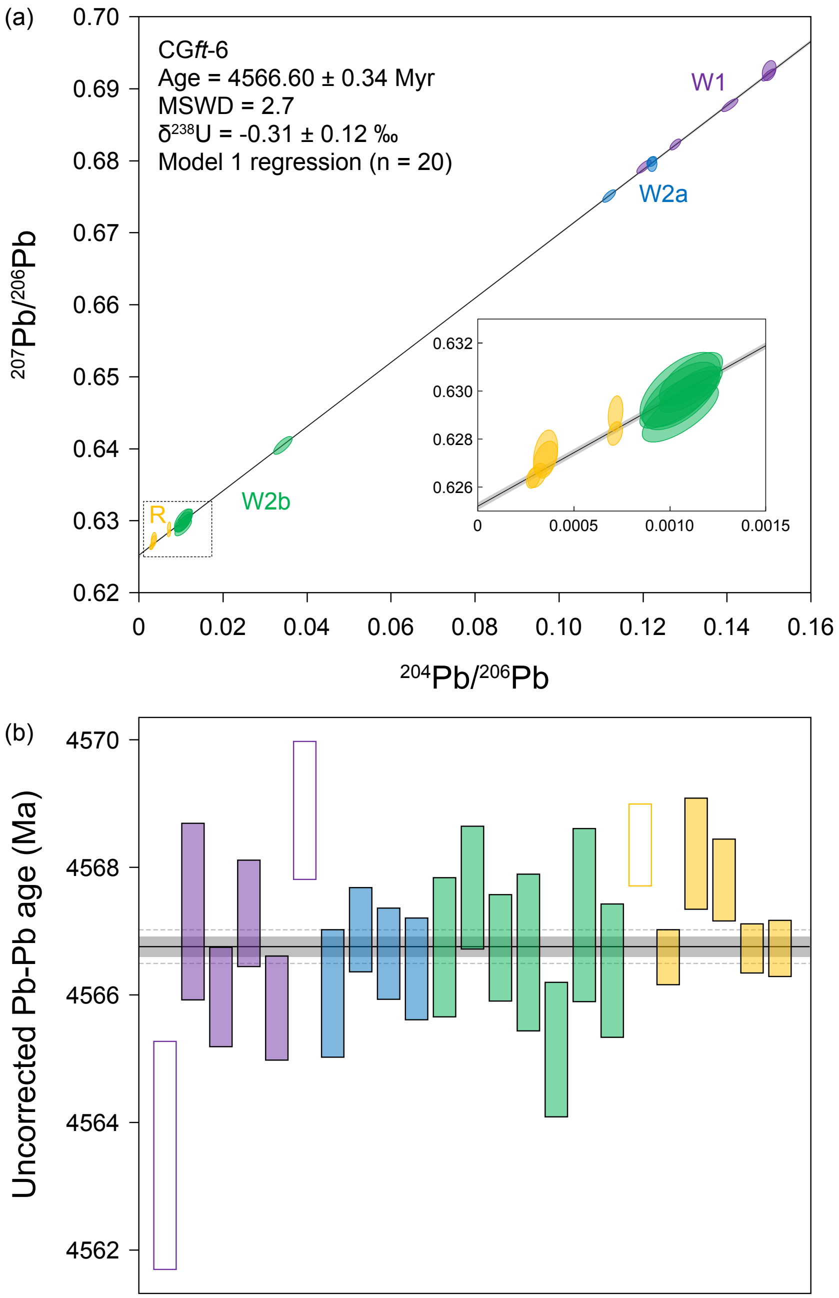

Figure 6.4: Pb-Pb isochron plot (a)and $^{207}Pb^*/^{206}Pb^*$ model age (b) calculated as the weighted average of each point age used for isochron construction. Both ages are identical within their uncertainties.

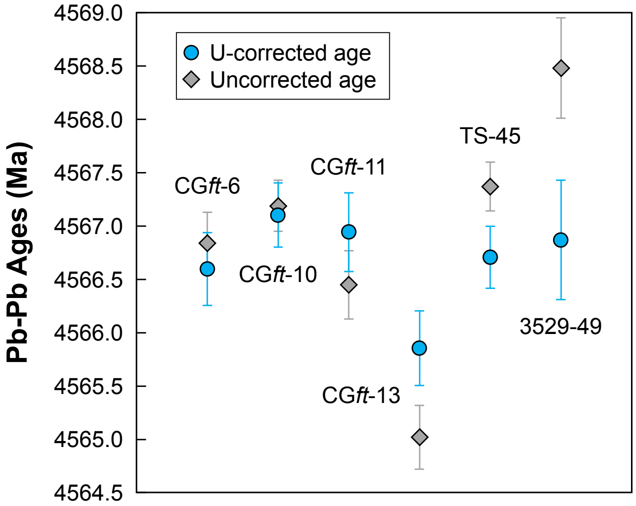

Figure 6.5: Pb-Pb age of 6 CAIs investigated in this study. The uncorrected Pb-Pb ages assumed CAIs have an average terrestrial zircon-like $^{238}U/^{235}U$ value of 137.818 (Hiess et al. 2012) for Pb-Pb age calculation.

6.3.4 Al-Mg ages

The ^{26}Al-^{26}Mg isochrons are shown in **Table 5.2**. The inferred $^{26}Al/^{27}Al$ ratios range from $(4.61 \pm 0.07)\times10^{-5}$ to $(5.60 \pm 0.13)\times10^{-5}$, corresponding to relative ages of -0.065 ± 0.022 to 0.120 ± 0.014 Myr.

6.4 Discussion

6.4.1 Comparison of the Pb-Pb ages between CAIs from different host chondrites

Except for CG*ft*-13, the remaining 5 CAIs define a single population, with all ages overlapping within uncertainty (MSWD = 1.9). This age is also consistent with the age of the CAI SJ101, the only other Allende CAI for which a U-corrected Pb-Pb age is available (Amelin et al. 2010). The outlier CG*ft*-13 shows evidence of more extensive secondary alterations compared with the other more pristine CAIs, which can disturb the Pb-Pb system. Pooling the 5 newly determined CAIs and SJ101 yields an average age of 4566.87 ± 0.15 Myr for CAIs from Allende (MSWD = 1.59). In contrast, averaging the three U-corrected ages available for Efremovka CAIs defines a mean age of 4567.25 ± 0.17 Myr (MSWD = 0.29) (Connelly et al. 2012). The two average ages are resolved and differ by 0.37 ± 0.23 Myr, with Efremovka CAIs being older than their Allende counterparts (**Fig. 6.6**)

This observation raises the question of the origin of the age difference for CAIs from different host meteorites. Several hypotheses can be considered. (i) This age difference between CAIs may record primary signature: *i.e.,* their true time of condensation. This scenario, in which CAIs would condense of a 0.37 Myr time interval, conflicts with the much shorter condensation time interval derived from

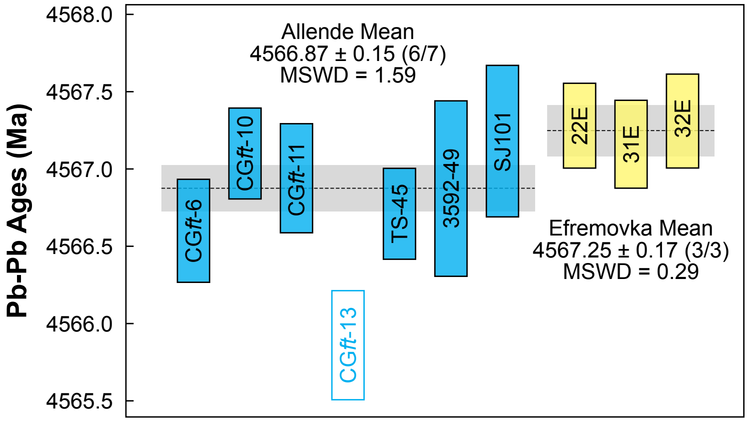

Figure 6.6: U corrected Pb-Pb ages of CAIs from Allende (blue) and Efremovka (yellow). The white box with blue border represents outlier CG*ft*-13, which is not included in the average age calculation. The Efremovka CAIs ages reported by Connelly et al. (2012) assumed a ^{238}U/^{235}U value of 137.844 for CRM-145 and were here renormalized to a ^{238}U/^{235}U value of 137.837 to keep all ages consistent and comparable. This normalization leads to a systematic -0.07 Myr age difference compared with data reported in Connelly et al. (2012).

^{26}Al-^{26}Mg)(Desch et al. 2023). (ii) The difference in Pb-Pb ages may be due to resetting during transient heating events in the nebula. CAIs residing in different regions could be exposed to different degree of transient heating events before they were transported to their host chondrite forming region (Desch et al. 2018). Finally, (iii) age difference could stem from disturbance of the Pb-Pb system by secondary alteration processes. The oxidized CV3 chondrite Allende have undergone more extensive aqueous alteration than the reduced CV chondrite Efremovka, as evidenced by the abundant secondary phases in Allende CAIs(*e.g.,* Krot et al. 1995). The disturbance caused by parent body alteration can explain the younger ages and larger variability of CAIs ages from Allende than Efremovka. This is consistent with the fact that the age of CG*ft*-13, the most altered of CAIs analyzed in this study, is ∼1 Myr younger than other Allende CAIs.

6.4.2 Decoupled resetting of Pb-Pb and Al-Mg chronometers

The age discrepancy between CAIs from different CV3 meteorites adds further complexity to defining the t_0 of the SS. So far, only CAIs from CV chondrites have been dated with high-precision Pb-Pb method because of their large size. With the presence of resetting and/or disturbance on the Pb-Pb system, it would be more challenging to reconstruct a reliable t_0. Another problem raised from the resetting absolute ages is whether the Al-Mg system was reset at the same time, and to the same extent, as the Pb-Pb system. The initial ^{26}Al/^{27}Al for CAIs in comparison with their Pb-Pb ages are plotted in **Fig. 6.7**. It is noticeable that not all the CAIs fall on the evolution line with canonical ^{26}Al/^{27}Al ratio. This observation can be explained by either (i) heterogeneous distribution of ^{26}Al/^{27}Al ratios in the CAI forming region or (ii) decoupled resetting between Pb-Pb and Al-Mg chronometers. However, if the heterogeneous ^{26}Al/^{27}Al ratios account for the discrepancies of two chronometers, ^{26}Al/^{27}Al should be $\sim 2\times10^{-4}$, which is hard to reconcile with the astrophysics models. The mismatch between Pb-Pb and Al-Mg ages can be readily explained by the Pb-Pb system can be more easily reset without significant impact on the Al-Mg system.

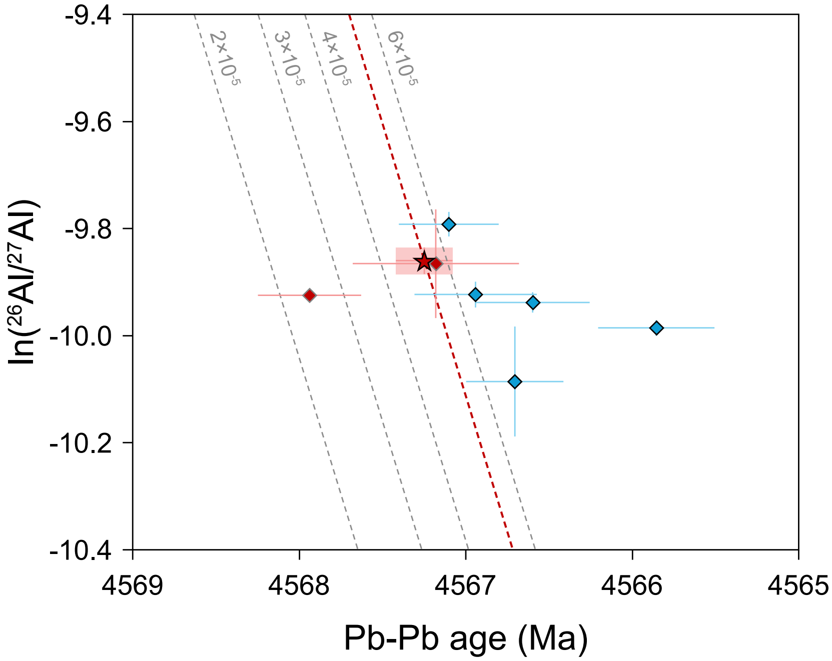

Figure 6.7: Comparison of ^{26}Al-^{26}Mg and Pb-Pb ages by the plot of ^{26}Al/^{27}Al (natural log scale) versus Pb-Pb ages. The ln(^{26}Al/^{27}Al) is linearly correlated with the age of the CAI. The red star denotes the average age of CAIs, with Pb-Pb age of 4567.25 ± 0.17 Myr (Connelly et al. 2012) and ^{26}Al/^{27}Al ratio of 5.23×10^{-5} (Jacobsen et al. 2008. The red and blue diamonds represent the CAI data from literature and this study, respectively. The dash lines show the evolution of ^{26}Al/^{27}Al with the time with different ^{26}Al/^{27}Al ratios, with the red dash line is the canonical value.

BIBLIOGRAPHY

Abe, M., Suzuki, T., Fujii, Y., Hada, M., and Hirao, K. (2008). An ab initio molecular orbital study of the nuclear volume effects in uranium isotope fractionations. *The Journal of Chemical Physics* 129.16. DOI: 10.1063/1.2992616.

Abshire, M. L., Romaniello, S. J., Kuzminov, A. M., Cofrancesco, J., Severmann, S., and Riedinger, N. (2020). Uranium isotopes as a proxy for primary depositional redox conditions in organic-rich marine systems. *Earth and Planetary Science Letters* 529, 115878. DOI: 10.1016/j.epsl.2019.115878.

Al.-Zamel, A., Bou-Rabee, F., Olszewski, M., and Bem, H. (2005). Natural radionuclides and ^{137}Cs activity concentration in the bottom sediment cores from Kuwait Bay. *Journal of Radioanalytical and Nuclear Chemistry* 266, 269–276. DOI: 10.1007/s10967-005-0903-6.

Alamelu, D. and Jagadish, K. S. (2016). Determination of isotopic composition of uranium samples using alpha spectrometry. *Journal of Radioanalytical and Nuclear Chemistry* 310, 541–546. DOI: 10.1007/s10967-016-4874-6.

Albalat, E., Telouk, P., and Albarède, F. (2012). Er and Yb isotope fractionation in planetary materials. *Earth and Planetary Science Letters* 355, 39–50. DOI: 10.1016/j.epsl.2012.08.021.

Amakawa, H., Ingri, J., Masuda, A., and Shimizu, H. (1991). Isotopic compositions of Ce, Nd and Sr in ferromanganese nodules from the Pacific and Atlantic Oceans, the Baltic and Barents Seas, and the Gulf of Bothnia. *Earth and Planetary Science Letters* 105.4, 554–565. DOI: 10.1016/0012-821x(91)90192-k.

Amelin, Y., Kaltenbach, A., Iizuka, T., Stirling, C. H., Ireland, T. R., Petaev, M., and Jacobsen, S. B. (2010). U–Pb chronology of the Solar System's oldest solids with variable ^{238}U/^{235}U. *Earth and Planetary Science Letters* 300.3-4, 343–350. DOI: 10.1016/j.epsl.2010.10.015.

Amelin, Y., Kaltenbach, A., and Stirling, C. H. (2011). The U–Pb systematics and cooling rate of plutonic angrite NWA 4590. In: *42^{nd} Lunar and Planetary Science Conference*. 1608, 1682.

Anbar, A. D., Duan, Y., Lyons, T. W., Arnold, G. L., Kendall, B., Creaser, R. A., Kaufman, A. J., Gordon, G. W., Scott, C., Garvin, J., et al. (2007). A whiff of oxygen before the great oxidation event? *Science* 317.5846, 1903–1906. DOI: 10.1126/science.1140325.

Andersen, M. B., Stirling, C. H., Porcelli, D., Halliday, A. N., Andersson, P., and Baskaran, M. (2007). The tracing of riverine U in Arctic seawater with very precise ^{234}U/^{238}U measurements. *Earth and Planetary Science Letters* 259.1-2, 171–185. DOI: 10.1016/j.epsl.2007.04.051.

Andersen, M. B., Stirling, C. H., Zimmermann, B., and Halliday, A. (2010). Precise determination of the open ocean ^{234}U/^{238}U composition. *Geochemistry, Geophysics, Geosystems* 11.12. DOI: 10.1029/2010GC003318.

Andersen, M. B., Romaniello, S., Vance, D., Little, S., Herdman, R., and Lyons, T. (2014). A modern framework for the interpretation of ^{238}U/^{235}U in studies of ancient ocean redox. *Earth and Planetary Science Letters* 400, 184–194. DOI: 10.1016/j.epsl.2014.05.051.

Andersen, M. B., Elliott, T., Freymuth, H., Sims, K. W., Niu, Y., and Kelley, K. A. (2015). The terrestrial uranium isotope cycle. *Nature* 517.7534, 356–359. DOI: 10.1038/nature14062.

Andersen, M. B., Vance, D., Morford, J. L., Bura-Nakić, E., Breitenbach, S. F., and Och, L. (2016). Closing in on the marine ^{238}U/^{235}U budget. *Chemical Geology* 420, 11–22. DOI: 10.1016/j.chemgeo.2015.10.041.

Andersen, M. B., Stirling, C. H., and Weyer, S. (2017). Uranium isotope fractionation. *Reviews in Mineralogy and Geochemistry* 82.1, 799–850. DOI: 10.2138/rmg.2017.82.19.

Andersen, M. B., Matthews, A., Vance, D., Bar-Matthews, M., Archer, C., and Souza, G. de (2018). A 10-fold decline in the deep Eastern Mediterranean thermohaline overturning circulation during the last interglacial period. *Earth and Planetary Science Letters* 503, 58–67. DOI: 10.1016/j.epsl.2018.09.013.

Andersen, M. B., Matthews, A., Bar-Matthews, M., and Vance, D. (2020). Rapid onset of ocean anoxia shown by high U and low Mo isotope compositions of sapropel S1. *Geochemical Perspectives Letters* 15, 10–14. DOI: 10.7185/geochemlet.2027.

Andreasen, R. and Sharma, M. (2006). Solar nebula heterogeneity in p-process samarium and neodymium isotopes. *Science* 314.5800, 806–809. DOI: 10.1126/science.1131708.

Andreasen, R. and Sharma, M. (2007). Mixing and homogenization in the early solar system: clues from Sr, Ba, Nd, and Sm isotopes in meteorites. *The Astrophysical Journal* 665.1, 874. DOI: 10.1086/518819.

Arden, J. W. (1977). Isotopic composition of uranium in chondritic meteorites. *Nature* 269.5631, 788–789. DOI: 10.1038/269788a0.

Arnold, G. L., Anbar, A., Barling, J., and Lyons, T. (2004). Molybdenum isotope evidence for widespread anoxia in mid-Proterozoic oceans. *Science* 304.5667, 87–90. DOI: 10.1126/science.1091785.

Asael, D., Tissot, F. L., Reinhard, C. T., Rouxel, O., Dauphas, N., Lyons, T. W., Ponzevera, E., Liorzou, C., and Chéron, S. (2013). Coupled molybdenum, iron and uranium stable isotopes as oceanic paleoredox proxies during the Paleoproterozoic Shunga Event. *Chemical Geology* 362, 193–210. DOI: 10.1016/j.chemgeo.2013.08.003.

Aston, F. (1931). Constitution of thallium and uranium. *Nature* 128.3234, 725–725. DOI: 10.1038/128725a0.

Avanzinelli, R., Prytulak, J., Skora, S., Heumann, A., Koetsier, G., and Elliott, T. (2012). Combined ^{238}U–^{230}Th and ^{235}U–^{231}Pa constraints on the transport of slab-derived material beneath the Mariana Islands. *Geochimica et Cosmochimica Acta* 92, 308–328. DOI: 10.1016/j.gca.2012.06.020.

Avanzinelli, R., Casalini, M., Elliott, T., and Conticelli, S. (2018). Carbon fluxes from subducted carbonates revealed by uranium excess at Mount Vesuvius, Italy. *Geology* 46.3, 259–262. DOI: 10.1130/G39766.1.

Awudu, A. and Darko, E. (2011). ^{234}U/^{238}U and ^{235}U/^{238}U ratios in domestic water from the environs of Obuasi mine in Ghana. *Journal of Radioanalytical and Nuclear Chemistry* 287.1, 129–134. DOI: 10.1007/s10967-010-0662-x.

Azmy, K., Kendall, B., Brand, U., Stouge, S., and Gordon, G. W. (2015). Redox conditions across the Cambrian–Ordovician boundary: Elemental and isotopic signatures retained in the GSSP carbonates. *Palaeogeography, Palaeoclimatology, Palaeoecology* 440, 440–454. DOI: 10.1016/j.palaeo.2015.09.014.

Barescut, J., Sahoo, S., Yoshida, S., Tokonami, S., Yonehara, H., Tsygankov, N., and Zamostyan, P. (2009). Isotopic composition of Uranium in soil and ground water samples collected around 30 km Chernobyl Exclusion Zone. *Radioprotection* 44.5, 785–790. DOI: 10.1051/radiopro/20095141.

Barkley, D., Blanchette, M., Cassidy, R., and Elchuk, S. (1986). Dynamic chromatographic systems for the determination of rare earths and thorium in samples from uranium ore refining processes. *Analytical Chemistry* 58.11, 2222–2226. DOI: 10.1021/ac00124a023.

Barrat, J., Taylor, R., Andre, J., Nesbitt, R., and Lecuyer, C. (2000). Strontium isotopes in biogenic phosphates from a Neogene marine formation: implications for palaeoseawater studies. *Chemical Geology* 168.3-4, 325–332. DOI: 10.1016/S0009-2541(00)00200-X.

Barshick, C., Shaw, R., Young, J., and Ramsey, J. (1995). Evaluation of the precision and accuracy of a uranium isotopic analysis using glow discharge optogalvanic spectroscopy. *Analytical Chemistry* 67.20, 3814–3818. DOI: 10.1021/ac00116a033.

Bartlett, R., Elrick, M., Wheeley, J. R., Polyak, V., Desrochers, A., and Asmerom, Y. (2018). Abrupt global-ocean anoxia during the Late Ordovician–early Silurian detected using uranium isotopes of marine carbonates. *Proceedings of the National Academy of Sciences* 115.23, 5896–5901. DOI: 10.1073/pnas.1802438115.

Basu, A., Sanford, R. A., Johnson, T. M., Lundstrom, C. C., and Löffler, F. E. (2014). Uranium isotopic fractionation factors during U(VI) reduction by bacterial isolates. *Geochimica et Cosmochimica Acta* 136, 100–113. DOI: 10.1016/j.gca.2014.02.041.

Basu, A., Brown, S. T., Christensen, J. N., DePaolo, D. J., Reimus, P. W., Heikoop, J. M., Woldegabriel, G., Simmons, A. M., House, B. M., Hartmann, M., et al. (2015). Isotopic and geochemical tracers for U(VI) reduction and U mobility at an in situ recovery U mine. *Environmental Science & Technology* 49.10, 5939–5947. DOI: 10.1021/acs.est.5b00701.

Basu, A., Wanner, C., Johnson, T. M., Lundstrom, C. C., Sanford, R. A., Sonnenthal, E. L., Boyanov, M. I., and Kemner, K. M. (2020). Microbial U isotope fractionation depends on the U(VI) reduction rate. *Environmental Science & Technology* 54.4, 2295–2303. DOI: 10.1021/acs.est.9b05935.

Baudin, G., Blain, C., Hagemann, R., Kremer, M., Lucas, M., and Merlivat, L. (1972). Quelques données nouvelles sur les réactions nucléaires en chaine qui se sont produites dans le gisement d'Oklo. *Comptes rendus de l'Académie des Sciences*, 2291–2294.

Becker, M. A., Seidemann, D. E., Chamberlain Jr, J. A., Buhl, D., and Slattery, W. (2008). Strontium isotopic signatures in the enameloid and dentine of upper Cretaceous shark teeth from western Alabama: paleoecologic and geochronologic implications. *Palaeogeography, Palaeoclimatology, Palaeoecology* 264.1-2, 188–194. DOI: `10.1016/j.palaeo.2008.04.006`.

Bennett, V. C., Brandon, A. D., and Nutman, A. P. (2007). Coupled ^{142}Nd-^{143}Nd isotopic evidence for Hadean mantle dynamics. *Science* 318.5858, 1907–1910. DOI: `10.1126/science.1145928`.

Betti, M., Tamborini, G., and Koch, L. (1999). Use of secondary ion mass spectrometry in nuclear forensic analysis for the characterization of plutonium and highly enriched uranium particles. *Analytical Chemistry* 71.14, 2616–2622. DOI: `10.1021/ac981184r`.

Bigeleisen, J. (1996). Nuclear size and shape effects in chemical reactions. Isotope chemistry of the heavy elements. *Journal of the American Chemical Society* 118.15, 3676–3680. DOI: `10.1021/ja954076k`.

Bizzarro, M., Paton, C., Larsen, K., Schiller, M., Trinquier, A., and Ulfbeck, D. (2011). High-precision Mg-isotope measurements of terrestrial and extraterrestrial material by HR-MC-ICPMS—implications for the relative and absolute Mg-isotope composition of the bulk silicate Earth. *Journal of Analytical Atomic Spectrometry* 26.3, 565–577. DOI: `10.1039/C0JA00190B`.

Blake, J. and Schramm, D. (1973). ^{247}Cm as a short-lived r-process chronometer. *Nature Physical Science* 243.130, 138–140. DOI: `10.1038/physci243138a0`.

Bleise, A., Danesi, P. R., and Burkart, W. (2003). Properties, use and health effects of depleted uranium (DU): a general overview. *Journal of environmental radioactivity* 64.2-3, 93–112. DOI: `10.1016/S0265-931X(02)00041-3`.

Blichert-Toft, J., Chauvel, C., and Albarède, F. (1997). Separation of Hf and Lu for high-precision isotope analysis of rock samples by magnetic sector-multiple collector ICP-MS. *Contributions to Mineralogy and Petrology* 127.3, 248–260. DOI: `10.1007/s004100050278`.

Blichert-Toft, J., Boyet, M., Télouk, P., and Albarède, F. (2002). ^{147}Sm–^{143}Nd and ^{176}Lu–^{176}Hf in eucrites and the differentiation of the HED parent body. *Earth and Planetary Science Letters* 204.1-2, 167–181. DOI: `10.1016/s0012-821x(02)00976-7`.

Blichert-Toft, J. and Puchtel, I. S. (2010). Depleted mantle sources through time: evidence from Lu–Hf and Sm–Nd isotope systematics of Archean komatiites. *Earth and Planetary Science Letters* 297.3-4, 598–606. DOI: `10.1016/j.epsl.2010.07.012`.

Blichert-Toft, J., Göpel, C., Chaussidon, M., and Albarède, F. (2020). Th/U variability in Allende chondrules. *Geochimica et Cosmochimica Acta* 280, 378–394. DOI: 10.1016/j.gca.2020.04.006.

Bodu, R., Bouzigues, H., Morin, N., and Pfiffelmann, J.-P. (1972). Sur I'existence anomalies isotopiques rencontrees dan I'uranium du Gabon. *Comptes rendus de l'Académie des Sciences* 275, 1731–1736.

Bollard, J., Connelly, J. N., Whitehouse, M. J., Pringle, E. A., Bonal, L., Jørgensen, J. K., Nordlund, Å., Moynier, F., and Bizzarro, M. (2017). Early formation of planetary building blocks inferred from Pb isotopic ages of chondrules. *Science Advances* 3.8, e1700407. DOI: 10.1126/sciadv.1700407.

Bollard, J., Kawasaki, N., Sakamoto, N., Olsen, M., Itoh, S., Larsen, K., Wielandt, D., Schiller, M., Connelly, J. N., Yurimoto, H., et al. (2019). Combined U-corrected Pb-Pb dating and ^{26}Al-^{26}Mg systematics of individual chondrules–Evidence for a reduced initial abundance of ^{26}Al amongst inner Solar System chondrules. *Geochimica et Cosmochimica Acta* 260, 62–83. DOI: 10.1016/j.gca.2019.06.025.

Bopp, C. J. I., Lundstrom, C. C., Johnson, T. M., and Glessner, J. J. (2009). Variations in ^{238}U/^{235}U in uranium ore deposits: Isotopic signatures of the U reduction process? *Geology* 37.7, 611–614. DOI: 10.1130/G25550A.1.

Bopp, C. J. I., Lundstrom, C. C., Johnson, T. M., Sanford, R. A., Long, P. E., and Williams, K. H. (2010). Uranium ^{238}U/^{235}U isotope ratios as indicators of reduction: results from an in situ biostimulation experiment at Rifle, Colorado, USA. *Environmental Science & Technology* 44.15, 5927–5933. DOI: 10.1021/es100643v.

Borg, L. E., Nyquist, L. E., Taylor, L. A., Wiesmann, H., and Shih, C.-Y. (1997). Constraints on Martian differentiation processes from Rb–Sr and Sm–Nd isotopic analyses of the basaltic shergottite QUE 94201. *Geochimica et cosmochimica acta* 61.22, 4915–4931. DOI: 10.1016/s0016-7037(97)00276-7.

Bosio, G., Malinverno, E., Collareta, A., Di Celma, C., Gioncada, A., Parente, M., Berra, F., Marx, F. G., Vertino, A., Urbina, M., et al. (2020). Strontium Isotope Stratigraphy and the thermophilic fossil fauna from the middle Miocene of the East Pisco Basin (Peru). *Journal of South American Earth Sciences* 97, 102399. DOI: 10.1016/j.jsames.2019.102399.

Botella, H., Valenzuela-Ríos, J. I., and Martínez-Pérez, C. (2009). Tooth replacement rates in early chondrichthyans: a qualitative approach. *Lethaia* 42.3, 365–376. DOI: 10.1111/j.1502-3931.2009.00152.x.

Boulyga, S. F., Becker, J. S., Matusevitch, J. L., and Dietze, H.-J. (2000). Isotope ratio measurements of spent reactor uranium in environmental samples by using inductively coupled plasma mass spectrometry. *International Journal of Mass Spectrometry* 203.1-3, 143–154. DOI: 10.1016/S1387-3806(00)00296-7.

Boulyga, S. F. and Becker, J. S. (2001). Determination of uranium isotopic composition and ^{236}U content of soil samples and hot particles using inductively coupled plasma mass spectrometry. *Fresenius' journal of Analytical Chemistry* 370, 612–617. DOI: 10.1007/s002160100838.

Boulyga, S. F., Testa, C., Desideri, D., and Becker, J. S. (2001). Optimisation and application of ICP-MS and alpha-spectrometry for determination of isotopic ratios of depleted uranium and plutonium in samples collected in Kosovo. *Journal of Analytical Atomic Spectrometry* 16.11, 1283–1289. DOI: 10.1039/b103178n.

Boulyga, S. F. and Becker, J. S. (2002). Isotopic analysis of uranium and plutonium using ICP-MS and estimation of burn-up of spent uranium in contaminated environmental samples. *Journal of Analytical Atomic Spectrometry* 17.9, 1143–1147. DOI: 10.1039/b202196j.

Boulyga, S. F. and Prohaska, T. (2008). Determining the isotopic compositions of uranium and fission products in radioactive environmental microsamples using laser ablation ICP–MS with multiple ion counters. *Analytical and bioAnalytical Chemistry* 390, 531–539.

Boulyga, S. F., Koepf, A., Konegger-Kappel, S., Macsik, Z., and Stadelmann, G. (2016). Uranium isotope analysis by MC-ICP-MS in sub-ng sized samples. *Journal of Analytical Atomic Spectrometry* 31.11, 2272–2284. DOI: 10.1039/c6ja00238b.

Boulyga, S., Konegger-Kappel, S., Richter, S., and Sangely, L. (2015). Mass spectrometric analysis for nuclear safeguards. *Journal of Analytical Atomic Spectrometry* 30.7, 1469–1489. DOI: 10.1039/c4ja00491d.

Bouvier, A. and Boyet, M. (2016). Primitive Solar System materials and Earth share a common initial ^{142}Nd abundance. *Nature* 537.7620, 399–402. DOI: 10.1038/nature19351.

Bouvier, A., Vervoort, J. D., and Patchett, P. J. (2008). The Lu–Hf and Sm–Nd isotopic composition of CHUR: constraints from unequilibrated chondrites and implications for the bulk composition of terrestrial planets. *Earth and Planetary Science Letters* 273.1-2, 48–57. DOI: 10.1016/j.epsl.2008.06.010.

Bouvier, A. and Wadhwa, M. (2010). The age of the Solar System redefined by the oldest Pb–Pb age of a meteoritic inclusion. *Nature geoscience* 3.9, 637–641. DOI: 10.1038/ngeo941.

Bouvier, A., Brennecka, G., and Wadhwa, M. (2011a). Absolute chronology of the first solids in the Solar System. In: *Workshop on formation of the first solids in the solar system*. Vol. 1639, 9054.

Bouvier, A., Spivak-Birndorf, L. J., Brennecka, G. A., and Wadhwa, M. (2011b). New constraints on early Solar System chronology from Al–Mg and U–Pb isotope systematics in the unique basaltic achondrite Northwest Africa 2976. *Geochimica et Cosmochimica Acta* 75.18, 5310–5323. DOI: 10.1016/j.gca.2011.06.033.

Boyer, T. P., Antonov, J. I., Baranova, O. K., Garcia, H. E., Johnson, D. R., Mishonov, A. V., O'Brien, T. D., Seidov, D., Smolyar, I., Zweng, M. M., et al. (2009). World ocean database 2009.

Boyet, M. and Carlson, R. W. (2005). ^{142}Nd evidence for early (> 4.53 Ga) global differentiation of the silicate Earth. *Science* 309.5734, 576–581. DOI: 10.1126/science.1113634.

Brennecka, G. A., Weyer, S., Wadhwa, M., Janney, P., Zipfel, J., and Anbar, A. D. (2010a). ^{238}U/^{235}U variations in meteorites: Extant ^{247}Cm and implications for Pb-Pb dating. *Science* 327.5964, 449–451. DOI: `10.1126/science.1180871`.

Brennecka, G. A., Borg, L. E., Hutcheon, I. D., Sharp, M. A., and Anbar, A. D. (2010b). Natural variations in uranium isotope ratios of uranium ore concentrates: Understanding the ^{238}U/^{235}U fractionation mechanism. *Earth and Planetary Science Letters* 291.1-4, 228–233. DOI: `10.1016/j.epsl.2010.01.023`.

Brennecka, G. A., Herrmann, A. D., Algeo, T. J., and Anbar, A. D. (2011a). Rapid expansion of oceanic anoxia immediately before the end-Permian mass extinction. *Proceedings of the National Academy of Sciences* 108.43, 17631–17634. DOI: `10.1073/pnas.1106039108`.

Brennecka, G. A., Wasylenki, L. E., Bargar, J. R., Weyer, S., and Anbar, A. D. (2011b). Uranium isotope fractionation during adsorption to Mn-oxyhydroxides. *Environmental Science & Technology* 45.4, 1370–1375. DOI: `10.1021/es103061v`.

Brennecka, G. A. and Wadhwa, M. (2012). Uranium isotope compositions of the basaltic angrite meteorites and the chronological implications for the early Solar System. *Proceedings of the National Academy of Sciences* 109.24, 9299–9303. DOI: `10.1073/pnas.1114043109`.

Brennecka, G. A., Budde, G., and Kleine, T. (2015). Uranium isotopic composition and absolute ages of Allende chondrules. *Meteoritics & Planetary Science* 50.12, 1995–2002. DOI: `10.1111/maps.12567`.

Brennecka, G. A., Amelin, Y., and Kleine, T. (2018). Uranium isotope ratios of Muonionalusta troilite and complications for the absolute age of the IVA iron meteorite core. *Earth and Planetary Science Letters* 490, 1–10. DOI: `10.1016/j.epsl.2018.03.010`.

Broecker, W. S. and Peng, T.-H. (1982). Tracers in the Sea. Vol. 690. Lamont-Doherty Geological Observatory, Columbia University Palisades, New York. DOI: `doi:10.1017/S0033822200005221`.

Bros, R., Turpin, L., Gauthier-Lafaye, F., Holliger, P., and Stille, P. (1993). Occurrence of naturally enriched ^{235}U: Implications for plutonium behaviour in natural environments. *Geochimica et Cosmochimica Acta* 57.6, 1351–1356. DOI: `10.1016/0016-7037(93)90072-5`.

Bros, R., Carpena, J., Sere, V., and Beltritti, A. (1996). Occurrence of Pu and fissiogenic REE in hydrothermal apatites from the fossil nuclear reactor 16 at Oklo (Gabon). *Radiochimica Acta* 74.s1, 277–282. DOI: `10.1524/ract.1996.74.special-issue.277`.

Bros, R., Hidaka, H., Kamei, G., and Ohnuki, T. (2003). Mobilization and mechanisms of retardation in the Oklo natural reactor zone 2 (Gabon)—inferences from U, REE, Zr, Mo and Se isotopes. *Applied Geochemistry* 18.12, 1807–1824. DOI: `10.1016/S0883-2927(03)00113-6`.

Brown, S. T., Basu, A., Christensen, J. N., Reimus, P., Heikoop, J., Simmons, A., Woldegabriel, G., Maher, K., Weaver, K., Clay, J., et al. (2016). Isotopic evidence for reductive immobilization of uranium across a roll-front mineral deposit. *Environmental Science & Technology* 50.12, 6189–6198. DOI: `10.1021/acs.est.6b00626`.

Brown, S. T., Basu, A., Ding, X., Christensen, J. N., and DePaolo, D. J. (2018). Uranium isotope fractionation by abiotic reductive precipitation. *Proceedings of the National Academy of Sciences* 115.35, 8688–8693. DOI: `10.1073/pnas.1805234115`.

Bruggmann, S., Gilleaudeau, G., Romaniello, S., Severmann, S., Canfield, D., Anbar, A., Scholz, F., and Frei, R. (2022). Uranium isotope cycling on the highly productive Peruvian margin. *Chemical Geology* 590, 120705. DOI: `10.1016/j.chemgeo.2021.120705`.

Brüske, A., Weyer, S., Zhao, M.-Y., Planavsky, N., Wegwerth, A., Neubert, N., Dellwig, O., Lau, K., and Lyons, T. (2020a). Correlated molybdenum and uranium isotope signatures in modern anoxic sediments: Implications for their use as paleo-redox proxy. *Geochimica et Cosmochimica Acta* 270, 449–474. DOI: `10.1016/j.gca.2019.11.031`.

Brüske, A., Martin, A., Rammensee, P., Eroglu, S., Lazarov, M., Albut, G., Schuth, S., Aulbach, S., Schoenberg, R., Beukes, N., et al. (2020b). The onset of oxidative weathering traced by uranium isotopes. *Precambrian research* 338, 105583. DOI: `10.1016/j.precamres.2019.105583`.

Buchholz, B., Brown, T., Hamilton, T., Hutcheon, I., Marchetti, A., Martinelli, R., Ramon, E., Tumey, S., and Williams, R. (2007). Investigating uranium isotopic distributions in environmental samples using AMS and MC-ICPMS. *Nuclear Instruments and Methods in Physics Research Section B: Beam Interactions with Materials and Atoms* 259.1, 733–738. DOI: `10.1016/j.nimb.2007.01.248`.

Budde, G., Marquez, R., Ivanova, M., and Tissot, F. (2023). Molybdenum Isotope Systematics of Calcium-Aluminum-Rich Inclusions. *55th Lunar and Planetary Science Conference* 2806, 2203.

Budde, G., Ebel, D. S., Chaussidon, M., and Kleine, T. (2019). Combined Al-Mg and Hf-W Isotope Systematics of a Large Type B CAI. In: *2019 Goldschmidt Conference*. 421.

Bullock, E. S., MacPherson, G. J., Nagashima, K., Krot, A. N., Petaev, M. I., Jacobsen, S. B., and Ulyanov, A. A. (2012). Forsterite-bearing type B refractory inclusions from CV3 chondrites: From aggregates to volatilized melt droplets. *Meteoritics & Planetary Science* 47.12, 2128–2147. DOI: `10.1111/j.1945-5100.2012.01396.x`.

Bura-Nakić, E., Andersen, M. B., Archer, C., Souza, G. F. de, Marguš, M., and Vance, D. (2018). Coupled Mo-U abundances and isotopes in a small marine euxinic basin: constraints on processes in euxinic basins. *Geochimica et Cosmochimica Acta* 222, 212–229. DOI: `10.1016/j.gca.2017.10.023`.

Bura-Nakić, E., Sondi, I., Mikac, N., and Andersen, M. B. (2020). Investigating the molybdenum and uranium redox proxies in a modern shallow anoxic carbonate rich marine sediment setting of the Malo Jezero (Mljet Lakes, Adriatic Sea). *Chemical Geology* 533, 119441. DOI: 10.1016/j.chemgeo.2019.119441.

Burkhardt, C., Borg, L., Brennecka, G., Shollenberger, Q., Dauphas, N., and Kleine, T. (2016). A nucleosynthetic origin for the Earth's anomalous ^{142}Nd composition. *Nature* 537.7620, 394–398. DOI: 10.1038/nature18956.

Burkhardt, C., Dauphas, N., Hans, U., Bourdon, B., and Kleine, T. (2019). Elemental and isotopic variability in solar system materials by mixing and processing of primordial disk reservoirs. *Geochimica et Cosmochimica Acta* 261, 145–170. DOI: 10.1016/j.gca.2019.07.003.

Callis, E. and Abernathey, R. (1991). High-precision isotopic analyses of uranium and plutonium by total sample volatilization and signal integration. *International Journal of Mass Spectrometry and ion processes* 103.2-3, 93–105. DOI: 10.1016/0168-1176(91)80081-W.

Campbell, D. (1973). Rapid rare earth separation by pressurized ion exchange chromatography. *Journal of Inorganic and Nuclear Chemistry* 35.11, 3911–3919. DOI: 10.1016/0022-1902(73)80085-5.

Campbell, D. (1976). Separation of lanthanides and trivalent actinides with pressurized ion exchange. *Separation and Purification Methods* 5.1, 97–138. DOI: 10.1080/03602547608066049.

Cao, M., Daines, S. J., Lenton, T. M., Cui, H., Algeo, T. J., Dahl, T. W., Shi, W., Chen, Z.-Q., Anbar, A., and Zhou, Y.-Q. (2020). Comparison of Ediacaran platform and slope δ^{238}U records in South China: Implications for global-ocean oxygenation and the origin of the Shuram Excursion. *Geochimica et Cosmochimica Acta* 287, 111–124. DOI: 10.1016/j.gca.2020.04.035.

Carlson, R. W., Boyet, M., and Horan, M. (2007). Chondrite barium, neodymium, and samarium isotopic heterogeneity and early earth differentiation. *Science* 316.5828, 1175–1178. DOI: 10.1126/science.1140189.

Caro, G., Bourdon, B., Birck, J.-L., and Moorbath, S. (2003). ^{146}Sm–^{142}Nd evidence from Isua metamorphosed sediments for early differentiation of the Earth's mantle. *Nature* 423.6938, 428–432. DOI: 10.1038/nature01668.

Caro, G., Bourdon, B., Birck, J.-L., and Moorbath, S. (2006). High-precision ^{142}Nd/^{144}Nd measurements in terrestrial rocks: constraints on the early differentiation of the Earth's mantle. *Geochimica et Cosmochimica Acta* 70.1, 164–191. DOI: 10.1016/j.gca.2005.08.015.

Caro, G., Bourdon, B., Halliday, A. N., and Quitté, G. (2008). Super-chondritic Sm/Nd ratios in Mars, the Earth and the Moon. *Nature* 452.7185, 336–339. DOI: 10.1038/nature06760.

Casalini, M. (2018). ^{98}Mo/^{95}Mo and ^{238}U/^{235}U in lamproites, shoshonites, and high-K calc-alkaline rocks from Western Alps: inferences on their genesis. *Italian Journal of Geosciences* 137.3, 465–477. DOI: 10.3301/IJG.2018.20.

Catanzaro, E. J., Murphy, T. J., Garner, E. L., and Shields, W. R. (1966). Absolute isotopic abundance ratios and atomic weight of magnesium. *Journal of research of the National Bureau of Standards. Section A, Physics and chemistry* 70.6, 453. DOI: 10.6028/jres.070A.037.

Chabaux, F., Riotte, J., Clauer, N., and France-Lanord, C. (2001). Isotopic tracing of the dissolved U fluxes of Himalayan rivers: implications for present and past U budgets of the Ganges-Brahmaputra system. *Geochimica et Cosmochimica Acta* 65.19, 3201–3217. DOI: 10.1016/S0016-7037(01)00669-X.

Chabaux, F., Riotte, J., and Dequincey, O. (2003). U-Th-Ra fractionation during weathering and river transport. *Reviews in Mineralogy and geochemistry* 52.1, 533–576. DOI: 10.2113/0520533.

Chase, Z., Anderson, R. F., and Fleisher, M. Q. (2001). Evidence from authigenic uranium for increased productivity of the glacial Subantarctic Ocean. *Paleoceanography* 16.5, 468–478. DOI: 10.1029/2000PA000542.

Chen, J. (1988). ^{238}U, ^{235}U, ^{234}U in Lunar and Terrestrial Samples and the Determination of $\lambda_{238}/\lambda_{234}$. In: *Lunar and Planetary Science Conference*. Vol. 19.

Chen, J. and Wasserburg, G. (1980). A search for isotopic anomalies in uranium. *Geophysical Research Letters* 7.4, 275–278. DOI: 10.1029/GL007i004p00275.

Chen, J. and Wasserburg, G. (1981a). Cm/U, Th/U, and ^{235}U/^{238}U in meteorites. *Meteoritics* 16, 301.

Chen, J. and Wasserburg, G. (1981b). Precise isotopic analysis of uranium in picomole and subpicomole quantities. *Analytical Chemistry* 53.13, 2060–2067. DOI: 10.1021/ac00236a027.

Chen, J. and Wasserburg, G. (1981c). The isotopic composition of uranium and lead in Allende inclusions and meteoritic phosphates. *Earth and Planetary Science Letters* 52.1, 1–15. DOI: 10.1016/0012-821X(81)90202-8.

Chen, J., Edwards, R. L., and Wasserburg, G. J. (1986). ^{238}U, ^{234}U and ^{232}Th in seawater. *Earth and Planetary Science Letters* 80.3-4, 241–251. DOI: 10.1016/0012-821X(86)90108-1.

Chen, J., Algeo, T. J., Zhao, L., Chen, Z.-Q., Cao, L., Zhang, L., and Li, Y. (2015). Diagenetic uptake of rare earth elements by bioapatite, with an example from Lower Triassic conodonts of South China. *Earth-science reviews* 149, 181–202. DOI: 10.1016/j.earscirev.2015.01.013.

Chen, J., Montañez, I. P., Zhang, S., Isson, T. T., Macarewich, S. I., Planavsky, N. J., Zhang, F., Rauzi, S., Daviau, K., Yao, L., et al. (2022a). Marine anoxia linked to abrupt global warming during Earth's penultimate icehouse. *Proceedings of the National Academy of Sciences* 119.19, e2115231119. DOI: 10.1073/pnas.2115231119.

Chen, X., Tissot, F., Jansen, M., Bekker, A., Liu, C., Nie, N., Halverson, G., Veizer, J., and Dauphas, N. (2021a). The uranium isotopic record of shales and carbonates through geologic time. *Geochimica et Cosmochimica Acta* 300, 164–191. DOI: 10.1016/j.gca.2021.01.040.

Chen, X., Romaniello, S. J., Herrmann, A. D., Wasylenki, L. E., and Anbar, A. D. (2016). Uranium isotope fractionation during coprecipitation with aragonite and calcite. *Geochimica et Cosmochimica Acta* 188, 189–207. DOI: 10.1016/j.gca.2016.05.022.

Chen, X., Romaniello, S. J., and Anbar, A. D. (2017). Uranium isotope fractionation induced by aqueous speciation: Implications for U isotopes in marine $CaCO_3$ as a paleoredox proxy. *Geochimica et Cosmochimica Acta* 215, 162–172. DOI: 10.1016/j.gca.2017.08.006.

Chen, X., Romaniello, S. J., Herrmann, A. D., Samankassou, E., and Anbar, A. D. (2018a). Biological effects on uranium isotope fractionation ($^{238}U/^{235}U$) in primary biogenic carbonates. *Geochimica et Cosmochimica Acta* 240, 1–10. DOI: 10.1016/j.gca.2018.08.028.

Chen, X., Romaniello, S. J., Herrmann, A. D., Hardisty, D., Gill, B. C., and Anbar, A. D. (2018b). Diagenetic effects on uranium isotope fractionation in carbonate sediments from the Bahamas. *Geochimica et Cosmochimica Acta* 237, 294–311. DOI: 10.1016/j.gca.2018.06.026.

Chen, X., Zheng, W., and Anbar, A. D. (2020). Uranium isotope fractionation ($^{238}U/^{235}U$) during U (VI) uptake by freshwater plankton. *Environmental Science & Technology* 54.5, 2744–2752. DOI: 10.1021/acs.est.9b06421.

Chen, X., Romaniello, S. J., McCormick, M., Sherry, A., Havig, J. R., Zheng, W., and Anbar, A. D. (2021b). Anoxic depositional overprinting of $^{238}U/^{235}U$ in calcite: When do carbonates tell black shale tales? *Geology* 49.10, 1193–1197. DOI: 10.1130/G48949.1.

Chen, X., Robinson, S. A., Romaniello, S. J., and Anbar, A. D. (2022b). $^{238}U/^{235}U$ in calcite is more susceptible to carbonate diagenesis. *Geochimica et Cosmochimica Acta* 326, 273–287. DOI: 10.1016/j.gca.2022.03.027.

Cheng, H., Edwards, R. L., Hoff, J., Gallup, C. D., Richards, D., and Asmerom, Y. (2000). The half-lives of uranium-234 and thorium-230. *Chemical Geology* 169.1-2, 17–33. DOI: 10.1016/S0009-2541(99)00157-6.

Cheng, H., Edwards, R. L., Shen, C.-C., Polyak, V. J., Asmerom, Y., Woodhead, J., Hellstrom, J., Wang, Y., Kong, X., Spötl, C., et al. (2013). Improvements in ^{230}Th dating, ^{235}Th and ^{234}U half-life values, and U–Th isotopic measurements by multi-collector inductively coupled plasma mass spectrometry. *Earth and Planetary Science Letters* 371, 82–91. DOI: 10.1016/j.epsl.2013.04.006.

Cheng, K., Elrick, M., and Romaniello, S. J. (2020a). Early Mississippian ocean anoxia triggered organic carbon burial and late Paleozoic cooling: Evidence from uranium isotopes recorded in marine limestone. *Geology* 48.4, 363–367. DOI: 10.1130/G46950.1.

Cheng, M., Li, C., Jin, C., Wang, H., Algeo, T. J., Lyons, T. W., Zhang, F., and Anbar, A. (2020b). Evidence for high organic carbon export to the early Cambrian seafloor. *Geochimica et Cosmochimica Acta* 287, 125–140. DOI: 10.1016/j.gca.2020.01.050.

Chernyshev, I., Golubev, V., Chugaev, A., and Baranova, A. (2014). ^{238}U/^{235}U isotope ratio variations in minerals from hydrothermal uranium deposits. *Geochemistry International* 52, 1013–1029.

Cherry, L. B., Gilleaudeau, G. J., Grazhdankin, D. V., Romaniello, S. J., Martin, A. J., and Kaufman, A. J. (2022). A diverse Ediacara assemblage survived under low-oxygen conditions. *Nature Communications* 13.1, 7306. DOI: `10.1038/s41467-022-35012-y`.

Chiu, C. F., Sweere, T. C., Clarkson, M. O., Souza, G. F. de, Hennekam, R., and Vance, D. (2022). Co-variation systematics of uranium and molybdenum isotopes reveal pathways for descent into euxinia in Mediterranean sapropels. *Earth and Planetary Science Letters* 585, 117527. DOI: `10.1016/j.epsl.2022.117527`.

Choppin, G. and Chopoorian, J. (1961). Complexes of the lanthanide elements with α-hydroxy carboxylate ligands. *Journal of Inorganic and Nuclear Chemistry* 22.1-2, 97–113. DOI: `10.1016/0022-1902(61)80234-0`.

Choppin, G. R. (1956). Separation of the lanthanides by ion exchange with alpha-hydroxy isobutyric acid. University of California Radiation Laboratory.

Christensen, J. N., Dresel, P. E., Conrad, M. E., Maher, K., and DePaolo, D. J. (2004). Identifying the sources of subsurface contamination at the Hanford Site in Washington using high-precision uranium isotopic measurements. *Environmental Science & Technology* 38.12, 3330–3337. DOI: `10.1021/es034700q`.

Clarkson, M. O., Stirling, C. H., Jenkyns, H. C., Dickson, A. J., Porcelli, D., Moy, C. M., Pogge von Strandmann, P. A., Cooke, I. R., and Lenton, T. M. (2018). Uranium isotope evidence for two episodes of deoxygenation during Oceanic Anoxic Event 2. *Proceedings of the National Academy of Sciences* 115.12, 2918–2923. DOI: `10.1073/pnas.1715278115`.

Clarkson, M. O., Müsing, K., Andersen, M. B., and Vance, D. (2020). Examining pelagic carbonate-rich sediments as an archive for authigenic uranium and molybdenum isotopes using reductive cleaning and leaching experiments. *Chemical Geology* 539, 119412. DOI: `10.1016/j.chemgeo.2019.119412`.

Clarkson, M. O., Hennekam, R., Sweere, T. C., Andersen, M. B., Reichart, G.-J., and Vance, D. (2021a). Carbonate associated uranium isotopes as a novel local redox indicator in oxidatively disturbed reducing sediments. *Geochimica et Cosmochimica Acta* 311, 12–28. DOI: `10.1016/j.gca.2021.07.025`.

Clarkson, M. O., Lenton, T. M., Andersen, M. B., Bagard, M.-L., Dickson, A. J., and Vance, D. (2021b). Upper limits on the extent of seafloor anoxia during the PETM from uranium isotopes. *Nature communications* 12.1, 399. DOI: `10.1038/s41467-020-20486-5`.

Claverie, F., Hubert, A., Berail, S., Donard, A., Pointurier, F., and Pécheyran, C. (2016). Improving Precision and Accuracy of Isotope Ratios from Short Transient Laser Ablation-Multicollector-Inductively Coupled Plasma Mass Spectrometry Signals: Application to Micrometer-Size Uranium Particles. *Analytical Chemistry* 88.8, 4375–4382. DOI: `10.1021/acs.analchem.5b04802`.

Cole, D. B., Planavsky, N. J., Longley, M., Böning, P., Wilkes, D., Wang, X., Swanner, E. D., Wittkop, C., Loydell, D. K., Busigny, V., et al. (2020). Uranium isotope fractionation in non-sulfidic anoxic settings and the global uranium isotope mass balance. *Global Biogeochemical Cycles* 34.8, e2020GB006649. DOI: `10.1029/2020GB006649`.

Condon, D. J., McLean, N., Noble, S. R., and Bowring, S. A. (2010). Isotopic composition (^{238}U/^{235}U) of some commonly used uranium reference materials. *Geochimica et Cosmochimica Acta* 74.24, 7127–7143. DOI: `10.1016/j.gca.2010.09.019`.

Connelly, J. N., Bizzarro, M., Krot, A. N., Nordlund, Å., Wielandt, D., and Ivanova, M. A. (2012). The absolute chronology and thermal processing of solids in the solar protoplanetary disk. *Science* 338.6107, 651–655. DOI: `10.1126/science.1226919`.

Connelly, J. N., Bollard, J., and Bizzarro, M. (2017). Pb–Pb chronometry and the early solar system. *Geochimica et Cosmochimica Acta* 201, 345–363. DOI: `10.1016/j.gca.2016.10.044`.

Cooke, I., Sapah, M. S., Kaltenbach, A., Stirling, C. H., and Amelin, Y. (2013). Uranium Isotopic Composition and Trace Element Abundances of CAIs from CV Chondrite Northwest Africa 4502. In: *44th Lunar and Planetary Science Conference*, Abstract #1709.

Côté, B., Eichler, M., Yagüe López, A., Vassh, N., Mumpower, M. R., Világos, B., Soós, B., Arcones, A., Sprouse, T. M., Surman, R., et al. (2021). ^{129}I and ^{247}Cm in meteorites constrain the last astrophysical source of solar r-process elements. *Science* 371.6532, 945–948. DOI: `10.1126/science.aba1111`.

Cowan, G. A. and Adler, H. H. (1976). The variability of the natural abundance of ^{235}U. *Geochimica et Cosmochimica Acta* 40.12, 1487–1490. DOI: `10.1016/0883-2927(89)90058-9`.

Curtis, D., Benjamin, T., Gancarz, A., Loss, R., Rosman, K., DeLaeter, J., Delmore, J. E., and Maeck, W. J. (1989). Fission product retention in the Oklo natural fission reactors. *Applied Geochemistry* 4.1, 49–62. DOI: `10.1016/0016-7037(76)90087-9`.

Dahl, T. W., Boyle, R. A., Canfield, D. E., Connelly, J. N., Gill, B. C., Lenton, T. M., and Bizzarro, M. (2014). Uranium isotopes distinguish two geochemically distinct stages during the later Cambrian SPICE event. *Earth and planetary science letters* 401, 313–326. DOI: `10.1016/j.epsl.2014.05.043`.

Dahl, T. W., Connelly, J., Kouchinsky, A., Gill, B. C., Månsson, S., and Bizzarro, M. (2017). Reorganisation of Earth's biogeochemical cycles briefly oxygenated the oceans 520 Myr ago. *Geochemical Perspectives Letters* 43, 210–220. DOI: `10.7185/geochemlet.1724`.

Dahl, T. W., Connelly, J. N., Li, D., Kouchinsky, A., Gill, B. C., Porter, S., Maloof, A. C., and Bizzarro, M. (2019). Atmosphere–ocean oxygen and productivity dynamics during early animal radiations. *Proceedings of the National Academy of Sciences* 116.39, 19352–19361. DOI: `10.1073/pnas.1901178116`.

Danesi, P., Markowicz, A., Chinea-Cano, E., Burkart, W., Salbu, B., Donohue, D., Ruedenauer, F., Hedberg, M., Vogt, S., Zahradnik, P., et al. (2003a). Depleted uranium particles in selected Kosovo samples. *Journal of environmental radioactivity* 64.2-3, 143–154. DOI: 10.1016/S0265-931X(02)00045-0.

Danesi, P., Bleise, A., Burkart, W., Cabianca, T., Campbell, M., Makarewicz, M., Moreno, J., Tuniz, C., and Hotchkis, M. (2003b). Isotopic composition and origin of uranium and plutonium in selected soil samples collected in Kosovo. *Journal of environmental radioactivity* 64.2-3, 121–131. DOI: 10.1016/S0265-931X(02)00043-7.

Dang, D., Wang, W., Gibson, T., Kunzmann, M., Andersen, M., Halverson, G., and Evans, R. (2022). Authigenic uranium isotopes of late Proterozoic black shale. *Chemical Geology* 588, 120644. DOI: 10.1016/j.chemgeo.2021.120644.

Dang, D. H., Novotnik, B., Wang, W., Georg, R. B., and Evans, R. D. (2016). Uranium isotope fractionation during adsorption,(co) precipitation, and biotic reduction. *Environmental Science & Technology* 50.23, 12695–12704. DOI: 10.1016/j.chemgeo.2021.120644.

Dang, D. H., Evans, R. D., Wang, W., Omanović, D., El Houssainy, A., Lenoble, V., Mullot, J.-U., Mounier, S., and Garnier, C. (2018). Uranium isotope geochemistry in modern coastal sediments: Insights from Toulon Bay, France. *Chemical Geology* 481, 133–145. DOI: 10.1016/j.chemgeo.2018.01.032.

Dansgaard, W. (1964). Stable isotopes in precipitation. *tellus* 16.4, 436–468. DOI: 10.1111/j.2153-3490.1964.tb00181.x.

Dauphas, N. and Schauble, E. A. (2016). Mass fractionation laws, mass-independent effects, and isotopic anomalies. *Annual Review of Earth and Planetary Sciences* 44, 709–783. DOI: 10.1146/annurev-earth-060115-012157.

Davis, A. M. (2022). Short-Lived Nuclides in the Early Solar System: Abundances, Origins, and Applications. *Annual Review of Nuclear and Particle Science* 72, 339–363. DOI: 10.1146/annurev-nucl-010722-074615.

Davis, A. M., Richter, F. M., Mendybaev, R. A., Janney, P. E., Wadhwa, M., and McKeegan, K. D. (2015). Isotopic mass fractionation laws for magnesium and their effects on ^{26}Al–^{26}Mg systematics in solar system materials. *Geochimica et Cosmochimica Acta* 158, 245–261. DOI: 10.1016/j.gca.2015.01.034.

De Laeter, J., Rosman, K., and Smith, C. (1980). The Oklo natural reactor: cumulative fission yields and retentivity of the symmetric mass region fission products. *Earth and Planetary Science Letters* 50.1, 238–246. DOI: 10.1016/0012-821X(80)90135-1.

Debaille, V., Brandon, A., Yin, Q.-Z., and Jacobsen, B. (2007). Coupled ^{142}Nd–^{143}Nd evidence for a protracted magma ocean in Mars. *Nature* 450.7169, 525–528. DOI: 10.1038/nature06317.

Deelstra, H. and Verbeek, F. (1965). The separation of the lanthanides and yttrium by cation exchange elution with ammonium α-hydroxyisobutyrate and lactate. *Journal of Chromatography A* 17, 558–566. DOI: 10.1016/s0021-9673(00)99910-2.

Del Rey, Á., Rasmussen, C. M. Ø., Calner, M., Wu, R., Asael, D., and Dahl, T. W. (2022). Stable ocean redox during the main phase of the Great Ordovician Biodiversification Event. *Communications Earth & Environment* 3.1, 220. DOI: `10.1038/s43247-022-00548-w`.

Dempster, A. J. (1935). Isotopic constitution of uranium. *Nature* 136.3431, 180–180. DOI: `10.1038/136180a0`.

DePaolo, D. J. and Wasserburg, G. (1976). Nd isotopic variations and petrogenetic models. *Geophysical Research Letters* 3.5, 249–252. DOI: `10.1029/gl003i005p00249`.

Dera, G., Pucéat, E., Pellenard, P., Neige, P., Delsate, D., Joachimski, M. M., Reisberg, L., and Martinez, M. (2009). Water mass exchange and variations in seawater temperature in the NW Tethys during the Early Jurassic: evidence from neodymium and oxygen isotopes of fish teeth and belemnites. *Earth and Planetary Science Letters* 286.1-2, 198–207. DOI: `10.1016/j.epsl.2009.06.027`.

Desch, S. J., Kalyaan, A., and Alexander, C. M. (2018). The effect of Jupiter's formation on the distribution of refractory elements and inclusions in meteorites. *The Astrophysical Journal Supplement Series* 238.1, 11. DOI: `10.3847/1538-4365/aad95f`.

Desch, S. J., Dunlap, D. R., Williams, C. D., Mane, P., and Dunham, E. T. (2023). Statistical chronometry of Meteorites: II. Initial abundances and homogeneity of short-lived radionuclides. *Icarus* 402, 115611. DOI: `10.1016/j.icarus.2023.115611`.

Di, Y. (2023). The initial ^{87}Sr/^{86}Sr of the Solar System.

Dickson, A. J., Bagard, M.-L., Katchinoff, J. A., Davies, M., Poulton, S. W., and Cohen, A. S. (2021). Isotopic constraints on ocean redox at the end of the Eocene. *Earth and Planetary Science Letters* 562, 116814. DOI: `10.1016/j.epsl.2021.116814`.

Dickson, A. J., Idiz, E., Porcelli, D., Murphy, M. J., Celestino, R., Jenkyns, H. C., Poulton, S. W., Hesselbo, S. P., Hooker, J. N., Ruhl, M., et al. (2022). No effect of thermal maturity on the Mo, U, Cd, and Zn isotope compositions of Lower Jurassic organic-rich sediments. *Geology* 50.5, 598–602. DOI: `10.1130/G49724.1`.

Dodson, M. (1963). A theoretical study of the use of internal standards for precise isotopic analysis by the surface ionization technique: Part I-General first-order algebraic solutions. *Journal of Scientific Instruments* 40.6, 289. DOI: `10.1088/0950-7671/40/6/307`.

Donard, A., Pointurier, F., Pottin, A.-C., Hubert, A., and Pécheyran, C. (2017). Determination of the isotopic composition of micrometric uranium particles by UV femtosecond laser ablation coupled with sector-field single-collector ICP-MS. *Journal of Analytical Atomic Spectrometry* 32.1, 96–106. DOI: `10.1039/c6ja00071a`.

Duarte, C. and Szeles, M. (1994). An improved method for determination of uranium isotopic composition in urine by alpha spectrometry. *Journal of Radioanalytical and Nuclear Chemistry* 177.1, 73–79. DOI: `10.1007/BF02132411`.

Dunk, R., Mills, R., and Jenkins, W. (2002). A reevaluation of the oceanic uranium budget for the Holocene. *Chemical Geology* 190.1-4, 45–67. DOI: 10.1016/S0009-2541(02)00110-9.

Ehret, D. J., Macfadden, B. J., Jones, D. S., Devries, T. J., Foster, D. A., and Salas-Gismondi, R. (2012). Origin of the white shark *Carcharodon* (Lamniformes: Lamnidae) based on recalibration of the Upper Neogene Pisco Formation of Peru. *Palaeontology* 55.6, 1139–1153. DOI: 10.1111/j.1475-4983.2012.01201.x.

Ejnik, J. W., Todorov, T. I., Mullick, F. G., Squibb, K., McDiarmid, M. A., and Centeno, J. A. (2005). Uranium analysis in urine by inductively coupled plasma dynamic reaction cell mass spectrometry. *Analytical and bioAnalytical Chemistry* 382, 73–79. DOI: 10.1007/s00216-005-3173-9.

Ejnik, J., Carmichael, A., Hamilton, M., McDiarmid, M., Squibb, K., Boyd, P., and Tardiffs, W. (2000). Determination of the isotopic composition of uranium in urine by inductively coupled plasma mass spectrometry. *Health physics* 78.2, 143–146. DOI: 10.1097/00004032-200002000-00003.

Elderfield, H. and Pagett, R. (1986). Rare earth elements in ichthyoliths: variations with redox conditions and depositional environment. *Science of the Total Environment* 49, 175–197. DOI: 10.1016/0048-9697(86)90239-1.

Elliott, T., Plank, T., Zindler, A., White, W., and Bourdon, B. (1997). Element transport from slab to volcanic front at the Mariana arc. *Journal of Geophysical Research: Solid Earth* 102.B7, 14991–15019. DOI: 10.1029/97JB00788.

Elrick, M., Polyak, V., Algeo, T. J., Romaniello, S., Asmerom, Y., Herrmann, A. D., Anbar, A. D., Zhao, L., and Chen, Z.-Q. (2017). Global-ocean redox variation during the middle-late Permian through Early Triassic based on uranium isotope and Th/U trends of marine carbonates. *Geology* 45.2, 163–166. DOI: 10.1130/G38585.1.

Elrick, M., Gilleaudeau, G. J., Romaniello, S. J., Algeo, T. J., Morford, J. L., Sabbatino, M., Goepfert, T. J., Cleal, C., Cascales-Miñana, B., and Chernyavskiy, P. (2022). Major Early-Middle Devonian oceanic oxygenation linked to early land plant evolution detected using high-resolution U isotopes of marine limestones. *Earth and Planetary Science Letters* 581, 117410. DOI: 10.1016/j.epsl.2022.117410.

Enax, J., Prymak, O., Raabe, D., and Epple, M. (2012). Structure, composition, and mechanical properties of shark teeth. *Journal of structural biology* 178.3, 290–299. DOI: 10.1016/j.jsb.2012.03.012.

Eugster, O., Tera, F., Burnett, D., and Wasserburg, G. (1970). Isotopic composition of gadolinium and neutron-capture effects in some meteorites. *Journal of Geophysical Research* 75.14, 2753–2768. DOI: 10.1029/jb075i014p02753.

Faure, G. and Mensing, T. M. (2005). Principles and applications. John Wiley & Sons, Inc.

Fernández-Dıaz, M., Quejido, A., Crespo, M., Villar, L. P. del, Martın-Sánchez, A., and Lozano, J. (2000). Uranium isotopic data in uraninite spent fuel from the Bangombe natural nuclear reactor (Gabon) and its surroundings. *Applied Radiation and Isotopes* 53.1-2, 91–96. DOI: 10.1016/S0969-8043(00)00118-4.

Fiedler, R. (1995). Total evaporation measurements: experience with multi-collector instruments and a thermal ionization quadrupole mass spectrometer. *International Journal of Mass Spectrometry and ion processes* 146, 91–97. DOI: 10.1016/0168-1176(95)04197-S.

Fischer, J., Voigt, S., Franz, M., Schneider, J. W., Joachimski, M. M., Tichomirowa, M., Götze, J., and Furrer, H. (2012). Palaeoenvironments of the late Triassic Rhaetian Sea: implications from oxygen and strontium isotopes of hybodont shark teeth. *Palaeogeography, Palaeoclimatology, Palaeoecology* 353, 60–72. DOI: 10.1016/j.palaeo.2012.07.002.

Fischer, J., Schneider, J. W., Voigt, S., Joachimski, M. M., Tichomirowa, M., Tütken, T., Götze, J., and Berner, U. (2013). Oxygen and strontium isotopes from fossil shark teeth: environmental and ecological implications for Late Palaeozoic European basins. *Chemical Geology* 342, 44–62. DOI: 10.1016/j.chemgeo.2013.01.022.

Frei, R., Gaucher, C., Poulton, S. W., and Canfield, D. E. (2009). Fluctuations in Precambrian atmospheric oxygenation recorded by chromium isotopes. *Nature* 461.7261, 250–253. DOI: 10.1038/nature08266.

Freymuth, H., Andersen, M. B., and Elliott, T. (2019). Uranium isotope fractionation during slab dehydration beneath the Izu arc. *Earth and Planetary Science Letters* 522, 244–254. DOI: 10.1016/j.epsl.2019.07.006.

Friedman, A., Milsted, J., Metta, D., Henderson, D., Lerner, J., Harkness, A., and Rok Op, D. (1966). Alpha decay half lives of ^{148}Gd ^{150}Gd and ^{146}Sm. *Radiochimica Acta* 5.4, 192–194. DOI: 10.1524/ract.1966.5.4.192.

Fujikawa, Y., Shizuma, K., Endo, S., and Fukui, M. (2003). Anomalous ^{235}U/^{238}U ratios and metal elements detected in the black rain from the Hiroshima A-bomb. *Health physics* 84.2, 155–162. DOI: 10.1097/00004032-200302000-00002.

Fukuda, K., Tenner, T. J., Kimura, M., Tomioka, N., Siron, G., Ushikubo, T., Chaumard, N., Hertwig, A. T., and Kita, N. T. (2022). A temporal shift of chondrule generation from the inner to outer Solar System inferred from oxygen isotopes and Al-Mg chronology of chondrules from primitive CM and CO chondrites. *Geochimica et Cosmochimica Acta* 322, 194–226. DOI: 10.1016/j.gca.2021.12.027.

Fuping, H., Haddad, P. R., Jackson, P. E., and Carnevale, J. (1993). Studies on the retention behaviour of α-hydroxyisobutyric acid complexes of thorium (IV) and uranyl ion in reversed-phase high-performance liquid chromatography. *Journal of Chromatography A* 640.1-2, 187–194. DOI: 10.1016/0021-9673(93)80181-7.

Galy, A., Yoffe, O., Janney, P. E., Williams, R. W., Cloquet, C., Alard, O., Halicz, L., Wadhwa, M., Hutcheon, I. D., Ramon, E., et al. (2003). Magnesium isotope heterogeneity of the isotopic standard SRM980 and new reference materials for magnesium-isotope-ratio measurements. *Journal of Analytical Atomic Spectrometry* 18.11, 1352–1356. DOI: 10.1039/B309273A.

Ganapathy, R. (1978). Reagent grade uranium salts: isotopic composition by neutron activation. *Journal of Radioanalytical and Nuclear Chemistry* 44.1, 199–206. DOI: 10.1007/BF02517690.

Gannoun, A., Boyet, M., Rizo, H., and El Goresy, A. (2011). ^{146}Sm–^{142}Nd systematics measured in enstatite chondrites reveals a heterogeneous distribution of ^{142}Nd in the solar nebula. *Proceedings of the National Academy of Sciences* 108.19, 7693–7697. DOI: 10.1073/pnas.1017332108.

Garcia-Valls, R., Hrdlicka, A., Perutka, J., Havel, J., Deorkar, N. V., Tavlarides, L. L., Munoz, M., and Valiente, M. (2001). Separation of rare earth elements by high performance liquid chromatography using a covalent modified silica gel column. *Analytica Chimica Acta* 439.2, 247–253. DOI: 10.1016/S0003-2670(01)01044-3.

Garçon, M., Boyet, M., Carlson, R. W., Horan, M. F., Auclair, D., and Mock, T. D. (2018). Factors influencing the precision and accuracy of Nd isotope measurements by thermal ionization mass spectrometry. *Chemical Geology* 476, 493–514. DOI: 10.1016/j.chemgeo.2017.12.003.

Gaschnig, R. M., Rader, S. T., Reinhard, C. T., Owens, J. D., Planavsky, N., Wang, X., Asael, D., Greaney, A., and Helz, R. (2021). Behavior of the Mo, Tl, and U isotope systems during differentiation in the Kilauea Iki lava lake. *Chemical Geology* 574, 120239. DOI: 10.1016/j.chemgeo.2021.120239.

Gauthier-Lafaye, F., Holliger, P., and Blanc, P.-L. (1996). Natural fission reactors in the Franceville basin, Gabon: A review of the conditions and results of a "critical event" in a geologic system. *Geochimica et Cosmochimica Acta* 60.23, 4831–4852. DOI: 10.1016/S0016-7037(96)00245-1.

Gilleaudeau, G. J., Romaniello, S. J., Luo, G., Kaufman, A. J., Zhang, F., Klaebe, R. M., Kah, L. C., Azmy, K., Bartley, J. K., Zheng, W., et al. (2019). Uranium isotope evidence for limited euxinia in mid-Proterozoic oceans. *Earth and Planetary Science Letters* 521, 150–157. DOI: 10.1016/j.epsl.2019.06.012.

Ginder-Vogel, M., Criddle, C. S., and Fendorf, S. (2006). Thermodynamic constraints on the oxidation of biogenic UO_2 by Fe (III)(hydr) oxides. *Environmental Science & Technology* 40.11, 3544–3550. DOI: 10.1021/es052305p.

Ginter, M., Hampe, O., and Duffin, C. (2010). Chondrichthyes: Paleozoic Elasmobranchii: Teeth. Handbook of paleoichthyology. München: Verlag Dr Friedrich Pfeil.

Goldmann, A., Brennecka, G., Noordmann, J., Weyer, S., and Wadhwa, M. (2015). The uranium isotopic composition of the Earth and the Solar System. *Geochimica et Cosmochimica Acta* 148, 145–158. DOI: 10.1016/j.gca.2014.09.008.

Golubev, V., Chernyshev, I., Chugaev, A., Eremina, A., Baranova, A., and Krupskaya, V. (2013). U-Pb systems and U isotopic composition of the sandstone-hosted paleovalley Dybryn uranium deposit, Vitim uranium district, Russia. *Geology of Ore Deposits* 55, 399–410. DOI: 10.1134/S1075701513060044.

Gothmann, A. M., Higgins, J. A., Adkins, J. F., Broecker, W., Farley, K. A., McKeon, R., Stolarski, J., Planavsky, N., Wang, X., and Bender, M. L. (2019). A Cenozoic record of seawater uranium in fossil corals. *Geochimica et Cosmochimica Acta* 250, 173–190. DOI: 10.1016/j.gca.2019.01.039.

Goto, K. T., Anbar, A. D., Gordon, G. W., Romaniello, S. J., Shimoda, G., Takaya, Y., Tokumaru, A., Nozaki, T., Suzuki, K., Machida, S., et al. (2014). Uranium isotope systematics of ferromanganese crusts in the Pacific Ocean: Implications for the marine ^{238}U/^{235}U isotope system. *Geochimica et Cosmochimica Acta* 146, 43–58. DOI: 10.1016/j.gca.2014.10.003.

Gray, C., Papanastassiou, D., and Wasserburg, G. (1973). The identification of early condensates from the solar nebula. *Icarus* 20.2, 213–239. DOI: 10.1016/0019-1035(73)90052-3.

Gray, P. J., Zhang, L., Xu, H., McDiarmid, M., Squibb, K., and Centeno, J. A. (2012). Determination of ^{236}U/^{238}U and ^{235}U/^{238}U isotope ratios in human urine by inductively coupled plasma mass spectrometry. *Microchemical Journal* 105, 94–100. DOI: 10.1016/j.microc.2012.07.004.

Grossman, L. (1972). Condensation in the primitive solar nebula. *Geochimica et Cosmochimica Acta* 36.5, 597–619. DOI: 10.1016/0016-7037(72)90078-6.

Guillong, M., Heimgartner, P., Kopajtic, Z., Günther, D., and Günther-Leopold, I. (2007). A laser ablation system for the analysis of radioactive samples using inductively coupled plasma mass spectrometry. *Journal of Analytical Atomic Spectrometry* 22.4, 399–402. DOI: 10.1039/b616364e.

Günther-Leopold, I., Kivel, N., Kobler Waldis, J., and Wernli, B. (2008). Characterization of nuclear fuels by ICP mass-spectrometric techniques. *Analytical and bioAnalytical Chemistry* 390, 503–510. DOI: 10.1007/s00216-007-1644-x.

Gwiazda, R., Squibb, K., McDiarmid, M., and Smith, D. (2004). Detection of depleted uranium in urine of veterans from the 1991 Gulf War. *Health physics* 86.1, 12–18. DOI: 10.1097/00004032-200401000-00004.

Hamer, A. and Robbins, E. (1960). A search for variations in the natural abundance of uranium-235. *Geochimica et Cosmochimica Acta* 19. DOI: 10.1016/0016-7037(60)90047-8.

Hamilton, E. and Stevens, H. (1985). Some observations on the geochemistry and isotopic composition of uranium in relation to the reprocessing of nuclear fuels. *Journal of environmental radioactivity* 2.1, 23–40. DOI: 10.1016/0265-931X(85)90023-2.

Harvey, J. and Baxter, E. F. (2009). An improved method for TIMS high precision neodymium isotope analysis of very small aliquots (1–10áng). *Chemical Geology* 258.3-4, 251–257. DOI: 10.1016/j.chemgeo.2008.10.024.

Hättig, K., Stevens, K., Thies, D., Schweigert, G., and Mutterlose, J. (2019). Evaluation of shark tooth diagenesis-screening methods and the application of their stable oxygen isotope data for palaeoenvironmental reconstructions. *Journal of the Geological Society* 176.3, 482–491. DOI: 10.1144/jgs2018-190.

Hayashi, T., Tanimizu, M., and Tanaka, T. (2004). Origin of negative Ce anomalies in Barberton sedimentary rocks, deduced from La–Ce and Sm–Nd isotope systematics. *Precambrian Research* 135.4, 345–357. DOI: `10.1016/j.precamres.2004.09.004`.

Henderson, G. M., Slowey, N. C., and Haddad, G. A. (1999). Fluid flow through carbonate platforms: constraints from ^{234}U/^{238}U and Cl$^-$ in Bahamas pore-waters. *Earth and Planetary Science Letters* 169.1-2, 99–111. DOI: `10.1016/S0012-821X(99)00065-5`.

Herrmann, A. D., Gordon, G. W., and Anbar, A. D. (2018). Uranium isotope variations in a dolomitized Jurassic carbonate platform (Tithonian; Franconian Alb, Southern Germany). *Chemical Geology* 497, 41–53. DOI: `10.1016/j.chemgeo.2018.08.017`.

Hidaka, H., Ebihara, M., and Shima, M. (1995). Determination of the isotopic compositions of samarium and gadolinium by thermal ionization mass spectrometry. *Analytical chemistry* 67.8, 1437–1441. DOI: `10.1021/ac00104a021`.

Hidaka, H. and Holliger, P. (1998). Geochemical and neutronic characteristics of the natural fossil fission reactors at Oklo and Bangombé, Gabon. *Geochimica et Cosmochimica Acta* 62.1, 89–108. DOI: `10.1016/S0016-7037(97)00319-0`.

Hidaka, H., Holliger, P., and Gauthier-Lafaye, F. (1999). Tc/Ru fractionation in the Oklo and Bangombé natural fission reactors, Gabon. *Chemical geology* 155.3-4, 323–333. DOI: `10.1016/S0009-2541(98)00173-9`.

Hidaka, H. and Gauthier-Lafaye, F. (2000). Redistribution of fissiogenic and non-fissiogenic REE, Th and U in and around natural fission reactors at Oklo and Bangombé, Gabon. *Geochimica et Cosmochimica Acta* 64.12, 2093–2108. DOI: `10.1016/S0016-7037(00)00364-1`.

Hidaka, H., Yoneda, S., and Nishiizumi, K. (2009). Cosmic-ray exposure histories of Martian meteorites studied from neutron capture reactions of Sm and Gd isotopes. *Earth and Planetary Science Letters* 288.3-4, 564–571. DOI: `10.1016/j.epsl.2009.10.019`.

Hiess, J., Condon, D. J., McLean, N., and Noble, S. R. (2012). ^{238}U/^{235}U systematics in terrestrial uranium-bearing minerals. *Science* 335.6076, 1610–1614. DOI: `10.1126/science.1215507`.

Hines, S. K., Southon, J. R., and Adkins, J. F. (2015). A high-resolution record of Southern Ocean intermediate water radiocarbon over the past 30,000 years. *Earth and Planetary Science Letters* 432, 46–58. DOI: `10.1016/j.epsl.2015.09.038`.

Holliger, P. and Devillers, C. (1981). Contributionàl'étude de la température dans les réacteurs fossiles d'Oklo par la mesure du rapport isotopique du lutétium. *Earth and Planetary Science Letters* 52.1, 76–84. DOI: `10.1016/0012-821X(81)90209-0`.

Holmden, C., Amini, M., and Francois, R. (2015). Uranium isotope fractionation in Saanich Inlet: A modern analog study of a paleoredox tracer. *Geochimica et Cosmochimica Acta* 153, 202–215. DOI: `10.1016/j.gca.2014.11.012`.

Hood, A. v., Planavsky, N. J., Wallace, M. W., Wang, X., Bellefroid, E. J., Gueguen, B., and Cole, D. B. (2016). Integrated geochemical-petrographic insights from component-selective δ^{238}U of Cryogenian marine carbonates. *Geology* 44.11, 935–938. DOI: `10.1130/G38533.1`.

Hood, A. v., Planavsky, N. J., Wallace, M. W., and Wang, X. (2018). The effects of diagenesis on geochemical paleoredox proxies in sedimentary carbonates. *Geochimica et Cosmochimica Acta* 232, 265–287. DOI: `10.1016/j.gca.2018.04.022`.

Horan, P., Dietz, L., and Durakovic, A. (2002). The quantitative analysis of depleted uranium isotopes in British, Canadian, and US Gulf War veterans. *Military Medicine* 167.8, 620–627. DOI: `10.1093/milmed/167.8.620`.

Horie, K., Hidaka, H., and Gauthier-Lafaye, F. (2004). Isotopic evidence for trapped fissiogenic REE and nucleogenic Pu in apatite and Pb evolution at the Oklo natural reactor. *Geochimica et Cosmochimica Acta* 68.1, 115–125. DOI: `10.1016/S0016-7037(03)00415-0`.

Horwitz, E. P., Dietz, M. L., Chiarizia, R., Diamond, H., Essling, A. M., and Graczyk, D. (1992). Separation and preconcentration of uranium from acidic media by extraction chromatography. *Analytica Chimica Acta* 266.1, 25–37. DOI: `10.1016/0003-2670(92)85276-C`.

Howe, S. E., Davidson, C. M., and McCartney, M. (2002). Determination of uranium concentration and isotopic composition by means of ICP-MS in sequential extracts of sediment from the vicinity of a uranium enrichment plant. *Journal of Analytical Atomic Spectrometry* 17.5, 497–501. DOI: `10.1039/b200270c`.

Hu, J., Dauphas, N., Tissot, F., Yokochi, R., Ireland, T., Zhang, Z., Davis, A., Ciesla, F., Grossman, L., Charlier, B., et al. (2021). Heating events in the nascent solar system recorded by rare earth element isotopic fractionation in refractory inclusions. *Science Advances* 7.2, eabc2962. DOI: `10.1126/sciadv.abc2962`.

Huang, F., Glessner, J., Ianno, A., Lundstrom, C., and Zhang, Z. (2009). Magnesium isotopic composition of igneous rock standards measured by MC-ICP-MS. *Chemical Geology* 268.1-2, 15–23. DOI: `10.1016/j.chemgeo.2009.07.003`.

Hubert, A., Claverie, F., Pécheyran, C., and Pointurier, F. (2014). Measurement of the isotopic composition of uranium micrometer-size particles by femtosecond laser ablation-inductively coupled plasma mass spectrometry. *Spectrochimica Acta Part B: Atomic Spectroscopy* 93, 52–60. DOI: `10.1016/j.sab.2013.12.007`.

Huck, C. E., Flierdt, T. van de, Jiménez-Espejo, F. J., Bohaty, S. M., Röhl, U., and Hammond, S. J. (2016). Robustness of fossil fish teeth for seawater neodymium isotope reconstructions under variable redox conditions in an ancient shallow marine setting. *Geochemistry, Geophysics, Geosystems* 17.3, 679–698. DOI: `10.1002/2015GC006218`.

Hyun, S. P., Fox, P. M., Davis, J. A., Campbell, K. M., Hayes, K. F., and Long, P. E. (2009). Surface complexation modeling of U (VI) adsorption by aquifer sediments from a former mill tailings site at Rifle, Colorado. *Environmental Science & Technology* 43.24, 9368–9373. DOI: `10.1021/es902164n`.

Hyung, E. and Jacobsen, S. B. (2020). The ^{142}Nd/^{144}Nd variations in mantle-derived rocks provide constraints on the stirring rate of the mantle from the Hadean to the present. *Proceedings of the National Academy of Sciences* 117.26, 14738–14744.

Iacumin, P., Bocherens, H., Mariotti, A., and Longinelli, A. (1996). Oxygen isotope analyses of co-existing carbonate and phosphate in biogenic apatite: a way to monitor diagenetic alteration of bone phosphate? *Earth and Planetary Science Letters* 142.1-2, 1–6. DOI: `10.1016/0012-821X(96)00093-3`.

Iizuka, T., Amelin, Y., Kaltenbach, A., Koefoed, P., and Stirling, C. H. (2014). U–Pb systematics of the unique achondrite Ibitira: Precise age determination and petrogenetic implications. *Geochimica et Cosmochimica Acta* 132, 259–273. DOI: `10.1016/j.gca.2014.02.017`.

Ireland, T., Tissot, F., Yokochi, R., and Dauphas, N. (2013). Teflon-HPLC: A novel chromatographic system for application to isotope geochemistry and other industries. *Chemical Geology* 357, 203–214. DOI: `10.1016/j.chemgeo.2013.08.001`.

Iturbe, J. (1992). Determination of ^{234}U/^{238}U and ^{235}U/^{238}U ratios from commercially available uranium compounds by α-spectrometry. *Journal of Radioanalytical and Nuclear Chemistry* 166.4, 263–272. DOI: `10.1007/BF02163832`.

Ivanova, M., Krot, A., and MacPherson, G. (2015). Genetic link between Fluffy Type A, compact Type A and Type B CAIs from CV3 chondrites NWA 3118 and Efremovka. In: *46th Lunar and Planetary Science Conference*. 1832, 2371.

Jacobsen, B., Yin, Q.-z., Moynier, F., Amelin, Y., Krot, A. N., Nagashima, K., Hutcheon, I. D., and Palme, H. (2008). ^{26}Al–^{26}Mg and ^{207}Pb–^{206}Pb systematics of Allende CAIs: Canonical solar initial ^{26}Al/^{27}Al ratio reinstated. *Earth and Planetary Science Letters* 272.1-2, 353–364. DOI: `10.1016/j.epsl.2008.05.003`.

Jacobsen, S. B. and Wasserburg, G. (1980). Sm-Nd isotopic evolution of chondrites. *Earth and Planetary Science Letters* 50.1, 139–155. DOI: `10.1016/0012-821x(80)90125-9`.

Jacobsen, S. B. and Wasserburg, G. (1984). Sm-Nd isotopic evolution of chondrites and achondrites, II. *Earth and Planetary Science Letters* 67.2, 137–150. DOI: `10.1016/0012-821x(84)90109-2`.

Jacquet, E., Pignatale, F. C., Chaussidon, M., and Charnoz, S. (2019). Fingerprints of the protosolar cloud collapse in the Solar System. II. Nucleosynthetic anomalies in meteorites. *The Astrophysical Journal* 884.1, 32. DOI: `10.3847/1538-4357/ab38c1`.

Jaffey, A., Flynn, K., Glendenin, L., Bentley, W. t., and Essling, A. (1971). Precision measurement of half-lives and specific activities of ^{235}U and ^{238}U. *Physical review C* 4.5, 1889. DOI: `10.1103/PhysRevC.4.1889`.

Jansen, C. A., Burkhardt, C., Marrocchi, Y., Schneider, J. M., Wölfer, E., and Kleine, T. (2024). Condensate evolution in the solar nebula inferred from combined Cr, Ti, and O isotope analyses of amoeboid olivine aggregates. *Earth and Planetary Science Letters* 627, 118567. DOI: `10.1016/j.epsl.2024.118567`.

Jeffery, P. and Reynolds, J. (1961). Origin of excess Xe^{129} in stone meteorites. *Journal of Geophysical Research* 66.10, 3582–3583. DOI: 10.1029/JZ066i010p03582.

Jemison, N. E., Shiel, A. E., Johnson, T. M., Lundstrom, C. C., Long, P. E., and Williams, K. H. (2018). Field application of $^{238}U/^{235}U$ measurements to detect reoxidation and mobilization of U(IV). *Environmental Science & Technology* 52.6, 3422–3430. DOI: 10.1021/acs.est.7b05162.

Jemison, N. E., Bizjack, M. T., Johnson, T. M., and Druhan, J. L. (2020). Influence of physical and chemical hydrology on bioremediation of a U-contaminated aquifer informed by reactive transport modeling incorporating $^{238}U/^{235}U$ ratios. *Geochimica et Cosmochimica Acta* 269, 303–328. DOI: 10.1016/j.gca.2019.10.031.

Jemison, N. E., Johnson, T. M., Shiel, A. E., and Lundstrom, C. (2016). Uranium isotopic fractionation induced by U(VI) adsorption onto common aquifer minerals. *Environmental Science & Technology* 50.22, 12232–12240. DOI: 10.1021/acs.est.6b03488.

Ji, A. P., Frebel, A., Chiti, A., and Simon, J. D. (2016). R-process enrichment from a single event in an ancient dwarf galaxy. *Nature* 531.7596, 610–613. DOI: 10.1038/nature17425.

John, S. G. and Adkins, J. F. (2010). Analysis of dissolved iron isotopes in seawater. *Marine Chemistry* 119.1-4, 65–76. DOI: 10.1016/j.marchem.2010.01.001.

Joshi, L., Zingde, M., and Desai, B. (1983). Radiochemical determination of uranium and studies of $^{234}U/^{238}U$ and $^{235}U/^{238}U$ activity ratios in estuarine sediments of mindola river. *Journal of Radioanalytical and Nuclear Chemistry* 76.1, 97–104. DOI: 10.1007/BF02519659.

Jost, A. B., Bachan, A., De Schootbrugge, B. van, Lau, K. V., Weaver, K. L., Maher, K., and Payne, J. L. (2017). Uranium isotope evidence for an expansion of marine anoxia during the end-T riassic extinction. *Geochemistry, Geophysics, Geosystems* 18.8, 3093–3108. DOI: 10.1002/2017GC006941.

Kane, J. S. (1998). A history of the development and certification of NIST glass SRMs 610-617. *Geostandards Newsletter* 22.1, 7–13. DOI: 10.1111/j.1751-908X.1998.tb00541.x.

Kappel, S., Boulyga, S. F., and Prohaska, T. (2012). Direct uranium isotope ratio analysis of single micrometer-sized glass particles. *Journal of environmental radioactivity* 113, 8–15. DOI: 10.1016/j.jenvrad.2012.03.017.

Kappel, S., Boulyga, S. F., Dorta, L., Günther, D., Hattendorf, B., Koffler, D., Laaha, G., Leisch, F., and Prohaska, T. (2013). Evaluation strategies for isotope ratio measurements of single particles by LA-MC-ICPMS. *Analytical and bioAnalytical Chemistry* 405, 2943–2955. DOI: 10.1007/s00216-012-6674-3.

Keatley, A. C., Dunne, J. A., Martin, T. L., Nita, D. C., Andersen, M. B., Scott, T. B., Richards, D. A., and Awbery, R. P. (2021). Uranium isotope variation within vein-type uranium ore deposits. *Applied Geochemistry* 131, 104977. DOI: 10.1016/j.apgeochem.2021.104977.

Keegan, E., Richter, S., Kelly, I., Wong, H., Gadd, P., Kuehn, H., and Alonso-Munoz, A. (2008). The provenance of Australian uranium ore concentrates by elemental and isotopic analysis. *Applied Geochemistry* 23.4, 765–777. DOI: `10.1016/j.apgeochem.2007.12.004`.

Kendall, B., Brennecka, G. A., Weyer, S., and Anbar, A. D. (2013). Uranium isotope fractionation suggests oxidative uranium mobilization at 2.50 Ga. *Chemical Geology* 362, 105–114. DOI: `10.1016/j.chemgeo.2013.08.010`.

Kendall, B., Komiya, T., Lyons, T. W., Bates, S. M., Gordon, G. W., Romaniello, S. J., Jiang, G., Creaser, R. A., Xiao, S., McFadden, K., et al. (2015). Uranium and molybdenum isotope evidence for an episode of widespread ocean oxygenation during the late Ediacaran Period. *Geochimica et Cosmochimica Acta* 156, 173–193. DOI: `10.1016/j.gca.2015.02.025`.

Kendall, B., Wang, J., Zheng, W., Romaniello, S. J., Over, D. J., Bennett, Y., Xing, L., Kunert, A., Boyes, C., and Liu, J. (2020). Inverse correlation between the molybdenum and uranium isotope compositions of Upper Devonian black shales caused by changes in local depositional conditions rather than global ocean redox variations. *Geochimica et Cosmochimica Acta* 287, 141–164. DOI: `10.1016/j.gca.2020.01.026`.

Kigoshi, K. (1971). Alpha-recoil thorium-234: dissolution into water and the uranium-234/uranium-238 disequilibrium in nature. *Science* 173.3991, 47–48. DOI: `10.1126/science.173.3991.47`.

Kikawada, Y., Suzuki, H., Yamauchi, R., Oia, T., and Hirose, K. (2015). ^{235}U/^{238}U isotope ratios in monthly atmospheric deposits collected at Akita, Japan in 1977 and 1978. *Procedia Earth and Planetary Science* 15, 675–679. DOI: `10.1016/j.proeps.2015.08.083`.

Kikuchi, M. and Hidaka, H. (2009). In-situ U-Pb analyses of highly altered zircon from sediments overlying the Bangombé natural fission reactor, Gabon. *Geosciences Journal* 13, 257–264. DOI: `10.1007/s12303-009-0025-1`.

Kim, S. L., Eberle, J. J., Bell, D. M., Fox, D. A., and Padilla, A. (2014). Evidence from shark teeth for a brackish Arctic Ocean in the Eocene greenhouse. *Geology* 42.8, 695–698. DOI: `10.1130/G35675.1`.

Kim, S. L., Zeichner, S. S., Colman, A. S., Scher, H. D., Kriwet, J., Mörs, T., and Huber, M. (2020). Probing the ecology and climate of the Eocene Southern Ocean with sand tiger sharks *Striatolamia macrota*. *Paleoceanography and paleoclimatology* 35.12, e2020PA003997. DOI: `10.1029/2020PA003997`.

Kipp, M. A., Li, H., Ellwood, M. J., John, S. G., Middag, R., Adkins, J. F., and Tissot, F. L. H. (2022). ^{238}U, ^{235}U and ^{234}U in seawater and deep-sea corals: A high-precision reappraisal. *Geochimica et Cosmochimica Acta* 336, 231–248. DOI: `10.1016/j.gca.2022.09.018`.

Kipp, M. A. and Tissot, F. L. (2022). Inverse methods for consistent quantification of seafloor anoxia using uranium isotope data from marine sediments. *Earth and Planetary Science Letters* 577, 117240. DOI: `10.1016/j.epsl.2021.117240`.

Kips, R., Leenaers, A., Tamborini, G., Betti, M., Van den Berghe, S., Wellum, R., and Taylor, P. (2007). Characterization of uranium particles produced by hydrolysis of UF_6 using SEM and SIMS. *Microscopy and Microanalysis* 13.3, 156–164. DOI: 10.1017/S1431927607070341.

Kips, R., Weber, P. K., Kristo, M. J., Jacobsen, B., and Ramon, E. C. (2019). Microscale isotopic variation in uranium fuel pellets with implications for nuclear forensics. *Analytical Chemistry* 91.18, 11598–11605. DOI: 10.1021/acs.analchem.9b01737.

Kirchenbaur, M., Maas, R., Ehrig, K., Kamenetsky, V. S., Strub, E., Ballhaus, C., and Muenker, C. (2016). Uranium and Sm isotope studies of the supergiant Olympic Dam Cu–Au–U–Ag deposit, South Australia. *Geochimica et Cosmochimica Acta* 180, 15–32. DOI: 10.1016/j.gca.2016.01.035.

Kita, N. T., Yin, Q.-Z., MacPherson, G. J., Ushikubo, T., Jacobsen, B., Nagashima, K., Kurahashi, E., Krot, A. N., and Jacobsen, S. B. (2013). ^{26}Al-^{26}Mg isotope systematics of the first solids in the early solar system. *Meteoritics & Planetary Science* 48.8, 1383–1400. DOI: 10.1111/maps.12141.

Klug, S., Tütken, T., Wings, O., Pfretzschner, H.-U., and Martin, T. (2010). A Late Jurassic freshwater shark assemblage (Chondrichthyes, Hybodontiformes) from the southern Junggar Basin, Xinjiang, Northwest China. *Palaeobiodiversity and Palaeoenvironments* 90, 241–257. DOI: 10.1007/s12549-010-0032-2.

Knyazev, D. A. and Myasoedov, N. F. (2001). Specific effects of heavy nuclei in chemical equilibrium. *Separation Science and Technology* 36.8-9, 1677–1696. DOI: 10.1081/SS-100104758.

Kocsis, L., Vennemann, T. W., and Fontignie, D. (2007). Migration of sharks into freshwater systems during the Miocene and implications for Alpine paleoelevation. *Geology* 35.5, 451–454. DOI: 10.1130/G23404A.1.

Kocsis, L., Vennemann, T. W., Hegner, E., Fontignie, D., and Tütken, T. (2009). Constraints on Miocene oceanography and climate in the Western and Central Paratethys: O-, Sr-, and Nd-isotope compositions of marine fish and mammal remains. *Palaeogeography, Palaeoclimatology, Palaeoecology* 271.1-2, 117–129. DOI: 10.1016/j.palaeo.2008.10.003.

Kocsis, L., Ounis, A., Chaabani, F., and Salah, N. M. (2013). Paleoenvironmental conditions and strontium isotope stratigraphy in the Paleogene Gafsa Basin (Tunisia) deduced from geochemical analyses of phosphatic fossils. *International Journal of Earth Sciences* 102, 1111–1129. DOI: 10.1007/s00531-012-0845-5.

Kocsis, L., Gheerbrant, E., Mouflih, M., Cappetta, H., Yans, J., and Amaghzaz, M. (2014). Comprehensive stable isotope investigation of marine biogenic apatite from the late Cretaceous–early Eocene phosphate series of Morocco. *Palaeogeography, Palaeoclimatology, Palaeoecology* 394, 74–88. DOI: 10.1016/j.palaeo.2013.11.002.

Kohn, M. J., Schoeninger, M. J., and Barker, W. W. (1999). Altered states: effects of diagenesis on fossil tooth chemistry. *Geochimica et Cosmochimica Acta* 63.18, 2737–2747. DOI: 10.1016/S0016-7037(99)00208-2.

Kohn, M. J. and Cerling, T. E. (2002). Stable isotope compositions of biological apatite. *Reviews in mineralogy and geochemistry* 48.1, 455–488. DOI: `10.2138/rmg.2002.48.12`.

Kolodny, Y., Luz, B., and Navon, O. (1983). Oxygen isotope variations in phosphate of biogenic apatites, I. Fish bone apatite—rechecking the rules of the game. *Earth and Planetary Science Letters* 64.3, 398–404. DOI: `10.1016/0012-821X(83)90100-0`.

Kolodny, Y. and Raab, M. (1988). Oxygen isotopes in phosphatic fish remains from Israel: paleothermometry of tropical Cretaceous and Tertiary shelf waters. *Palaeogeography, Palaeoclimatology, Palaeoecology* 64.1-2, 59–67. DOI: `10.1016/0031-0182(88)90142-3`.

Kolodny, Y., Luz, B., and Taylor, H. (1991). Oxygen isotopes in phosphates of fossil fish—Devonian to Recent. In: *Stable isotope geochemistry: A tribute to Samuel Epstein*. Vol. 3. The Geochemical Society, Special Publication, 105–119.

Kööp, L., Davis, A. M., Nakashima, D., Park, C., Krot, A. N., Nagashima, K., Tenner, T. J., Heck, P. R., and Kita, N. T. (2016a). A link between oxygen, calcium and titanium isotopes in ^{26}Al-poor hibonite-rich CAIs from Murchison and implications for the heterogeneity of dust reservoirs in the solar nebula. *Geochimica et Cosmochimica Acta* 189, 70–95. DOI: `10.1016/j.gca.2016.05.014`.

Kööp, L., Nakashima, D., Heck, P. R., Kita, N. T., Tenner, T. J., Krot, A. N., Nagashima, K., Park, C., and Davis, A. M. (2016b). New constraints on the relationship between ^{26}Al and oxygen, calcium, and titanium isotopic variation in the early Solar System from a multielement isotopic study of spinel-hibonite inclusions. *Geochimica et Cosmochimica Acta* 184, 151–172. DOI: `10.1016/j.gca.2016.04.018`.

Kööp, L., Nakashima, D., Heck, P. R., Kita, N. T., Tenner, T. J., Krot, A. N., Nagashima, K., Park, C., and Davis, A. M. (2018). A multielement isotopic study of refractory FUN and F CAIs: Mass-dependent and mass-independent isotope effects. *Geochimica et Cosmochimica Acta* 221, 296–317. DOI: `10.1016/j.gca.2017.04.029`.

Korkisch, J. (2017). CRC Handbook of Ion Exchange Resins. Vol. 6. Routledge.

Krachler, M., Varga, Z., Nicholl, A., Wallenius, M., and Mayer, K. (2018). Spatial distribution of uranium isotopes in solid nuclear materials using laser ablation multi-collector ICP-MS. *Microchemical Journal* 140, 24–30. DOI: `10.1016/j.microc.2018.03.038`.

Kraiem, M., Richter, S., Erdmann, N., Kühn, H., Hedberg, M., and Aregbe, Y. (2012). Characterizing uranium oxide reference particles for isotopic abundances and uranium mass by single particle isotope dilution mass spectrometry. *Analytica Chimica Acta* 748, 37–44. DOI: `10.1016/j.aca.2012.08.030`.

Kraiem, M., Essex, R., Mathew, K., Orlowicz, G., and Soriano, M. (2013). Recertification of the CRM 125-A UO2 fuel pellet standard for uranium isotopic composition. *International Journal of Mass Spectrometry* 352, 37–43. DOI: `10.1016/j.ijms.2013.05.007`.

Krestianinov, E., Amelin, Y., Yin, Q.-Z., Cary, P., Huyskens, M. H., Miller, A., Dey, S., Hibiya, Y., Tang, H., Young, E. D., et al. (2023). Igneous meteorites suggest Aluminium-26 heterogeneity in the early Solar Nebula. *Nature Communications* 14.1, 4940. DOI: `10.1038/s41467-023-40026-1`.

Krot, A. N., Scott, E. R., and Zolensky, M. E. (1995). Mineralogical and chemical modification of components in CV3 chondrites: Nebular or asteroidal processing? *Meteoritics* 30.6, 748–775. DOI: `10.1111/j.1945-5100.1995.tb01173.x`.

Krystek, P. and Ritsema, R. (2002). Determination of uranium in urine–measurement of isotope ratios and quantification by use of inductively coupled plasma mass spectrometry. *Analytical and bioAnalytical Chemistry* 374, 226–229. DOI: `10.1007/s00216-002-1424-6`.

Ku, T.-L., Mathieu, G. G., and Knauss, K. G. (1977). Uranium in open ocean: concentration and isotopic composition. *Deep Sea Research* 24.11, 1005–1017. DOI: `10.1016/0146-6291(77)90571-9`.

Kuffmeier, M., Haugbølle, T., and Nordlund, Å. (2017). Zoom-in simulations of protoplanetary disks starting from GMC scales. *The Astrophysical Journal* 846.1, 7. DOI: `10.3847/1538-4357/aa7c64`.

Kunzendorf, H. (1968). Determination of the isotopic composition of natural and slightly enriched uranium by alpha-spectrometry. *Nuclear instruments and methods* 63.2, 152–156. DOI: `10.1016/0029-554X(68)90320-0`.

Laboratory, N. B. (2010). Certificate of Analysis, CRM 145 Uranyl (Normal) Nitrate Assay and Isotopic Solution: Argonne, Illinois, New Brunswick Laboratory. *U.S. Department of Energy.*

Lancelot, J. R., Vitrac, A., and Allegre, C. J. (1975). The Oklo natural reactor: Age and evolution studies by UPb and RbSr systematics. *Earth and planetary science letters* 25.2, 189–196. DOI: `10.1016/0012-821X(75)90195-8`.

Langmuir, D. (1978). Uranium solution-mineral equilibria at low temperatures with applications to sedimentary ore deposits. *Geochimica et Cosmochimica Acta* 42.6, 547–569. DOI: `10.1016/0016-7037(78)90001-7`.

Larsen, K. K., Trinquier, A., Paton, C., Schiller, M., Wielandt, D., Ivanova, M. A., Connelly, J. N., Nordlund, Å., Krot, A. N., and Bizzarro, M. (2011). Evidence for magnesium isotope heterogeneity in the solar protoplanetary disk. *The Astrophysical Journal Letters* 735.2, L37. DOI: `10.1088/2041-8205/735/2/L37`.

Larsen, K. K., Wielandt, D., Schiller, M., Krot, A., and Bizzarro, M. (2020). Episodic formation of refractory inclusions in the Solar System and their presolar heritage. *Earth and Planetary Science Letters* 535, 116088. DOI: `10.1016/j.epsl.2020.116088`.

Lau, K. V., Maher, K., Altiner, D., Kelley, B. M., Kump, L. R., Lehrmann, D. J., Silva-Tamayo, J. C., Weaver, K. L., Yu, M., and Payne, J. L. (2016). Marine anoxia and delayed Earth system recovery after the end-Permian extinction. *Proceedings of the National Academy of Sciences* 113.9, 2360–2365. DOI: `10.1073/pnas.1515080113`.

Lau, K. V., Macdonald, F. A., Maher, K., and Payne, J. L. (2017). Uranium isotope evidence for temporary ocean oxygenation in the aftermath of the Sturtian Snowball Earth. *Earth and Planetary Science Letters* 458, 282–292. DOI: `10.1016/j.epsl.2016.10.043`.

Lau, K. V., Hancock, L. G., Severmann, S., Kuzminov, A., Cole, D. B., Behl, R. J., Planavsky, N. J., and Lyons, T. W. (2022). Variable local basin hydrography and productivity control the uranium isotope paleoredox proxy in anoxic black shales. *Geochimica et Cosmochimica Acta* 317, 433–456. DOI: `10.1016/j.gca.2021.10.011`.

Lécuyer, C., Grandjean, P., O'Neil, J. R., Cappetta, H., and Martineau, F. (1993). Thermal excursions in the ocean at the Cretaceous—Tertiary boundary (northern Morocco): δ^{18}O record of phosphatic fish debris. *Palaeogeography, Palaeoclimatology, Palaeoecology* 105.3-4, 235–243. DOI: `10.1016/0031-0182(93)90085-W`.

Lécuyer, C., Picard, S., Garcia, J.-P., Sheppard, S. M., Grandjean, P., and Dromart, G. (2003). Thermal evolution of Tethyan surface waters during the Middle-Late Jurassic: Evidence from δ^{18}O values of marine fish teeth. *Paleoceanography* 18.3. DOI: `10.1029/2002PA000863`.

Lécuyer, C., Reynard, B., and Grandjean, P. (2004). Rare earth element evolution of Phanerozoic seawater recorded in biogenic apatites. *Chemical Geology* 204.1-2, 63–102. DOI: `10.1016/j.chemgeo.2003.11.003`.

Lécuyer, C., Amiot, R., Touzeau, A., and Trotter, J. (2013). Calibration of the phosphate δ^{18}O thermometer with carbonate–water oxygen isotope fractionation equations. *Chemical Geology* 347, 217–226. DOI: `10.1016/j.chemgeo.2013.03.008`.

Lee, S.-G. and Tanaka, T. (2019). Determination of Eu isotopic ratio by multi-collector inductively coupled plasma mass spectrometry using a Sm internal standard. *Spectrochimica Acta Part B: Atomic Spectroscopy* 156, 42–50. DOI: `10.1016/j.sab.2019.04.011`.

Lee, T., Papanastassiou, D., and Wasserburg, G. (1976). Demonstration of ^{26}Mg excess in Allende and evidence for ^{26}Al. *Geophysical Research Letters* 3.1, 109–112. DOI: `10.1029/GL003i001p00041`.

Lefebvre, P., Noël, V., Lau, K. V., Jemison, N. E., Weaver, K. L., Williams, K. H., Bargar, J. R., and Maher, K. (2019). Isotopic fingerprint of uranium accumulation and redox cycling in floodplains of the Upper Colorado River Basin. *Environmental Science & Technology* 53.7, 3399–3409. DOI: `10.1021/acs.est.8b05593`.

Lefebvre, P., Gourgiotis, A., Mangeret, A., Sabatier, P., Le Pape, P., Diez, O., Louvat, P., Menguy, N., Merrot, P., Baya, C., et al. (2021). Diagenetic formation of uranium-silica polymers in lake sediments over 3,300 years. *Proceedings of the National Academy of Sciences* 118.4, e2021844118. DOI: `10.1073/pnas.2021844118`.

Lefebvre, P., Le Pape, P., Mangeret, A., Gourgiotis, A., Sabatier, P., Louvat, P., Diez, O., Mathon, O., Hunault, M. O., Baya, C., et al. (2022). Uranium sorption to organic matter and long-term accumulation in a pristine alpine wetland.

Geochimica et Cosmochimica Acta 338, 322–346. DOI: 10.1016/j.gca.2022.10.018.

LeGrande, A. N. and Schmidt, G. A. (2006). Global gridded data set of the oxygen isotopic composition in seawater. *Geophysical Research Letters* 33.12. DOI: 10.1029/2006GL026011.

Lewis, J. A. and Jones, R. H. (2019). Primary feldspar in the Semarkona LL 3.00 chondrite: Constraints on chondrule formation and secondary alteration. *Meteoritics & Planetary Science* 54.1, 72–89. DOI: 10.1111/maps.13194.

Lewis, L., Knight, K., Matzel, J., Prussin, S., Zimmer, M., Kinman, W., Ryerson, F., and Hutcheon, I. (2015). Spatially-resolved analyses of aerodynamic fallout from a uranium-fueled nuclear test. *Journal of environmental radioactivity* 148, 183–195. DOI: 10.1016/j.jenvrad.2015.04.006.

Leya, I., Wieler, R., and Halliday, A. N. (2003). The influence of cosmic-ray production on extinct nuclide systems. *Geochimica et Cosmochimica Acta* 67.3, 529–541. DOI: 10.1016/s0016-7037(02)01091-8.

Li, D., Peng, J., Chew, D., Liang, Y., Hollings, P., Fu, Y., Dong, Y., and Sun, X. (2023). Dating rare earth element enrichment in deep-sea sediments using U-Pb geochronology of bioapatite. *Geology* 51.5, 428–433. DOI: 10.1130/G50938.1.

Li, H. and Tissot, F. L. (2023). UID: The uranium isotope database. *Chemical Geology* 618, 121221. DOI: 10.1016/j.chemgeo.2022.121221.

Li, J., Azmy, K., and Kendall, B. (2022). The Mo-and U-isotope signatures in alternating shales and carbonate beds of rhythmites: A comparison and implications for redox conditions across the Cambrian-Ordovician boundary. *Chemical Geology* 602, 120882. DOI: 10.1016/j.chemgeo.2022.120882.

Li, S., Jagoutz, E., Chen, Y., and Li, Q. (2000). Sm–Nd and Rb–Sr isotopic chronology and cooling history of ultrahigh pressure metamorphic rocks and their country rocks at Shuanghe in the Dabie Mountains, Central China. *Geochimica et Cosmochimica Acta* 64.6, 1077–1093. DOI: 10.1016/s0016-7037(99)00319-1.

Li, W., Czaja, A. D., Van Kranendonk, M. J., Beard, B. L., Roden, E. E., and Johnson, C. M. (2013). An anoxic, Fe (II)-rich, U-poor ocean 3.46 billion years ago. *Geochimica et Cosmochimica Acta* 120, 65–79. DOI: 10.1016/j.gca.2013.06.033.

Li, Z., Cao, M., Loyd, S. J., Algeo, T. J., Zhao, H., Wang, X., Zhao, L., and Chen, Z.-Q. (2020). Transient and stepwise ocean oxygenation during the late Ediacaran Shuram Excursion: Insights from carbonate δ238U of northwestern Mexico. *Precambrian Research* 344, 105741. DOI: 10.1016/j.precamres.2020.105741.

Lindahl, P., Olszewski, G., and Eriksson, M. (2021). Performance and optimisation of triple quadrupole ICP-MS for accurate measurement of uranium isotopic ratios. *Journal of Analytical Atomic Spectrometry* 36.10, 2164–2172. DOI: 10.1039/d1ja00177a.

Liu, M.-C., Chaussidon, M., Göpel, C., and Lee, T. (2012). A heterogeneous solar nebula as sampled by CM hibonite grains. *Earth and Planetary Science Letters* 327, 75–83. DOI: 10.1016/j.epsl.2012.02.016.

Liu, M.-C., McKeegan, K. D., Harrison, T. M., Jarzebinski, G., and Vltava, L. (2018). The Hyperion-II radio-frequency oxygen ion source on the UCLA ims1290 ion microprobe: Beam characterization and applications in geochemistry and cosmochemistry. *International Journal of Mass Spectrometry* 424, 1–9. DOI: 10.1016/j.ijms.2017.11.007.

Liu, M., Chen, D., Jiang, L., Stockey, R. G., Aseal, D., Zhang, B., Liu, K., Yang, X., Yan, D., and Planavsky, N. J. (2022). Oceanic anoxia and extinction in the latest Ordovician. *Earth and Planetary Science Letters* 588, 117553. DOI: 10.1016/j.epsl.2022.117553.

Livermore, B., Dahl, T., Bizzarro, M., and Connelly, J. (2020). Uranium isotope compositions of biogenic carbonates–Implications for U uptake in shells and the application of the paleo-ocean oxygenation proxy. *Geochimica et Cosmochimica Acta* 287, 50–64. DOI: 10.1016/j.gca.2020.07.005.

Livermore, B. D., Connelly, J. N., Moynier, F., and Bizzarro, M. (2018). Evaluating the robustness of a consensus ^{238}U/^{235}U value for U-Pb geochronology. *Geochimica et Cosmochimica Acta* 237, 171–183.

Lloyd, N. S., Chenery, S., and Parrish, R. R. (2009). The distribution of depleted uranium contamination in Colonie, NY, USA. *Science of the total environment* 408.2, 397–407. DOI: 10.1016/j.scitotenv.2009.09.024.

Longerich, H. P., Jackson, S. E., and Günther, D. (1996). Inter-laboratory note. Laser ablation inductively coupled plasma mass spectrometric transient signal data acquisition and analyte concentration calculation. *Journal of Analytical Atomic Spectrometry* 11.9, 899–904. DOI: 10.1039/JA9961100899.

Longinelli, A. (1966). Ratios of oxygen-18: oxygen-16 in phosphate and carbonate from living and fossil marine organisms. *Nature* 211.5052, 923–927. DOI: 10.1038/211923a0.

Loss, R., Rosman, K., De Laeter, J., Curtis, D., Benjamin, T., Gancarz, A., Maeck, W., and Delmore, J. (1989). Fission-product retentivity in peripheral rocks at the Oklo natural fission reactors, Gabon. *Chemical geology* 76.1-2, 71–84. DOI: 10.1088/2041-8205/735/2/L37.

Lounsbury, M. (1956). The natural abundances of the uranium isotopes. *Canadian Journal of Chemistry* 34.3, 259–264. DOI: 10.1139/v56-039.

Lu, X., Kendall, B., Stein, H. J., Li, C., Hannah, J. L., Gordon, G. W., and Ebbestad, J. O. R. (2017). Marine redox conditions during deposition of Late Ordovician and Early Silurian organic-rich mudrocks in the Siljan ring district, central Sweden. *Chemical Geology* 457, 75–94. DOI: 10.1016/j.chemgeo.2017.03.015.

Lu, X., Dahl, T. W., Zheng, W., Wang, S., and Kendall, B. (2020). Estimating ancient seawater isotope compositions and global ocean redox conditions by coupling the molybdenum and uranium isotope systems of euxinic organic-rich mudrocks. *Geochimica et Cosmochimica Acta* 290, 76–103. DOI: 10.1016/j.gca.2020.08.032.

Lu, X., Edwards, C. T., and Kendall, B. (2023). No evidence for expansion of global ocean euxinia during the base Stairsian mass extinction event (Tremadocian, Early Ordovician). *Geochimica et Cosmochimica Acta* 341, 116–131. DOI: `10.1016/j.gca.2022.11.028`.

Lugmair, G., Scheinin, N., and Marti, K. (1975). Sm–Nd age and history of Apollo 17 basalt 75075-Evidence for early differentiation of the lunar exterior. In: *Lunar and Planetary Science Conference*. Vol. 6, 1419–1429.

Luu, T.-H., Chaussidon, M., Mishra, R. K., Rollion-Bard, C., Villeneuve, J., Srinivasan, G., and Birck, J.-L. (2013). High precision Mg isotope measurements of meteoritic samples by secondary ion mass spectrometry. *Journal of Analytical Atomic Spectrometry* 28.1, 67–76. DOI: `10.1039/C2JA30187C`.

Luu, T.-H., Hin, R. C., Coath, C. D., and Elliott, T. (2019). Bulk chondrite variability in mass independent magnesium isotope compositions–Implications for initial solar system ^{26}Al/^{27}Al and the timing of terrestrial accretion. *Earth and Planetary Science Letters* 522, 166–175. DOI: `10.1016/j.epsl.2019.06.033`.

MacPherson, G., Kita, N., Ushikubo, T., Bullock, E., and Davis, A. (2012). Well-resolved variations in the formation ages for Ca–Al-rich inclusions in the early Solar System. *Earth and Planetary Science Letters* 331, 43–54. DOI: `10.1016/j.epsl.2012.03.010`.

MacPherson, G., Bullock, E., Tenner, T., Nakashima, D., Kita, N., Ivanova, M., Krot, A., Petaev, M., and Jacobsen, S. (2017). High precision Al–Mg systematics of forsterite-bearing Type B CAIs from CV3 chondrites. *Geochimica et Cosmochimica Acta* 201, 65–82. DOI: `10.1016/j.gca.2016.12.006`.

Maden, C., Trinquier, A., Fauré, A.-L., Hubert, A., Pointurier, F., Rickli, J., and Bourdon, B. (2018). Design of a prototype thermal ionization cavity source intended for isotope ratio analysis. *International Journal of Mass Spectrometry* 434, 70–80. DOI: `10.1016/j.ijms.2018.09.006`.

Makishima, A. and Nakamura, E. (1991). Precise measurement of cerium isotope composition in rock samples. *Chemical Geology: Isotope Geoscience section* 94.1, 1–11. DOI: `10.1016/s0009-2541(10)80012-9`.

Mänd, K., Lalonde, S. V., Robbins, L. J., Thoby, M., Paiste, K., Kreitsmann, T., Paiste, P., Reinhard, C. T., Romashkin, A. E., Planavsky, N. J., et al. (2020). Palaeoproterozoic oxygenated oceans following the Lomagundi–Jatuli Event. *Nature Geoscience* 13.4, 302–306. DOI: `10.1038/s41561-020-0558-5`.

Marin, R. C., Sarkis, J. E., and Nascimento, M. R. (2013a). The use of LA-SF-ICP-MS for nuclear forensics purposes: uranium isotope ratio analysis. *Journal of Radioanalytical and Nuclear Chemistry* 295, 99–104. DOI: `10.1007/s10967-012-1980-y`.

Marin, R. C., Sarkis, J. E., and Nascimento, M. R. (2013b). The use of LA-SF-ICP-MS for nuclear forensics purposes: uranium isotope ratio analysis. *Journal of Radioanalytical and Nuclear Chemistry* 295, 99–104. DOI: `10.1007/s10967-012-1980-y`.

Marks, N., Borg, L., Hutcheon, I., Jacobsen, B., and Clayton, R. (2014). Samarium–neodymium chronology and rubidium–strontium systematics of an Allende calcium–aluminum-rich inclusion with implications for ^{146}Sm half-life. *Earth and Planetary Science Letters* 405, 15–24. DOI: `10.1016/j.epsl.2014.08.017`.

Marquez, R. T. and Tissot, F. L. (2022). COSMO: Double spike optimization for sample-limited analyses of isotopically anomalous materials. *Chemical Geology* 612, 121095. DOI: `10.1016/j.chemgeo.2022.121095`.

Martin, A. J. and Synge, R. L. (1941). A new form of chromatogram employing two liquid phases: A theory of chromatography. 2. Application to the micro-determination of the higher monoamino-acids in proteins. *Biochemical Journal* 35.12, 1358. DOI: `10.1042/bj0351358`.

Martin, A. N., Markowska, M., Chivas, A. R., and Weyer, S. (2023). Assessing the reliability of modern marine stromatolites as archives for the uranium isotope paleoredox proxy. *Geochimica et Cosmochimica Acta* 345, 75–89. DOI: `10.1016/j.gca.2023.01.011`.

Martin, E. and Haley, B. (2000). Fossil fish teeth as proxies for seawater Sr and Nd isotopes. *Geochimica et Cosmochimica Acta* 64.5, 835–847. DOI: `10.1016/S0016-7037(99)00376-2`.

Martin, E. and Scher, H. (2004). Preservation of seawater Sr and Nd isotopes in fossil fish teeth: bad news and good news. *Earth and Planetary Science Letters* 220.1-2, 25–39. DOI: `10.1016/S0012-821X(04)00030-5`.

Massart, D. and Bossaert, W. (1968). The prediction of elution maxima in the gradient elution of rare earths. *Journal of Chromatography A* 32, 195–200. DOI: `10.1016/S0021-9673(01)80485-4`.

Mathew, K., Mason, P., Voeks, A., and Narayanan, U. (2012). Uranium isotope abundance ratios in natural uranium metal certified reference material 112-A. *International Journal of Mass Spectrometry* 315, 8–14. DOI: `10.1016/j.ijms.2012.02.005`.

Mathew, K., O'Connor, G., Hasozbek, A., and Kraiem, M. (2013). Total evaporation method for uranium isotope-amount ratio measurements. *Journal of Analytical Atomic Spectrometry* 28.6, 866–876. DOI: `10.1039/c2ja30321c`.

Matsui, M., Aoki, T., and Kumagai, T. (1981). Forced-Flow Chromatography of Rare Earths Using Sensitive Spectrophotometry (Commemoration Issue Dedicated to Professor Megumi Tashiro on the Occation of His Retirement). *Bulletin of the Institute for Chemical Research, Kyoto University* 59.3, 207–211.

McCormack, J., Griffiths, M. L., Kim, S. L., Shimada, K., Karnes, M., Maisch, H., Pederzani, S., Bourgon, N., Jaouen, K., Becker, M. A., et al. (2022). Trophic position of Otodus megalodon and great white sharks through time revealed by zinc isotopes. *Nature Communications* 13.1, 2980. DOI: `10.1038/s41467-022-30528-9`.

McDonald, B. S., Partin, C. A., Sageman, B., and Holmden, C. (2022). Uranium isotope reconstruction of ocean deoxygenation during OAE 2 hampered by uncertainties in fractionation factors and local U-cycling. *Geochimica et Cosmochimica Acta* 331, 143–164. DOI: 10.1016/j.gca.2022.05.010.

McManus, J., Berelson, W. M., Klinkhammer, G. P., Hammond, D. E., and Holm, C. (2005). Authigenic uranium: relationship to oxygen penetration depth and organic carbon rain. *Geochimica et Cosmochimica Acta* 69.1, 95–108. DOI: 10.1016/j.gca.2004.06.023.

Meija, J., Coplen, T. B., Berglund, M., Brand, W. A., De Bièvre, P., Gröning, M., Holden, N. E., Irrgeher, J., Loss, R. D., Walczyk, T., et al. (2016). Atomic weights of the elements 2013 (IUPAC Technical Report). *Pure and Applied Chemistry* 88.3, 265–291. DOI: 10.1515/pac-2015-0305.

Meisel, T., Schöner, N., Paliulionyte, V., and Kahr, E. (2002). Determination of rare earth elements, Y, Th, Zr, Hf, Nb and Ta in geological reference materials G-2, G-3, SCo-1 and WGB-1 by sodium peroxide sintering and inductively coupled plasma-mass spectrometry. *Geostandards newsletter* 26.1, 53–61. DOI: 10.1111/j.1751-908x.2002.tb00623.x.

Merle, R., Amelin, Y., Yin, Q.-Z., Huyskens, M. H., Sanborn, M. E., Nagashima, K., Yamashita, K., Ireland, T. R., Krot, A. N., and Sieber, M. J. (2020). Exploring the efficiency of stepwise dissolution in removal of stubborn non-radiogenic Pb in chondrule U-Pb dating. *Geochimica et Cosmochimica Acta* 277, 1–20. DOI: 10.1016/j.gca.2020.03.010.

Metzger, S. C., Rogers, K. T., Bostick, D. A., McBay, E. H., Ticknor, B. W., Manard, B. T., and Hexel, C. R. (2019). Optimization of uranium and plutonium separations using TEVA and UTEVA cartridges for MC-ICP-MS analysis of environmental swipe samples. *Talanta* 198, 257–262. DOI: 10.1016/j.talanta.2019.02.034.

Metzger, S. C., Manard, B. T., Bostick, D. A., Ticknor, B. W., Rogers, K. T., McBay, E. H., Glasgow, D. C., Zirakparvar, N. A., and Hexel, C. R. (2021). An approach to separating Pu, U, and Ti from high-purity graphite for isotopic analysis by MC-ICP-MS. *Journal of Analytical Atomic Spectrometry* 36.6, 1150–1158. DOI: 10.1039/D1JA00079A.

Meyers, L. A., LaMont, S. P., Stalcup, A. M., and Spitz, H. B. (2014). Uranium isotopic signatures measured in samples of dirt collected at two former uranium facilities. *Journal of Radioanalytical and Nuclear Chemistry* 301, 307–313. DOI: 10.1007/s10967-014-3187-x.

Miall, A. D. (1979). Mesozoic and Tertiary geology of Banks Island, Arctic Canada: the history of an unstable craton margin. Vol. 387. Ottawa, Canada: Geological Survey of Canada.

Millard, A. R. and Hedges, R. E. (1996). A diffusion-adsorption model of uranium uptake by archaeological bone. *Geochimica et Cosmochimica Acta* 60.12, 2139–2152. DOI: 10.1016/0016-7037(96)00050-6.

Miller, R. F., Cloutier, R., and Turner, S. (2003). The oldest articulated chondrichthyan from the Early Devonian period. *Nature* 425.6957, 501–504. DOI: 10.1038/nature02001.

Mine, A., Waldeck, A., Olack, G., Hoerner, M., Alex, S., and Colman, A. (2017). Microprecipitation and δ^{18}O analysis of phosphate for paleoclimate and biogeochemistry research. *Chemical Geology* 460, 1–14. DOI: 10.1016/j.chemgeo.2017.03.032.

Minteer, M., Winkler, P., Wyatt, B., Moreland, S., Johnson, J., and Winters, T. (2007). Reliability of using ^{238}U/^{235}U and ^{234}U/^{238}U ratios from alpha spectrometry as qualitative indicators of enriched uranium contamination. *Health physics* 92.5, 488–495. DOI: 10.1097/01.HP.0000254847.21026.7c.

Mishra, R. K. and Chaussidon, M. (2014). Timing and extent of Mg and Al isotopic homogenization in the early inner Solar System. *Earth and Planetary Science Letters* 390, 318–326. DOI: 10.1016/j.epsl.2013.12.042.

Mishra, S., Kasar, S., Takamasa, A., Veerasamy, N., and Sahoo, S. (2019). Measurement of uranium distribution coefficient and ^{235}U/^{238}U ratio in soils affected by Fukushima dai-ichi nuclear power plant accident. *Journal of environmental radioactivity* 198, 36–42. DOI: 10.1016/j.jenvrad.2018.12.019.

Montoya-Pino, C., Weyer, S., Anbar, A. D., Pross, J., Oschmann, W., Schootbrugge, B. van de, and Arz, H. W. (2010). Global enhancement of ocean anoxia during Oceanic Anoxic Event 2: A quantitative approach using U isotopes. *Geology* 38.4, 315–318. DOI: 10.1130/G30652.1.

Moreno, E. C., Kresak, M., and Zahradnik, R. T. (1974). Fluoridated hydroxyapatite solubility and caries formation. *Nature* 247.5435, 64–65. DOI: 10.1038/247064a0.

Münker, C., Weyer, S., Scherer, E., and Mezger, K. (2001). Separation of high field strength elements (Nb, Ta, Zr, Hf) and Lu from rock samples for MC-ICPMS measurements. *Geochemistry, Geophysics, Geosystems* 2.12. DOI: 10.1029/2001gc000183.

Murphy, M. J., Stirling, C. H., Kaltenbach, A., Turner, S. P., and Schaefer, B. F. (2014). Fractionation of ^{238}U/^{235}U by reduction during low temperature uranium mineralisation processes. *Earth and Planetary Science Letters* 388, 306–317.

Nanne, J. A., Nimmo, F., Cuzzi, J. N., and Kleine, T. (2019). Origin of the noncarbonaceous–carbonaceous meteorite dichotomy. *Earth and Planetary Science Letters* 511, 44–54. DOI: 10.1016/j.epsl.2019.01.027.

Nash, K. L. and Jensen, M. P. (2001). Analytical-scale separations of the lanthanides: A review of techniques and fundamentals. *Separation Science and Technology* 36.5-6, 1257–1282. DOI: 10.1081/ss-100103649.

Neuilly, M., Bussac, J., Frejacques, C., Nief, G., Vendryes, G., and Yvon, J. (1972). Sur l'existence, dans un passé reculé, d'une réaction en chaine naturelle de fissions dans le gisement d'uranium d'Oklo (Gabon). *Comptes Rendus de l'Académie des Sciences* 275, 1847–1849.

Nier, A. O. (1938). The isotopic constitution of calcium, titanium, sulphur and argon. *Physical Review* 53.4, 282. DOI: 10.1103/PhysRev.53.282.

Nier, A. O. (1939). The isotopic constitution of uranium and the half-lives of uranium isotopes. *Physical Review* 55 (2), 150–153. DOI: `10.1103/PhysRev.55.150`.

Nir-El, Y. (2000). Isotopic analysis of uranium in U_3O_8 by passive gamma-ray spectrometry. *Applied Radiation and Isotopes* 52.3, 753–757. DOI: `10.1016/S0969-8043(99)00240-7`.

Noordmann, J., Weyer, S., Montoya-Pino, C., Dellwig, O., Neubert, N., Eckert, S., Paetzel, M., and Böttcher, M. (2015). Uranium and molybdenum isotope systematics in modern euxinic basins: Case studies from the central Baltic Sea and the Kyllaren fjord (Norway). *Chemical Geology* 396, 182–195. DOI: `10.1016/j.chemgeo.2014.12.012`.

Noordmann, J., Weyer, S., Georg, R. B., Jöns, S., and Sharma, M. (2016). $^{238}U/^{235}U$ isotope ratios of crustal material, rivers and products of hydrothermal alteration: new insights on the oceanic U isotope mass balance. *Isotopes in environmental and health studies* 52.1-2, 141–163. DOI: `10.1080/10256016.2015.1047449`.

O'Neil, J., Carlson, R. W., Francis, D., and Stevenson, R. K. (2008). Neodymium-142 evidence for Hadean mafic crust. *Science* 321.5897, 1828–1831. DOI: `10.1126/science.1161925`.

Ochoa, D., Salas-Gismondi, R., DeVries, T. J., Baby, P., Muizon, C. de, Altamirano, A., Barbosa-Espitia, A., Foster, D. A., Quispe, K., Cardich, J., et al. (2021). Late Neogene evolution of the Peruvian margin and its ecosystems: a synthesis from the Sacaco record. *International Journal of Earth Sciences* 110, 995–1025. DOI: `10.1007/s00531-021-02003-1`.

Oliveira, O. and Sarkis, J. (2002). Isotope measurements in uranium using a quadrupole inductively coupled plasma mass spectrometer (ICPMS). *Journal of Radioanalytical and Nuclear Chemistry* 253.3, 345–350. DOI: `10.1023/A:1020444814314`.

Ostrander, C. M., Kendall, B., Gordon, G. W., Nielsen, S. G., Zheng, W., and Anbar, A. D. (2022). Shale heavy metal isotope records of low environmental O_2 between two archean oxidation events. *Frontiers in Earth Science* 10, 833609. DOI: `10.3389/feart.2022.833609`.

Ounis, A., Kocsis, L., Chaabani, F., and Pfeifer, H.-R. (2008). Rare earth elements and stable isotope geochemistry ($\delta^{13}C$ and $\delta^{18}O$) of phosphorite deposits in the Gafsa Basin, Tunisia. *Palaeogeography, Palaeoclimatology, Palaeoecology* 268.1-2, 1–18. DOI: `10.1016/j.palaeo.2008.07.005`.

Owens, S., Buesseler, K., and Sims, K. (2011). Re-evaluating the ^{238}U-salinity relationship in seawater: Implications for the ^{238}U–^{234}Th disequilibrium method. *Marine Chemistry* 127.1-4, 31–39. DOI: `10.1016/j.marchem.2011.07.005`.

Padilla, A., Eberle, J. J., Gottfried, M. D., Sweet, A. R., and Hutchison, J. H. (2014). A sand tiger shark–dominated fauna from the Eocene Arctic greenhouse. *Journal of Vertebrate Paleontology* 34.6, 1307–1316. DOI: `10.1080/02724634.2014.880446`.

Pan, L., Desch, S. J., Scannapieco, E., and Timmes, F. (2012). Mixing of clumpy supernova ejecta into molecular clouds. *The Astrophysical Journal* 756.1, 102. DOI: `10.1088/0004-637X/756/1/102`.

Pan, W., Cao, M., Du, Y., Cheng, M., Zhou, Y.-Q., Algeo, T. J., Zhao, M.-Y., Thibault, N., Li, C., Wei, G.-Y., et al. (2021). Paired U and Mo isotope evidence for pervasive anoxia in the Cryogenian early interglacial ocean. *Precambrian Research* 361, 106244. DOI: 10.1016/j.precamres.2021.106244.

Pape, J., Mezger, K., Bouvier, A.-S., and Baumgartner, L. P. (2019). Time and duration of chondrule formation: Constraints from 26Al-26Mg ages of individual chondrules. *Geochimica et cosmochimica acta* 244, 416–436. DOI: 10.1016/j.gca.2018.10.017.

Pappas, R. S., Ting, B. G., and Paschal, D. C. (2003). A practical approach to determination of low concentration uranium isotope ratios in small volumes of urine. *Journal of Analytical Atomic Spectrometry* 18.10, 1289–1292. DOI: 10.1039/b305515a.

Parrish, R. R., Thirlwall, M. F., Pickford, C., Horstwood, M., Gerdes, A., Anderson, J., and Coggon, D. (2006). Determination of ^{238}U/^{235}U, ^{236}U/^{238}U and uranium concentration in urine using SF-ICP-MS and MC-ICP-MS: an interlaboratory comparison. *Health physics* 90.2, 127–138. DOI: 10.1097/01.HP.0000174809.43871.54.

Patchett, P. and Tatsumoto, M. (1981). A routine high-precision method for Lu-Hf isotope geochemistry and chronology. *Contributions to Mineralogy and Petrology* 75, 263–267. DOI: 10.1007/bf01166766.

Paton, C., Schiller, M., and Bizzarro, M. (2013). Identification of an ^{84}Sr-depleted carrier in primitive meteorites and implications for thermal processing in the solar protoplanetary disk. *The Astrophysical Journal Letters* 763.2, L40. DOI: 10.1088/2041-8205/763/2/L40.

Pazukhin, E. and Rudya, K. (2002). Isotopic composition of uranium in lava-like fuel-containing masses from the fourth block and radioactive fallout of the Chernobyl NPP service area. *Radiochemistry* 44, 621–625. DOI: 10.1023/A:1022348914071.

Peńkin, M., Boulyga, S., Dabbs, B., Fischer, D., Humphrey, M., Kochetkov, A., Koepf, A., and Sturm, M. (2018). Isotopic composition of commercially available uranium chemicals and elemental analysis standards. *Journal of Radioanalytical and Nuclear Chemistry* 316, 791–798. DOI: 10.1007/s10967-018-5740-5.

Peres, P., Hedberg, P., Walton, S., Montgomery, N., Cliff, J., Rabemananjara, F., and Schuhmacher, M. (2013). Nuclear safeguards applications using LG-SIMS with automated screening capabilities. *Surface and interface analysis* 45.1, 561–565. DOI: https://onlinelibrary.wiley.com/doi/10.1002/sia.5015.

Phan, T. T., Gardiner, J. B., Capo, R. C., and Stewart, B. W. (2018). Geochemical and multi-isotopic (^{87}Sr/^{86}Sr, ^{143}Nd/^{144}Nd, ^{238}U/^{235}U) perspectives of sediment sources, depositional conditions, and diagenesis of the Marcellus Shale, Appalachian Basin, USA. *Geochimica et Cosmochimica Acta* 222, 187–211. DOI: 10.1016/j.gca.2017.10.021.

Picard, S., Garcia, J.-P., Lécuyer, C., Sheppard, S. M., Cappetta, H., and Emig, C. C. (1998). δ^{18}O values of coexisting brachiopods and fish: Temperature differences and estimates of paleo–water depths. *Geology* 26.11, 975–978. DOI: 10.1130/0091-7613(1998)026<0975:OVOCBA>2.3.CO;2.

Pignatale, F. C., Charnoz, S., Chaussidon, M., and Jacquet, E. (2018). Making the planetary material diversity during the early assembling of the solar system. *The Astrophysical journal letters* 867.2, L23. DOI: 10.3847/2041-8213/aaeb22.

Pike, A. W. and Hedges, R. E. (2001). Sample geometry and U uptake in archaeological teeth: implications for U-series and ESR dating. *Quaternary science reviews* 20.5-9, 1021–1025. DOI: 10.1016/S0277-3791(00)00063-9.

Pimentel-Galvan, M., Lau, K. V., Maher, K., Mukerji, T., Lehrmann, D. J., Altiner, D., and Payne, J. L. (2022). Duration and Intensity of End-Permian Marine Anoxia. *Geochemistry, Geophysics, Geosystems* 23.1, e2021GC010130. DOI: 10.1029/2021gc010130.

Pin, C. and Gannoun, A. (2017). Integrated extraction chromatographic separation of the lithophile elements involved in long-lived radiogenic isotope systems (Rb–Sr, U–Th–Pb, Sm–Nd, La–Ce, and Lu–Hf) useful in geochemical and environmental sciences. *Analytical Chemistry* 89.4, 2411–2417. DOI: 10.1021/acs.analchem.6b04289.

Piralla, M., Villeneuve, J., Schnuriger, N., Bekaert, D. V., and Marrocchi, Y. (2023). A unified chronology of dust formation in the early solar system. *Icarus* 394, 115427. DOI: 10.1016/j.icarus.2023.115427.

Placzek, C. J., Heikoop, J. M., House, B., Linhoff, B. S., and Pelizza, M. (2016). Uranium isotope composition of waters from South Texas uranium ore deposits. *Chemical geology* 437, 44–55. DOI: 10.1016/j.chemgeo.2016.05.008.

Pogge von Strandmann, P. A., Stüeken, E. E., Elliott, T., Poulton, S. W., Dehler, C. M., Canfield, D. E., and Catling, D. C. (2015). Selenium isotope evidence for progressive oxidation of the Neoproterozoic biosphere. *Nature communications* 6.1, 10157. DOI: 10.1038/ncomms10157.

Pointurier, F., Pottin, A.-C., and Hubert, A. (2011). Application of nanosecond-UV laser ablation–inductively coupled plasma mass spectrometry for the isotopic analysis of single submicrometer-size uranium particles. *Analytical Chemistry* 83.20, 7841–7848. DOI: 10.1021/ac201596t.

Pointurier, F., Hubert, A., and Pottin, A.-C. (2013). Performance of laser ablation: quadrupole-based ICP-MS coupling for the analysis of single micrometric uranium particles. *Journal of Radioanalytical and Nuclear Chemistry* 296.2, 609–616. DOI: 10.1021/ac201596t.

Polyak, V. J., Curry, B. H., Lavery, D. J., Strasberg, Z. L., Cutler, S., Song, W., Crossey, L. J., Karlstrom, K. E., and Asmerom, Y. (2023). Large negative δ^{238}U anomalies in endogenic-type travertine systems. *Geology* 51.11, 1048–1052. DOI: 10.1130/G51333.1.

Pöml, P., Burakov, B., Geisler, T., Walker, C., Grange, M., Nemchin, A., Berndt, J., Fonseca, R., Bottomley, P., and Hasnaoui, R. (2013). Micro-analytical uranium isotope and chemical investigations of zircon crystals from the Chernobyl "lava" and their nuclear fuel inclusions. *Journal of nuclear materials* 439.1-3, 51–56. DOI: 10.1016/j.jnucmat.2013.03.031.

Pourjavid, M. R., Norouzi, P., and Ganjali, M. R. (2009). Light lanthanides determination by fast Fourier transform continuous cyclic voltammetry after separation by ion-exchange chromatography. *International Journal of Electrochemical Science* 4.7, 923–942. DOI: 10.1016/S1452-3981(23)15196-0.

Pourkhorsandi, H., Debaille, V., De Jong, J., and Armytage, R. M. (2021). Cerium stable isotope analysis of synthetic and terrestrial rock reference materials by MC-ICPMS. *Talanta* 224, 121877. DOI: 10.1016/j.talanta.2020.121877.

Pourmand, A., Dauphas, N., and Ireland, T. J. (2012). A novel extraction chromatography and MC-ICP-MS technique for rapid analysis of REE, Sc and Y: Revising CI-chondrite and Post-Archean Australian Shale (PAAS) abundances. *Chemical Geology* 291, 38–54. DOI: 10.1016/j.chemgeo.2011.08.011.

Pucéat, E., Lécuyer, C., Sheppard, S. M., Dromart, G., Reboulet, S., and Grandjean, P. (2003). Thermal evolution of Cretaceous Tethyan marine waters inferred from oxygen isotope composition of fish tooth enamels. *Paleoceanography* 18.2. DOI: 10.1029/2002PA000823.

Qaim, S., Ollig, H., and Blessing, G. (1979). Separation of lanthanides by preparative high pressure liquid chromatography. *Radiochimica Acta* 26.1, 59–62. DOI: 10.1524/ract.1979.26.1.59.

Quemet, A., Maloubier, M., Dalier, V., and Ruas, A. (2014). Development of an analysis method of minor uranium isotope ratio measurements using electron multipliers in thermal ionization mass spectrometry. *International Journal of Mass Spectrometry* 374, 26–32. DOI: 10.1016/j.ijms.2014.10.008.

Quemet, A., Maloubier, M., and Ruas, A. (2016). Contribution of the Faraday cup coupled to 10^{12} Ω current amplifier to uranium 235/238 and 234/238 isotope ratio measurements by thermal ionization mass spectrometry. *International Journal of Mass Spectrometry* 404, 35–39. DOI: 10.1016/j.ijms.2016.04.005.

Rademacher, L. K., Lundstrom, C. C., Johnson, T. M., Sanford, R. A., Zhao, J., and Zhang, Z. (2006). Experimentally determined uranium isotope fractionation during reduction of hexavalent U by bacteria and zero valent iron. *Environmental Science & Technology* 40.22, 6943–6948. DOI: 10.1021/es0604360.

Ranebo, Y., Eriksson, M., Tamborini, G., Niagolova, N., Bildstein, O., and Betti, M. (2007). The use of SIMS and SEM for the characterization of individual particles with a matrix originating from a nuclear weapon. *microscopy and microanalysis* 13.3, 179–190. DOI: 10.1017/S1431927607070353.

Ranebo, Y., Hedberg, P., Whitehouse, M., Ingeneri, K., and Littmann, S. (2009). Improved isotopic SIMS measurements of uranium particles for nuclear safeguard purposes. *Journal of Analytical Atomic Spectrometry* 24.3, 277–287. DOI: 10.1039/b810474c.

Raut, N. M., Jaison, P., and Aggarwal, S. K. (2004). Separation and determination of lanthanides, thorium and uranium using a dual gradient in reversed-phase liquid chromatography. *Journal of Chromatography A* 1052.1-2, 131–136. DOI: 10.1016/j.chroma.2004.08.054.

Rehkämper, M., Gärtner, M., Galer, S., and Goldstein, S. (1996). Separation of Ce from other rare-earth elements with application to Sm–Nd and La–Ce chronometry. *Chemical Geology* 129.3-4, 201–208. DOI: `10.1016/0009-2541(95)00143-3`.

Render, J., Fischer-Gödde, M., Burkhardt, C., and Kleine, T. (2017). The cosmic molybdenum-neodymium isotope correlation and the building material of the Earth. *Geochemical Perspectives Letters* 3, 170–178. DOI: `10.7185/geochemlet.1720`.

Rey, Á. del, Havsteen, J. C., Bizzarro, M., and Dahl, T. W. (2020). Untangling the diagenetic history of uranium isotopes in marine carbonates: A case study tracing the δ^{238}U composition of late Silurian oceans using calcitic brachiopod shells. *Geochimica et Cosmochimica Acta* 287, 93–110. DOI: `10.1016/j.gca.2020.06.002`.

Reynard, B., Lécuyer, C., and Grandjean, P. (1999). Crystal-chemical controls on rare-earth element concentrations in fossil biogenic apatites and implications for paleoenvironmental reconstructions. *Chemical Geology* 155.3-4, 233–241. DOI: `10.1016/S0009-2541(98)00169-7`.

Richter, F. M., Janney, P. E., Mendybaev, R. A., Davis, A. M., and Wadhwa, M. (2007). Elemental and isotopic fractionation of Type B CAI-like liquids by evaporation. *Geochimica et Cosmochimica Acta* 71.22, 5544–5564. DOI: `10.1016/j.gca.2007.09.005`.

Richter, S., Alonso, A., De Bolle, W., Wellum, R., and Taylor, P. (1999a). Isotopic “fingerprints" for natural uranium ore samples. *International Journal of Mass Spectrometry* 193.1, 9–14. DOI: `10.1016/S1387-3806(99)00102-5`.

Richter, S., Alonso, A., Wellum, R., and Taylor, P. D. (1999b). The isotopic composition of commercially available uranium chemical reagents. *Journal of Analytical Atomic Spectrometry* 14.5, 889–891. DOI: `10.1039/a900774a`.

Richter, S. and Goldberg, S. (2003). Improved techniques for high accuracy isotope ratio measurements of nuclear materials using thermal ionization mass spectrometry. *International Journal of Mass Spectrometry* 229.3, 181–197. DOI: `10.1016/S1387-3806(03)00338-5`.

Richter, S., Alonso, A., De Bolle, W., Kühn, H., Verbruggen, A., Wellum, R., and Taylor, P. (2005). Re-certification of a series of uranium isotope reference materials: IRMM-183, IRMM-184, IRMM-185, IRMM-186 and IRMM-187. *International Journal of Mass Spectrometry* 247.1-3, 37–39. DOI: `10.1016/j.ijms.2005.07.008`.

Richter, S., Alonso, A., Truyens, J., Kühn, H., Verbruggen, A., and Wellum, R. (2006). REIMEP 18: Inter-Laboratory Comparison for the Measurement of Uranium Isotopic Ratios in Nitric Acid Solution Report to Participants. *European Commission Joint Research Centre, Scientific and Technical Research Series: EUR 22244 EN.*

Richter, S., Alonso-Munoz, A., Eykens, R., Jacobsson, U., Kuehn, H., Verbruggen, A., Aregbe, Y., Wellum, R., and Keegan, E. (2008). The isotopic composition of natural uranium samples—Measurements using the new $n(^{233}\text{U})/n(^{236}\text{U}))$ double spike IRMM-3636. *International Journal of Mass Spectrometry* 269.1-2, 145–148. DOI: 10.1016/j.ijms.2007.09.012.

Richter, S., Eykens, R., Kühn, H., Aregbe, Y., Verbruggen, A., and Weyer, S. (2010). New average values for the $n(^{238}\mathrm{U})/n(^{235}\mathrm{U})$ isotope ratios of natural uranium standards. *International Journal of Mass Spectrometry* 295.1-2, 94–97. DOI: 10.1016/j.ijms.2010.06.004.

Richter, S., Kühn, H., Aregbe, Y., Hedberg, M., Horta-Domenech, J., Mayer, K., Zuleger, E., Bürger, S., Boulyga, S., Köpf, A., et al. (2011). Improvements in routine uranium isotope ratio measurements using the modified total evaporation method for multi-collector thermal ionization mass spectrometry. *Journal of Analytical Atomic Spectrometry* 26.3, 550–564. DOI: 10.1007/s10967-018-6166-9.

Richter, S., Venchiarutti, C., Hennessy, C., Jacobsson, U., Bujak, R., Truyens, J., and Aregbe, Y. (2018). Preparation and certification of the uranium nitrate solution reference materials series IRMM-2019 to IRMM-2029 for the isotopic composition. *Journal of Radioanalytical and Nuclear Chemistry* 318, 1359–1368. DOI: 10.1007/s10967-018-6166-9.

Rizo, H., Boyet, M., Blichert-Toft, J., and Rosing, M. (2011). Combined Nd and Hf isotope evidence for deep-seated source of Isua lavas. *Earth and Planetary Science Letters* 312.3-4, 267–279. DOI: 10.1016/j.epsl.2011.10.014.

Robinson, L. F., Belshaw, N. S., and Henderson, G. M. (2004). U and Th concentrations and isotope ratios in modern carbonates and waters from the Bahamas. *Geochimica et Cosmochimica Acta* 68.8, 1777–1789. DOI: 10.1016/j.gca.2003.10.005.

Robinson, L. F., Adkins, J. F., Keigwin, L. D., Southon, J., Fernandez, D. P., Wang, S., and Scheirer, D. S. (2005). Radiocarbon variability in the western North Atlantic during the last deglaciation. *Science* 310.5753, 1469–1473. DOI: 10.1126/science.1114832.

Rodríguez-Alvarez, M. and Sanchez, F. (1995). Behavior of uranium along Jucar River (Eastern Spain): determination of $^{234}\mathrm{U}/^{238}\mathrm{U}$ and $^{235}\mathrm{U}/^{238}\mathrm{U}$ ratios. *Journal of Radioanalytical and Nuclear Chemistry* 190.1, 113–120. DOI: 10.1007/BF02035642.

Roebbert, Y., Rosendahl, C. D., Brown, A., Schippers, A., Bernier-Latmani, R., and Weyer, S. (2021). Uranium isotope fractionation during the anoxic mobilization of noncrystalline U(IV) by ligand complexation. *Environmental Science & Technology* 55.12, 7959–7969. DOI: 10.1021/acs.est.0c08623.

Rolison, J. M., Stirling, C. H., Middag, R., and Rijkenberg, M. J. (2017). Uranium stable isotope fractionation in the Black Sea: Modern calibration of the $^{238}\mathrm{U}/^{235}\mathrm{U}$ paleo-redox proxy. *Geochimica et Cosmochimica Acta* 203, 69–88. DOI: 10.1016/j.gca.2016.12.014.

Romaniello, S. J., Herrmann, A. D., and Anbar, A. D. (2013). Uranium concentrations and $^{238}\mathrm{U}/^{235}\mathrm{U}$ isotope ratios in modern carbonates from the Bahamas: Assessing a novel paleoredox proxy. *Chemical Geology* 362, 305–316. DOI: 10.1016/j.chemgeo.2013.10.002.

Ronzani, A.-L., Hubert, A., Pointurier, F., Marie, O., Clavier, N., Humbert, A.-C., Aupiais, J., and Dacheux, N. (2019). Determination of the isotopic composition of single sub-micrometer-sized uranium particles by laser ablation coupled with multi-collector inductively coupled plasma mass spectrometry. *Rapid Communications in Mass Spectrometry* 33.5, 419–428. DOI: 10.1002/rcm.8366.

Rosholt, J., Butler, A., Garner, E., and Shields, W. (1965). Isotope fractionation of uranium in sandstone, Powder River basin, Wyoming, and Slick Rock District, Colorado. *Economic Geology* 60.2, 199–213. DOI: 10.2113/gsecongeo.60.2.199.

Rosholt, J. and Tatsumoto, M. (1970). Isotopic composition of uranium and thorium in Apollo 11 samples. In: *Proceedings Apollo 11 Lunar Science Conference*. Vol. 1, 1499.

Rosholt, J. N., Shields, W. R., and Garner, E. L. (1963). Isotopic fractionation of uranium in sandstone. *Science* 139.3551, 224–226. DOI: 10.1126/science.139.3551.224.

Rosholt, J. N. and Tatsumoto, M. (1971). Isotopic composition of thorium and uranium in Apollo 12 samples. In: *Proceedings of the Lunar Science Conference*. Vol. 2, 1577.

Roth, E. (1977). The discovery and study of the nuclear reactor in Oklo. *Journal of RadioAnalytical Chemistry* 37, 65–78. DOI: 10.1007/BF02520518.

Rouxel, O. J., Bekker, A., and Edwards, K. J. (2005). Iron isotope constraints on the Archean and Paleoproterozoic ocean redox state. *Science* 307.5712, 1088–1091. DOI: 10.1126/science.1105692.

Rovan, L. and Štrok, M. (2019). Optimization of the sample preparation and measurement protocol for the analysis of uranium isotopes by MC-ICP-MS without spike addition. *Journal of Analytical Atomic Spectrometry* 34.9, 1882–1891. DOI: 10.1039/c9ja00144a.

Rudge, J. F., Reynolds, B. C., and Bourdon, B. (2009). The double spike toolbox. *Chemical Geology* 265.3-4, 420–431. DOI: 10.1016/j.chemgeo.2009.05.010.

Rudnick, R. and Gao, S. (2014). Composition of the Continental Crust. In: *Treatise on Geochemistry (Second Edition)*. Ed. by H. D. Holland and K. K. Turekian. Second Edition. Oxford: Elsevier, 1–51. DOI: 10.1016/B978-0-08-095975-7.00301-6.

Sahoo, S. K., Isobe, H., Sato, T., Fujimoto, K., and Nakamura, Y. (2002). Precise determination of ^{235}U/^{238}U isotope ratio in soil samples by using thermal ionisation mass spectrometry. *Journal of Radioanalytical and Nuclear Chemistry* 252.2, 241–245. DOI: 10.1023/A:1015745717871.

Sahoo, S. K., Nakamura, Y., Shiraishi, K., and Masuda, A. (2004). Accurate measurement of uranium isotope ratios in soil samples using thermal ionization mass spectrometry equipped with a warp energy filter. *International Journal of Environmental Analytical Chemistry* 84.12, 919–926. DOI: 10.1080/03067310410001729015.

Saji, N. S., Wielandt, D., Holst, J. C., and Bizzarro, M. (2020). Solar system Nd isotope heterogeneity: Insights into nucleosynthetic components and protoplanetary disk evolution. *Geochimica et Cosmochimica Acta* 281, 135–148. DOI: 10.1016/j.gca.2020.05.006.

Sands, D., De Laeter, J., and Rosman, K. (2001). Measurements of neutron capture effects on Cd, Sm and Gd in lunar samples with implications for the neutron energy spectrum. *Earth and Planetary Science Letters* 186.3-4, 335–346. DOI: 10.1016/s0012-821x(01)00231-x.

Schauble, E. A. (2007). Role of nuclear volume in driving equilibrium stable isotope fractionation of mercury, thallium, and other very heavy elements. *Geochimica et Cosmochimica Acta* 71.9, 2170–2189. DOI: 10.1016/j.gca.2007.02.004.

Schiller, M., Connelly, J. N., Glad, A. C., Mikouchi, T., and Bizzarro, M. (2015a). Early accretion of protoplanets inferred from a reduced inner solar system ^{26}Al inventory. *Earth and Planetary Science Letters* 420, 45–54. DOI: 10.1016/j.epsl.2015.03.028.

Schiller, M., Paton, C., and Bizzarro, M. (2015b). Evidence for nucleosynthetic enrichment of the protosolar molecular cloud core by multiple supernova events. *Geochimica et cosmochimica acta* 149, 88–102. DOI: 10.1016/j.gca.2014.11.005.

Schiller, M., Bizzarro, M., and Fernandes, V. A. (2018). Isotopic evolution of the protoplanetary disk and the building blocks of Earth and the Moon. *Nature* 555.7697, 507–510. DOI: 10.1038/nature25990.

Schmitz, B., ÅBERG, G., Werdelin, L., Forey, P., and Bendix-Almgreen, S. E. (1991). ^{87}Sr/^{86}Sr, Na, F, Sr, and La in skeletal fish debris as a measure of the paleosalinity of fossil-fish habitats. *Geological Society of America Bulletin* 103.6, 786–794. DOI: 10.1130/0016-7606(1991)103<0786:SSNFSA>2.3.CO;2.

Schmitz, B., Ingram, S. L., Dockery III, D. T., and Åberg, G. (1997). Testing ^{87}Sr/^{86}Sr as a paleosalinity indicator on mixed marine, brackish-water and terrestrial vertebrate skeletal apatite in late Paleocene-early Eocene near-coastal sediments, Mississippi. *Chemical Geology* 140.3-4, 275–287. DOI: 10.1016/S0009-2541(97)00023-5.

Schramel, P. (2002). Determination of ^{235}U and ^{238}U in urine samples using sector field inductively coupled plasma mass spectrometry. *Journal of Chromatography B* 778.1-2, 275–278. DOI: 10.1016/S0378-4347(01)00462-5.

Scott, C., Lyons, T., Bekker, A., Shen, Y.-a., Poulton, S., Chu, X.-l., and Anbar, A. (2008). Tracing the stepwise oxygenation of the Proterozoic ocean. *Nature* 452.7186, 456–459. DOI: 10.1038/nature06811.

Segal, I., Halicz, L., and Platzner, I. T. (2003). Accurate isotope ratio measurements of ytterbium by multiple collection inductively coupled plasma mass spectrometry applying erbium and hafnium in an improved double external normalization procedure. *Journal of Analytical Atomic Spectrometry* 18.10, 1217–1223. DOI: 10.1039/b307016f.

Senftle, F., Stieff, L., Cuttitta, F., and Kuroda, P. K. (1957). Comparison of the isotopic abundance of U^{235} and U^{238} and the radium activity ratios in Colorado Plateau uranium ores. *Geochimica et Cosmochimica Acta* 11.3, 189–193. DOI: `10.1016/0016-7037(57)90081-9`.

Shannon, R. D. (1976). Revised effective ionic radii and systematic studies of interatomic distances in halides and chalcogenides. *Acta crystallographica section A: crystal physics, diffraction, theoretical and general crystallography* 32.5, 751–767. DOI: `10.1107/s0567739476001551`.

Sharp, Z. D., Atudorei, V., and Furrer, H. (2000). The effect of diagenesis on oxygen isotope ratios of biogenic phosphates. *American Journal of Science* 300.3, 222–237. DOI: `10.2475/ajs.300.3.222`.

Shaw, H. and Wasserburg, G. (1985). Sm-Nd in marine carbonates and phosphates: Implications for Nd isotopes in seawater and crustal ages. *Geochimica et Cosmochimica Acta* 49.2, 503–518. DOI: `10.1016/0016-7037(85)90042-0`.

Shemesh, A., Kolodny, Y., and Luz, B. (1983). Oxygen isotope variations in phosphate of biogenic apatites, II. Phosphorite rocks. *Earth and Planetary Science Letters* 64.3, 405–416. DOI: `10.1016/0012-821X(83)90101-2`.

Shibahara, Y., Kubota, T., Fujii, T., Fukutani, S., Takamiya, K., Konno, M., Mizuno, S., and Yamana, H. (2016). Determination of isotopic ratios of plutonium and uranium in soil samples by thermal ionization mass spectrometry. *Journal of Radioanalytical and Nuclear Chemistry* 307, 2281–2287. DOI: `10.1007/s10967-015-4551-1`.

Shiel, A. E., Laubach, P. G., Johnson, T. M., Lundstrom, C. C., Long, P. E., and Williams, K. H. (2013). No measurable changes in $^{238}U/^{235}U$ due to desorption–adsorption of U (VI) from groundwater at the Rifle, Colorado, integrated field research challenge site. *Environmental science & technology* 47.6, 2535–2541. DOI: `10.1021/es303913y`.

Shiel, A. E., Johnson, T., Lundstrom, C., Laubach, P., Long, P., and Williams, K. (2016). Reactive transport of uranium in a groundwater bioreduction study: Insights from high-temporal resolution $^{238}U/^{235}U$ data. *Geochimica et Cosmochimica Acta* 187, 218–236. DOI: `10.1016/j.gca.2016.05.020`.

Shimamura, T. and Lugmair, G. (1981). U-isotopic abundances. In: *Lunar and Planetary Science Conference*. Vol. 12, 976–978.

Shimizu, H., Umemoto, N., Masuda, A., and Appel, P. (1990). Sources of iron-formations in the Archean Isua and Malene supracrustals, West Greenland: Evidence from La-Ce and Sm-Nd isotopic data and REE abundances. *Geochimica et Cosmochimica Acta* 54.4, 1147–1154. DOI: `10.1016/0016-7037(90)90445-q`.

Shinonaga, T., Esaka, F., Magara, M., Klose, D., and Donohue, D. (2008). Isotopic analysis of single uranium and plutonium particles by chemical treatment and mass spectrometry. *Spectrochimica Acta Part B: Atomic Spectroscopy* 63.11, 1324–1328. DOI: `10.1016/j.sab.2008.09.001`.

Shollenberger, Q. R., Wittke, A., Render, J., Mane, P., Schuth, S., Weyer, S., Gussone, N., Wadhwa, M., and Brennecka, G. A. (2019). Combined mass-dependent and nucleosynthetic isotope variations in refractory inclusions and their mineral separates to determine their original Fe isotope compositions. *Geochimica et Cosmochimica Acta* 263, 215–234. DOI: 10.1016/j.gca.2019.07.021.

Shollenberger, Q. R. and Brennecka, G. A. (2020). Dy, Er, and Yb isotope compositions of meteorites and their components: Constraints on presolar carriers of the rare earth elements. *Earth and Planetary Science Letters* 529, 115866. DOI: 10.1016/j.epsl.2019.115866.

Simon, J. I. and Young, E. D. (2011). Resetting, errorchrons and the meaning of canonical CAI initial ^{26}Al/^{27}Al values. *Earth and Planetary Science Letters* 304.3-4, 468–482. DOI: 10.1016/j.epsl.2011.02.023.

Siron, G., Fukuda, K., Kimura, M., and Kita, N. T. (2021). New constraints from ^{26}Al-^{26}Mg chronology of anorthite bearing chondrules in unequilibrated ordinary chondrites. *Geochimica et cosmochimica acta* 293, 103–126. DOI: 10.1016/j.gca.2020.10.025.

Sisson, D., Mode, V. A., and Campbell, D. O. (1972). High-speed separation of the rare earths by ion exchange part II. *Journal of Chromatography A* 66.1, 129–135. DOI: 10.1016/s0021-9673(01)82936-8.

Sivaraman, N., Kumar, R., Subramaniam, S., and Vasudeva Rao, P. (2002). Separation of lanthanides using ion-interaction chromatography with HDEHP coated columns. *Journal of Radioanalytical and Nuclear Chemistry* 252, 491–495. DOI: 10.1023/a:1015894418606.

Smith, H. L. and Hoffman, D. C. (1956). Ion-exchange separations of the lanthanides and actinides by elution with ammonium alpha-hydroxy-isobutyrate. *Journal of Inorganic and Nuclear Chemistry* 3.3-4, 243–247. DOI: 10.1016/0022-1902(56)80025-0.

Smith, L. A. (1961). Variations in the uranium-235 content of fifteen ores. Oak Ridge Gaseous Diffusion Plant, Union Carbide Nuclear Company.

Snow, J. E. and Friedrich, J. M. (2005). Multiple ion counting ICPMS double spike method for precise U isotopic analysis at ultra-trace levels. *International Journal of Mass Spectrometry* 242.2-3, 211–215. DOI: 10.1016/j.ijms.2004.11.024.

Sobotovich, E. and Bondarenko, G. (2001). Isotopic composition of uranium in the products of accidental ejection from the Chernobyl NPP. In: *Radionuclides and Heavy Metals in Environment*. Springer, 77–84. DOI: 10.1007/978-94-010-0993-5_12.

Song, H., Song, H., Algeo, T. J., Tong, J., Romaniello, S. J., Zhu, Y., Chu, D., Gong, Y., and Anbar, A. D. (2017). Uranium and carbon isotopes document global-ocean redox-productivity relationships linked to cooling during the Frasnian-Famennian mass extinction. *Geology* 45.10, 887–890. DOI: 10.1130/G39393.1.

Spano, T. L., Simonetti, A., Balboni, E., Dorais, C., and Burns, P. C. (2017). Trace element and U isotope analysis of uraninite and ore concentrate: applications for nuclear forensic investigations. *Applied Geochemistry* 84, 277–285. DOI: 10.1016/j.apgeochem.2017.07.003.

Spivak-Birndorf, L. J., Bouvier, A., Benedix, G. K., Hammond, S., Brennecka, G. A., Howard, K., Rogers, N., Wadhwa, M., Bland, P. A., Spurnŷ, P., et al. (2015). Geochemistry and chronology of the Bunburra Rockhole ungrouped achondrite. *Meteoritics & Planetary Science* 50.5, 958–975. DOI: 10.1111/maps.12443.

Staudigel, H., Doyle, P., and Zindler, A. (1985). Sr and Nd isotope systematics in fish teeth. *Earth and Planetary Science Letters* 76.1-2, 45–56. DOI: 10.1016/0012-821X(85)90147-5.

Stebelkov, V., Elantyev, I., Hedberg, M., Wallenius, M., and Faure, A.-L. (2018). Determination of isotopic composition of uranium in the CMX-4 samples by SIMS. *Journal of Radioanalytical and Nuclear Chemistry* 315.2, 417–423. DOI: 10.1007/s10967-017-5664-5.

Stefánka, Z., Katona, R., and Varga, Z. (2008). Laser ablation assisted ICP-MS as a tool for rapid categorization of seized uranium oxide materials based on isotopic composition determination. *Journal of Analytical Atomic Spectrometry* 23.7, 1030–1033. DOI: 10.1039/b804199g.

Steiger, R. H. and Jäger, E. (1977). Subcommission on geochronology: convention on the use of decay constants in geo-and cosmochronology. *Earth and planetary science letters* 36.3, 359–362. DOI: 10.1016/0012-821X(77)90060-7.

Stirling, C. H., Halliday, A. N., and Porcelli, D. (2005). In search of live ^{247}Cm in the early solar system. *Geochimica et Cosmochimica Acta* 69.4, 1059–1071. DOI: 10.1016/j.gca.2004.06.034.

Stirling, C. H., Halliday, A. N., Potter, E.-K., Andersen, M. B., and Zanda, B. (2006). A low initial abundance of ^{247}Cm in the early solar system and implications for r-process nucleosynthesis. *Earth and Planetary Science Letters* 251.3-4, 386–397. DOI: 10.1016/j.epsl.2006.09.023.

Stirling, C. H., Andersen, M. B., Potter, E.-K., and Halliday, A. N. (2007). Low-temperature isotopic fractionation of uranium. *Earth and Planetary Science Letters* 264.1-2, 208–225. DOI: 10.1016/j.epsl.2007.09.019.

Stirling, C. H., Andersen, M. B., Warthmann, R., and Halliday, A. N. (2015). Isotope fractionation of ^{238}U and ^{235}U during biologically-mediated uranium reduction. *Geochimica et Cosmochimica Acta* 163, 200–218. DOI: 10.1016/j.gca.2015.03.017.

Stockey, R. G., Cole, D. B., Planavsky, N. J., Loydell, D. K., Frŷda, J., and Sperling, E. A. (2020). Persistent global marine euxinia in the early Silurian. *Nature Communications* 11.1, 1804. DOI: 10.1038/s41467-020-15400-y.

Story, J. N. and Fritz, J. S. (1974). Forced-flow chromatography of the lanthanides with continuous in-stream detection. *Talanta* 21.8, 892–894. DOI: 10.1016/0039-9140(74)80228-6.

Strelow, F. (1980). Quantitative separation of lanthanides and scandium from barium, strontium and other elements by cation-exchange chromatography in nitric acid. *Analytica Chimica Acta* 120, 249–254. DOI: 10.1016/s0003-2670(01)84368-3.

Stylo, M., Neubert, N., Roebbert, Y., Weyer, S., and Bernier-Latmani, R. (2015a). Mechanism of uranium reduction and immobilization in Desulfovibrio vulgaris biofilms. *Environmental science & technology* 49.17, 10553–10561. DOI: 10.1021/acs.est.5b01769.

Stylo, M., Neubert, N., Wang, Y., Monga, N., Romaniello, S. J., Weyer, S., and Bernier-Latmani, R. (2015b). Uranium isotopes fingerprint biotic reduction. *Proceedings of the National Academy of Sciences* 112.18, 5619–5624. DOI: 10.1073/pnas.1421841112.

Sus, F., Krtil, J., Bulovič, V., Klosová, E., and Maksimovič, Z. (1979). Determination of isotopic composition and concentration of uranium, plutonium and neodymium by mass-spectrometric isotope dilution in the irradiated fuel of the Czechoslovak atomic power station A-1. *Journal of RadioAnalytical Chemistry* 51, 143–151. DOI: 10.1007/BF02519932.

Suzuki, D., Saito-Kokubu, Y., Sakurai, S., Lee, C.-G., Magara, M., Iguchi, K., and Kimura, T. (2010). A new method for isotope ratio measurement of uranium in trace amount by thermal ionization mass spectrometry: the continuous heating method. *International Journal of Mass Spectrometry* 294.1, 23–27. DOI: 10.1016/j.ijms.2010.04.007.

Sweet, A. (2012). Applied research report on 5 outcrop samples collected by Andrew Miall from northern Banks Island. *NWT (NTS Map Sheets 098E/01, 08, 09): Geological Survey of Canada Paleontological report ARS-2012-01.*

Tamborini, G. (2004). SIMS analysis of uranium and actinides in microparticles of different origin. *Microchimica Acta* 145, 237–242. DOI: 10.1007/s00604-003-0160-8.

Tamborini, G., Betti, M., Forcina, V., Hiernaut, T., Giovannone, B., and Koch, L. (1998). Application of secondary ion mass spectrometry to the identification of single particles of uranium and their isotopic measurement. *Spectrochimica Acta Part B: Atomic Spectroscopy* 53.9, 1289–1302. DOI: 10.1016/S0584-8547(98)00121-9.

Tanaka, T. and Masuda, A. (1982). The La–Ce geochronometer: a new dating method. *Nature* 300.5892, 515–518. DOI: 10.1038/300515a0.

Tanaka, T., Shimizu, H., Kawata, Y., and Masuda, A. (1987). Combined La–Ce and Sm–Nd isotope systematics in petrogenetic studies. *Nature* 327.6118, 113–117. DOI: 10.1038/327113a0.

Tang, H., Liu, M.-C., McKeegan, K. D., Tissot, F. L., and Dauphas, N. (2017). In situ isotopic studies of the U-depleted Allende CAI Curious Marie: Pre-accretionary alteration and the co-existence of ^{26}Al and ^{36}Cl in the early solar nebula. *Geochimica et Cosmochimica Acta* 207, 1–18. DOI: 10.1016/j.gca.2017.03.001.

Tang, H., Szumila, I., Trail, D., and Young, E. D. (2021). Experimental determination of the effect of Cr on Mg isotope fractionation between spinel and forsterite. *Geochimica et Cosmochimica Acta* 296, 152–169. DOI: `10.1016/j.gca.2020.12.028`.

Tarhan, L. G., Planavsky, N. J., Wang, X., Bellefroid, E. J., Droser, M. L., and Gehling, J. G. (2018). The late-stage "ferruginization" of the Ediacara Member (Rawnsley Quartzite, South Australia): Insights from uranium isotopes. *Geobiology* 16.1, 35–48. DOI: `10.1111/gbi.12262`.

Tatsumoto, M. and Rosholt, J. N. (1970). Age of the moon: An isotopic study of uranium-thorium-lead systematics of lunar samples. *Science* 167.3918, 461–463. DOI: `10.1126/science.167.3918.461`.

Tatsumoto, M. and Shimamura, T. (1980). Evidence for live ^{247}Cm in the early solar system. *Nature* 286.5769, 118–122. DOI: `10.1038/286118a0`.

Taylor, R. N., Croudace, I. W., Warwick, P. E., and Dee, S. J. (1998). Precise and rapid determination of ^{238}U/^{235}U and uranium concentration in soil samples using thermal ionisation mass spectrometry. *Chemical geology* 144.1-2, 73–80. DOI: `10.1016/S0009-2541(97)00118-6`.

Telus, M., Dauphas, N., Moynier, F., Tissot, F. L., Teng, F.-Z., Nabelek, P. I., Craddock, P. R., and Groat, L. A. (2012). Iron, zinc, magnesium and uranium isotopic fractionation during continental crust differentiation: The tale from migmatites, granitoids, and pegmatites. *Geochimica et Cosmochimica Acta* 97, 247–265. DOI: `10.1016/j.gca.2012.08.024`.

Teng, F.-Z., Wadhwa, M., and Helz, R. T. (2007). Investigation of magnesium isotope fractionation during basalt differentiation: implications for a chondritic composition of the terrestrial mantle. *Earth and Planetary Science Letters* 261.1-2, 84–92. DOI: `10.1016/j.epsl.2007.06.004`.

Teng, F.-Z., Li, W.-Y., Ke, S., Yang, W., Liu, S.-A., Sedaghatpour, F., Wang, S.-J., Huang, K.-J., Hu, Y., Ling, M.-X., et al. (2015). Magnesium isotopic compositions of international geological reference materials. *Geostandards and Geoanalytical Research* 39.3, 329–339. DOI: `10.1111/j.1751-908X.2014.00326.x`.

Thiagarajan, N., Gerlach, D., Roberts, M. L., Burke, A., McNichol, A., Jenkins, W. J., Subhas, A. V., Thresher, R. E., and Adkins, J. F. (2013). Movement of deep-sea coral populations on climatic timescales. *Paleoceanography* 28.2, 227–236. DOI: `10.1002/palo.20023`.

Thomas, D. B., McGoverin, C. M., Fordyce, R. E., Frew, R. D., and Gordon, K. C. (2011). Raman spectroscopy of fossil bioapatite—a proxy for diagenetic alteration of the oxygen isotope composition. *Palaeogeography, Palaeoclimatology, Palaeoecology* 310.1-2, 62–70. DOI: `10.1016/j.palaeo.2011.06.016`.

Thrane, K., Connelly, J. N., Bizzarro, M., Meyer, B. S., et al. (2010). Origin of excess ^{176}Hf in meteorites. *The Astrophysical Journal* 717.2, 861. DOI: `10.1088/0004-637x/717/2/861`.

Tissot, F. L. and Ibañez-Mejia, M. (2021). Unlocking the single-crystal record of heavy stable isotopes. *Elements: An International Magazine of Mineralogy, Geochemistry, and Petrology* 17.6, 389–394. DOI: 10.2138/gselements.17.6.389.

Tissot, F. L. H. and Dauphas, N. (2015). Uranium isotopic compositions of the crust and ocean: Age corrections, U budget and global extent of modern anoxia. *Geochimica et Cosmochimica Acta* 167, 113–143. DOI: 10.1016/j.gca.2015.06.034.

Tissot, F. L. H., Dauphas, N., and Grossman, L. (2016). Origin of uranium isotope variations in early solar nebula condensates. *Science Advances* 2.3, e1501400. DOI: 10.1126/sciadv.1501400.

Tissot, F. L. H., Dauphas, N., and Grove, T. L. (2017). Distinct $^{238}U/^{235}U$ ratios and REE patterns in plutonic and volcanic angrites: Geochronologic implications and evidence for U isotope fractionation during magmatic processes. *Geochimica et Cosmochimica Acta* 213, 593–617. DOI: 10.1016/j.gca.2017.06.045.

Tissot, F. L. H., Chen, C., Go, B. M., Naziemiec, M., Healy, G., Bekker, A., Swart, P. K., and Dauphas, N. (2018). Controls of eustasy and diagenesis on the $^{238}U/^{235}U$ of carbonates and evolution of the seawater ($^{234}U/^{238}U$) during the last 1.4 Myr. *Geochimica et Cosmochimica Acta* 242, 233–265. DOI: 10.1016/j.gca.2018.08.022.

Tissot, F. L. H., Ibanez-Mejia, M., Boehnke, P., Dauphas, N., McGee, D., Grove, T. L., and Harrison, T. M. (2019a). $^{238}U/^{235}U$ measurement in single-zircon crystals: implications for the Hadean environment, magmatic differentiation and geochronology. *Journal of Analytical Atomic Spectrometry* 34.10, 2035–2052. DOI: 10.1039/C9JA00205G.

Tissot, F. L. H., Burkhardt, C., Budde, G., and Kleine, T. (2019b). Multi-elemental and isotopic characterization of coarse-grained Allende CAIs. In: *50th Annual Lunar and Planetary Science Conference*. 2132, 3136.

Todorov, T. I., Xu, H., Ejnik, J. W., Mullick, F. G., Squibb, K., McDiarmid, M. A., and Centeno, J. A. (2009). Depleted uranium analysis in blood by inductively coupled plasma mass spectrometry. *Journal of Analytical Atomic Spectrometry* 24.2, 189–193. DOI: 10.1039/b816058a.

Tolmachyov, S. Y., Kuwabara, J., and Noguchi, H. (2004). Flow injection extraction chromatography with ICP-MS for thorium and uranium determination in human body fluids. *Journal of Radioanalytical and Nuclear Chemistry* 261, 125–131. DOI: 10.1023/B:JRNC.0000030945.53499.1c.

Tostevin, R., Clarkson, M. O., Gangl, S., Shields, G. A., Wood, R. A., Bowyer, F., Penny, A. M., and Stirling, C. H. (2019). Uranium isotope evidence for an expansion of anoxia in terminal Ediacaran oceans. *Earth and Planetary Science Letters* 506, 104–112. DOI: 10.1016/j.epsl.2018.10.045.

Toyoda, K. and Tokonami, M. (1990). Diffusion of rare-earth elements in fish teeth from deep-sea sediments. *Nature* 345.6276, 607–609. DOI: 10.1038/345607a0.

Tribovillard, N., Algeo, T. J., Lyons, T., and Riboulleau, A. (2006). Trace metals as paleoredox and paleoproductivity proxies: an update. *Chemical geology* 232.1-2, 12–32. DOI: 10.1016/j.chemgeo.2006.02.012.

Trinquier, A., Elliott, T., Ulfbeck, D., Coath, C., Krot, A. N., and Bizzarro, M. (2009). Origin of nucleosynthetic isotope heterogeneity in the solar protoplanetary disk. *Science* 324.5925, 374–376. DOI: 10.1126/science.1168221.

Trinquier, A., Maden, C., Fauré, A.-L., Hubert, A., Pointurier, F., Bourdon, B., and Schönbächler, M. (2019). More than five percent ionization efficiency by cavity source thermal ionization mass spectrometry for uranium subnanogram amounts. *Analytical Chemistry* 91.9, 6190–6199. DOI: 10.1021/acs.analchem.9b00849.

Tripathi, R., Sahoo, S., Mohapatra, S., Lenka, P., Dubey, J., and Puranik, V. (2013). Study of uranium isotopic composition in groundwater and deviation from secular equilibrium condition. *Journal of Radioanalytical and Nuclear Chemistry* 295, 1195–1200. DOI: 10.1007/s10967-012-1992-7.

Trotter, J. A. and Eggins, S. M. (2006). Chemical systematics of conodont apatite determined by laser ablation ICPMS. *Chemical Geology* 233.3-4, 196–216. DOI: 10.1016/j.chemgeo.2006.03.004.

Trueman, C. N. and Tuross, N. (2002). Trace elements in recent and fossil bone apatite. *Reviews in mineralogy and geochemistry* 48.1, 489–521. DOI: 10.2138/rmg.2002.48.13.

Tuli, J. K. et al. (1995). Nuclear wallet cards. Brookhaven National Laboratory.

Tütken, T., Vennemann, T. W., and Pfretzschner, H.-U. (2011). Nd and Sr isotope compositions in modern and fossil bones–Proxies for vertebrate provenance and taphonomy. *Geochimica et Cosmochimica Acta* 75.20, 5951–5970. DOI: 10.1016/j.gca.2011.07.024.

Tütken, T., Weber, M., Zohar, I., Helmy, H., Bourgon, N., Lernau, O., Jochum, K. P., and Sisma-Ventura, G. (2020). Strontium and oxygen isotope analyses reveal Late Cretaceous shark teeth in Iron Age strata in the Southern Levant. *Frontiers in Ecology and Evolution* 8, 570032. DOI: 10.3389/fevo.2020.570032.

Uvarova, Y. A., Kyser, T. K., Geagea, M. L., and Chipley, D. (2014). Variations in the uranium isotopic compositions of uranium ores from different types of uranium deposits. *Geochimica et Cosmochimica Acta* 146, 1–17. DOI: 10.1016/j.gca.2014.09.034.

Van der Walt, T., Strelow, F., and Verheij, R. (1985). Influence of crosslinkage on the distribution coefficients and anion exchange behavior of some elements in hydrochloric acid. *Solvent Extraction and Ion Exchange* 3.5, 723–740. DOI: 10.1080/07366298508918536.

Van Orman, J. A., Cherniak, D. J., and Kita, N. T. (2014). Magnesium diffusion in plagioclase: Dependence on composition, and implications for thermal resetting of the 26Al–26Mg early solar system chronometer. *Earth and Planetary Science Letters* 385, 79–88. DOI: 10.1016/j.epsl.2013.10.026.

Varga, Z., Krachler, M., Nicholl, A., Ernstberger, M., Wiss, T., Wallenius, M., and Mayer, K. (2018). Accurate measurement of uranium isotope ratios in solid samples by laser ablation multi-collector inductively coupled plasma mass spectrometry. *Journal of Analytical Atomic Spectrometry* 33.6, 1076–1080. DOI: 10.1039/c8ja00006a.

Varga, Z. (2008). Application of laser ablation inductively coupled plasma mass spectrometry for the isotopic analysis of single uranium particles. *Analytica Chimica Acta* 625.1, 1–7. DOI: 10.1016/j.aca.2008.07.012.

Veerasamy, N., Takamasa, A., Murugan, R., Kasar, S., Aono, T., Inoue, K., Fukushi, M., and Sahoo, S. K. (2020). Chemical separation of uranium and precise measurement of 234U/238U and 235U/238U ratios in soil samples using multi collector inductively coupled plasma mass spectrometry. *Molecules* 25.9, 2138. DOI: 10.3390/molecules25092138.

Vennemann, T. W. and Hegner, E. (1998). Oxygen, strontium, and neodymium isotope composition of fossil shark teeth as a proxy for the palaeoceanography and palaeoclimatology of the Miocene northern Alpine Paratethys. *Palaeogeography, Palaeoclimatology, Palaeoecology* 142.3-4, 107–121. DOI: 10.1016/S0031-0182(98)00062-5.

Vennemann, T. W., Hegner, E., Cliff, G., and Benz, G. (2001). Isotopic composition of recent shark teeth as a proxy for environmental conditions. *Geochimica et Cosmochimica Acta* 65.10, 1583–1599. DOI: 10.1016/S0016-7037(00)00629-3.

Verbruggen, A., Alonso, A., Eykens, R., Kehoe, F., Kuhn, H., Richter, S., and Aregbe, Y. (2008). Preparation and certification of IRMM-3636, IRMM-3636a and IRMM-3636b. *JRC Scientific and Technical Reports.*

Vermeesch, P. (2018). IsoplotR: A free and open toolbox for geochronology. *Geoscience Frontiers* 9.5, 1479–1493. DOI: 10.1016/j.gsf.2018.04.001.

Villeneuve, J., Chaussidon, M., and Libourel, G. (2009). Homogeneous distribution of ^{26}Al in the solar system from the Mg isotopic composition of chondrules. *Science* 325.5943, 985–988. DOI: 10.1126/science.1173907.

Waddell, L. M. and Moore, T. C. (2008). Salinity of the Eocene Arctic Ocean from oxygen isotope analysis of fish bone carbonate. *Paleoceanography* 23.1. DOI: 10.1029/2007PA001451.

Wadhwa, M., Kita, N., Nakashima, D., Bullock, E., MacPherson, G., and Bouvier, A. (2014). High Precision ^{26}Al-^{26}Mg Systematics for an Almost Pristine Refractory Inclusion: Implications for the Absolute Age of the Solar System. In: *45th Lunar and Planetary Science Conference*, Abstract #2698.

Walder, A. J. and Freedman, P. A. (1992). Communication. Isotopic ratio measurement using a double focusing magnetic sector mass analyser with an inductively coupled plasma as an ion source. *Journal of Analytical Atomic Spectrometry* 7.3, 571–575. DOI: 10.1039/JA9920700571.

Wall, J. D. and Krumholz, L. R. (2006). Uranium reduction. *Annual Review of Microbiology* 60, 149–166.

Wang, M., Audi, G., Wapstra, A., Kondev, F., MacCormick, M., Xu, X., and Pfeiffer, B. (2012). The Ame2012 atomic mass evaluation. *Chinese physics C* 36.12, 1603. DOI: 10.1088/1674-1137/36/12/003.

Wang, W.-q., Zhang, F., Shen, S.-z., Bizzarro, M., Garbelli, C., Zheng, Q.-f., Zhang, Y.-c., Yuan, D.-x., Shi, Y.-k., Cao, M., et al. (2022). Constraining marine anoxia under the extremely oxygenated Permian atmosphere using uranium isotopes in calcitic brachiopods and marine carbonates. *Earth and Planetary Science Letters* 594, 117714. DOI: 10.1016/j.epsl.2022.117714.

Wang, X., Johnson, T. M., and Lundstrom, C. C. (2015a). Isotope fractionation during oxidation of tetravalent uranium by dissolved oxygen. *Geochimica et Cosmochimica Acta* 150, 160–170. DOI: 10.1016/j.gca.2014.12.007.

Wang, X., Johnson, T. M., and Lundstrom, C. C. (2015b). Low temperature equilibrium isotope fractionation and isotope exchange kinetics between U(IV) and U(VI). *Geochimica et Cosmochimica Acta* 158, 262–275.

Wang, X., Planavsky, N. J., Reinhard, C. T., Hein, J. R., and Johnson, T. M. (2016). A Cenozoic seawater redox record derived from $^{238}U/^{235}U$ in ferromanganese crusts. *American Journal of Science* 316.1, 64–83. DOI: 10.2475/01.2016.02.

Wang, X., Planavsky, N. J., Hofmann, A., Saupe, E. E., De Corte, B. P., Philippot, P., LaLonde, S. V., Jemison, N. E., Zou, H., Ossa, F. O., et al. (2018). A Mesoarchean shift in uranium isotope systematics. *Geochimica et Cosmochimica Acta* 238, 438–452. DOI: 10.1016/j.gca.2018.07.024.

Wang, X., Ossa, F. O., Hofmann, A., Agangi, A., Paprika, D., and Planavsky, N. J. (2020). Uranium isotope evidence for Mesoarchean biological oxygen production in shallow marine and continental settings. *Earth and Planetary Science Letters* 551, 116583. DOI: 10.1016/j.epsl.2020.116583.

Wang, X. T., Sigman, D. M., Prokopenko, M. G., Adkins, J. F., Robinson, L. F., Hines, S. K., Chai, J., Studer, A. S., Martínez-García, A., Chen, T., et al. (2017). Deep-sea coral evidence for lower Southern Ocean surface nitrate concentrations during the last ice age. *Proceedings of the National Academy of Sciences* 114.13, 3352–3357. DOI: 10.1073/pnas.1615718114.

Warneke, T., Croudace, I. W., Warwick, P. E., and Taylor, R. N. (2002). A new ground-level fallout record of uranium and plutonium isotopes for northern temperate latitudes. *Earth and Planetary Science Letters* 203.3-4, 1047–1057. DOI: 10.1016/S0012-821X(02)00930-5.

Wasserburg, G., Papanastassiou, D., Nenow, E., and Bauman, C. (1969). A programmable magnetic field mass spectrometer with on-line data processing. *Review of Scientific Instruments* 40.2, 288–295. DOI: 10.1063/1.1683921.

Wasserburg, G., Jacobsen, S., DePaolo, D., McCulloch, M., and Wen, T. (1981). Precise determination of SmNd ratios, Sm and Nd isotopic abundances in standard solutions. *Geochimica et Cosmochimica Acta* 45.12, 2311–2323. DOI: 10.1016/0016-7037(81)90085-5.

Wasserburg, G., Wimpenny, J., and Yin, Q.-Z. (2012). Mg isotopic heterogeneity, Al-Mg isochrons, and canonical ^{26}Al/^{27}Al in the early solar system. *Meteoritics & Planetary Science* 47.12, 1980–1997. DOI: `10.1111/maps.12014`.

Watrous, M. G. and Delmore, J. E. (2011). Measurement of trace uranium isotopes using a porous ion emitter. *International Journal of Mass Spectrometry* 303.1, 1–5. DOI: `10.1016/j.ijms.2010.11.016`.

Wei, G.-Y., Planavsky, N. J., Tarhan, L. G., Chen, X., Wei, W., Li, D., and Ling, H.-F. (2018). Marine redox fluctuation as a potential trigger for the Cambrian explosion. *Geology* 46.7, 587–590. DOI: `10.1130/G40150.1`.

Wei, G.-Y., Planavsky, N. J., Tarhan, L. G., He, T., Wang, D., Shields, G. A., Wei, W., and Ling, H.-F. (2020). Highly dynamic marine redox state through the Cambrian explosion highlighted by authigenic δ^{238}U records. *Earth and Planetary Science Letters* 544, 116361. DOI: `10.1016/j.epsl.2020.116361`.

Wei, G.-Y., Planavsky, N. J., He, T., Zhang, F., Stockey, R. G., Cole, D. B., Lin, Y.-B., and Ling, H.-F. (2021). Global marine redox evolution from the late Neoproterozoic to the early Paleozoic constrained by the integration of Mo and U isotope records. *Earth-Science Reviews* 214, 103506. DOI: `10.1016/j.earscirev.2021.103506`.

Weyer, S., Anbar, A., Gerdes, A., Gordon, G., Algeo, T., and Boyle, E. (2008). Natural fractionation of ^{238}U/^{235}U. *Geochimica et Cosmochimica Acta* 72.2, 345–359. DOI: `10.1016/j.gca.2007.11.012`.

White, D. A., Elrick, M., Romaniello, S., and Zhang, F. (2018). Global seawater redox trends during the Late Devonian mass extinction detected using U isotopes of marine limestones. *Earth and Planetary Science Letters* 503, 68–77. DOI: `10.1016/j.epsl.2018.09.020`.

White, W. M. and Hofmann, A. W. (1982). Sr and Nd isotope geochemistry of oceanic basalts and mantle evolution. *Nature* 296.5860, 821–825. DOI: `10.1038/296821a0`.

Willig, M. and Stracke, A. (2018). Accurate and precise measurement of Ce isotope ratios by thermal ionization mass spectrometry (TIMS). *Chemical Geology* 476, 119–129. DOI: `10.1016/j.chemgeo.2017.11.010`.

Willig, M. and Stracke, A. (2019). Earth's chondritic light rare earth element composition: Evidence from the Ce–Nd isotope systematics of chondrites and oceanic basalts. *Earth and Planetary Science Letters* 509, 55–65. DOI: `10.1016/j.epsl.2018.12.004`.

Wombacher, F., Eisenhauer, A., Heuser, A., and Weyer, S. (2009). Separation of Mg, Ca and Fe from geological reference materials for stable isotope ratio analyses by MC-ICP-MS and double-spike TIMS. *Journal of Analytical Atomic Spectrometry* 24.5, 627–636. DOI: `10.1039/B820154D`.

Xiao, G., Jones, R. L., Saunders, D., and Caldwell, K. L. (2014). Determination of ^{234}U/^{238}U, ^{235}U/^{238}U and ^{236}U/^{238}U isotope ratios in urine using sector field inductively coupled plasma mass spectrometry. *Radiation Protection Dosimetry* 162.4, 618–624. DOI: `10.1093/rpd/ncu023`.

Yamamoto, K., Asanuma, H., Takahashi, H., and Hirata, T. (2021). In situ isotopic analysis of uranium using a new data acquisition protocol for 10^{13} ohm Faraday amplifiers. *Journal of Analytical Atomic Spectrometry* 36.3, 668–675. DOI: 10.1039/d0ja00498g.

Yamamoto, M., Kawabata, Y., Murata, Y., and Komura, K. (2002). Variation of uranium isotopic composition in soil within the JCO grounds from the 30 September 1999 criticality accident at JCO, Tokai-Mura, Japan. *Health physics* 83.2, 197–203. DOI: 10.1097/00004032-200208000-00005.

Yang, L. and Ciesla, F. J. (2012). The effects of disk building on the distributions of refractory materials in the solar nebula. *Meteoritics & Planetary Science* 47.1, 99–119. DOI: 10.1111/j.1945-5100.2011.01315.x.

Yang, S. and Liu, Y. (2016). Nuclear field shift effects on stable isotope fractionation: a review. *Acta Geochimica* 35, 227–239. DOI: 10.1007/s11631-016-0109-3.

Yang, S., Kendall, B., Lu, X., Zhang, F., and Zheng, W. (2017). Uranium isotope compositions of mid-Proterozoic black shales: Evidence for an episode of increased ocean oxygenation at 1.36 Ga and evaluation of the effect of post-depositional hydrothermal fluid flow. *Precambrian Research* 298, 187–201. DOI: 10.1016/j.precamres.2017.06.016.

Yang, Y.-h., Zhang, H.-f., Chu, Z.-y., Xie, L.-w., and Wu, F.-y. (2010). Combined chemical separation of Lu, Hf, Rb, Sr, Sm and Nd from a single rock digest and precise and accurate isotope determinations of Lu–Hf, Rb–Sr and Sm–Nd isotope systems using Multi-Collector ICP-MS and TIMS. *International Journal of Mass Spectrometry* 290.2-3, 120–126. DOI: 10.1016/j.ijms.2009.12.011.

Yomogida, T., Esaka, F., and Magara, M. (2017). Chemical state and isotope ratio analysis of individual uranium particles by a combination of micro-Raman spectroscopy and secondary ion mass spectrometry. *Analytical Methods* 9.44, 6261–6266. DOI: 10.1039/c7ay01815k.

Young, E., Tonui, E., Manning, C., Schauble, E., and Macris, C. (2009). Spinel–olivine magnesium isotope thermometry in the mantle and implications for the Mg isotopic composition of Earth. *Earth and Planetary Science Letters* 288.3-4, 524–533. DOI: 10.1016/j.epsl.2009.10.014.

Zazzo, A., Lécuyer, C., Sheppard, S. M., Grandjean, P., and Mariotti, A. (2004a). Diagenesis and the reconstruction of paleoenvironments: a method to restore original δ^{18}O values of carbonate and phosphate from fossil tooth enamel. *Geochimica et Cosmochimica Acta* 68.10, 2245–2258. DOI: 10.1016/j.gca.2003.11.009.

Zazzo, A., Lécuyer, C., and Mariotti, A. (2004b). Experimentally-controlled carbon and oxygen isotope exchange between bioapatites and water under inorganic and microbially-mediated conditions. *Geochimica et Cosmochimica Acta* 68.1, 1–12. DOI: 10.1016/S0016-7037(03)00278-3.

Zhang, F., Algeo, T. J., Romaniello, S. J., Cui, Y., Zhao, L., Chen, Z.-Q., and Anbar, A. D. (2018a). Congruent Permian-Triassic δ^{238}U records at Panthalassic and Tethyan sites: Confirmation of global-oceanic anoxia and validation of the U-isotope paleoredox proxy. *Geology* 46.4, 327–330. DOI: 10.1130/G39695.1.

Zhang, F., Xiao, S., Kendall, B., Romaniello, S. J., Cui, H., Meyer, M., Gilleaudeau, G. J., Kaufman, A. J., and Anbar, A. D. (2018b). Extensive marine anoxia during the terminal Ediacaran Period. *Science advances* 4.6, eaan8983. DOI: 10.1126/sciadv.aan8983.

Zhang, F., Romaniello, S. J., Algeo, T. J., Lau, K. V., Clapham, M. E., Richoz, S., Herrmann, A. D., Smith, H., Horacek, M., and Anbar, A. D. (2018c). Multiple episodes of extensive marine anoxia linked to global warming and continental weathering following the latest Permian mass extinction. *Science advances* 4.4, e1602921. DOI: 10.1126/sciadv.1602921.

Zhang, F., Xiao, S., Romaniello, S. J., Hardisty, D., Li, C., Melezhik, V., Pokrovsky, B., Cheng, M., Shi, W., Lenton, T. M., et al. (2019a). Global marine redox changes drove the rise and fall of the Ediacara biota. *Geobiology* 17.6, 594–610. DOI: 10.1111/gbi.12359.

Zhang, F., Algeo, T. J., Cui, Y., Shen, J., Song, H., Sano, H., Rowe, H. D., and Anbar, A. D. (2019b). Global-ocean redox variations across the Smithian-Spathian boundary linked to concurrent climatic and biotic changes. *Earth-Science Reviews* 195, 147–168. DOI: 10.1016/j.earscirev.2018.10.012.

Zhang, F., Dahl, T. W., Lenton, T. M., Luo, G., Shen, S.-z., Algeo, T. J., Planavsky, N., Liu, J., Cui, Y., Qie, W., et al. (2020a). Extensive marine anoxia associated with the Late Devonian Hangenberg Crisis. *Earth and Planetary Science Letters* 533, 115976. DOI: 10.1016/j.epsl.2019.115976.

Zhang, F., Shen, S.-z., Cui, Y., Lenton, T. M., Dahl, T. W., Zhang, H., Zheng, Q.-f., Wang, W., Krainer, K., and Anbar, A. D. (2020b). Two distinct episodes of marine anoxia during the Permian-Triassic crisis evidenced by uranium isotopes in marine dolostones. *Geochimica et Cosmochimica Acta* 287, 165–179. DOI: 10.1016/j.gca.2020.01.032.

Zhang, F., Lenton, T. M., Rey, Á. del, Romaniello, S. J., Chen, X., Planavsky, N. J., Clarkson, M. O., Dahl, T. W., Lau, K. V., Wang, W., et al. (2020c). Uranium isotopes in marine carbonates as a global ocean paleoredox proxy: a critical review. *Geochimica et Cosmochimica Acta* 287, 27–49. DOI: 10.1016/j.gca.2020.05.011.

Zhang, F., Stockey, R. G., Xiao, S., Shen, S.-z., Dahl, T. W., Wei, G.-Y., Cao, M., Li, Z., Kang, J., Cui, Y., et al. (2022). Uranium isotope evidence for extensive shallow water anoxia in the early Tonian oceans. *Earth and Planetary Science Letters* 583, 117437. DOI: 10.1016/j.epsl.2022.117437.

Zhang, Q., Ding, L., Chen, X., Brennecka, G. A., Sun, Y., Ma, X., Gao, B., Zhang, Q., and Willems, H. (2023). The large decline in carbonate δ^{238}U from a PETM section at Tingri (South Tibet) was driven by local sea-level changes, not global oceanic anoxia. *Earth and Planetary Science Letters* 612, 118164. DOI: 10.1016/j.epsl.2023.118164.

Zhang, X. Z., Esaka, F., Esaka, K. T., Magara, M., Sakurai, S., Usuda, S., and Watanabe, K. (2007). Application of inductively coupled plasma mass spectrometry to the determination of uranium isotope ratios in individual particles for nuclear safeguards. *Spectrochimica Acta Part B: Atomic Spectroscopy* 62.10, 1130–1134. DOI: 10.1016/j.sab.2007.06.013.

Zhao, H., Algeo, T. J., Liu, Y., Chen, Z.-Q., Zhang, L., Hu, Z., and Li, Z. (2020). Lower Triassic carbonate δ^{238}U record demonstrates expanded oceanic anoxia during Smithian Thermal Maximum and improved ventilation during Smithian-Spathian boundary cooling event. *Palaeogeography, Palaeoclimatology, Palaeoecology* 539, 109393. DOI: 10.1016/j.palaeo.2019.109393.

Zoriy, M., Kayser, M., Izmer, A., Pickhardt, C., and Becker, J. S. (2005). Determination of uranium isotopic ratios in biological samples using laser ablation inductively coupled plasma double focusing sector field mass spectrometry with cooled ablation chamber. *International Journal of Mass Spectrometry* 242.2-3, 297–302. DOI: 10.1016/j.ijms.2004.10.026.